Queen Mary University of London

School of Physics and Astronomy

Astronomy Unit

Doctoral Thesis

Disc and Planet Evolution in Circumbinary Systems

Author:
Matthew M. Mutter

Supervisor:
Dr. Richard P. Nelson

A thesis submitted in partial fulfillment of the requirements for the Degree of Doctor of Philosophy

December 22, 2017

Declaration

I, Matthew M. Mutter, confirm that the research included within this thesis is my own work or that where it has been carried out in collaboration with, or supported by others, that this is duly acknowledged below and my contribution indicated. Previously published material is also acknowledged below.

I attest that I have exercised reasonable care to ensure that the work is original, and does not to the best of my knowledge break any UK law, infringe any third party's copyright or other Intellectual Property Right, or contain any confidential material.

I accept that the College has the right to use plagiarism detection software to check the electronic version of the thesis.

I confirm that this thesis has not been previously submitted for the award of a degree by this or any other university.

The copyright of this thesis rests with the author and no quotation from it or information derived from it may be published without the prior written consent of the author.

Signed:

Date:

Details of collaboration and publications can be found below. All the work in this thesis has been undertaken in collaboration with my supervisor, Professor Richard Nelson. In addition, the projects presented in Chapters 3, 4, and 5 were undertaken in collaboration with Dr Arnaud Pierens of the Université de Bordeaux and Laboratoire d'Astrophysique de Bordeaux, France. Unless otherwise stated, all figures in this thesis have been created by the author. This work was supported by an STFC PhD studentship, grant no. STFC ST/K50225X/1. Computer time for the simulations was provided by: HPC resources of Cines under the allocation A0010406957 made by GENCI (Grand Equipement National de Calcul Intensif); Queen Mary's MidPlus computational facilities, supported by QMUL Research-IT and funded by EPSRC grant EP/K000128/1; and the DiRAC Complexity system, operated by the University of Leicester IT Services, which forms part of the STFC DiRAC HPC Facility (www.dirac.ac.uk). This equipment is funded by BIS National E-Infrastructure capital grant ST/K000373/1 and STFC DiRAC Operations grant ST/K0003259/1. DiRAC is part of the National E-Infrastructure. This research was also supported in part by the National Science Foundation under Grant No. NSF PHY-1125915.

Work in this thesis has been published in the following peer-reviewed papers, in collaboration with the listed authors:

Mutter, M. M., Pierens A., Nelson R. P., 2017a. "The role of disc self-gravity in circumbinary planet systems – I. Disc structure and evolution". *MNRAS*, 465, 4, 117.06, p. 4735.

Mutter, M. M., Pierens A., Nelson R. P., 2017b. "The role of disc self-gravity in circumbinary planet systems – II. Planet evolution". *MNRAS*, 469, 4, 117.06, p. 4504.

"*Never try to tell everything you know. It may take too short a time.*"

—Norman Ford

Abstract

Matthew M. Mutter

Disc and Planet Evolution in Circumbinary Systems

The inner regions of discs around close binary systems are dominated by tidally-truncated eccentric cavities. These are believed to play a key role in dictating where planets formed in these circumbinary discs halt their disc-driven migration. In this thesis we present work examining processes which could impact the evolution and structure of this region, and the planets which interact with it.

First, we investigate the role of self-gravity and disc-mass on circumbinary discs and planets. The greatest impact of self-gravity was found in discs around highly-eccentric binaries, and in discs with high masses. In these cases, self-gravity acts to compact the scale of the inner cavity region. For the highest disc masses, additional eccentric features arise in the outer disc. A range of scenarios examining planetary migration, accretion and disc dissipation find that if planets form and evolve in a high-mass environment, the disc structures formed by self-gravity can leave a fingerprint on the planetary architecture once the disc has dissipated.

We also significantly modify the publicly available FARGO-ADSG hydrodynamical code, to include radiative effects such as disc irradiation by the binary stars, radiative transport and disc surface cooling. We present preliminary results of simulations of adiabatic circumbinary discs with these effects included, and consider also the migration of protoplanets within them. Fully radiative discs produce a smaller inner cavity than obtained in previous isothermal models – a promising result for the end point of planet migration in these discs.

Whilst we have found significant alteration of the circumbinary enviroment by self-gravity and radiative effects, future simulations that capture the 3-D nature of these discs will be required to fully describe the observed architecture of the circumbinary systems.

Acknowledgements

Firstly I would like to thank my supervisor, Professor Richard Nelson, for his support and mentorship throughout the years of my PhD. You always have a different approach to a problem. Your time, wisdom, and knowledge have been invaluable; thank you.

My time at Queen Mary has been a great couple of years. For this, the academic and administrative staff of the School of Physics and Astronomy are to thank. Your hard work provides a friendly, supportive and smooth-running environment.

My fellow PhD students in the Astronomy Unit, are also to thank. I have learnt a huge amount from all of you – although perhaps too much cosmology – as well as making some great friends. For my sanity I have the seminars, pints, coffee, and pizza, with all of you to thank.

There are a few people I must thank for inspiring me in the first place to pursue a degree and PhD in science. Two teachers during my early school career, David Turner and Andy Hills, piqued my interest in the fields of chemistry and physics, which made it extremely difficult to choose between studying a degree in either. Studying Natural Sciences at UCL allowed me to pursue both. The lectures of Professors Ian Howarth and Serena Viti soon made up my mind I wanted to study Astrophysics.

I would like to thank the rest of my friends, family, and my girlfriend. To all of you, your support and humour will always be appreciated. To my parents, Jo and David, thank you for always encouraging me, and instilling a perseverance and resilience which has been invaluable. The two of you have always extolled the virtues of hard-work by leading by example. Finally to Hazel; who has probably had to put up with me wittering on about science in the last ten years more than anyone, and always been there for me. I aim to repay your kindness, patience, love, wit, and loyalty with the same.

Thank you.

Contents

List of Figures

List of Tables

List of Abbreviations

Observations	
RV	**R**adial **V**elocity
TTV	**T**ransit **T**iming **V**ariation
TDV	**T**ransit **D**uration **V**ariation
MS	**M**ain **S**equence
PMS	**P**re **M**ain **S**equence
ZAMS	**Z**ero **A**ge **M**ain **S**equence
YSO	**Y**oung **S**tellar **O**bject
FUV	**F**ar **U**ltra**v**iolet
EUV	**E**xtreme **U**ltra**v**iolet
CB	**C**ircum**b**inary
CBP	**C**ircum**b**inary **P**lanet
CBD	**C**ircum**b**inary **D**isc
PPD	**P**roto**p**lanetary **D**isc
SMA	**S**emi-**m**ajor **A**xis
LoP	**L**ongitude **o**f **P**ericentre
Theory	
MMSN	**M**inimum **M**ass **S**olar/**S**tellar **N**ebula
HD	**H**ydro**d**ynamics
MHD	**M**agneto**h**ydro**d**ynamics
MRI	**M**agneto-**r**otational **I**nstability
GI	**G**ravitational **I**nstability
WKB	**W**entzel-**K**ramers-**B**rillouin (approximation)
LR	**L**indblad **R**esonance
SG	**S**elf **G**ravity/**G**ravitating
RT	**R**ay-**t**raced
FLD	**F**lux-**L**imited **D**iffusion
EoS	**E**quation **o**f **S**tate
SD	**S**urface **D**ensity
CFL	**C**ourant-**F**reidrich-**L**evy (criterion)
VST	**V**iscous **S**tress **T**ensor
VNR	**v**on **N**eumann-**R**ichtmeyer (factor)
FARGO	**F**ast **A**dvection in **R**otating **G**aseous **O**bjects
GS	**G**auss-**S**eidel
SOR	**S**uccessive **O**ver-**R**elaxation
FFT	**F**ast **F**ourier **T**ransform

SPH	**S**moothed **P**article **H**ydrodynamics
PPA	**P**iecewise **P**arabolic **A**lgorithm
	General
IAU	**I**nternational **A**stronomical **U**nion
EM	**E**lectro**m**agnetic (spectrum)
n-D	**n**-**D**imension(s/al)
LHS	**L**eft-**h**and-**s**ide
RHS	**R**ight-**h**and-**s**ide
ODE	**O**rdinary **D**ifferential **E**quation
PDE	**P**artial **D**ifferential **E**quation

Physical Constants

Constant Name	Symbol	Value [SI]
	Physical	
Gravitational Constant	G	$6.6741 \times 10^{-11}\,\mathrm{m^3 \cdot kg^{-1} \cdot s^{-2}}$
Speed of Light	c	$2.9979 \times 10^{8}\,\mathrm{m \cdot s^{-1}}$
Stefan-Boltzmann Constant	σ_r	$5.6704 \times 10^{-8}\,\mathrm{J \cdot s \cdot m^{-2} \cdot K^{-4}}$
Radiation Constant	a_r	$7.5657 \times 10^{-16}\,\mathrm{J \cdot m^{-3} \cdot K^{-4}}$
Ideal Gas Constant	$\mathcal{R}$	$8.3145\,\mathrm{J \cdot K^{-1} \cdot mol^{-1}}$
	Conversion	
Solar mass	$\mathrm{M}_\odot$	$1.9885 \times 10^{30}\,\mathrm{kg}$
Solar radius	$\mathrm{R}_\odot$	$6.9566 \times 10^{8}\,\mathrm{m}$
Jupiter mass	$\mathrm{M}_{\mathrm{Jup}}$	$1.8980 \times 10^{27}\,\mathrm{kg}$
Jupiter radius	$\mathrm{R}_{\mathrm{Jup}}$	$6.9911 \times 10^{7}\,\mathrm{m}$
Earth mass	$\mathrm{M}_\oplus$	$5.9722 \times 10^{24}\,\mathrm{kg}$
Astronomical Unit	au	$1.4959 \times 10^{11}\,\mathrm{m}$

List of Symbols

Symbol	Meaning
	Geometry
r	Cylindrical (or Spherical) radius
ϕ	Cylindrical (or Spherical) azimuthal angle
z	Height above disc mid-plane
i	Radial direction mesh index
j	Azimuthal direction mesh index
	Stellar/Binary Properties
$M_\star$ or $M_{\mathrm{s},k}$	Stellar mass, or mass of star k
$R_\star$ or $R_{\mathrm{s},k}$	Stellar radius, or radius of star k
$F_\star$	Stellar Flux
$T_{\mathrm{s},k}$	Surface temperature of star k
$\mathbf{r}_{\mathrm{s},k}$	Position vector of star k
a_{b}	Binary semi-major axis
e_{b}	Binary eccentricity
ω_{b}	Binary longitude of pericentre
μ_{b}	Binary mass ratio fraction
Ω_{b}	Binary orbital frequency
P_{b}	Binary orbital period
R_{Roche}	Roche lobe approximation
A	Binary orbital separation
	Planetary Properties
R_{p}	Radius of planet
m_{p}	Mass of planet
q_{p}	Planet mass ratio
r_{p}	Planetary orbital radius
a_{p}	Planetary semi-major axis
i	Planetary orbital inclination
e_{p}	Planet eccentricity
ω_{p}	Planet's longitude of pericentre
Ω_{p}	Orbital frequency of planet
R_{Hill}	Hill sphere radius of planet

Hydrodynamics	
Σ	Surface density
ρ	Midplane density
c_s	Sound-speed in the disc
υ	Velocity
e	Thermal energy density
p	Pressure
t	Time
Φ	Gravitational Potential
Disc Properties	
H	Disc scale height
h	Disc aspect ratio
Ω	Orbital frequency
Ω_{K}	Keplerian orbital frequency
κ	Epicyclic frequency
f_{gap}	Cavity gap function
R_{gap}	Gap function transition radius
$\mathcal{X}$	Disc mass scaling factor
ϵ	Disc albedo
W_g	Disc geometry factor
β	Viscous outflow constant
ω_{c}	Disc cell longitude of pericentre
ω_{d}	Mass-weighted average disc longitude of pericentre
e_{c}	Disc cell eccentricity
e_{d}	Mass-weighted average disc eccentricity
Viscosity	
η	Dynamic viscosity
ζ	Bulk viscosity
ν	Kinematic viscosity
α	α-model kinematic viscosity parameter
$\prime\sigma_{ik}$	Viscous Stress Tensor
$\sigma_{k,l}$	k, l component of the Viscous Stress Tensor
f_k^{visc}	k-th component of the viscous force
Q^{visc}	Viscous heating term
q_k^{visc}	k-th component of the artificial viscosity pressure
$Q_{\mathrm{art}}^{\mathrm{visc}}$	Artifical viscosity heating term
C_{VNR}	von Neumann-Richtmeyer factor for artificial viscous spreading

Thermodynamics/Radiative Processes	
u	Specific thermal energy
c_p	Specific heat capacity at constant pressure
c_v	Specific heat capacity at constant volume
μ	Mean molecular weight
γ	Adiabatic index
f	Disc flaring index
τ	Mean vertical or length optical depth
$\tau_{\rm eff}$	Effective vertical optical depth
$\kappa_{\rm R}$	Rosseland mean opacity
$\kappa_\star$	High-energy photon group mean opacity
E	Radiation energy density
T	Midplane temperature
$T_{\rm eff}$	Effective temperature at disc photosphere
$T_{\rm irr}$	Irradiative temperature at disc midplane
Q_-	Radiative Cooling term
$Q_{\rm irr}$	Irradiative heating term
Disc Torques	
$\Gamma_{\rm L}$	Lindblad torque
$\Gamma_{\rm C}$	Corotation torque
Γ_0	Torque normalisation
α	Surface density power-law index
β	Temperature power-law index
ζ	Disc entropy power-law index
x_s	Horseshoe region width or half-width of corotation region
b	Softening parameter
General Theory	
$a_{\rm c}$	Critical stability limit radius
Q	Toomre parameter
ϵ	Gravitational potential smoothing length
ϵ_{sg}	Self-gravity potential smoothing length
R_e	Reynolds number
ω	Over-relaxation parameter
ρ	Spectral radius for relaxation problems
$\mathcal{F}$	Fourier transform
$\mathcal{F}^{-1}$	Inverse Fourier Transfrom
K	Green kernel
S	Disc mass distribution kernel
D	Diffusion coefficient
λ	Flux-limiter

Dedicated to all my Friends and Family...

Formation and Evolution of (Circumbinary) Planetary Systems

Chapter Contents

In this Chapter several topics will be introduced, relevant to the work presented in this thesis on circumbinary disc and planet evolution. In Section 1.1 the field of exoplanets will be covered; starting with the numerous methods to detect them, notable examples, and a look at the population as a whole. We then examine the environment in which we think all exoplanets are born – protoplanetary discs – in Section 1.2. In Sections 1.3 and 1.4 we discuss the current state of the literature dealing with how planets form and interact with their surroundings in the disc. Throughout this Chapter we highlight the key findings pertaining to circumbinary planet detection, formation, and evolution.

1.1 An Abundance of Exoplanets

Since the advent of Copernican cosmological theory, Earth's place at the centre of the cosmos has been eroded and replaced. Earth's fall from cosmic significance is due to some of the most profound scientific ideas and breakthroughs. From Copernicus, through Galileo and Newton, to Einstein and Hubble, our understanding of the Earth's place in the solar system, the galaxy, and the universe has been cemented. The search for, and discovery of exoplanets – planets around stars other than our own – is just one more step in this journey. The philosophy of exoplanets in modern science goes back to Giordano Bruno (1548–1600). He proposed that the stars were just other Suns, holding their own exo-stellar systems of planets – exoplanets. He even alluded to the possibility of life on these planets; views which may have played a role in his execution for heresy by the Roman Catholic Inquisition.

For over two centuries exoplanets remained in the realm of philosophy. It wasn't until 1855 that the tools of modern scientific practice were applied to the problem. The periodicity of errors in the binary orbit of the *70 Ophiuchi* system were proposed by Captain W. S. Jacob, to be due to a third, less massive body – a planet (Jacob 1855). Whilst this claim was refuted and proved wrong, it was the start of several other claims over the next century. It wasn't until 1992 that the first detection of a planet around a star other than our own was confirmed; Wolszczan and Frail (1992) detected at least two terrestrial-size planets (now named

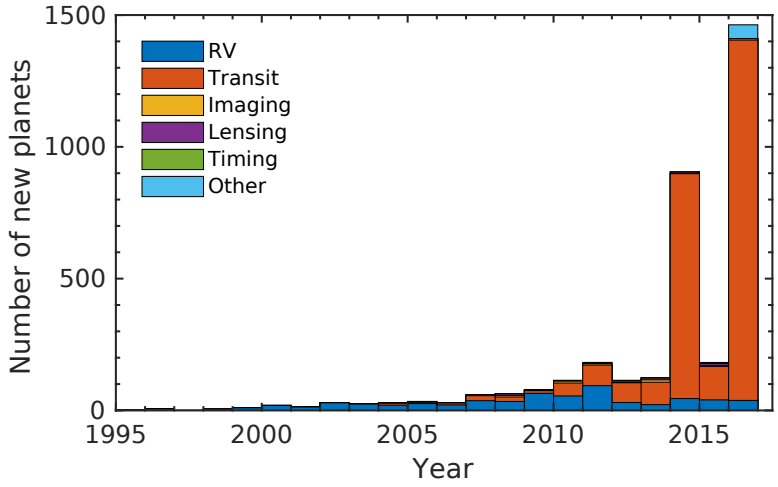

FIGURE 1.1: Histogram showing the number of new exoplanet discoveries per year, stacked by detection method. This plot contains 3493 confirmed exoplanets taken from the Open Exoplanet Catalogue. One can see the clear impact of the launch of the *Kepler* spacecraft in 2009, which uses the transit method to detect exoplanets.

Draugr and *Poltergeist*[1]) around the pulsar *PSR B1257+12*, with pulsar timing variations. With the Radial-Velocity variation or RV technique, Mayor and Queloz (1995) discovered the first exoplanet orbiting a main-sequence star *51 Pegasi b*, or *Dimeridium*. *Upsilon Andromedae* was the first main-sequence star to have a system of multiple planets detected (Lissauer 1999); *Kepler-16 b* was the first planet detected around a main-sequence binary system – a circumbinary planet (Doyle et al. 2011). Since 1992, numerous detection methods have been used to find and characterise thousands of exoplanets; to paraphrase Stephen King, "*...there are other Worlds than these.*"

1.1.1 Detection Methods

The "exoplanet revolution" can be summarised by Fig. 1.1. This figure contains information on 3493 confirmed exoplanets in 2575 systems. The data to produce this figure, and several others throughout this section, were taken from the Open Exoplanet Catalogue[2] (Rein 2012) on the 5th September 2017. This population of planets forms an invaluable tool for testing theories of disc evolution and planet

[1] IAU. Final results of NameExoWorlds public vote released. 2015
[2] https://github.com/openexoplanetcatalogue/

TABLE 1.1: A breakdown of the total number of planets detected by each method described in Sec. 1.1.1. This table was produced with data from the Open Exoplanet Catalogue on the 5th September 2017

Method	Confirmed Planets
Radial Velocity	635
Transit	2698
Direct Imaging	48
Microlensing	38
Pulsar Timing	18
Unspecified	56
Total	3493

formation, however before we cover these topics, we will briefly describe the methods used to detect and characterise this growing number of exoplanets.

Radial-Velocity Technique

The gravitational influence of other bodies in stellar systems cause the star and planets to orbit their common centre-of-mass. If the orbital plane of the planet is misaligned with respect to the sky, an observer can monitor the periodic Doppler shifting of the spectral lines in the light of the parent star due to its motion back and forth along the line of sight. This Doppler shift is due to variations in the star's radial velocity, which assuming a circular orbit is equal to:

$$v_{\text{radial}} = \frac{m_{\text{p}}}{M_{\star}} \sqrt{\frac{GM_{\star}}{r}} \sin i_{\text{p}}, \tag{1.1}$$

where m_{p} is the mass of the planet, $M_{\star}$ is the mass of the host star, G is the gravitational constant, r is the distance between the star and the planet, and i_{p} is the orbital inclination of the planet. See Fig. 1.2a for an example of the periodicity imposed on the radial velocity signal from a star by an orbiting planet, taken from the detection of *51 Pegasi b* (Mayor and Queloz 1995). The radial velocity signal is dependent on the ratio between the planet and star masses, as well as the orbital separation, making this method sensitive to finding massive planets or planets orbiting close to their star. The effect of these biases can be seen in Fig. 1.2b. From the periodicity of the variations in the radial velocity signal, the orbital period of the planet can be found, and hence the mean orbital separation deduced. Radial velocity measurements are usually taken as part of

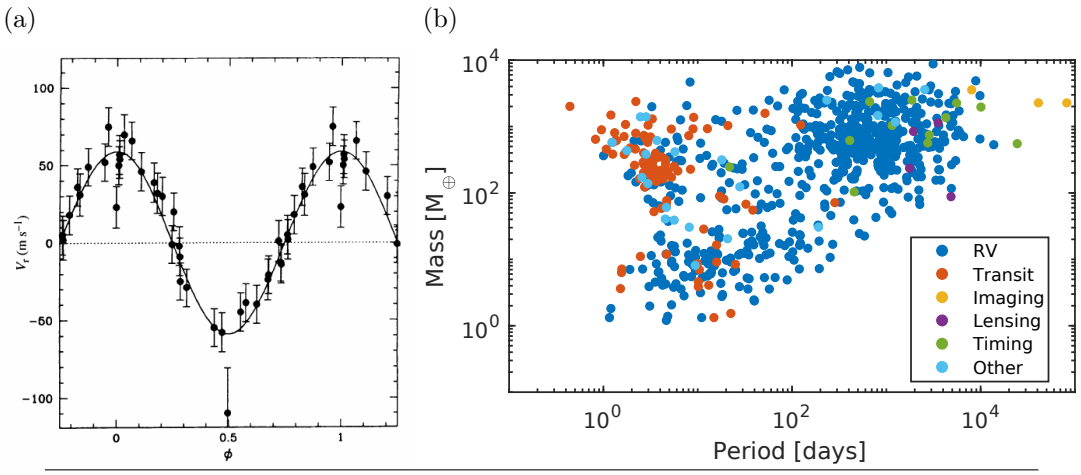

FIGURE 1.2: For many years the Radial-Velocity was the most successful detection method. It was used to detect the first exoplanet around a main-sequence star. *(a)* A phase-folded radial velocity curve showing the shift imposed on the host star by *51 Pegasi b* – figure taken from Mayor and Queloz (1995). *(b)* Period-Mass distribution for the 1246 planets with known masses. A bias towards short period, massive planets can be seen for the RV method. Due to the geometric nature of this detection method, without exterior data, only a minimum mass can be deduced for the orbiting planet.

large surveys – with ground-based telescopes – monitoring many stars at a time for a given length of time. Due to the finite length of these surveys there exists an upper bound to the orbital period of planets this technique can detect. If there are multiple planets in a system, each periodic signal can be decomposed from the radial velocity measurements – with enough signal to noise and coverage. An observer monitoring the solar system for example, could observe an impact on the solar motion from Jupiter of $12\,\mathrm{ms}^{-1}$, whilst the Earth induces a reflex motion of only $0.1\,\mathrm{ms}^{-1}$. One of the largest sources of uncertainties in using this method to characterise planets is the error on the mass estimate of the star itself – in order to accurately characterise a planet, its host star must be well characterised beforehand.

Since radial velocity data only gives the line of sight radial velocity, the mass determination of a perturbing exoplanet depends on its orbital inclination relative to the line of sight measured from the plane of the sky. There is no way of deducing the inclination directly with the radial velocity method, so only $m_p \sin i_\mathrm{p}$, or the minimum mass can be obtained. If a radial velocity detection can be followed up with transit observations (see next section), then this degeneracy breaks, since $i_\mathrm{p} \sim 90°$ for a transiting exoplanet. A combination of the mass from

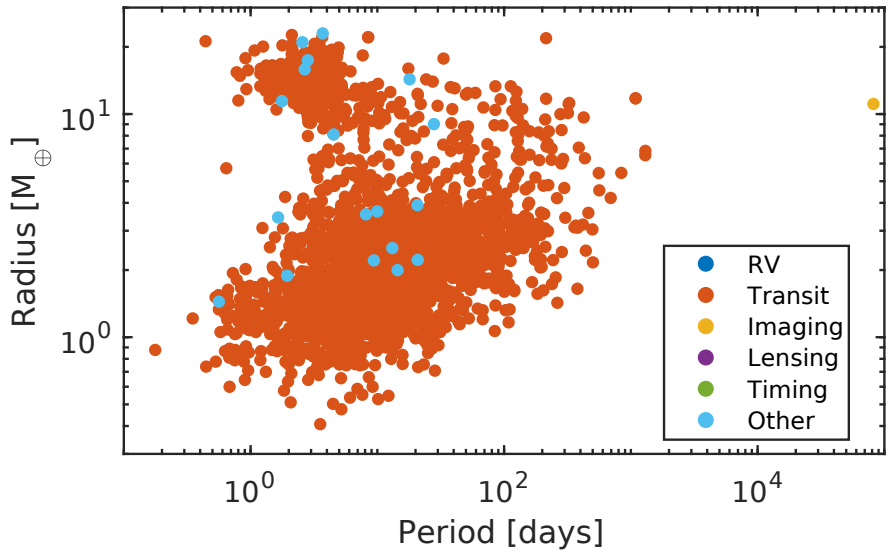

FIGURE 1.3: Period-radius distribution of planets with measured radii, which as of 5th September 2017 is 2734. The success of the *Kepler* mission, which detects exoplanets via the transit method can be clearly seen, accounting for many of these detections. The biases towards detecting planets with large radii, and those on close-in orbits can be seen, with fewer low-mass planets at large semi-major axes (and hence long periods) detected.

radial velocity measurements, and radius from transit measurements, yields the density of the planet, enabling conclusions about the bulk composition to be made. The eccentricity of the planet's orbit affects the radial velocity semi-amplitude $\left(K \propto 1/\sqrt{1-e_{\mathrm{p}}^2}\right)$ so may be infered from the shape of the radial velocity curve.

Transit Method

If an exoplanet's orbital plane is edge-on (or nearly edge-on) to an observer's line-of-sight, when it passes in front of its host star it will block a portion of the flux emitted by the star. The probability of an exoplanet transiting between the observer and parent star is proportional to the ratio of the star's radius and the planet's semi-major axis. The chance of detection decreases the further away an exoplanet orbits its parent star, making the transit method most effective for close-in planets. The reduction in observed stellar flux a transiting exoplanet induces is directly proportional to the ratio of cross-sectional surface areas of the

planet and star:

$$\frac{\Delta F_\star}{F_\star} = \left(\frac{R_\mathrm{p}}{R_\star}\right)^2 \tag{1.2}$$

Since small planets have small cross-sectional areas compared to their parent stars, they only induce small reductions in flux during transit. Using the planets in the solar system again as examples, Jupiter would cause a drop of just 1% in the flux of the Sun, whilst Earth would only give a 0.01% decrease. The small reduction in flux caused by a transiting Earth-sized planet is comparable to the cumulative effect of numerous systematics which arise when measuring photometric fluxes. It is necessary to observe the star for multiple planetary orbits, as this gives sufficient signal-to-noise, allowing for the modelling and subtraction of systematics. Typically 3 or more transits are required to confirm the detection of a planet causing a dip in the star's flux of $\sim$ 1%. This criteria ensures that an object with a true periodicity has been detected. More are required when the reduction in flux is comparable to the systematic effects. Other tests are also required to discount false positive signatures, such as eclipsing binaries or blended objects, as without their exclusion, planetary distributions and occurrence rates would be inaccurate.

Due to these reasons of probability of detection and false positive likelihood, it is necessary to continuously monitor a large number of stars for a long period of time in order to build sufficient statistics to detect potential exoplanets. The requirement for multiple transit observations and the finite length of observing campaigns puts a limit on the orbital period of planets able to be detected and confirmed. The highly successful *Kepler* mission performed a transit survey of approximately 150,000 stars for 3.5 yr in the constellations *Cygnus* and *Lyra*. With the above requirements, the exoplanet with the longest orbital period detected by *Kepler* is *KIC 11442793 h* with an orbital period of 331.6 days (Cabrera et al. 2014), although an exoplanet with only two transits has been confirmed through statistical validation, with an orbital period of 704.2 days (Kipping et al. 2014, *Kepler-421 b*).

From the shape of the transit, or the photometric light curve, the orbital eccentricity of the planet can be detected (Seager and Mallén-Ornelas 2003), although limb and gravitational darkening need to be considered (Csizmadia et al. 2013). In systems where planets transit their host star, a number of other techniques can be used to further characterise the planet. As the quantity being fitted is the ratio

of the surface areas of the star and planet, like the RV method, the uncertainty on the stellar radius is one of the largest sources of error in determining the planetary radius. High-resolution spectroscopy can be used to probe the atmosphere of the planet: during the primary eclipse the atmosphere of the planet may absorb portions of the stellar spectrum due to the presence of atomic or molecular species; whilst during a secondary eclipse (when the planet passes behind the star), a similar process can be used on the light reflected or emitted by the planet. Transit ingresses/egresses can also yield information about the atmosphere's structure. The Rossiter-McLaughlin effect – the blocking of red-shifted then blue-shifted portions of spectral lines, as the planet passes in front of a rotating star – can be measured with spectroscopic methods during transit (McLaughlin 1924; Rossiter 1924; Fabrycky and Winn 2009). This effect measures the projected misalignment between the rotation axis of the star, and the orbital plane of the transiting planet, otherwise known as the sky projected obliquity. It can help constrain the formation mechanism of so-called hot-Jupiters (massive planets orbiting very close to their parent star), which the detection of *51 Pegasi b* prompted.

The orbit of an eclipsing body may be perturbed by other bodies in the system; the perturbation to the orbit of the eclipsing body can be detected as transit timing variations (variations in the time of the start of a predicted transit event) or transit duration variations (variations in the duration of the transit) (Ford et al. 2011, as well as Papers *II–VIII* in the *Transit Timing Observations from Kepler* series). *Kepler-11*, a system with 6 transiting planets, had the masses of these planets constrained with TTV analysis (Lissauer et al. 2011). Figure 1.4 shows the de-trended photometric light-curves for the 6 transiting planets. Whilst the depth of the transit depends on the ratio between the surface areas of the planet and star discussed earlier, the shape of the transit event depends on the eccentricity, semi-major axis, and argument of pericentre of the planet. TTV analysis is a powerful tool – when it can be used – not only constraining the upper and lower mass bounds, but also detecting non-transiting planets (Dawson et al. 2014, *Kepler-419 c*).

Direct Imaging

Perhaps the simplest technique conceptually, direct imaging is the only detection method which captures light emitted by the exoplanet itself. The apparent simplicity of pointing a telescope at a star and imaging the planets orbiting it is

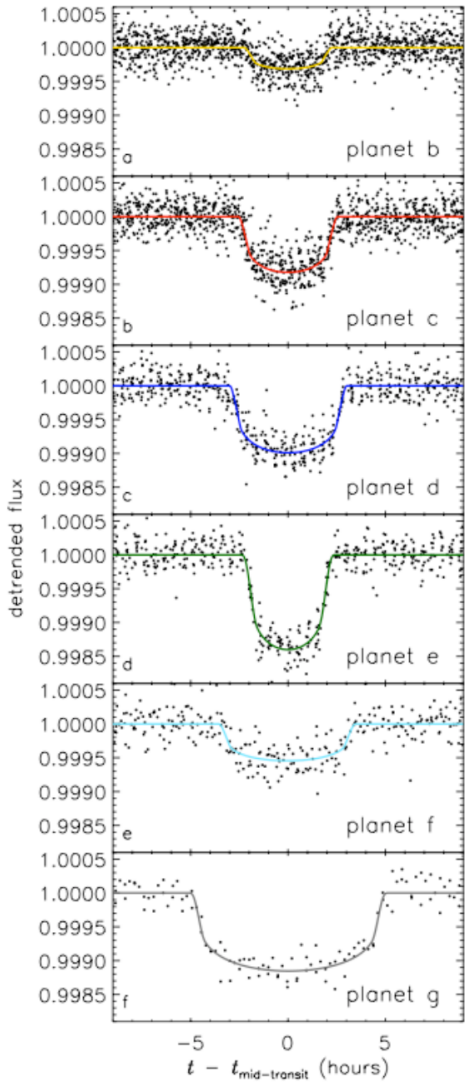

FIGURE 1.4: Phase-folded stacked (all observed transits are laid on top of each other) light-curves for the six planets detected in *Kepler-11*. Transits of different depths can be seen due to planets of differing radii. Image Credit: Lissauer et al. (2011).

undermined by the contrast in brightness between the host star and the planet. The ratio of the two can commonly be 6 orders of magnitude.

Despite this, direct imaging has been used to detect several exoplanets. By observing these systems in the infra-red portion of the EM spectrum, where the planetary emission is at its peak, and focusing on young stars where any planets still retain residual heat from their formation, can drastically reduce the contrast. A coronagraph can be used to block the glare of the host star, and adaptive optics can be used on ground-based telescopes, to aid in the chances of detection.

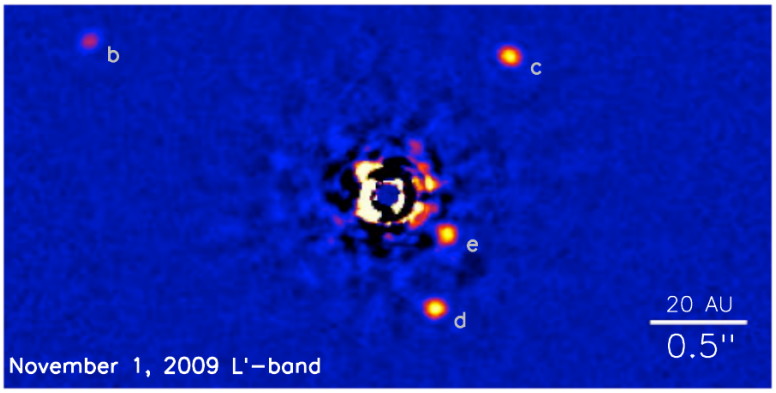

FIGURE 1.5: A direct image taken of four young exoplanets in the *HR 8799* system. These planets range from 4 to 10 Jupiter masses, on orbits 45 to 450 years long. Image Credit: Marois et al. (2010).

Direct imaging thus opens up a portion of the planetary period parameter space, unattainable with the methods explored so far.

Massive planets (above a sizeable fraction of a Jupiter mass), with a wide orbital separation from their host stars are the easiest targets for this method. Perhaps the most famous of the direct imaged systems is *HR 8799* (see Fig. 1.5), around which 4 exoplanets have been imaged (Marois et al. 2008, 2010).

Microlensing

If a foreground star approaches close to the line of sight between an observer and a more distant, background star, the curvature of space-time due to the mass of the foreground star will act as a lens, creating a distorted image of the distant star. The distant star appears as a ring with radius equal to the Einstein ring radius of the foreground star. At the distances concerned we are unable to resolve this lensing effect, so with photometry this appears simply as a characteristic increase in brightness of the distant star with respect to time, with the magnitude of the increase determined by the geometry of the system and the mass of the lens star.

A planet orbiting the foreground star will act as a secondary lens causing its own microlensing event to occur. Again, the geometry and masses of the bodies in the system will dictate the magnitude and timing of the lensing event. With unresolved photometry, this manifests itself as a further, shorter-lived increase in brightness; the magnification effect is greatest when the orbit of the planet

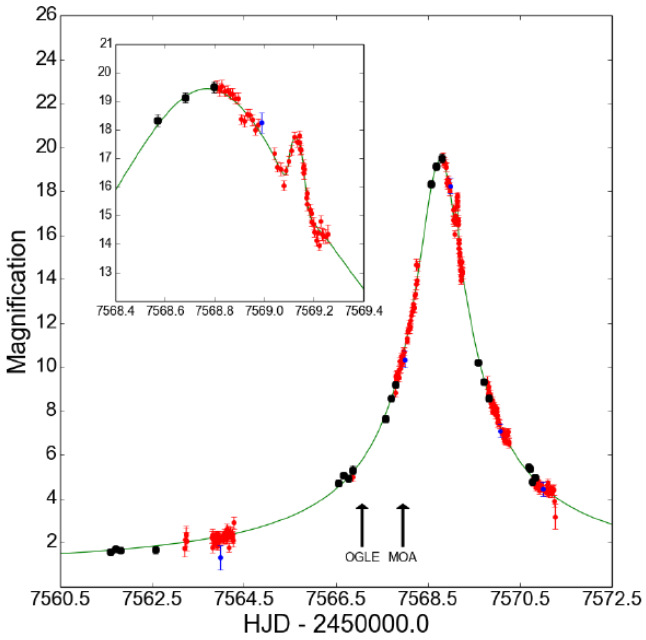

FIGURE 1.6: Light-curve of the photometry and modelling of the *OGLE 2016–BLG–1195Lb* microlensing event to that of a star+planet lens. The magnification due to the star is easily visible, with the secondary rise due to the planet visible in the inset. The lens properties defined for this event were a $0.2\,M_{\odot}$ host star with a $2\,M_{\oplus}$ planet at a separation of 2 au. Image Credit: Bond et al. (2017).

takes it closest to the Einstein ring radius of its parent star. A microlensing event due to the smallest star-planet mass ratio detected (Bond et al. 2017, *OGLE 2016–BLG–1195Lb*) is shown in Fig. 1.6.

The random nature of this method, and the ability of even very low-mass planets to create a microlensing signature, means that we are sampling the true underlying exoplanet population, free of biases. This has the possibility of making microlensing a very powerful tool in the field of exoplanet population statistics. This very same randomness is also a downside to this method. It makes follow-up and further characterisation of exoplanets discovered with this method almost impossible. These events also happen very rarely, making continuous monitoring of a huge sample of targets necessary. The microlensing events discovered to date have been with large scale sky surveys using networks of robotic telescopes, such as *MOA* or *OGLE*.

Pulsar Timing

As we have already mentioned, the first confirmed exoplanets were discovered in 1992 around the pulsar *PSR B1257+12* (Wolszczan and Frail 1992). This discovery was made with the pulsar timing technique. Pulsars are a class of neutron stars which rapidly rotate and emit collimated beams of EM radiation from their magnetic poles. If the star's rotational and magnetic axes are misaligned the orientation of the beams also rotate, appearing as a regular pulsating signal to a distant observer. The extremely regular rotation rates of these objects, means that any variation in the timing between beam signals can be attributed to the motion of the pulsar. Similar to the radial-velocity method, the gravitational tug of an orbiting planet affects the motion of the pulsar, causing variations in the beam timings, allowing the planet to be detected. This method is extremely accurate, able to detect very low-mass planets.

Other

Whilst the radial velocity method detects the radial motion of a star due to a perturbing planet through spectroscopy, it is also possible to detect the physical movement of the star in the sky with what is known as the astrometric method. When comparing the stars relative position against stable background stars, the target star will move back and forth in a periodic manner. Combined with parallax measurements giving us the distance to the star, it is possible to model the periodic oscillations in the star's movement, yielding the mass and period of orbiting exoplanets. To date no exoplanets have been detected with this astrometric method, however it is expected that the space mission *Gaia* will detect thousands of exoplanets around Sun-like stars, to a distance of 200 parsecs in coming years (Casertano et al. 2008; Perryman et al. 2014).

1.1.2 Circumbinary Planets

One of the first exoplanets detected was found to exist in a binary star system (actually a radio pulsar binary), *PSR B1620-26 b* (Thorsett et al. 1993). As of 5th September 2017, there are 158 planets in systems with two or more stars. The existence of planets in multiple star systems not only suggests that planet formation is a ubiquitous process, but must also be taken into account when

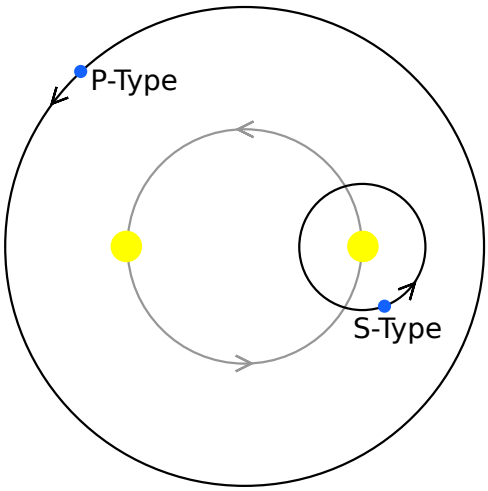

FIGURE 1.7: Two stable orbital types exist in a binary system. If a planet, or third body, orbits either the primary or secondary component of the binary it is known as a S-Type orbit. When the binary orbits both members of the system, it is a P-Type or circumbinary orbit.

looking at the true underlying population of exoplanets. The reasoning behind this is that at least one third of Main Sequence stars in the Milky Way galaxy are members of binary or multiple star systems (Lada 2006). In fact the multiplicity frequency of MS stars is a monotonically increasing function of mass (Duchêne and Kraus 2013), with solar-like stars between $0.7 < M_\star < 1.3\,\mathrm{M}_\odot$ having a multiplicity fraction of 44%. Thus, even if the frequency of planets in multiple systems is a fraction of what it is hypothesised to be around single stars (Cassan et al. 2012, an average > 1 planet per star in the Milky Way), then they would form a significant fraction of the overall population.

Of the known exoplanets in multiple systems, 22 exist in orbits which take them around at least two members of the multiple star system. In systems with only two stars, this is known as a P-Type or circumbinary orbit (see Fig. 1.7); the planet in *PSR B1620-26* is in a P-Type orbit around the two pulsars in the system. It is this class of exoplanets upon which this thesis will focus on, particularly the 11 transiting circumbinary planets discovered by *Kepler*, found around Main-Sequence short-period binaries. To search for circumbinary planets, *Kepler* monitored a catalogue of eclipsing binaries – binaries where the orbital plane lies completely or nearly edge-on to the observer. The two components of the binary periodically eclipse each other. This allows the radii of the two stars to be determined with great accuracy. Spectroscopic monitoring of the radial velocity variations the stars

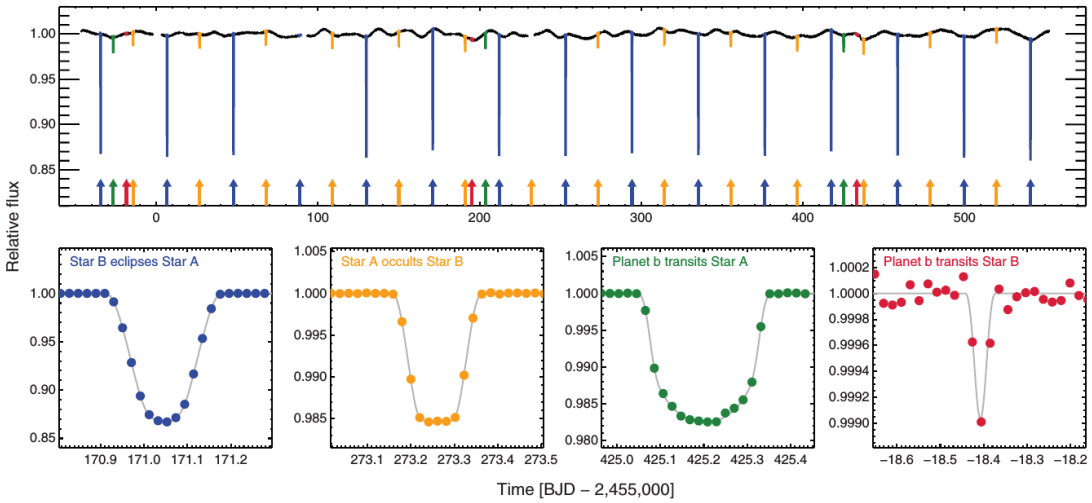

FIGURE 1.8: Photometric time-series showing various transit events in the *Kepler-16* system. The blue events are primary eclipses (when Star A eclipses Star B), the yellow are secondary (when Star B occults Star A), and the green and red events are the primary and secondary transits (when Planet b transits Star A and Star B respectively). The inserts show a zoomed in example of each of these events. Image Credit: Doyle et al. (2011).

means the masses can also be determined. The first circumbinary planet detected around a MS eclipsing binary was *Kepler-16 b* (Doyle et al. 2011). This was determined to be a Saturn-like planet in terms of radius and mass, in a co-planar orbit around $0.69\,M_{\odot}$ and $0.20\,M_{\odot}$ stellar components. Examining the light curve from this system (Fig. 1.8), 4 separate sets of eclipses can be seen. The one with the deepest reduction of flux is when the secondary component, Star B, eclipses the brighter primary component, Star A. Secondary eclipse events, when Star B occults Star A can also be seen. Tertiary and quaternary eclipses were determined to be due to the existence of a third body in the system – a planet, which transits both stars. The presence of a third body also effects the timings between successive eclipse events. Thus a TTV-like analysis can be used to constrain the mass and orbit of the planet, as the masses of the stars are already well known due to radial-velocity monitoring. This combination of radial-velocity monitoring, transit photometry and transit-eclipse timing variations allows the binary-planet system to be extremely well characterised.

This method has since been used to detect 10 other circumbinary planets in the *Kepler* field, in 8 binary systems – three planets in a multi-planet circumbinary system; *Kepler-47* with three planets. Although not all the planets are as well

TABLE 1.2: The *Kepler* circumbinary planets.

Planet	Reference
Kepler-16 (AB) b	Doyle et al. (2011)
Kepler-34 (AB) b	Welsh et al. (2012)
Kepler-35 (AB) b	Welsh et al. (2012)
Kepler-38 (AB) b	Orosz et al. (2012a)
Kepler-47 (AB) b	Orosz et al. (2012b)
Kepler-47 (AB) c	Orosz et al. (2012b)
PH-1 A(ab) b	Schwamb et al. (2013)
Kepler-413(AB) b	Kostov et al. (2014)
Kepler-453(AB) b	Welsh et al. (2015a)
Kepler-47 (AB) d	Welsh et al. (2015b)
Kepler-1647(AB) b	Kostov et al. (2016)

characterised as *Kepler-16 b*, the analysis able to be carried out on circumbinary systems allows bounds to be placed on parameters such as the orbital eccentricity and mass of the planet. Table 1.2 lists the 11 circumbinary planets, with their discovery/confirmation papers. Note that *PH-1 A(ab) b* is a planet around one binary pair in a quadruple star system – the only planet to be so. It was discovered by the citizen science project Planet Hunters[3], but has also been confirmed by *Kepler* (designation *Kepler-64 b*).

There are a few notable characteristics which the systems share. All the host systems are close-binaries, with periods between 7 and 41 days; the lack of detected planets around wider binaries is a selection bias, as the probability of detecting planetary transits in a finite observation time drops as the semi-major axis of the binary increases (Li et al. 2016). The lack of circumbinary planets around ultra-short period binaries is interesting though, as there is no selection bias due to the inverse of the above reasoning. One hypothesis put forward is that this may be a fingerprint of the mechanism which removed angular momentum from the system, allowing the semi-major axis of the binary to shrink, as it is unlikely ultra-short period binaries were formed in-situ (Welsh et al. 2014). It has also been shown that fewer co-planar planets are found in these systems, which could affect their chance of being detected (Armstrong et al. 2014).

With the exception of *Kepler-413 b* (Kostov et al. 2014), all the circumbinary planets are within 1° of co-planarity, i.e. the orbital planes of the binary and the

[3] https://www.planethunters.org/

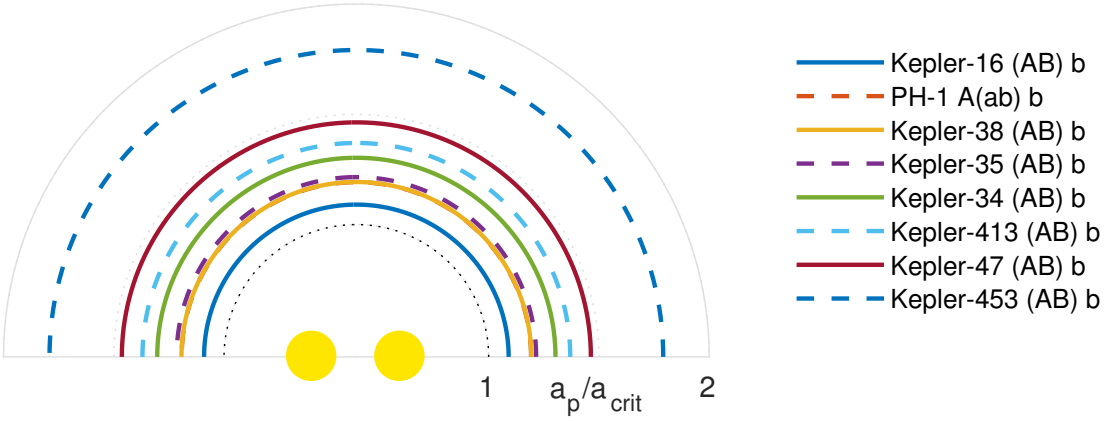

FIGURE 1.9: This plot shows the semi-major axis of the circumbinary planets scaled to the critical stability limit a_c (Eq. (1.3)), defined by Holman and Wiegert (1999), of the host binary. The outer planets in *Kepler-47* have been excluded, as well as *Kepler-1647 b* for clarity. The pile-up of planets close to this limit is clear.

planet are aligned. This could be evidence that the planets formed in a common circumbinary disc, which also orbited in the plane of the binary's orbit. We will discuss both the circumbinary disc itself, and planet formation within it in later sections. Armstrong et al. (2014) found that a preference for circumbinary planets to be close to co-planar is consistent with a planet formation rate consistent with the single star case. Whilst co-planarity does not seem to be an observational bias, it is worth noting this could also be a selection effect, as even a slight planetary inclination causes rapid precession of the orbit. *Kepler-413 b* has a precession period of 11 yr, one consequence of which is that it doesn't always transit both or one of the stars. In fact transits are only visible for 4 yr out of this period.

One of the most intriguing similarities is the grouping of the semi-major axes of the planets close to a stability limit defined semi-analytically by Holman and Wiegert (1999). For a binary with mass ratio fraction $\mu = M_B/(M_A + M_B)$, eccentricity e_b, and semi-major axis a_b, they found the critical stability limit for P-Type orbits to be:

$$a_c = a_b \left[1.6 + 5.10e_b - 2.22e_b^2 + 4.12\mu - 4.27e_b\mu - 5.09\mu^2 + 4.61e_b^2\mu^2\right]. \quad (1.3)$$

For an equal mass binary, with zero eccentricity, $a_c \approx 2.4\, a_b$. Holman and Wiegert (1999) found that planets with semi-major axes smaller than this, were either ejected from the system, or underwent scattering events with the binary. Figure 1.9 shows the semi-major axes of the *Kepler* circumbinary planets scaled to a_c in each

of the systems. Whilst the outer planets in *Kepler-47*, *Kepler-1647 b* have been excluded, the proximity of the planets to the limit of stability is clear. A possible mechanism to explain this concentration of planets will be discussed later; it has been noted, that if selection biases are taken under consideration there is evidence the observed pile-up is just an underlying log-uniform distribution (Li et al. 2016).

Of the planets in proximity to the stability limit, none are greater than Jupiter in size or mass. This is unlikely to be an observation bias, as more massive planets are easier to detect. Nelson (2003) found, in a theoretical study on giant planet evolution in circumbinary discs, that Jupiter-mass planets were captured into a 4 : 1 mean motion resonance with the binary, where they then underwent scattering and ejection events.

Despite these similarities, there is diversity within the population of binaries which host circumbinary planets: with primary star masses ranging from 0.69 to 1.53 $M_\odot$ (*Kepler-16*, *PH-1*); binary mass ratios (M_A/M_B) between 1.03 and 4.8 (*Kepler-34*, *Kepler-453*); and eccentricities ranging from near circular (0.007, *Kepler-16*) to significant (0.52, *Kepler-34*).

In the coming sections theories aiming to explain both the commonalities and diversity within this intriguing selection of planets will be discussed. The remainder of the thesis will then deal with our own investigations to increase the accuracy of these theories, as well as their predictive power, for future exoplanet detection missions and campaigns.

1.1.3 Discussion

The growing catalogue of discovered exoplanets is a fantastic resource for researchers studying topics such as protoplanetary disc evolution and planet formation theories. In the early years of exoplanet detection – due to the biases in the methods being used and available technology – only giant planets on close-in orbits were found. These systems, lacking the diversity of the planets found in our own solar system, prompted the commissioning of missions and instruments such as *Corot*, *HARPS*, and *Kepler*. These campaigns have been hugely successful finding not only a great number of exoplanets, but a huge diversity also. These include: hot Jupiters (Charbonneau et al. 2000, *HD 209458 b*); cold Jupiters (Wright et al. 2007, *HD 154345 b*); hot Neptunes (Butler et al. 2004, *GJ 436 b*); super Earths (Batalha et al. 2011, *Kepler-10 b*); and terrestrial planets (Angelo

et al. 2017, *Kepler-1649 b*). Planets have also been discovered on highly eccentric, inclined, and even retrograde orbits.

These planets can be found in systems where the architecture is as diverse as the planets themselves. *Wasp-47* (Hellier et al. 2012), a hot Jupiter, was found to have a super Earth (Howell et al. 2014) and a hot Neptune (Becker et al. 2015) orbiting interior to it, as well as a cold Jupiter (Neveu-VanMalle et al. 2016) orbiting exterior to it. Fabrycky et al. (2012) announced systems of multiple giant planets around the *Kepler-29, -30, -31 and -32* systems. Intriguing results of recent years include the compact systems of low-mass planets, such as (Lissauer et al. 2011, *Kepler-11*) and the 7 planet *TRAPPIST-1* (Gillon et al. 2016, 2017). Whilst these systems have all been detected with the transit or radial velocity methods, there also exist systems with multiple cool Jupiters such as *HR8799* (Marois et al. 2008).

Many exoplanet discoveries have prompted re-examination of the previously held paradigms, which were focused on recreating the planets and architecture seen in our own solar system. The goal of these models was to produce an inner system of small rocky worlds, with gas- and ice-giant planets exterior to them, all on roughly coplanar orbits. An outer system of analogous Kuiper belt and Oort cloud objects complete the picture. It is clear that the diversity of exoplanets goes far beyond that seen in our own solar system. The detection of planets around binary star systems, both in P- and S-Type orbits, is just another facet of this diversity.

To predict the architecture of planetary systems and planet characteristics, the theories of planet formation and evolution must explain the systems already found. A huge amount of work has already gone into describing individual systems, as well as recreating the statistics of the population as a whole. This latter approach, known as population synthesis (Mordasini et al. 2009, 2012; Alibert et al. 2013; Ida and Lin 2010), generally uses Monte-Carlo algorithms to cover huge areas of parameter space, instead of using computationally expensive approaches such as hydrodynamic modelling (disc-planet interactions) and N-body simulations (planet-planet interactions), which are the tools used in the first approach. Whilst we will focus on using existing systems to test the impact of additional physics on circumbinary disc and planet evolution, population synthesis models are an invaluable tool in comparing the large-scale properties of populated and observed populations. Armstrong et al. (2014) have shown that, even with the small

catalogue of detected circumbinary planets, meaningful statistical conclusions can be made about the nature of these systems.

The results from exoplanet detection campaigns have given theorists working in the fields of protoplanetary discs and planet formation numerous challenges; the detection of circumbinary planets was no different. Simulating the environment in which they form and evolve, and evaluating the role of different areas of physics, is our best tool for understanding this class of object, and making predictions for future missions. It seems likely that any theory of planet formation used to explain the diversity found in the exoplanet catalogue, must also hold around multiple star systems, including those with circumbinary planets. In the coming sections we will discuss: the birthplace of planets – protoplanetary discs, the prevailing planet formation theories, and how these planets interact with this environment; both in the context of the field of exoplanets as a whole, and with a focus on circumbinary planets.

1.2 Protoplanetary Discs

The idea that planets form and evolve in a protoplanetary disc is not a new one. It can be traced back to a work of Immanuel Kant, published in 1755 – his Universal Natural History and Theory of the Heavens – within which he set out the principle that the solar system formed from a cloud which collapsed towards the Sun, which the planets then grew from. The core concept behind this so-called nebula hypothesis has remained a cornerstone of stellar and planet formation since, with numerous refinements. The basic picture is that the Sun formed from a collapsing cloud of gas, the remainder of which became a disc of dust and gas due to conservation of momentum; the planets and other bodies in the solar system then formed from this reservoir of material.

The prograde, and approximately coplanar, nature of the orbits in the solar system are cited as evidence for this theory. The planets in the solar system also back a picture where small rocky planets form in the inner solar system, with more massive gas and ice giants forming in the outer disc, past the ice or snow-line, where volatiles are able to condense out. The reservoir of material at these locations allows the formation of giant planets, with extended envelopes. The architectures of many exoplanetary systems, and the population of hot Jupiters,

can not be explained solely by this picture; a mechanism called migration has to be invoked – to move planets through the disc from where they were initially formed to where they are observed.

To understand the environment in which planets form, both those around single stars and binary star systems, it is helpful and necessary to understand the environment in which they form. Throughout this section we will highlight key points in the formation, evolution and observations of protoplanetary discs, followed by ideas specific to circumbinary protoplanetary discs. For a more detailed picture of the protoplanetary disc we direct the reader to several reviews on the subject: Dullemond and Monnier (2010) on the protoplanetary disc within 0.1 au; Williams and Cieza (2011) on the disc beyond that; and Armitage (2011) on the topic of angular momentum transport in discs.

1.2.1 Formation

As a molecular cloud collapses under the action of its own gravity, a significant portion of the mass falls onto a central point source forming a protostar. A protoplanetary disc quickly forms as more distant material with higher angular momentum falls inward. As the core collapses, the disc cools down and it accretes on to the star. The collapse of the core opens a roughly spherical cavity in the surrounding envelope, evidenced by lower extinction in the mid-IR emissions (Enoch et al. 2009). We are left with a protostar surrounded by a protoplanetary disc and an envelope, which can now be considered to be a young stellar object (YSO), instead of a molecular cloud.

YSOs fall into different classes, separated by the gradient of the spectral energy distribution in the EM spectrum between 2–25 μm, $\alpha_{IR} = (\mathrm{d}\log \nu F_\nu) \,/\, (\mathrm{d}\log \nu)$; believed to indicate different stages in the evolution of the system (Williams and Cieza 2011):

- Class 0 – exhibit no optical or near-IR emission; the envelope mass is much greater than that of the star or the disc (Andre et al. 1993).

- Class I – positive gradient ($\alpha_{IR} > 0.3$); correspond to a star with a massive disc, roughly the same mass as the remaining envelope (Lada 1987).

- Class II – negative gradient ($-0.3 > \alpha_{IR} > -1.6$); the envelope is virtually depleted, and the disc has a mass of $\sim 1\%\, M_\star$; strong Hα and UV emissions indicate these are accreting discs (Lada 1987; Andre and Montmerle 1994).

- Class III – strongly negative gradient ($\alpha_{IR} < -1.6$); negligible envelopes and low-mass, quiescent discs, with little or no evidence of accretion (Lada 1987; Andre and Montmerle 1994).

Flat-spectrum sources ($0.3 > \alpha_{IR} > -0.3$), representing an intermediate stage between Class I and class II YSOs have also been discovered. Class I and II YSOs are called embedded objects, as they are still at the centre of a significant envelope. This embedded stage is thought to last around 1 Myr (Evans et al. 2009), whereas the disc lifetime after the embedded stage is 1–10 Myr (Wyatt 2008).

1.2.2 Properties

The first instruments able to image, and study, protoplanetary discs (the *Infrared Astronomical Satellite (IRAS)* and the *Hubble Space Telescope* in the optical band) allowed characteristics of the population to be defined. Protoplanetary discs contain material at different locations, and hence temperatures, consequently emitting over a range of wavelengths. Observing discs over multiple wavelength bands allows use to connect an emission feature with a given temperature, and hence radial location in the disc. One of the goals of studying these objects was to find the density and temperature distributions in these discs, as both of these impact on the formation and evolution of planetary bodies.

From early observations, such as Fig. 1.10a which shows a dark disc around a bright central object with the *Orion* nebula in the background, the distributions were thought to be smooth and described by power-law distributions. As instrumentation became more sophisticated, with telescopes such as *Spitzer*, *Herschel*, and the *SPHERE* imager on the *VLT*, and the telescope array *ALMA*, it became clear the picture was not so simple. Axisymmetric ring structures have now been

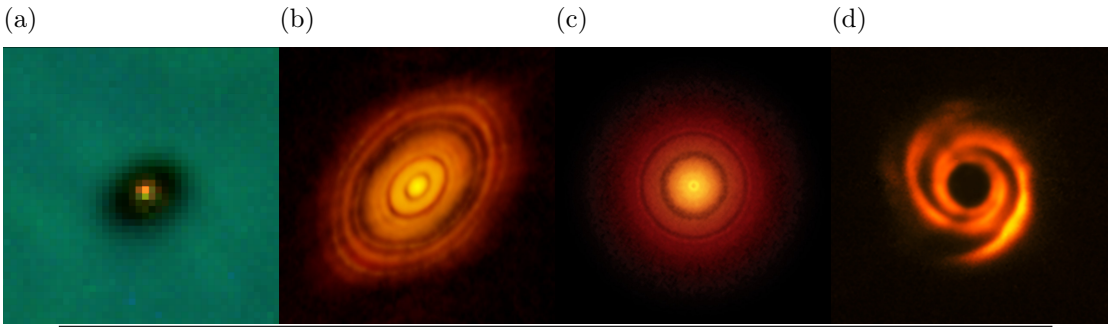

FIGURE 1.10: Observations of protoplanetary discs. *(a)* Image taken by the *Hubble Space Telescope* of a young star and protoplanetary disc in the *Orion* Nebula. Image Credit: C.R. O'Dell/Rice University; NASA *(b)* Image of radial structures in the young, massive *HL Tauri* protoplanetary disc, taken by *ALMA*. Image Credit: ALMA(ESO/NAOJ/NRAO); C. Brogan, B. Saxton (NRAO/AUI/NSF). *c* Radial structures in the old disc in *TW Hydrae*, also taken by *ALMA*. Image Credit: S. Andrews (Harvard-Smithsonian CfA); B. Saxton (NRAO/AUI/NSF); ALMA (ESO/NAOJ/NRAO). *(d)* A protoplanetary disc with non-axisymmetric features, around *HD 135344 B*, taken with the *SPHERE* instrument on the *VLT*. Image Credit: ESO, T. Stolker *et al.*

imaged around young, massive discs such as *HL Tauri* (ALMA Partnership et al. 2015), and old, depleted discs like *TW Hydrae*, the closest YSO to the Sun (Andrews et al. 2016). Several theories have been put forward to explain these highly structured discs: embedded planets (Dipierro et al. 2015; Picogna and Kley 2015); dust trapped at pressure maxima (Flock et al. 2015); enhanced dust growth near ice lines (Zhang et al. 2015), and the sintering of dust aggregates (Okuzumi et al. 2016). Discs with non-axisymmetric features have now also been imaged, the disc in *HD 135344 B* shows large-scale spiral features, as well as evidence of shadowing (Stolker et al. 2016).

Despite the perturbations to the discs seen in these images, there is still use in trying to fit power-law slopes to the underlying temperature and density distributions, especially as a tool to allow initialisation of simulated discs. An early model of protoplanetary discs, developed in the context of the solar system was the Minimum Mass Solar Nebula (or MMSN) model by (Weidenschilling 1977), later developed by (Hayashi 1981). It estimates the original mass distribution in the solar system. It uses the current location and composition of the planets, to estimate the minimum mass and distribution of solids required to form them. This includes the terrestrial planets in the inner solar system, the heavy elements thought to form the cores of the giant planets, the volatiles and ices which make

up their envelopes and comets, as well as asteroids and other rocky bodies; the combined mass of heavy elements was estimated to be around $15\,\mathrm{M}_{\oplus}$. Finally enough gas (hydrogen and helium) is distributed throughout the disc so that the gas-dust ratio is equal to that of the Sun. The result of this calculation yields a total mass $\sim 1.5\%\,\mathrm{M}_{\odot}$, spread out over a disc with radius $r_d = 40\,\mathrm{au}$, with the following distribution:

$$\Sigma = 1731\left(\frac{r}{1\,\mathrm{au}}\right)^{-\frac{3}{2}}\,\mathrm{gcm}^{-2} \tag{1.4}$$

Assuming a thin disc, the principle of hydrostatic equilibrium (the balance of pressure and gravity forces) along with the centripetal force due to its rotation, an equilibrium gas volume density profile can be derived. At a given radius r and altitude z in the disc it can shown:

$$\rho\left(r,z\right) = \frac{\Sigma_g\left(r\right)}{\sqrt{2\pi}H}\exp\left(-z^2/2H^2\right), \tag{1.5}$$

where the gas volume density decays as a Gaussian profile with z. In deriving this expression we have assumed that the equation of state and vertical temperature structure in the disc is isothermal. The assumption that the temperature is constant with z allows us to equate the pressure in the disc with the sound speed and density. H is associated with the disc thickness, which under the hydrostatic assumption is related to c_s/Ω, the sound speed c_s and orbital frequency Ω. The ratio between H and r is the disc aspect ratio, and is an important quantity in circumbinary disc and planet evolution, which we will discuss later.

1.2.3 Evolution

Two physical process dominate the evolution of protoplanetary discs; accretion, which dominates at early times and photo-evaporation, which eventually disperses the disc.

Accretion onto the central star is driven by the transport of angular momentum through the viscosity of the fluid in the disc. The disc will evolve as a viscous fluid throughout its lifetime, moving inwards as it ages, and accreting onto the central star (Pringle 1981; Papaloizou and Lin 1984; Papaloizou and Lin 1995). Viscosity is not the sole medium by which angular momentum can be transported in the disc; spiral waves, which may sufficiently steepen to become shocks, can also transport

angular momentum over large scales (Larson 1989; Livio and Spruit 1991), as well as tidal or gravitational interactions with companions or planets (Terquem 1998).

In order to derive accretion rates that match observations, a disc viscosity many orders of magnitude greater than that possible due to the interactions between molecules is required. The dominant physical process now believed to give rise to disc viscosity is due to magneto-hydrodynamic (MHD) turbulence; the magnetorotational instability (MRI) described by (Balbus and Hawley 1991), set up due to coupling between the disc material and a weak magnetic field present in the disc – perhaps a remnant of the collapsing molecular cloud. While this instability is believed to dominate hydrodynamic turbulent effects, the disc material must be ionised for this instability to develop. The orientation and strength of the magnetic field is also important. Bai and Stone (2013) find that for a weak vertical magnetic field the MRI is suppressed, but a laminar flow drives a magnetocentrifugal wind transporting angular momentum away from the disc, driving accretion onto the star.

If the MRI is active, Gammie (1996) suggested a dead zone ought to develop. A dead zone can arise when the disc is too cool to be collisionally ionised, and well-shielded enough that ionising high-energy radiation or cosmic rays cannot penetrate. The disc would then be vertically stratified, with viscous inner and outer regions, viscous active surface layers and a shielded dead zone layer. Whilst there is no observational evidence for this vertical structure, it is supported by MHD modelling (Terquem 2008, e.g.).

The existence of dead zones could play a role in planet formation models; in 3-D MHD shearing box or global disc simulations, Nelson and Gressel (2010) found that MHD turbulence can increase the velocity dispersion of planetesimals $<$ 10 km. This has a destructive effect during planetesimal collisions, suggesting that planetesimal accretion could occur primarily in non-turbulent dead zones. MHD simulations are expensive computationally to run for long physical time-scales, instead cheaper HD simulations can be run with a prescription for the viscosity due to MHD turbulence; one such prescription, the α-model (Shakura and Sunyaev 1973), supported by Balbus and Papaloizou (1999) is described in Sec. 2.1.1.

The second key physical process controlling the evolution of protoplanetary discs is photo-evaporation. High energy photons (FUV, EUV and X-ray) incident on the upper layers of the disc heat those regions until they have sufficient thermal

energy to escape the gravity of the central star; a photo-evaporative flow is driven from the disc surface (Dullemond et al. 2007; Clarke 2011; Alexander et al. 2014, etc.).

As accretion decreases the disc mass, the accretion rate falls, and photo-evaporation becomes important. When the rate of accretion falls below the rate of photo-evaporation, there is an imbalance between the depletion and supplying of material from the the outer disc. Over a viscous time-scale ($\leq 10^5$ yr), the inner disc becomes drained of material. With the depletion of the inner disc, the rest of the disc is no longer shielded from high-energy photons, which then begin to impact, and photo-evaporate the outer disc in an inside-out process; at which point accretion onto the central source is halted (Clarke et al. 2001).

With the removal of the disc, planet formation must proceed by dynamical processes, as disc-driven processes no longer occur. Although the impact of planet-planet or planet-planetesimal is important in the post-disc evolution of planetary systems, it is beyond the scope of this work.

1.2.4 Circumbinary Discs

Protoplanetary discs have been imaged around stars in binary systems, as well as discs misaligned by the presence of a stellar companion (Jensen and Akeson 2014). The presence of a stellar companion, especially on an inclined orbit, could have dramatic effects on the evolution and properties of the protoplanetary disc around members of binaries, such as truncation of the outer edge of the disc. In this thesis we will focus on the class of protoplanetary discs which are common to both members of a binary system. Whether binaries have circumbinary discs depends on their orbital separation. Wide binaries, with separations $d > 100$ au, show no sign of circumbinary discs; instead one or both members show evidence of individual protoplanetary discs – or in binary terminology, circumstellar discs. Close binaries ($d < 10$ au) host circumbinary discs, which at large distances resemble protoplanetary discs around single stars. Some evidence exists that intermediate separation ($10 < d < 100$ au) binaries can host both circumstellar discs around at least one member, as well as circumbinary discs (Mathieu et al. 2000; Kley and Burkert 2000). One of the most famous imaged circumbinary discs is *GG Tau*, an intermediate binary with a semi-major axis of 62 au (Yang et al. 2017), first imaged by Dutrey et al. (1994). The original discovery image can be seen

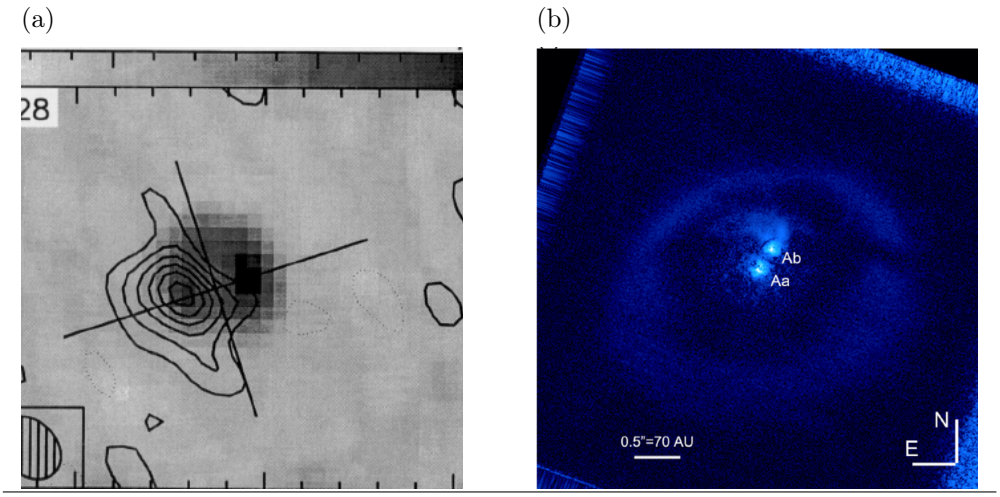

FIGURE 1.11: The original and latest images of the circumbinary disc in the *GG Tau* system. *(a)* Discovery image of the *GG Tau* circumbinary disc. The cross indicates the apparent disc plane and axis. The inner edge of the disc lies at 180 au. Image Credit: Dutrey et al. (1994), figure has been cropped by the author. *(b)* Scattered-light image in the infra-red region of the *GG Tau* system. In this image evidence of circumstellar material can be seen, as well as an arc of material connecting the circumbinary disc to the circumstellar disc of *GG Tau B*. Image Credit: Yang et al. (2017), image has been modified by the author.

in Fig. 1.11, along with the image taken with the infra-red polarimeter *HiCIAO* on the *Subaru* telescope (Yang et al. 2017).

Current state-of-the-art instrumentation can only resolve the outer portions of circumbinary protoplanetary discs. At this distance they look much like their counterparts around single stars; however theoretical studies of hydrodynamic discs around close-binary systems are able to model this region. Artymowicz et al. (1991) first undertook SPH simulations of the disc around a close-binary system. They found that the binary sweeps out a cavity in the material, leaving the area surrounding the binary depleted of (Fig. 1.12); the back-reaction between the disc and the binary lead to significant alteration of the binary orbital elements – in general the semi-axis decreases, and eccentricity increases. Later work in Artymowicz and Lubow (1994) found that the extent of this cavity depends weakly on the mass-ratio of the binary stars, and strongly on the eccentricity of the binary. More eccentric binaries create larger central cavities. The creation of the cavity is due to ordinary and eccentric Lindblad torques (which we will discuss later) tidally truncating the disc. These torques also act to suppress accretion of the circumbinary disc onto the central objects. Suppressing one of the key processes

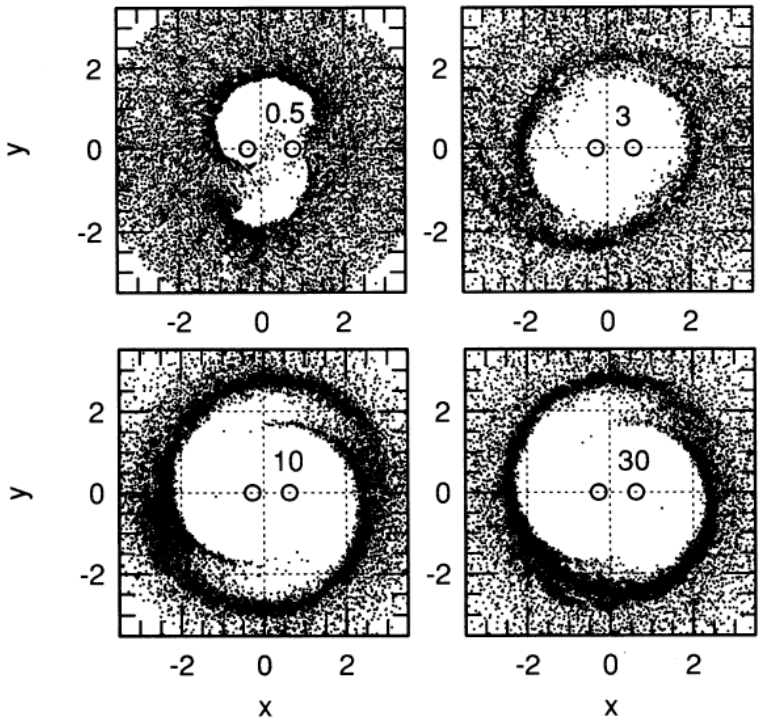

FIGURE 1.12: The creation of a cavity around an $e_b = 0.1$, $\mu_b = 0.3$ binary, in a SPH simulation. The edge of the cavity lies at approximately $2.3a_b$, just outside $3:1$ MMR with the binary. Readers will note the proximity of this location to the critical stability limit of Holman and Wiegert (1999), which for $e_b = 0.0$, $\mu_b = 0.5$ is equal to $2.4a_b$. Image Credit: Artymowicz and Lubow (1994).

in the evolution and dispersal of protoplanetary discs could act to lengthen the lifetime of circumbinary discs (Alexander 2012).

Depending on the properties of the binary the central cavity is usually not axisymmetric. Papaloizou et al. (2001) undertook an analysis examining the creation of the circumbinary cavity. A parametric instability is launched in the disc, generated by mode coupling between an $m = 1$ eccentric disturbance in the disc, and the $m = 1$ component of the binary potential, at the location of the $3:1$ eccentric Lindblad resonance. An $m = 2$ wave is launched with a wave-speed of $\Omega_b/2$ transporting angular momentum outwards leading to eccentricity growth of the disc material. For this non-linear mode coupling to exist in the disc, the binary must have a non-zero eccentricity, or non unity mass ratio; however for binaries with a significant eccentricity, higher-order terms in the binary potential can contribute to the growth of disc eccentricity (Pierens and Nelson 2013). It must be noted that the findings of Papaloizou et al. (2001) were for extreme mass ratios, where

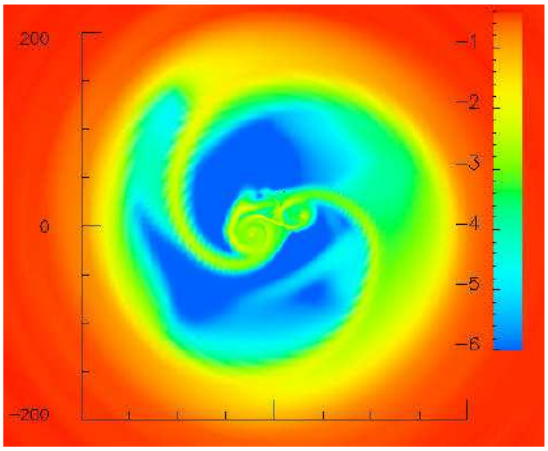

FIGURE 1.13: Simulated disc around the *GG Tau* system. Whilst the surface density scale is log-units, streamer channels bridging the cavity can be seen. Note the similarities with the observed image of the *GG Tau* system in Fig. 1.11. Image Credit: Günther and Kley (2002).

the mass of the companion is more relevant to giant planets or brown dwarfs, not for two stellar mass bodies. The interactions are more akin to planet-disc interactions than a true stellar binary interacting with a disc.

The orbits of gas fluid elements align in these systems. When the fluid is moving slowest, at apocentre, this creates an asymmetric high surface density feature just exterior to the cavity. Further interaction between the binary and this feature cause it to precess, leading to oscillations in the eccentricity of the disc; maxima occurring when the longitude of pericentre of the binary and disc align (Pelupessy and Portegies Zwart 2013; Pierens and Nelson 2013; Kley and Haghighipour 2014).

Whilst accretion is inhibited onto the central binary, it is not altogether halted. Simulations have shown that material can form streamer channels, or spiral arms, down which material can flow. These channels connect the edge of the cavity with the circumstellar discs surrounding the binary components. Figure 1.13 shows examples of these features, as well as the spiral arm connecting the two circumstellar discs, for a simulated *GG Tau* system. The arc feature noted in Yang et al. (2017) could be evidence of one of these spiral arms.

The gravitational influence of close binaries on circumbinary discs modifies the structure and dynamics of the inner region of circumbinary discs quite significantly from their single star counterparts. In the next section we will discuss the prevailing theories of planet formation, whether they can accurately describe the

observed population of exoplanets, and the impact the features discussed in this section have on them.

1.3 Planet Formation

In this section we will highlight the two main theories commonly put forward to model planet formation; the Gravitational Instability (GI) model and the Core Accretion paradigm. It is worth noting that these two theories are not mutually exclusive and can operate in different regimes; a system could in theory contain planets produced by each of these methods, dependent on conditions in the disc. We discuss where each of these methods works in explaining aspects of the exoplanet population, failures of each, and describe results from work studying the formation of planets in the challenging circumbinary environment.

1.3.1 Gravitational Instability

If protoplanetary discs are massive enough, they can fragment and collapse under their own self gravity against the forces of pressure and azimuthal shear. This is thought to be the formation scenario for Brown Dwarfs, but also for massive giant planets (Boss 1997; Stamatellos and Whitworth 2008). The gravitational collapse of these fragments is related to its cooling time and the Toomre instability parameter:

$$Q = \frac{c_s \kappa}{\pi G \Sigma}, \tag{1.6}$$

where c_s is the sound speed, κ is the epicyclic frequency and Σ is the surface density. For a Keplerian disc κ can be substituted with the Keplerian orbital frequency $\Omega_{\rm K}$. A disc is susceptible to collapse if $Q \leq 1$. If the criteria for stability is not met, the cooling time in the disc dictates the non-linear response of the disc. If a clump can equilibriate its temperature with its surroundings on a timescale $\tau_c \leq 3\Omega^{-1}$ it can undergo fragmentation (Gammie 2001). If this cooling criterion is not met the disc can enter a gravito-turbulent state, where angular momentum is transported through the disc by spiral waves. Fragmentation and collapse occurs preferentially in cooler regions of the disc, so is more likely to occur in the outer disc, rather than the hotter inner disc. The inverse dependence

on Σ clearly means that massive discs are more likely to collapse, or over-dense regions in less massive discs.

For these reasons the Gravitational Instability model has been used to explain the formation of giant planets at large distances from their parent stars (e.g. the four super-Jovian planets in *HR 8799*). It has been unable to explain the formation of planets in the inner regions of the disc, where the fragments are unable to form due to long cooling time-scales. Problems also arise when trying to create intermediate mass planets. More recently a modified version of gravitational instability has been proposed, where tidal downsizing of inwardly migrating giant planets can reproduce the observed exoplanet statistics to some extent, and intermediate mass planets (Nayakshin 2015; Nayakshin and Fletcher 2015). The prevalence of discs in which self gravity induced collapse could occur, and the process of fragmentation itself are still open questions in this field.

1.3.2 Core Accretion

The second area of planet formation theory covered here is the core accretion model. Planets grow in a bottom-up approach; small dust grains coagulate into larger rocks, which grow and eventually form planetary sized bodies. Dust and icy volatiles which condensed out of the protoplanetary disc, settle towards the mid-plane of the disc, on a time-scale related to the disc and dust properties:

$$\tau_s = \frac{3\rho c_s}{4R_{\rm gr}\Omega^2\rho_{\rm gr}}, \tag{1.7}$$

where ρ is the disc density, c_s is the sound speed of the gas, and $R_{\rm gr}$ and $\rho_{\rm gr}$ are the radius and density of the dust grains. Dust settling times in typical protoplanetary discs range from $\sim 10^4\,$yr at $1\,$au, to $\sim 10^6\,$yr at $10\,$au. The concentration of settling dust grains at the mid-plane allows them to clump and grow through collisions (Helled et al. 2014). This process can grow μm sized dust grains to centimetre sized particles. At this size however growth by dust coagulation becomes inefficient; particles either bounce off each other when their collision velocity is low, or fragment at higher velocities. This inhibition of growth beyond centimetre scale is known as the bouncing barrier (Blum and Wurm 2008; Zsom et al. 2010; Kelling et al. 2014).

Up to this stage the dust particles have been orbiting in the disc in a mostly Keplerian manner, however at the cm scale and larger the grains become uncoupled

from the gas disc. They experience aerodynamic drag and drift radially inwards towards the central star, on a time-scale of $\sim 10^5$ years for centimetre- and metre-sized bodies. With the inefficient growth of pebbles beyond centimetre scales, and the rapid drift towards the star, the disc would be unable to form metre-sized bodies and above. One mechanism to overcome this, by converging pebbles and boulders at common locations, is known as the streaming instability. Pebbles clump together into a dense layer, accelerating the surrounding gas toward the Keplerian velocity. This reduces their drift rate by reducing the relative velocity between the pebbles and the gas till it is negligible (Johansen et al. 2007). This process continues until the concentration of pebbles increases until the clump becomes gravitationally unstable and collapses to form kilometre-sized bodies known as planetesimals. Collisions between pebbles in this over-dense layer could also account for the growth of planetesimals, by low-velocity collisional growth (Weidenschilling 2000). As more planetesimals form in the disc, collisions between them are more common, resulting in more massive planetesimals. The most massive planetesimals grow significantly faster due to gravitational focusing, as their collisional cross-sections are increased by a factor of $\sqrt{1 + v_{\rm esc}^2/v^2}$, where $v_{\rm esc}$ is the escape velocity from the more massive body, and v is the relative velocity of the less massive body being accreted.

When a small number of bodies grow considerably more massive than the rest – such that their escape velocities are much greater than the average velocity dispersion of smaller bodies in the disc – they undergo runaway growth, quickly doubling their mass. The rate of mass accretion of such a planetesimal of mass M and radius R, is given by the effective collisional cross-section, the number density of surrounding bodies being accreted n, and their average mass m and velocity dispersion v (Safronov 1972):

$$\frac{{\rm d}M}{{\rm d}t} = nmv\pi R_{\rm eff}^2 = nmv\pi R^2(1 + v_{\rm esc}^2/v^2). \tag{1.8}$$

Within the runaway growth regime, the doubling time is proportional to $M^{-1/3}$. The runaway growth regime ends when the gravitational influence of the massive body, stirs up the remaining planetesimals, increasing their velocity dispersion such that $v_{\rm esc} \approx v$.

When large planetesimals enter this regime, known as oligarchic growth (Kokubo and Ida 1998), they no longer undergo runaway growth since the gravitational focusing effect is less efficient (Kokubo and Ida 1998). In this regime the mass

doubling time is proportional to $M^{1/3}$, slower than that in the runaway growth phase. Planetary embryos grow by accreting material in their feeding zones until they reach their isolation masses, i.e. the feeding zones become empty. The isolation mass is given by:

$$M_{\rm iso} = \frac{(4\pi b a^2 \Sigma_s)^{3/2}}{\sqrt{3M_\star}}, \tag{1.9}$$

where a is the embryo's location in the disc, Σ_s is the local surface density of solids, and b is a constant defining the size of the feeding zone, typically equal to $2\sqrt{3}$. Multiple embryos, or oligarchs, are able to form in the disc, separated by several mutual Hill radii.

The isolation mass scales as $M_{\rm iso} \sim a^3$, oligarchs have different masses depending on where they are forming: close to the star, their masses are small, typically between a Mars and an Earth mass; at larger radii, this isolation mass is on the order of a few Earth masses, consistent with the expected core masses of the giant planets. In the low mass regime, this is in good agreement with the expected isolation masses which formed the precursors of the terrestrial bodies in the solar System (Chambers and Wetherill 1998). The formation time-scale of oligarchs is similar to the disc lifetime, measured in millions of years. These cores, forming before the disc dissipates, are able to accrete gas from their surroundings forming gaseous envelopes. If they form early enough, they can accrete enough mass to undergo runaway gas accretion, quickly growing in size to become gas giants. A comparison of the abundance of hydrogen and helium in the envelopes of the ice giants and gas giants, suggests that Uranus and Neptune's cores formed slowly. Jupiter and Saturn were able to undergo runaway gas accretion before the disc dissipated, whereas Neptune and Uranus were not (Lissauer 1995; Thommes et al. 2003).

The accretion of gaseous envelopes can occur when the escape velocity from the planet is greater than the local sound speed in the gas. If the accreted gaseous envelope has a comparable mass to that of the core mass, runaway gas accretion can occur allowing the the formation of a gas giant. This process is very slow for low-mass cores since they have low escape velocities, resulting in negligible gaseous accretion over the lifetime of the disc. Pollack et al. (1996) found that a 10 Earth mass core was required for significant gas accretion, and runaway accretion to occur over the lifetime of discs. More recent work has found that cores with masses as low as 3 Earth masses are capable of becoming gas giants

before the end of the disc lifetime, if the opacity of the envelope material is reduced – possibly through grain growth or settling (Movshovitz et al. 2010).

The core accretion model is typically cited to explain the formation of planets orbiting close to their central stars, like the terrestrial planets in our solar system (Chambers and Wetherill 1998). It is inefficient at forming massive long period planets like those detected by direct imaging, except in massive protoplanetary discs, where the gravitational instability paradigm may be more appropriate. More recently however, the accretion of pebbles on to small cores has been proposed as a formation mechanism for giant and terrestrial planets irrespective of radial location (Chambers 2014; Lambrechts et al. 2014; Bitsch et al. 2015; Levison et al. 2015a,b). Models of in-situ formation have also been proposed for planets in the inner regions of the disc. In these models, planetary migration through interactions with the disc are neglected, and planets form through the accretion of material in their local vicinity arising from massively enhanced solid surface densities compared to those found in typical models of protoplanetary discs (Chiang and Laughlin 2013; Chatterjee and Tan 2014, 2015).

1.3.3 Planet Formation in Circumbinary Discs

Planets in circumbinary discs are thought to be able to form following the two prescriptions above. The class of circumbinary planets we are most interested in are the *Kepler* close-in planets around short period binaries. We will therefore focus on the Core Accretion model to form the sub-Jovian mass planets around these systems. Circumbinary systems have been hailed as ideal test-beds for the robustness of planet formation theories. As we will see below, the environment created by the tidal torque of the binary in the disc is quite extreme. The detection of planets around these systems (as well as other extreme systems, such as pulsar systems) suggest that planet formation in nature is ubiquitous. Our theories of planet formation must be able to recreate these architectures.

Whilst the same processes are thought to function in single and binary-star systems alike, significant challenges have been found in recreating the *Kepler* circumbinary planets in the vicinity of their observed orbits. Formation of planets in-situ must occur under the strong gravitational influence of the binary, as well as the asymmetric gas disc. One of the biggest barriers in this problem is bringing

sufficient numbers of planetesimals together in a manner which leads to consistent mass growth.

Work by Scholl et al. (2007), before the discovery of the *Kepler* circumbinary planets, found that the tidal influence of the binary companion could excite the eccentricity of planetesimals, but with their pericentres aligned. At first glance this is promising, as this acts to reduce the relative velocities between colliding bodies. This pericentre alignment effect is size-dependent however. The orbits of different sized bodies cross, increasing the relative velocity between them, leading to erosive collisions. Large scale spiral waves, or asymmetric features in the disc, which we see in circumbinary discs, can also lead to high impact velocities (Marzari et al. 2008; Kley and Nelson 2010).

Work to form *Kepler-16 b* in-situ, shortly after its discovery, found the above to be true. The eccentricity of planetesimals, and interaction with the perturbed disc, made it extremely difficult to form protoplanetary cores from planetesimals. In fact, dependent on the binary and disc parameters, planetesimal accretion could be inhibited even out to 10 au (Paardekooper et al. 2012; Meschiari 2012a,b; Lines et al. 2014, 2015, 2016).

The above factors suggest that the protoplanetary cores of the planets detected in these systems did not form close to their observed locations. Whilst they may have accreted smaller bodies and gas in this vicinity, the cores themselves must have formed in the outer disc where the influence of the binary is negligible and the circumbinary protoplanetary discs resemble those around single stars. To reach their current location in close proximity to their host binaries, they must have undergone migration from where they were formed.

1.3.4 Discussion

Many of the exoplanets discovered prove difficult to form with the theory of planet formation alone – either the Gravitational Instability or Core Accretion model. The first exoplanet discovered around a Main Sequence star (Mayor and Queloz 1995, *51 Pegasi b*), a member of a class of planets known as hot Jupiters, was a huge problem for giant planet formation theory. Giant planets were believed to form in the outer disc, where there is a wealth of planet building materials beyond the snow line. It became clear that there must be significant post-formation

interaction to alter the orbits of planets to produce the range of exoplanets we observe, including circumbinary planets.

Planet-Planet Interactions

Multiple planets can interact in a variety of ways; summarised in a review by Davies et al. (2014). Collisions can occur; either catastrophically disrupting the bodies or resulting in a merger. Orbital resonances between planets can have a number of effects; planets can become locked into mean-motion resonances making them migrate with each other (Snellgrove et al. 2001), although resonant chains have been found to be unstable (Terquem and Papaloizou 2007; Rein 2012; Goldreich and Schlichting 2014). Planets near commensurability can be stable, allowing super-Earths and hot-Neptunes to be found in close proximity to each other (Terquem and Papaloizou 2007; Hands et al. 2014), a finding which agrees with many observed exoplanetary systems.

Interactions between planets can lead to eccentricity growth, which can lead to scattering and ejection from the system (Cresswell and Nelson 2006). Such a mechanism could explain the proximity of the *Kepler* circumbinary planets; in such an event one of the planets is scattered into the outer disc on a highly eccentric orbit, whereas the other is scattered onto an orbit in the inner disc (Kley and Haghighipour 2015). The Kozai-Lidov mechanism by which eccentricity and inclination can be interchanged (Kozai 1962; Lidov 1962), can significantly alter planetary orbits; (Wu and Murray 2003) suggested the presence of a binary companion in the *HD 80606* system could facilitate Kozai oscillations, pumping the eccentricity of the planet to its observed value of 0.93. The inclination of the circumbinary planet *Kepler-413 b* could be explained with Kozai-Lidov interactions with a third stellar component on an exterior orbit (Kostov et al. 2014). Planet-planet interactions can reproduce the eccentricity distribution of the observed exoplanet population (Chatterjee et al. 2008).

In what could be considered a sub-set of planet-planet interactions, planetesimal-planet interaction can also result in orbital alteration of the planet. In what is considered the debris of planet formation, planets can interact with swarms of planetesimals, exchanging orbital energy in the process. In the solar system it is theorised that Jupiter may have drifted slightly inwards with this mechanism whilst Saturn, Uranus, Neptune moved outwards. This theory has been proposed

to explain: the current location of the Kuiper Belt (Levison and Morbidelli 2003); the capture of Kuiper Belt objects into mean motion resonances (Malhotra 1995); and even provides a mechanism for the Late Heavy Bombardment of the inner planets (Gomes et al. 2005; Tsiganis et al. 2005).

Star-Planet Interactions

Planets such as hot Jupiters, orbiting close to their parent star, may have had their orbits circularised by tidal interaction with the star (Rasio et al. 1996); or they may have become tidally locked, so that one face of the planet is always facing the star (Jackson et al. 2008; Chernov et al. 2017). Planets this close to their parent star are also subject to extremely strong irradiation. This can photo-evaporate the upper layers of the atmosphere, leading to significant atmosphere loss (Hébrard et al. 2004), as has been observed for *HD 209458 b* (Charbonneau et al. 2002). Giant planets may even have their atmospheres completely stripped, leaving a rocky core behind. In circumbinary systems, the interaction between the binary and any planets, will dominate for much of the lifetime of the system, as the disc-phase only lasts a small portion of this time. Whilst we have already discussed the critical stability around close-binaries a_c, it has also been shown that mean-motion-resonances of the form $n : 1$ with the binary are unstable (Dvorak 1986; Nelson 2003; Kley and Haghighipour 2014; Kostov et al. 2014; Kostov 2015). If the planet finds itself close to these locations when the disc disperses it may undergo scattering events, or be ejected from the system.

Disc-Planet Interactions

Gravitational interaction with the protoplanetary disc can significantly alter the semi-major axis of embedded planets, in a process known as migration. The eccentricity and inclination of protoplanets can also be changed via this interaction. As part of the focus of this thesis is on disc-planet interactions within circumbinary discs, the next Section of this Chapter will look at this subject in some detail.

1.4 Disc-Planet Interactions

Planetary migration due to interaction between the disc and embedded planets has been cited as one of the dominant mechanisms in explaining the orbital locations of planets unable to be explained by the theories of planet formation alone. Among these planets which, require significant alteration of their semi-major axes, are the circumbinary planets around close binaries. Depending on the mass of the planet, that of the star and disc, as well as properties of the disc, the migration can fall into one of several regimes, based on the nomenclature of Ward (1997).

1.4.1 Type I Migration

If the ratio of the planet's mass to the mass of the central star is small, ($q \lesssim h^3$, where h is the aspect ratio of the disc) then the perturbation to the disc by the planet is small and can be considered to be linear to good approximation (Korycansky and Papaloizou 1996). For a disc with h = 0.05, a common value used in the literature, this corresponds to a planet mass of much less than $40\,\mathrm{M}_{\oplus}$. This regime could be used to model the migration scenarios of many of the classes of exoplanets discovered such as super Earths and hot Neptunes (if the mass of the host star is $\sim 1\,\mathrm{M}_{\odot}$). Several components have been found to contribute to Type I migration, which will be outlined below.

Lindblad Torque

Locations exist in the disc where material regularly encounters the gravitational potential of the planet, and experiences repeated periodic forces. These locations, known as Lindblad resonance radii, occur interior and exterior to the orbit of planet, where they are respectively called the Inner and Outer Lindblad resonances (ILR and OLR for short). The potential of the planet launches waves at these locations, transferring angular momentum between the planet and the disc. For a planet on a circular orbit in a Keplerian disc, and neglecting the forces of pressure, viscosity and self-gravity, these radii occur at:

$$r_{\mathrm{ILR}} = \left(\frac{m}{m+1}\right)^{2/3} a_{\mathrm{p}}, \quad \text{and} \quad r_{\mathrm{OLR}} = \left(\frac{m}{m-1}\right)^{2/3} a_{\mathrm{p}}, \tag{1.10}$$

where m (an integer ≥ 2) is the inverse wave-number corresponding to a periodic azimuthal component of the planet's Fourier decomposed potential, rotating with the planet's orbital frequency (Goldreich and Tremaine 1979). If pressure in the disc is included the Lindblad resonance locations pile up for $m \gg 1$ at locations corresponding to $r_{\rm LR} = a_{\rm p} \pm \frac{2}{3}H$. The contribution of the high m modes to the total Lindblad torque is diminished leading to what is described as the torque cut-off (Artymowicz 1993).

The cumulative torque due to the waves launched at the Lindblad resonant radii, is called the Lindblad torque. The density perturbation in the disc material is a spiral density wave (Ogilvie and Lubow 2002). The inner wave – at a location interior to the planet – leads the planet and applies a positive torque, pulling the planet forward. The outer wave – launched exterior to the planet – pulls back on the planet, applying a negative torque. Individually, a positive torque will cause outwards migration and a negative torque will decrease the semi-major axis of the planet; however the resultant torque is the net action of the two, known as the differential Lindblad torque.

With the decomposed planet potential modes mentioned above, an analytical expression for the total torque can be derived by calculating the torque due to the superposition of potential modes by using the linearised equations of hydrodynamics and the WKB approximation (Goldreich and Tremaine 1979; Lin and Papaloizou 1979). With the linearised fluid equations in (Paardekooper and Papaloizou 2008), a 2-D disc with surface density profile $\Sigma \propto r^{-a}$ and temperature profile $T \propto r^{-b}$, the linearised differential Lindblad torque can be written (Paardekooper et al. 2010):

$$\gamma \frac{\Gamma_{\rm L}}{\Gamma_0} = -2.5 - 1.7b + 0.1a, \quad \text{where} \quad \Gamma_0 = \frac{q^2}{h^2}\Sigma_{\rm p} r_{\rm p}^4 \Omega_{\rm p}^2, \tag{1.11}$$

where γ is the adiabatic exponent, Γ_0 is a normalisation factor, and the subscript p denotes at the planet's location. For generalised profiles of Σ and T this agrees well with numerical simulations (Masset 2011). This treatment of the Lindblad torque takes into account the energy balance available in non-isothermal discs, which can not only alter the strength of the torque, but also its sign (Paardekooper and Mellema 2006). When calculating the Lindblad torque numerically on a planet, a correct gravitational softening parameter must be used in the potential of the planet for 2-D and 3-D simulations to be comparable (Tanaka et al. 2002; Müller et al. 2012).

The inclusion of self-gravity, shifts the location of the Lindblad resonances closer to the planet. This makes the strength of the differential Lindblad torque more negative, increasing the rate of inwards migration (Huré and Pierens 2005; Baruteau and Masset 2008b).

For typical values, an Earth-mass planet at 1 au migrates inwards on a time-scale of 4×10^5 yr. A Neptune-mass planet at the same initial orbital radius would migrate on a shorter time-scale of 2×10^4 yr (as the Lindblad torque increases with planet mass). Comparing this with the estimated life-times of protoplanetary discs (1–10 Myr) it becomes clear that protoplanets will migrate through the disc far too rapidly, either piling up in the outer disc, or be engulfed by the central star. The disparity between these time-scales is one of the problems present in migration theory.

Papaloizou and Larwood (2000) showed that for eccentric planets, the differential Lindblad torque becomes more positive with increasing eccentricity. With sufficient eccentricity ($e \approx 1.1H/r$) the torque reverses and becomes positive. Cresswell et al. (2007) noted however that a positive torque does not always lead to outwards migration, due to the energy being removed from the planet's orbit through eccentricity damping by the disc.

Corotation Torque

In addition to the interaction at Lindblad resonances, a strong interaction also occurs between the planet and the material in the vicinity of the planet's orbital radius, or in corotation. Goldreich and Tremaine (1979) used the same linear analysis described for the Lindblad torque, to derive expressions for the linear corotation torque. In the linear regime, for typical surface density profiles, the total torque acting on the planet is dominated by the differential Lindblad torque (Tanaka et al. 2002).

Disc material which is nearly co-orbital, orbiting just interior or exterior to the planet's orbit, will librate on orbits known as horseshoe trajectories, for the shape they trace when plotted in the co-rotating frame of the planet. A schematic of a fluid element on such a horseshoe orbit is shown in Fig. 1.14. Ward (1991) included the effect of this material in the calculation of the corotation torque, which is missing from the linear theory. A torque can arise due to a lack of symmetry between exchange of material from the inner to outer disc behind the

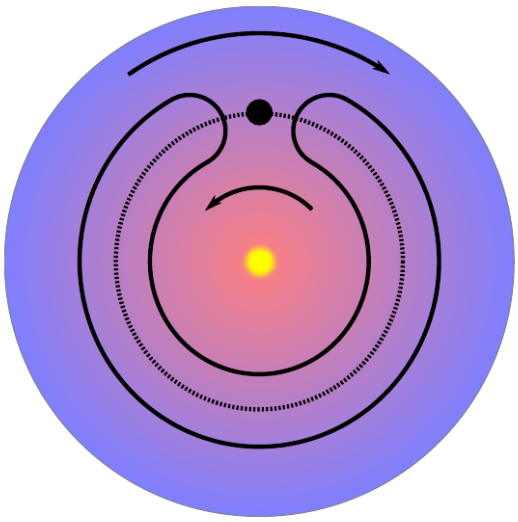

FIGURE 1.14: Schematic of the disc in the vicinity of a planet. The cool outer disc, co-orbital region, and hot inner disc can be seen. The direction of flow of a fluid element on a horseshoe orbit can be seen, in the frame of the orbiting planet. When an element ahead of the planet undergoes a horseshoe turn it moves from a slower-rotating, cool region to a hotter, faster-rotating portion of the disc (and vice versa for an element trailing the planet).

planet, and the reverse leading the planet. This torque is a non-linear contribution to the corotation torque; labelled the vortensity-related horseshoe drag, as the source of the asymmetry is caused by the vortensity gradient in the disc, where vortensity is the specific vorticity, $\left(\frac{1}{\Sigma}\nabla \times \vec{v}\right)|_z$. If horseshoe turns can occur in the disc, the linear corotation torque is replaced by the vortensity-related horseshoe drag (except in cases of significant viscosity); the horseshoe drag is an order of magnitude greater than the linear corotation torque, as softening in the potential goes to zero (Paardekooper and Papaloizou 2009a,b). Density perturbations due to interaction with material in the corotation region can be seen in Fig. 1.15.

In discs with an adiabatic equation of state, another contribution to the non-linear corotation torque can arise, fuelled by conservation of entropy. Material moved from the cool exterior to the warm interior of the disc will become more dense in order to maintain hydrostatic equilibrium – with the reverse happening in the opposite direction (Paardekooper and Mellema 2006; Baruteau and Masset 2008a; Paardekooper and Papaloizou 2008). A region of high density ahead of the planet, and a less dense region behind, exerts a positive torque on the planet, which can reduce the total torque acting on the planet, slowing down Type I migration,

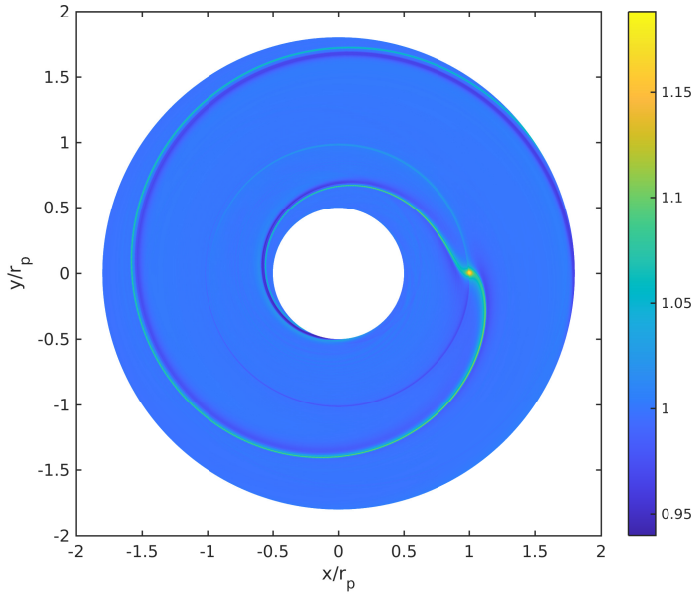

FIGURE 1.15: The relative density perturbation to a disc by a $5\,M_\oplus$ planet. The spiral density wakes associated with the Lindblad resonances can be seen, as well as the density perturbation in the corotation region. The material can be seen to be perturbed by its encounter with the planet, return to its equilibrium within half an horseshoe orbit, before encountering the planet once again. This plot was created with a high resolution FARGO simulation, using an adiabatic equation of state, where the disc temperature is relaxed over a timescale of 11 orbital periods.

or even leading to outwards migration. Paardekooper et al. (2010) were able to calculate an expression for the full non-linear horseshoe drag acting on a planet; with a surface density profile $\Sigma \propto r^{-a}$, temperature profile $T \propto r^{-b}$, and an adiabatic exponent γ;

$$\gamma \frac{\Gamma_c}{\Gamma_0} = 1.1 \left(\frac{3}{2} - a \right) + 7.9 \frac{\zeta}{\gamma} \tag{1.12}$$

where $\zeta = b - (\gamma - 1)\, a$ is the entropy gradient. The first and second terms on the right hand side correspond to the vortensity- and entropy-related corotation torques respectively; a result in good agreement with earlier work by Masset and Casoli (2009).

In an inviscid disc, the corotation region has a finite reservoir of angular momentum which will eventually be depleted when exchanges over the horseshoe region have mixed the corotation region sufficiently to wipe out the vortensity gradient. At this point this contribution to the corotation torque is thought to be saturated, and no longer operates. In a viscous disc, the disc continuously seeks to relax back

to its initial vortensity profile, so the vortensity-related horseshoe drag does not saturate.

Thermal diffusion is also required to unsaturate the entropy-related corotation torque. In an adiabatic disc without thermal diffusion, cool disc material moved to the inner disc will remain cool until moved back to the outer disc – the asymmetry of the horseshoe exchanges will be lost and the entropy-related corotation torque will saturate. For an optimally unsaturated corotation torque, displaced material should return to its equilibrium state on a time-scale shorter than the horseshoe libration period. One would like displaced disc material to return to its equilibrium state on a time-scale of some fraction of a horseshoe libration period. In a locally-isothermal disc, the entropy-related corotation torque approaches its linear value; just as for a disc with rapid viscous evolution, the vortensity-related corotation torque also approaches the linear limit. In an adiabatic disc, the corotation torque saturates. Paardekooper et al. (2011) found that the corotation torque is strongest when the viscous and thermal diffusion time-scales of material crossing the horseshoe region, are roughly equal to half the horseshoe libration time, where:

$$\tau_{\rm lib} = \frac{8\pi}{3\Omega_{\rm p} x_s}, \quad \tau_\nu = \frac{x_s^2 a_{\rm p}^2}{\nu}, \quad \text{and} \quad \tau_d = \frac{x_s^2 a_{\rm p}^2}{D}, \tag{1.13}$$

are the horseshoe libration time, the viscous diffusion time, and the thermal diffusion time respectively. Values with the p subscript refer to the properties of the planet, ν is the kinematic viscosity, D is the thermal diffusion coefficient, and x_s is the horseshoe half-width. This value is important in mediating the strength and saturation of the corotation torque. Numerous expressions have been cited for different conditions in the same context, but we cite the expression derived in Paardekooper et al. (2010) for a disc with adiabatic index γ, planet to primary mass ratio q, and a potential softening parameter b:

$$\frac{x_s}{r_{\rm p}} = \frac{1.1}{\gamma^{0.25}} \left(\frac{0.4}{b/h}\right)^{0.25} \sqrt{\frac{q}{h}}, \tag{1.14}$$

which holds for $b/h > 0.3$. For a locally-isothermal disc, and $b = 0.4h$, this reduces to $x_s = 1.1 r_{\rm p} \sqrt{q/h}$. Equation (1.14) takes into account the back-pressure caused by the Lindblad wake and other density-perturbations removed from the corotation region by a pressure scale height H.

The inclusion of self-gravity, which modified not only the location of the Lindblad

resonances but the strength of the Lindblad torque, has been shown to have a negligible impact on the non-linear corotation torque (Baruteau and Masset 2008b). If the corotation torque is calculated for a planet on an eccentric orbit (Fendyke and Nelson 2014), the horseshoe region narrows, diminishing the strength of the non-linear corotation torque. The ratio between the planet's eccentricity and the pressure in the disc, captured in h defines this reduction.

Given an unsaturated outward corotation torque comparable to the inward Lindblad torque, the possible existence of zero-torque radii arise. These locations, dependent on the properties of the disc and planet, are the result of the positive corotation torque balancing the negative Lindblad torque, leading to no net torque on the planet. Such locations could potentially act as planet traps, and catalyse the formation process by converging the material for planet formation to one location (Hellary and Nelson 2012; Cossou et al. 2013). Local disc structure can differ from the simple power-law prescription commonly assumed, possibly due to the radial structures seen in Fig. 1.10, many local zero-torque radii may exist (Coleman and Nelson 2016a). Planets of differing masses will also have different zero-torque radii (Coleman and Nelson 2014, 2016b), as well as planets on eccentric orbits – highly eccentric planets may not possess zero-torque radii (Fendyke and Nelson 2014).

1.4.2 Type II Migration

The previous section examined the disc response to a low-mass planet; such that the perturbation to the disc from the planet is balanced by the pressure and viscous forces within the disc. If the torque applied to the disc exceeds the capability of the viscosity to transport angular momentum across the horseshoe region of the planet, a gap will be created in the disc around the planet's orbital location (Lin and Papaloizou 1986). Density waves launched in these conditions carry away a portion of the gravitational torque, rather than depositing it in the vicinity of the planet, creating a pressure torque (Crida et al. 2006). The same authors found that with these two effects a gap will be opened in the disc if the following criterion is met:

$$\frac{3}{4}\frac{H}{R_{\rm Hill}} + \frac{50}{qR_e} \leq 1, \tag{1.15}$$

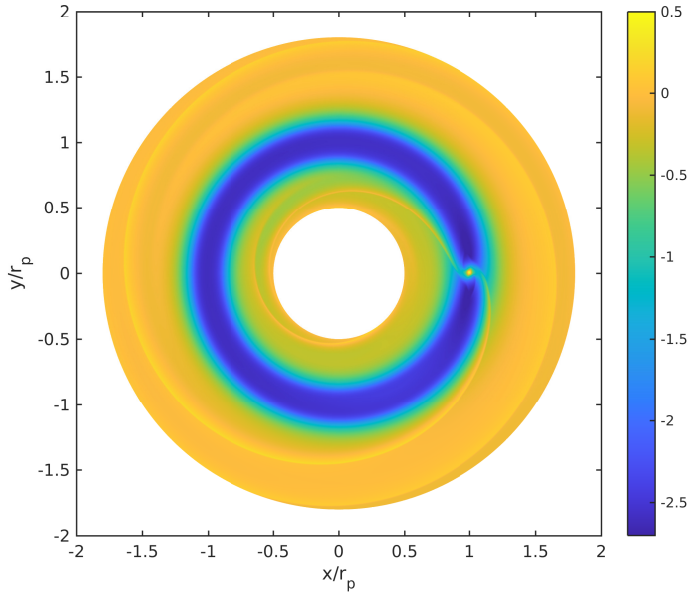

FIGURE 1.16: A Jovian mass planet opening a gap in $\alpha = 1 \times 10^{-3}$ viscosity disc, with aspect ratio $H/r = 0.05$. A base 10 logarithmic scaling of the relative density (Σ/Σ_0) is used. The co-orbital region with the planet is depleted of material, forming a gap. This figure was created from a high resolution FARGO simulation of an isothermal disc.

where $R_{\rm Hill} = r_{\rm p}\,(q/3)^{1/3}$ is the Hill radius of the planet, $R_e = r_{\rm p}^2\Omega_{\rm p}/\nu$ is the Reynolds number, determined by the kinematic viscosity in the disc. If we use the $\alpha-$model prescription to describe the turbulence in the disc (Shakura and Sunyaev 1973), Eq. (1.15) can be rewritten as:

$$\frac{h}{q^{1/3}} + \frac{50\alpha h^2}{q} \leq 1 \tag{1.16}$$

This is consistent with the requirement that $q \ll h^3$ for the perturbation to the disc by the planet to be linear. For typical disc conditions used through the literature, and within the work presented in this thesis ($h = 0.05$, $\alpha = 1 \times 10^{-3}$), this equates to $\approx 1{\rm M}_{\rm Jup}$. In regions where the disc is very thin (optically thin inner disc), or the viscosity is greatly diminished (shielded dead zones) a planet or core with a much lower mass could be sufficient to open a gap. In fact if a planet is held on a fixed orbit, either artificially, or at a zero-torque radius the criterion for gap opening can be a fraction of unity, due to non-linear steepening of density waves (Muto et al. 2010).

To open the gap the planet exchanges angular momentum with the material

around it. An imbalance between the torques from the interior and exterior material leads to migration. In general Type II migrations acts to reduce the semi-major axes of planets, moving them towards the central star, due to a greater torque originating from the exterior disc material. Viscous evolution of the disc tends to drift material inwards, so the inner disc depletes, whilst a pile-up on the other side of the gap leads to this scenario. Typical time-scales for type II migration are therefore similar to the disc's viscous time-scale, $\tau_\nu = r_\mathrm{p}^2/3\nu$; a Jupiter mass planet at 5 au in a typical protoplanetary disc, has a migration time of $\sim 5 \times 10^5$ yr.

1.4.3 Type III Migration

This third regime of planetary regime is a very specific case, which can operate for already migrating planets of intermediate mass, typically smaller than a few Saturn masses. In this picture we neglect the disc viscous drift which occurs over time-scales larger than the migration time-scale. Co-orbital material will migrate with the planet, at the same drift rate. As the planet migrates inwards, fluid elements circulating in the inner disc are caught in libration. They execute an outward horseshoe turn at conjunction with the planet; at the next conjunction however, the fluid elements have left the horseshoe region as the planet has kept migrating. They cannot perform an inward U-turn, and they are left circulating in the outer disc. During this crossing episode, a negative torque is exerted on the planet, whose migration is thus accelerated. The opposite of these processes can occur for an outwards migrating planet (Masset and Papaloizou 2003).

This feedback loop, which can cause extremely rapid migration either inwards or outwards, is reliant on the planet building up a sufficient co-orbital mass deficit. It only works for intermediate mass-planets as low-mass planets do not sufficiently alter the disc surface density of the disc, and high-mass planets carve too deep of a gap, leaving a very low co-orbital mass deficit. This unstable regime, which operates over a very specific range of planet masses and disc conditions, is known as Type III migration (as it was discovered after Type I and Type II – a common problem in astrophysical nomenclature!). Whether runaway migration is directed inwards or outwards depends on the initial direction of drift of the planet. Pepliński et al. (2008b,c) found that the sign of the initial drift is very sensitive to the asymmetry of the mass distribution in the horseshoe region. The

flow of this distribution around the planet, highly reliant on numerical resolution, also impacts on the initial direction (D'Angelo et al. 2005; Pepliński et al. 2008a). Any processes which increase the effective mass of the planet can destabilise the feedback loop, switching the migration regime to Type II. These may include accretion (Zhang et al. 2008) or self-gravity (D'Angelo and Lubow 2008). It is unclear whether the conditions for Type III run-away migration can exist in physical protoplanetary discs, so we will therefore not discuss the impacts this could have on simulated exoplanet populations.

1.4.4 Planet Evolution in Circumbinary Discs

The evidence gathered so far on the circumbinary planet population suggests that they formed in the common protoplanetary disc, left over from the stars' formation. Conservation of angular momentum would suggest, that without an exterior perturbing body, this disc would lie in the same plane as the binary orbital plane. Planets formed in this disc would at least start with a co-planar orbit. The co-planarity of the circumbinary planets is cited as evidence of this formation environment. The circumbinary disc in the vicinity of where these planets have been detected is heavily influenced by the gravitational and tidal influence of the binary members, carving out a cavity. For a binary with an eccentric orbit, or non-equal masses, this cavity is eccentric and precesses under its interaction with the binary.

As we have discussed in the previous section, this produces a number of challenges to forming these planets at this location. Collisional velocities between planetesimals are excited to such a degree, most collisions are catastrophically disruptive – an effect exacerbated when impactors of different sizes are considered. This suggests that these planets formed further out in the disc, and then migrated into the inner disc, where they are then observed today. Disc-planet interactions are the best argument we have for explaining this migration behaviour for the planets discovered.

As we have discussed in this section, Type I and Type II migration can occur on time-scales much shorter than the lifetime of the disc. The non-linear behaviour of the corotation torque is one useful mechanism for slowing down, and even reversing inwards migration in the Type I regime. To halt or inhibit migration in systems where this may not occur, at least temporarily, mechanisms such as

radial structures, massive vortices, and planet-planet interactions have been cited. To summarise, without additional mechanisms in place migration often has issues with stopping migrating planets at a range of radii.

Circumbinary discs do not have this problem; within them exists a defined scale. The strength of torques and the location of zero-torque radii depend, amongst other factors, on the surface density gradient. In regions of positive surface density gradient the co-rotation torque can become positive enough to counteract the negative Lindblad torque. The edge of the circumbinary cavity is a region of very positive surface density gradient. As we mentioned earlier this location is in close proximity to the critical stability limit defined by Holman and Wiegert (1999), near which the majority of observed circumbinary planets can be found.

A number of works, both before and after the discovery of the *Kepler* circumbinary planets, have studied disc-planet interactions in circumbinary discs. The interaction of giant migrating planets with circumbinary discs was first studied by Nelson (2003). This study showed that Jovian-mass formed a gap and underwent Type II migration into the inner disc. After migrating into the central cavity, they were captured into a $4:1$ mean-motion-resonance with the binary. These giant planets often underwent close-encounters with the binary, with scattering events ejecting them from the system. Lighter, Saturnian-mass planets underwent stable migration to the disc cavity where they then remained in stable orbits (Pierens and Nelson 2008a).

Less massive planets undergo Type-I migration until they are halted at the inner cavity edge by a strong positive co-rotation torque, counteracting the Lindblad torque – see Pierens and Nelson (2007, 2008a,b) for more details. The techniques developed in these works were then applied to a number of the newly discovered *Kepler* circumbinary systems, in attempts to explain and recreate the orbits of their planets (Pierens and Nelson 2013; Kley and Haghighipour 2014, 2015). Pierens and Nelson (2013) had difficulty recreating both the semi-major axes and eccentricities for the observed planets, with a range of disc parameters, under the assumption of an isothermal equation of state. Kley and Haghighipour (2014, 2015) included a more realistic equation of state and some radiation effects, as well as the role of multi-planet migration and interaction. These works also had difficulty in recreating all the observed properties of the *Kepler* circumbinary planets. Using 3-D SPH simulations Dunhill and Alexander (2013) argued the

near-circular orbit of *Kepler-16 b* hints that it formed in a massive disc in which the orbit of the planet is heavily damped by the disc.

The general picture from these studies suggest that whilst the central cavity can halt the migration of bodies (as long as they are not too massive), the final semi-major axis of the planet is too large, and the eccentricity is either over- or under-estimated. Many of the works either use a locally-isothermal equation of state, or neglect the full impact of the stars on the disc. A comparatively small range of disc parameters has been explored. Post-disc evolution, or planet-planet interactions (Kley and Haghighipour 2015) may help to recreate the observed circumbinary planet population. However, these processes use the end-point of disc-planet interactions as their input. A better understanding and modelling of the processes which shape the inner disc, in addition to the gravitational influence of the binary, is vital to accurately simulating the circumbinary environment. Capturing the true structure and evolution of physical circumbinary discs will likely enable disc-planet interaction calculations, mass-growth scenarios, and post-disc simulations to not only recreate circumbinary planet populations which resemble the observed ones – specific systems, and the whole – but also provide predictive insights on potential targets/neglected parameter space for future exoplanet detection campaigns.

The work presented throughout this thesis aims to examine two areas of disc physics which have not yet been investigated fully in the circumbinary regime – disc self-gravity, and radiative effects, including radiation transport, disc surface and mid-plane irradiation, and radiative cooling. We examine the impact of each of these topics on the evolution of the circumbinary environment, in a subset of the *Kepler* circumbinary planet hosting systems, especially on the inner disc structure. To assess the validity or accuracy of each, we also undertaken disc-planet interaction scenarios including migration and accretion.

Numerical Methods

Chapter Contents

In this Chapter we describe the form of the equations of hydrodynamics and outline several numerical methods used in their solution. We also give a description of the basic FARGO code used throughout the work in this thesis, as well as the implementation of extensions to the code which we use in our work.

2.1 Hydrodynamics

The equations of hydrodynamics, which can be used to model an enormous range of phenomena, can be derived from the requirements for conservation of mass, momentum and energy. For a fluid of density ρ, pressure p, velocity $\vec{v}$ and internal energy per unit volume e, and acting under pressure and gravitational forces, the equations read as follows:

$$\frac{\partial \rho}{\partial t} + \nabla \cdot (\rho \vec{v}) = 0, \tag{2.1}$$

$$\frac{\partial}{\partial t}(\rho \vec{v}) + \nabla \cdot (\rho \vec{v}\vec{v}) = -\nabla p - \rho \nabla \Phi, \tag{2.2}$$

$$\frac{\partial e}{\partial t} + \nabla \cdot (e\vec{v}) = -p\nabla \cdot \vec{v} + \mathcal{Q} - \Lambda, \tag{2.3}$$

where Φ is the gravitational potential of an external body acting upon the fluid, and $\mathcal{Q}$ and Λ are respectively heating and cooling terms. To close this set of equations we need an equation of state, which can relate the two state properties of pressure and internal energy. For the considerations required throughout this thesis, inter-molecular attraction and finite molecule size can be neglected, so a classical ideal gas law can be adopted:

$$p = \rho(\gamma - 1)e, \tag{2.4}$$

where γ is the adiabatic index and is equal to the ratio of the specific heats at constant pressure and constant volume. This value depends on the composition of the fluid under consideration, and its properties. To first degree a protoplanetary disc can be assumed to be purely made up of hydrogen molecules (H_2); for a diatomic molecule such as this $\gamma = 7/5 = 1.4$;

2.1.1 Viscosity

In Sections 1.2 and 1.4 we discussed the importance of viscosity on the evolution of protoplanetary discs, around both single and binary stars, as well as the role it plays in planetary evolution and migration. The force of viscosity on the fluid momenta can be described using the viscous stress tensor, from Landau and Lifshitz (1987) – note the change to index notation:

$$\frac{\partial}{\partial t}(\rho \upsilon_i) = \frac{\partial}{\partial x_k}\sigma'_{ik}, \tag{2.5}$$

where σ'_{ik}, the viscous stress tensor is defined as:

$$\sigma'_{ik} = \eta \left(\frac{\partial v_i}{\partial x_k} + \frac{\partial v_k}{\partial x_i} - \frac{2}{3}\delta_{ik}\frac{\partial v_l}{\partial x_l} \right) + \zeta \delta_{ik} \frac{\partial v_l}{\partial x_l}. \tag{2.6}$$

Two separate viscosity coefficients are involved in this form of the viscous stress tensor: the first, η, is the dynamic viscosity and the second, ζ, is the bulk viscosity. The bulk viscosity can be ignored in some circumstances, but may also be recast as an artificial viscosity used to spread shocks on a staggered grid – whilst we will not include it in our derivations here, it will resurface in future Sections. The dynamic viscosity is related to the kinematic viscosity by $\nu = \eta/\rho$. The addition of Eq. (2.6) to Eq. (2.5) results in the Navier-Stokes momentum equation. In the same summation notation as Eq. (2.6):

$$\rho \cdot \left(\frac{\partial v_j}{\partial t} + v_i \frac{\partial v_j}{\partial x_i} \right) = -\frac{\partial p}{\partial x_j} - \rho \cdot \frac{\partial \Phi}{\partial x_j} + \frac{\partial \sigma'_{ij}}{\partial x_j}. \tag{2.7}$$

This equation can be derived in a number of other co-ordinate systems, such as curvilinear systems, see Landau and Lifshitz (1987) for details. One can see that the viscous stress tensor acts as a friction force on the fluid. In 2-D cylindrical co-ordinates (r, ϕ) the components of the viscous stress tensor can be written as:

$$\sigma_{r,r} = 2\eta \left(\frac{\partial v_r}{\partial r} - \frac{1}{3}\mathrm{div}\,(\vec{v}) \right), \tag{2.8}$$

$$\sigma_{\phi,\phi} = 2\eta \left(\frac{1}{r}\frac{\partial v_\phi}{\partial \phi} + \frac{v_r}{r} - \frac{1}{3}\mathrm{div}\,(\vec{v}) \right), \tag{2.9}$$

$$\sigma_{r,\phi} = \eta \left(\frac{1}{r}\frac{\partial v_r}{\partial \phi} + r\frac{\partial}{\partial r}\left(\frac{v_\phi}{r}\right) \right), \tag{2.10}$$

$$\text{where } \mathrm{div}\,(\vec{v}) = \frac{1}{r}\frac{\partial}{\partial r}\,(r v_r) + \frac{1}{r}\frac{\partial}{\partial \phi}\,(v_\phi) \tag{2.11}$$

The force per unit volume which acts on the fluid in the r and ϕ directions can be found using the above equations and Eq. (2.5) (Nelson et al. 2000; D'Angelo et al. 2002; Masset 2002):

$$f_r^{\mathrm{visc}} = \left[\frac{\partial}{\partial r}\,(r\sigma_{r,r}) + \frac{\partial \sigma_{r,\phi}}{\partial \phi} - \sigma_{\phi,\phi} \right] \tag{2.12}$$

$$f_\phi^{\mathrm{visc}} = \left[\frac{\partial}{\partial r}\,(r\sigma_{r,\phi}) + \frac{\partial \sigma_{\phi,\phi}}{\partial \phi} + \sigma_{r,r} \right]. \tag{2.13}$$

The fluid viscosity can also have an impact on the energy equation, through viscous dissipation. In other words the mechanical work done by viscous forces is converted to heat and deposited into the internal energy of the fluid. From D'Angelo

et al. (2002, and then references therein) this contribution to the internal energy evolution can be written as a heating term:

$$\frac{\partial e}{\partial t} = Q^{\text{visc}} = \frac{1}{2\nu\Sigma}\left[\sigma_{r,r}^2 + \sigma_{r,\phi}^2 + \sigma_{\phi,\phi}^2\right] + \frac{2\nu\Sigma}{9}\text{div}^2\left(\vec{v}\right). \tag{2.14}$$

The α-Viscosity Model

A source of proposed turbulence – which accounts for the greater magnitude of viscosity needed to drive the viscous evolution of protoplanetary discs than molecular viscosity can provide – is that driven by hydrodynamic eddies. Without knowledge of the physics or mechanisms driving these eddies, Shakura and Sunyaev (1973) were able to use a dimensional argument to parametrise their effect. This turbulence should be characterised by their mean-scale length and their propagation speed. They argued that the mean-scale length should be set by the disc-scale height, H, and the propagation is defined by αc_s; c_s is the sound-speed within the disc, and α is a dimensionless constant meant to capture the physics which describes the source of the turbulence. It is this constant which lends its name to the model of viscosity which arises from this set of arguments:

$$\nu = \alpha c_s H. \tag{2.15}$$

For the regime of hydrodynamical discs considered within this thesis, α-values between $10^{-4} - 10^{-2}$ are employed. This range agrees with MHD simulations of protoplanetary discs, as well as leading to accurate accretion rates in T Tauri systems of $\dot{M} \approx 10^{-8}\,\text{M}_\odot\text{yr}^{-1}$.

2.2 Solution Methods

The equations of hydrodynamics form a set of coupled hyperbolic partial differential equations (or coupled mixed hyperbolic-parabolic partial differential equations with the inclusion of viscous diffusion). A number of solution methods and codes have been developed to solve these equations numerically. In this section we will focus on the concepts used in the grid-based, Eulerian code FARGO. The meaning of these terms, will become clear in the following subsections.

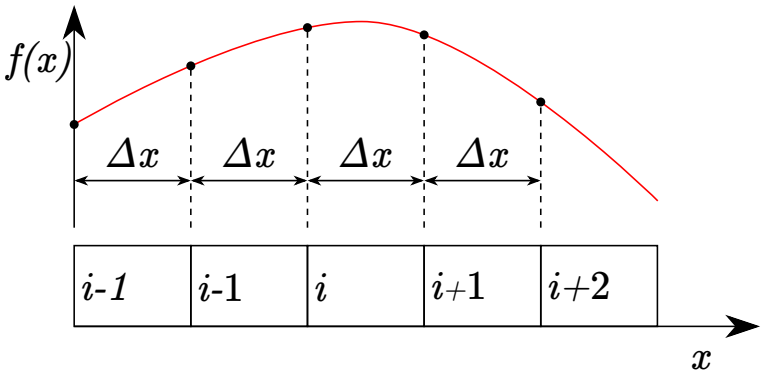

FIGURE 2.1: A schematic of a 1-D grid where x_i and $f(x_i)$ define the position and function value at every grid-point i. The grid-spacing may be constant or vary with x. This practice can be extended to an n-dimensional space, where the number of grid points, and their spacing, may differ in each direction.

2.2.1 Discretisation

The first step we take in solving the equations of hydrodynamics is defining the spatial regime in which they are acting. Whether in 1, 2 or 3-dimensions the spatial extent over which the equations hold can be split into a grid of points. Each point in this grid can be given a co-ordinate or position vector and the values of the hydrodynamic fields at this point. This process discretises the problem. As an example consider a 1-D line where x defines the position along it; along this line a function holds such that $f(x)$. We discretise this line into N points which span x from $x_0 - x_N$ and defining the function at every point $f(x_i)$. The spacing between neighbouring grid-points, $\Delta x = x_{i+1} - x_i$ may be constant, or vary with x (logarithmically for example). Figure 2.2 shows this schematically.

The process of discretising the spatial regime and equations of a problem onto a number of points results in a grid-based code. In the context of our problem, in a grid-based code the hydrodynamical quantities of pressure, density, energy and velocity can be defined on a 1-, 2- or 3-D grid, depending on the hydrodynamical problem you wish to solve. The grid can be Cartesian, cylindrical, spherical etc., and the space between neighbouring points is refered to as a cell, or the control volume. We are solving the hydrodynamical equations for both scalar quantities (pressure, density and energy), and vector fields (velocity), so we employ a staggered grid. Scalar fields are defined at the centre of each cell, and the i-th component of velocity fields are defined at the cell interfaces in the i-th

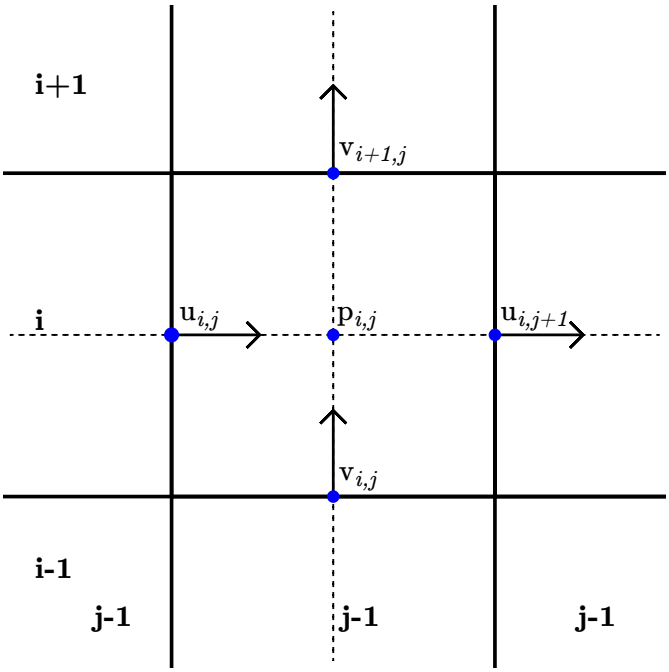

FIGURE 2.2: A schematic of a 2-D staggered grid where the indices i and j refer to their own dimension. Scalar quantities such as pressure, density and energy are defined at the cell centres and vector or tensor quantities are defined at cell interfaces.

direction, see Fig. 2.1 for an example of a 2-D staggered grid mesh. This makes the calculation of fluxes between cells more efficient, because the velocity field is already defined at the interfaces; it also makes the scheme 2nd order in space. When calculating the flux of quantities in the advective transport step, the scalar fields only need interpolating to the cell boundaries. Other codes which store all quantities at the cell centres, can then utilise the more complicated Godunov method to calculate cell fluxes.

The specification of a field at location $\mathbf{x}$ and time t is a Eulerian grid model; material is advected through the grid. Lagrangian codes, in which the advection of the fluid changes the grid are also used, as well as those in which there is no grid all, such as Smoothed Particle Hydrodynamics (SPH). Codes utilising these techniques were not used for the work contained in this thesis, so will not be discussed further.

2.2.2 Finite Differencing

One can employ the technique of finite-differencing to approximate the spatial gradients of fields discretised on a grid. A finite difference is simply an expression of the form:

$$\frac{f(x+b)-f(x+a)}{b-a}. \tag{2.16}$$

It is a common technique to solve differential equations on a grid. Unlike in true differentiation where the derivative of the function f at x is defined as:

$$f'(x)=\lim_{h\to 0}\frac{f(x+h)-f(x)}{h}. \tag{2.17}$$

Finite-differencing, as the name suggests, uses a finite size of h to approximate the derivative of f. There are three common methods of doing this for first-order derivatives which take the following form in index notation:

- Forward:
$$f'(x_i)=\frac{f(x_{i+1})-f(x_i)}{x_{i+1}-x_i},$$
- Backward:
$$f'(x_i)=\frac{f(x_i)-f(x_{i-1})}{x_i-x_{i-1}},$$
- Central:
$$f'(x_i)=\frac{f(x_{i+1})-f(x_{i-1})}{x_{i+1}-x_{i-1}}.$$

The central-differencing scheme can sometimes also be defined as the difference between the function at points $i\pm 1/2$. One can utilise this formulation for $f'\left(x_{i+1/2}\right)$ and $f'\left(x_{i-1/2}\right)$, and apply the central-difference formula for the derivative of f' at x, to obtain the 2nd-order derivative of f:

$$f''(x)=\frac{f(x_{i+1})-2f(x_i)+f(x_{i-1})}{(\Delta x)^2}, \tag{2.18}$$

assuming that the spacing Δx is constant throughout the mesh.

Finite-differencing is not the only method of representing and evaluating partial differential equations on a grid-based domain; the finite element or finite volume methods can also be used. For a detailed description and comparison of each of these methods see Peiró and Sherwin (2005).

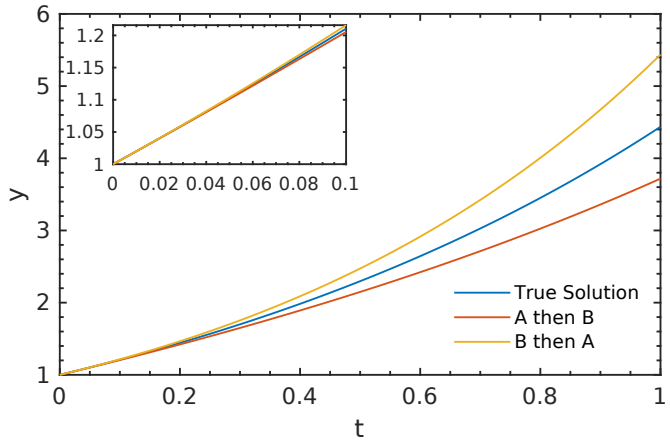

FIGURE 2.3: Comparison between the analytic solution to Eq. (2.20) ($y(t) = 2\exp(t) - 1$) and the two simple reconstructions using the two step Lie operator splitting algorithm described. It can be seen in the insert that the agreement between the approximation and the true solution is good for small t.

2.2.3 Operator Splitting

For an equation of the form:

$$\frac{\partial y}{\partial t} = Ay + By, \tag{2.19}$$

where A and B are differential operators, it can be shown that solving each operator separately and then combining them can provide a reasonable approximation to the true solution; whilst also being considerably easier to compute.

Whilst we will use this procedure to solve our set of coupled partial differential equations, for the moment consider a simple linear ordinary differential equation:

$$\frac{\partial y}{\partial t} = 1 + y \ , \qquad y(0) = 1. \tag{2.20}$$

With the simplest operator splitting algorithm we can write:

$$\frac{1}{2}\frac{\partial y}{\partial t}\Big|_A = y \implies y_A = \exp(2t), \tag{2.21}$$

$$\frac{1}{2}\frac{\partial y}{\partial t}\Big|_B = 1 \implies y_B = 1 + 2t. \tag{2.22}$$

The original equation can then be integrated to a time t by either using the solution y_A to time $t/2$ and then solution y_B to time t, or vice versa, using the solution y_B to time $t/2$ followed by the solution y_A to time t. This very simple formulation is

known as Lie splitting. One reconstruction tends to under-approximate the true solution whereas the other over-approximates, which can be seen in Fig. 2.3.

It can be seen that even for this very simple linear ODE example, if sufficiently small time integrations are used, a basic operator splitting algorithm can provide a reasonable approximation to the true solution. A Taylor expansion analysis of these AB/BA reconstructions can show that the splitting error is $\mathcal{O}(\Delta t)$. More complicated schemes exist, such as an ABA reconstruction (Strang splitting: the A solution is used for a quarter of t, the B solution for $t/4 \rightarrow 3t/4$, and the A solution again for the final quarter of t) which provide better accuracy.

This technique can be used to split PDEs both temporally and spatially. The algorithm used to obtain solutions to 1-D hydrodynamic equations can be extended to multiple dimensions, by splitting each operator into dimensions and solving each dimension separately. Evolution equations such as Eqs. (2.1)–(2.3) can be split temporally by solving for the source and sink terms first and then using the solution to carry out the advective transport step.

2.2.4 Advection Solver

The equations of hydrodynamics can be rewritten as independent advection-type equations of the form:

$$\frac{\partial q}{\partial t} + \frac{\partial}{\partial x_i}(q u_i) = 0, \tag{2.23}$$

where q is any of the hydrodynamic conserved quantities (including source terms such as pressure and a gravitational potential) and u_i is the velocity of the fluid in the direction i. As we have already mentioned, there exist a number of methods of solving this family of equations, but here we will focus on the finite-difference method. Under this formalism the value of q at the next time level depends on the differences between q and its neighbours at a the previous time step. The value q is updated with the flux of q. The technique of operator splitting can be used to separate each dimension into its own time-step, where the first sweep calculates the fluxes in the 1-direction and updates q and the second sweep updates q with the fluxes in the 2-direction, and so-on for further dimensions.

On a staggered-mesh code we can define the area centred on the value q as the control volume. For a 2-D static mesh the control volume of the value q at point i, j can be defined as $S_{i,j}$, or the surface area of the cell. Another way of

stating Eq. (2.23) is that the rate of change of the quantity of a variable q within the control volume $S_{i,j}$, is equal to the divergence of the flux of q through the control volume surfaces. In 2-D Eq. (2.23) can be written as 2 one-dimensional sweeps, with forward finite-differencing to approximate the flux divergences (Stone and Norman 1992). Starting with the sweep in the 1-direction:

$$\frac{S_{i,j}\left(q^{a}_{i,j} - q^{n}_{i,j}\right)}{\Delta t} = \left[\left(\tilde{A}_1 \upsilon_1 q^{*}\right)_{i,j} - \left(\tilde{A}_1 \upsilon_1 q^{*}_{1}\right)_{i+1,j}\right], \tag{2.24}$$

and followed by the sweep in the 2-direction:

$$\frac{S_{i,j}\left(q^{n+1}_{i,j} - q^{a}_{i,j}\right)}{\Delta t} = \left[\left(\tilde{A}_2 \upsilon_2 q^{*}\right)_{i,j} - \left(\tilde{A}_2 \upsilon_2 q^{*}_{2}\right)_{i,j+1}\right] \tag{2.25}$$

where $\tilde{A}_{k,i,j}$ is the face area of the control volume i, j in the direction k and $q^{*}_{k,i,j}$ is the value of $q_{i,j}$ interpolated to the control volume interface – again in the direction k. A simple Lie splitting reconstruction algorithm (AB), described above, is used to step the solution forwards in time.

Calculating stable and accurate values for q^{*} is key to developing a successful advection finite-differencing solver. A number of methods have been developed to calculate the face-centred upwinded values q^{*} of a zone-centred scalar q: first order Donor cell method, uses simple interpolation assuming q is constant over a cell; second order van Leer method, uses a piecewise linear function to represent the distribution of q within a zone (van Leer 1977); and third order PPA, which utilises parabolic interpolation within a zone to calculate q^{*} (Colella and Woodward 1984). Higher order methods may need to utilise a flux-limiter to minimise unphysical fluxes between cells near discontinuities – we will encounter such a flux limiter when we consider radiation transport through FLD in Sec. 3.2.3.

Using this method the disc material is advected through the grid with the velocity of the disc material, unlike a Godunov-like scheme which also considers the propagation of sound waves.

2.2.5 The Courant-Friedrich-Lewy Condition

Abbreviated to CFL, this term refers to a principle necessary for equations solved numerically on a grid to remain stable when integrated in time. Basically, the time-step must be sufficiently small to ensure that material, or information cannot propagate further than one cell in a time-step. Courant et al. (1928) showed that

one, algorithm dependent, necessary condition for the solution of the discretised difference equation to converge to the true solution of a partial differential equation is that:

$$\frac{u\Delta t}{\Delta x} < c_{\max}, \tag{2.26}$$

where $c_{\max}$ is a condition dependent on the solution method being considered. For a for an explicit solution scheme (values at time-level $n+1$ depend on values at time-level n) it is usually chosen close to 1. For an implicit scheme the stability of the integration is less sensitive to the choice of $c_{\max}$, and larger values can be used. The CFL condition can be used to choose a time-step such that $\frac{\Delta_x}{\Delta t}\frac{u}{c_{\max}}$ is less than a chosen Courant factor, which must be less than one.

Equation (2.26) can be rewritten for multiple, N dimensions, which results in a more restrictive condition:

$$\Delta t \sum_{i=1}^{N} \frac{u_i}{\Delta x_i} < c_{\max}. \tag{2.27}$$

The fluid velocity is not the sole propagator of information in a hydrodynamic disc. In the fluid there exists a speed at which waves can propagate – carrying information – the sound speed c_s. The wave-front of any given wave must not propagate more than one cell width in a time-step:

$$\frac{c_s \Delta t}{\min\left(\Delta x_i\right)} < c_{\max}. \tag{2.28}$$

Finally if an artificial viscosity is used to spread shocks, another time-step constraint arises from the restriction of shocks being spread further than a cell:

$$\Delta t \min\left(\frac{\Delta x_i}{4C_{\mathrm{VNR}}^2 \Delta u_i}\right)^{-1} < c_{\max}, \tag{2.29}$$

where C_{VNR} is von Neumann-Richtmyer's factor (Stone and Norman 1992; Masset 2000a) – a measure of the number of zones the artificial viscosity spreads shocks – typically between 1 and 2, and $\Delta u_i = \nabla_i \left(u_i \Delta x_i\right)$.

There are ways to increase the time-step beyond the CFL limit through careful consideration of the material transport velocity. Simulating the disc in a co-rotating frame, say with the orbital frequency of an embedded planet, is one such option. We will describe another method which gives its name to the numerical code used throughout this thesis in a later chapter – the FARGO technique.

2.2.6 Relaxation Methods

The CFL condition holds for any explicit method of integrating equations in time. In an explicit scheme the state of a system at a given time depends on the state of the system at the current time: $u(t + \Delta t) = f(u(t))$, where Δt must meet the CFL condition for the system for the integration of u to remain stable. Whilst FARGO utilises a solution method which uses this explicit time integration (also known as Forward Euler or Forward Time integration) to evolve the hydrodynamic variables, a different solution method will be required to solve a diffusion transport problem as part of our implementation of radiative effects in FARGO.

In this problem a CFL-like stability criterion results in a prohibitively small time-step, which would require many tens of thousands of sub time-steps for every hydrodynamical time-step. A more efficient method of solving this equation is to use an implicit time integration, $u(t + \Delta t) = f(u(t + \Delta t) + g(u(t))$, and make use of an iterative relaxation method to converge on the solution for $u(t + \Delta t)$.

In this subsection we will describe three relaxation techniques, using details from Young (1950), Varga (1962), and Press et al. (1992), which can be used to solve an elliptic partial differential equation of the form:

$$\frac{\partial u}{\partial t} = \nabla^2 u - \varphi \tag{2.30}$$

where a distribution u will relax to an equilibrium solution as $t \to \infty$, which will depend on the boundary values of the problem and any source terms φ.

For the remainder of this section we will consider this equation in two dimensions x and y.

$$\frac{\partial u}{\partial t} = \frac{\partial^2 u}{\partial x^2} + \frac{\partial^2 u}{\partial y^2} - \varphi. \tag{2.31}$$

Using forward time integration and central finite differencing in space (FTCS) to solve this equation numerically, expanding out the resulting expression and collecting like terms we end up with the following expression for u at time level $n + 1$:

$$u_{i,j}^{n+1} = u_{i,j}^n + \frac{\Delta t}{\Delta^2}\left(u_{i+1,j}^n + u_{i-1,j}^n + u_{i,j+1}^n + u_{i,j-1}^n - 4u_{i,j}^n\right) - \Delta t\varphi, \tag{2.32}$$

where we have assumed that $\Delta x = \Delta y = \Delta$. Using forward time integration on a 2-D grid results in a maximum time-step of $\Delta^2/4$ from a CFL-like stability

criteria. Substituting this into the above expression results in:

$$u_{i,j}^{n+1} = \frac{1}{4}\left(u_{i+1,j}^{n} + u_{i-1,j}^{n} + u_{i,j+1}^{n} + u_{i,j-1}^{n}\right) - \frac{\Delta^2}{4}\varphi, \tag{2.33}$$

The value $u_{i,j}^{n+1}$ depends on a simple average of its nearest neighbours plus any source terms. One sweep over the mesh will not result in the true solution for $u(t+\Delta t)$. Equation (2.33) must be used over multiple iterations, where the results from iteration k are used to obtain the results for iteration $k+1$. This procedure is repeated until convergence is reached. If we rewrite Eq. (2.33) in matrix notation – $\mathbf{A}\cdot\mathbf{u} = \mathbf{b}$, then convergence is reached when $||\mathbf{A}\cdot\mathbf{x}^n - \mathbf{b}|| < tol$, where tol is a factor usually of the form $tol = 10^{-p}$. This very simple relaxation method is known as the Jacobi method. One pays for its simplicity for a very slow rate of convergence. It can be shown that for a square grid of $I \times I$ points and a tolerance value p, the number of iterations required for convergence is $\approx \frac{pI^2}{2}$.

One improvement to the Jacobi method is the Gauss-Seidel (GS) method. Instead of iterating every $u_{i,j}$ from k to $k+1$ at once, values of u^{k+1} can be used in the calculation of other u values at iteration k as soon as they become available. If we proceed along a grid of u values in rows, incrementing j for a fixed i we can write:

$$u_{i,j}^{n+1} = \frac{1}{4}\left(u_{i+1,j}^{n} + u_{i-1,j}^{n+1} + u_{i,j+1}^{n} + u_{i,j-1}^{n+1}\right) - \frac{\Delta^2}{4}\varphi, \tag{2.34}$$

where the values of u at $i-1$ and $j-1$ are already updated to $k+1$ but are used in the update of $u_{i,j}$ at iteration k. Whilst this algorithm is actually computationally more efficient than the Jacobi method (only one array for u is needed as the old value of u can be overwritten with the new value of u as soon as it is computed) it only provides a fractional improvement to the convergence rate: $\approx \frac{pI^2}{4}$. When I can commonly be > 100 a factor of 2 improvement is little use.

A much better convergence rate can be obtained by over-correcting the value of u^r at the rth Gauss-Seidel iteration. The value of u^{k+1} is then a weighted average of u^r and u^k in an algorithm known as successive over-relaxation (SOR):

$$u_{i,j}^{k+1} = \omega u_{i,j}^{r} + (1-\omega)\, u_{i,j}^{k}, \tag{2.35}$$

where ω is the over-relaxation parameter and is between 1 and 2. Equation (2.34) can be rewritten, such that for every row in the matrix $\mathbf{A}$ there exists an equation:

$$a_{i,j}u_{i+1,j} + b_{i,j}u_{i-1,j} + c_{i,j}u_{i,j+1} + d_{i,j}u_{i,j-1} + e_{i,j}u_{i,j} = f_{i,j}, \tag{2.36}$$

where on our square grid $a = b = c = d = 1$, $e = -4$ and f is proportional to the source term. The Gauss-Seidel step can then be expressed as:

$$u^r_{i,j} = \frac{1}{e_{i,j}} \left(f_{i,j} - a_{i,j} u_{i+1,j} - b_{i,j} u_{i-1,j} - c_{i,j} u_{i,j+1} - d_{i,j} u_{i,j-1} \right) \tag{2.37}$$

which can then be substituted into Eq. (2.35). The residual $\zeta_{i,j}$, which can be used to determine if the algorithm has converged, can be written:

$$\zeta_{i,j} = a_{i,j} u_{i+1,j} + b_{i,j} u_{i-1,j} + c_{i,j} u_{i,j+1} + d_{i,j} u_{i,j-1} + e_{i,j} u_{i,j} - f_{i,j} \tag{2.38}$$

and used to simplify Eq. (2.35) to:

$$u^{k+1}_{i,j} = u^k_{i,j} - \omega \frac{\zeta_{i,j}}{e_{i,j}}, \tag{2.39}$$

The over-relaxation parameter, ω is problem dependent, but for the convergence rate $\propto \mathcal{O}(I)$ possible with this method to be obtained, it must be chosen correctly. The optimum value of ω depends on the spectral radius, which is the modulus of the largest eigenvalue of a matrix. For an $I \times J$ matrix, with fixed-value boundary conditions in the I direction and periodic boundary conditions in J the spectral radius can be shown to be:

$$\rho = \frac{\cos\left(\frac{\pi}{I}\right) + \left(\frac{\Delta x}{\Delta y}\right)^2 \cos\left(\frac{2\pi}{J}\right)}{1 + \left(\frac{\Delta x}{\Delta y}\right)^2}, \tag{2.40}$$

with ω:

$$\omega = 2 / \left(1 + \sqrt{1 - \rho^2}\right). \tag{2.41}$$

Examining Eq. (2.37) it can be seen that if the grid was divided into odd and even meshes, like the black and white squares of a chess-board, an odd value of $u^r_{i,j}$ only depends on even values of u^n. We can therefore do two half-sweeps per iteration. The first updates the odd u^n values to $n + 1$ with the even values at n. The second sweep updates the even values with the updated odd values. With this odd-even ordering another improvement to the algorithm can be made. The value of ω obtained from Eqs. (2.40) and (2.41) may be the optimal value to reach convergence, but it may not be the optimal initial value. It can often unnecessarily increase the error in the first iterations, before reducing it over I iterations. Using a process called Chebyshev acceleration, which updates ω after

every odd and even half-sweep:

$$\begin{aligned}
\omega(0) &= 1 \\
\omega(1/2) &= 1/\left(1-\rho^2/2\right) \\
&\vdots \\
\omega(n+1/2) &= 1/\left(1-\rho^2\omega(n)/4\right), n = 1/2, 1, \ldots, \infty \\
&\vdots \\
\omega(\infty) &= \omega_{\text{optimal}}
\end{aligned}$$

With this procedure the error always decreases after each iteration, which reduces the total number of iterations needed.

2.3 The FARGO Code

In this section we will describe the features of the numerical code FARGO (Masset 2000a,b)[1] – a code dedicated to modelling protoplanetary disc-planet interactions – developed by Frederic Masset[2]. It forms the basis of the code used for the numerous simulations carried out in Chapters 3–6. To solve the continuity and Navier-Stokes equations of hydrodynamics, for a viscous Keplerian disc, it uses the numerical methods described in the previous section. The hydrodynamic quantities are defined on a 2-D staggered polar r, ϕ mesh centred on the central object. The FARGO code considers the material contained within control volumes surrounding the points defined by the grid, so can be considered a finite volume method. On this grid the radial and azimuthal velocities, and the vertically averaged density – the surface density Σ are evolved in time. The gas pressure p is related to disc surface density and the gas temperature by an ideal equation of state ($p = R\Sigma T = \Sigma c_s^2$, where R is a constant and c_s is the isothermal sound-speed). In the basic version of FARGO the temperature is not evolved in the disc, resulting in a locally isothermal equation of state. For details of the implementation of an adiabatic equation of state see Section 2.3.4, and for the inclusion of radiative effects see Section 3.2.

[1] FARGO website
[2] Frederic's personal page

2.3.1 Initialisation

Before evolving the hydrodynamic quantities they must first be initialised. The surface density and temperature profiles are axisymmetric, depending on radius initially:

$$\Sigma(r) = \Sigma_0 \left(\frac{r}{r_0}\right)^{-a} \tag{2.42}$$

$$T(r) = T_0 \left(\frac{r}{r_0}\right)^{-1+2f} \tag{2.43}$$

where Σ_0 and T_0 are the surface density and temperatures values defined at radius r_0 (usually $r_0 = 1$). The value f is the disc flaring index, which describes the vertical shape of the disc. Using the condition for vertical hydrostatic equilibrium a disc scale height can be defined:

$$H(r) = c_s(r)/\Omega_{\mathrm{K}}(r), \tag{2.44}$$

where $\Omega_{\mathrm{K}}(r)$ is the Keplerian orbital frequency $\sqrt{GM_\star/r^3}$, G is the gravitational constant and $M_\star$ is the mass of the primary central object. The ideal equation of state therefore requires that:

$$H(r) = H_0 \left(\frac{r}{r_0}\right)^{1+f}. \tag{2.45}$$

The ratio of the disc height to the disc radius is known as the disc aspect ratio $h(r) = H(r)/r = h_0 (r/r_0)^f$. A disc where the disc height scales with r has a flaring index of 0 and the aspect ratio is constant.

To initialise the azimuthal velocity profile we balance the gravitational influence of the central object, the pressure force from the disc and the centrifugal force giving us:

$$\upsilon_\phi(r) = r\left(1 - (1 + a - 2f)h^2(r)\right)^{\frac{1}{2}} \Omega_{\mathrm{K}}(r). \tag{2.46}$$

The mass and angular momentum equations of conservation for a viscous disc can be used to define the initial radial velocity profile (Lynden-Bell and Pringle 1974), which is a viscous drift dependent on the kinematic viscosity profile. For the α-model describing the anomalous viscosity due to turbulence (Shakura and Sunyaev 1973, $\nu(r) = \alpha c_s H(r)$) this yields:

$$\upsilon_r(r) = -\frac{\nu(r_0)}{r_0}(1 + 2f - a)\left(\frac{r}{r_0}\right)^{-\frac{1}{2}+2f} \tag{2.47}$$

One can see that for specific choices of a and f the azimuthal velocity may be sub- or super-Keplerian, and the radial velocity profile may cause the disc to accrete onto the central object.

2.3.2 Gas Evolution

With the surface density and velocity profiles initialised, FARGO can now evolve them under the influences of pressure, gravity, centrifugal, viscosity (both physical and artificial) and advective transport. In $(r,\,\phi)$ co-ordinates the Navier-Stokes and continuity equations can be written:

$$\frac{\partial \Sigma}{\partial t} + \frac{1}{r}\frac{\partial}{\partial r}\left(r\Sigma v_r\right) + \frac{1}{r}\frac{\partial}{\partial \phi}\left(\Sigma v_\phi\right) = 0. \tag{2.48}$$

$$\frac{\partial v_r}{\partial t} + v_r\frac{\partial v_r}{\partial r} + v_\phi\frac{1}{r}\frac{\partial v_r}{\partial \phi} = \frac{v_\phi^2}{r} - \frac{1}{\Sigma}\frac{\partial p}{\partial r} - \frac{\partial \Phi}{\partial r} + \frac{1}{r}\frac{1}{\Sigma}f_r^{\text{visc}} - \frac{1}{\Sigma}\frac{\partial q_r^{\text{visc}}}{\partial r}. \tag{2.49}$$

$$\frac{\partial v_\phi}{\partial t} + v_r\frac{\partial v_\phi}{\partial r} + v_\phi\frac{\partial v_\phi}{\partial \phi} + \frac{v_r v_\phi}{r} = -\frac{1}{r}\frac{1}{\Sigma}\frac{\partial p}{\partial \phi} - \frac{1}{r}\frac{\partial \Phi}{\partial \phi} + \frac{1}{r}\frac{1}{\Sigma}f_\phi^{\text{visc}} - \frac{1}{r}\frac{1}{\Sigma}\frac{\partial q_\phi^{\text{visc}}}{\partial \phi}, \tag{2.50}$$

where the LHS of these equations is the advective transport portion of the evolution, and the RHS is the source part (the continuity equation doesn't have any source terms). The terms f_r^{visc} and f_ϕ^{visc} are the forces due to the kinematic viscosity given by Eqs. (2.12) and (2.13), with the viscosity coefficient in the viscous stress tensor components replaced with $\eta = \nu\Sigma$. The artificial viscosity used to spread shocks on a staggered mesh result in pressure-like forces which have the following form (Stone and Norman 1992):

$$q_r^{\text{visc}} = \begin{cases} C_{\text{vnr}}^2\Sigma\delta v_r^2 & \text{if } \delta v_r < 0 \\ 0 & \text{otherwise,} \end{cases} \quad \text{and} \quad q_\phi^{\text{visc}} = \begin{cases} C_{\text{vnr}}^2\Sigma\delta v_\phi^2 & \text{if } \delta v_\phi < 0 \\ 0 & \text{otherwise,} \end{cases} \tag{2.51}$$

$$\text{where } \delta v_r = \frac{\partial}{\partial r}\left(v_r\Delta r\right) \quad \text{and} \quad \delta v_\phi = \frac{1}{r}\frac{\partial}{\partial \phi}\left(v_\phi\Delta\phi\right),$$

and C_{vnr} is von Neumann-Richtmyer's constant defined earlier. The source term evolution is carried out in two steps in FARGO. In `Substep 1` the pressure, gravity, centrifugal and physical viscosity terms are used to evolve the radial and azimuthal velocities $\left(v\left(r,\,\phi\right)^t \rightarrow v\left(r,\,\phi\right)^{t+a}\right)$. In the second step, `Substep 2` the artificial viscosity is used to evolve the velocities $\left(v\left(r,\,\phi\right)^{t+a} \rightarrow v\left(r,\,\phi\right)^{t+b}\right)$.

With the source step complete FARGO can now carry out the advection step. As described in the previous section, in 2-D this can be carried out in two sweeps – one in each dimension. The fluxes of the hydrodynamic quantities must be calculated at each cell interface. On a staggered-mesh the velocities are already defined at the cell interfaces, so only Σ has to be interpolated from the cell centre values. To compute the fluxes we define five *momenta*: the surface density Σ, the radial momenta Σv_r at each radial cell interface, and the angular momentum $\Sigma r v_\phi$ at each azimuthal cell interface. The finite difference approach, and the interpolation of Σ to the cell interfaces can introduce significant numerical diffusion. To minimise this, we update the momenta with the fluxes of the specific momenta – each momenta divided by the surface density. We can rewrite Eqs. (2.24) and (2.25) under this constrained transport paradigm, for the update of each momenta q:

$$q^A_{i,j} = q_{i,j} + \frac{\Delta t}{S_{i,j}} \left[r_i \Delta\phi \Sigma^*_{i,j} v_{r_{i,j}} \left(\frac{q}{\Sigma}\right)^*_{i,j} - r_{i+1} \Delta\phi \Sigma^*_{i+1,j} v_{r_{i+1,j}} \left(\frac{q}{\Sigma}\right)^*_{i+1,j} \right], \quad (2.52)$$

in the r direction, followed by a sweep in the azimuthal direction:

$$q^B_{i,j} = q^A_{i,j} + \frac{\Delta t}{S_{i,j}} \left[\Delta r_i \Sigma^*_{i,j} v_{\phi_{i,j}} \left(\frac{q^A}{\Sigma}\right)^*_{i,j} - \Delta r_i \Sigma^*_{i,j+1} v_{\phi_{i,j+1}} \left(\frac{q^A}{\Sigma}\right)^*_{i,j+1} \right], \quad (2.53)$$

As specified in the previous section quantities superscripted with $*$ are computed at the cell interface in the relevant direction, interpolated with the 2nd-order upwind van Leer (1977) piecewise function.

2.3.3 The FARGO Algorithm

In reality FARGO carries out the radial transport step as normal but makes a modification to the azimuthal transport step. Developed in Masset (2000a) the FARGO algorithm, or **F**ast **A**dvection in **R**otating **G**aseous **O**bjects, splits the azimuthal transport step into two further sub-steps. The algorithm splits the azimuthal velocity into the following components (Masset 2000a; Gammie 2001; Baruteau and Masset 2008b):

$$v_\phi(i,j) = \underbrace{v_\phi(i,j) - \bar{v}_\phi(i)}_{v_\phi^{\mathrm{nu,res}}(i,j)} + \underbrace{\bar{v}_\phi(i) - N_i \frac{r_i \Delta\phi}{\Delta t}}_{v_\phi^{\mathrm{u,res}}(i)} - \underbrace{N_i \frac{r_i \Delta\phi}{\Delta t}}_{\text{azimuthal shift}} \quad (2.54)$$

In this decomposition $\bar{v}_\phi(i)$ is the average azimuthal velocity in each radial ring i and $N_i = E\left[\bar{v}_\phi(i)\,\Delta t / r_i \Delta\phi\right]$ where $E[X]$ denotes the nearest integer to the real

value X. Two azimuthal transport steps of the form Eq. (2.53) are undertaken, with $v_\phi(i,\, j)$ replaced first with the non-uniform residual velocity $v_\phi^{\mathrm{nu,res}}(i,\, j)$, with the result of this step being updated again with the uniform residual velocity $v_\phi^{\mathrm{u,res}}(i)$ transport step. After these transport steps each momenta is azimuthally shifted by N_i zones. This splitting technique allows a relaxation of the CFL condition in the azimuthal direction; instead of reading:

$$\frac{r\Delta\phi}{\Delta t}\frac{v_\phi}{c_{\max}} < 1, \tag{2.55}$$

which can be very restrictive especially at small radii, we can use:

$$\frac{r\Delta\phi}{\Delta t}\frac{(v_\phi - \bar{v}_\phi)}{c_{\max}} < 1. \tag{2.56}$$

In much of the disc, the actual azimuthal velocity will not be significantly different to the average azimuthal velocity at the given radius, so the non-uniform residual velocity will be small, resulting in a larger maximum time-step from this constraint. The azimuthal shift introduced by the FARGO algorithm introduces an additional CFL condition. Two cells in neighbouring radial rings which share the same azimuth, should not be separated by the transport step:

$$\frac{\Delta\phi}{\Delta t}\frac{1}{(\Omega(r) - \Omega(r+\Delta r))} < c_{\max}. \tag{2.57}$$

Whilst the FARGO algorithm can result in a time-step 14 times larger than the maximum time-step without it (Baruteau and Masset 2008b), it restricts how the computational domain can be decomposed for parallel computing. Usually a hydro-code could split the mesh both radially and azimuthally into domains, with each CPU dealing with a specific sub-grid. The communication of quantities needed for the computation of the FARGO algorithm between CPUs would negate any speed up gained. In FARGO therefore the domain is split only radially, with each CPU hosting N radial zones.

2.3.4 Implementation of an Adiabatic Equation of State

In the basic version of FARGO, whilst an equation of state is adopted which relates the pressure, surface density and temperature in the disc, the temperature profile is assumed to be static, resulting in a locally isothermal approximation. In FARGO-ADSG, developed in Baruteau (2008), Baruteau and Masset (2008a), and Baruteau and Masset (2008b), the temporal evolution of the energy equation (Eq. (2.3)) is

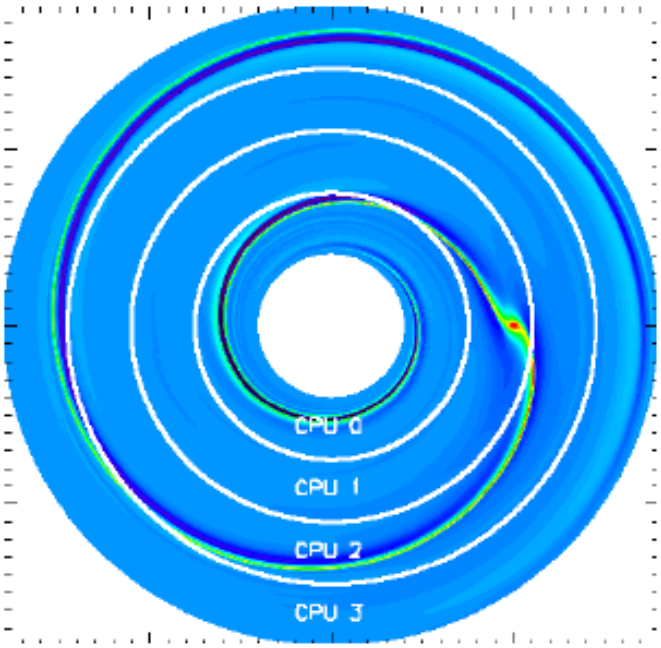

FIGURE 2.4: Due to the implementation of the azimuthal transport step, FARGO utilises a purely radial domain decomposition in its parallel computing MPI implementation. Image Credit: Baruteau (2008)

considered, along with an adiabatic equation of state. In this subsection we will describe how this is implemented within FARGO-ADSG.

We will still make use of the ideal gas law:

$$p = \frac{\mathcal{R}\Sigma T}{\mu}, \tag{2.58}$$

where $\mathcal{R}$ is the gas constant and μ is the mean molecular weight of the fluid. For an ideal gas the specific thermal energy content, u, is a function of temperature, $u = u(T)$, captured to good approximation by $u = c_v T$, where c_v is the specific heat capacity at constant volume $(\partial u/\partial T)_v$. The specific enthalpy of the gas, h also scales with temperature, with the scaling factor being the specific heat capacity at constant pressure, $c_p = (\partial h/\partial T)_p$. Such gases, where c_v and c_p are constant, are known as polytropic gases, with their equation of state relying on the adiabatic index $\gamma = c_p/c_v$. The Mayer formula connects the two specific heats: $\mathcal{R}/\mu = c_p - c_v$. Rearranging this formula yields $c_v = \mathcal{R}/\mu(\gamma - 1)$. The expression for u can now be expressed as:

$$u\Sigma = e = p/(\gamma - 1), \tag{2.59}$$

where e is defined as the thermal energy per unit surface area. This equation of state describes how a change in thermal energy can affect the pressure of the gas, and if given the surface density as well, the temperature of the disc. Many of the same sources which affect the evolution of the Navier-Stokes equation also impact the thermal energy evolution. The following energy equation is the one implemented in the publicly available version of FARGO-ADSG:

$$\frac{\partial e}{\partial t} + \nabla \cdot (e\upsilon) = -p\nabla \cdot \upsilon + Q^{\text{visc}} + Q^{\text{visc}}_{\text{art}}, \tag{2.60}$$

where Q^{visc} is the viscous dissipation heating term defined in Sec. 2.1.1:

$$Q^{\text{visc}} = \frac{1}{2\nu\Sigma}\left[\sigma^2_{r,r} + \sigma^2_{r,\phi} + \sigma^2_{\phi,\phi}\right] + \frac{2\nu\Sigma}{9}\text{div}^2\left(\vec{v}\right), \tag{2.61}$$

with the components of the viscous stress tensor given in Eqs. (2.8)–(2.10). The artificial viscosity introduced to smooth shocks also introduces a heating flux:

$$Q^{\text{visc}}_{\text{art}} = -q^{\text{visc}}_r \frac{\partial \upsilon_r}{\partial r} - q^{\text{visc}}_\phi \frac{1}{r}\frac{\partial \upsilon_\phi}{\partial \phi} \tag{2.62}$$

where q^{visc}_r and q^{visc}_ϕ are given by Eq. (2.51).

FARGO-ADSG initialises the thermal energy per unit area of the disc in such a way that the initial surface density and temperature profiles defined above, are the same whether or not an energy equation is involved:

$$e\left(r\right) = e_0\left(\frac{r}{r_0}\right)^{-1-a+2f} \quad \text{where} \quad e_0 = \frac{\mathcal{R}}{\mu\left(\gamma-1\right)}\Sigma_0 T_0. \tag{2.63}$$

In FARGO-ADSG the energy equation is evolved in much the same way as the Navier-Stokes equations. In `Substep 2` the artificial viscosity updates the energy at the same time as the velocity update. The other source terms – pressure work and viscous dissipation – are carried out in `Substep 3`, which uses a predictor-corrector integrator to calculate the updated energy:

$$e^{\text{pred}}_{i,j} = e^{t+b}_{i,j} + \Delta t\left[Q^{\text{visc}}_{i,j} - p^{t+b}_{i,j}\nabla \cdot \upsilon^{t+b}_{i,j}\right] \tag{2.64}$$

$$p^{\text{pred}}_{i,j} = \left(\gamma-1\right)e^{\text{pred}}_{i,j} \tag{2.65}$$

$$e^{\text{n+c}}_{i,j} = e^{t+b}_{i,j} + \Delta t\left[Q^{\text{visc}}_{i,j} - \frac{1}{2}\left(p^{t+b}_{i,j} + p^{\text{pred}}_{i,j}\right)\nabla \cdot \upsilon^{t+b}_{i,j}\right] \tag{2.66}$$

After the source steps, the energy per unit area is advected through the disc by the same constrained transport mechanism, updated with the flux of e/Σ, through the radial and FARGO sub-steps.

2.3.5 Implementation of Disc Self-Gravity

In this subsection we briefly describe the implementation of disc self-gravity in the FARGO-ADSG code, which we use heavily in our work in this thesis. For a detailed description of the background theory, issues and implementation we direct the reader to Section 3.2 of Clément Baruteau's thesis (Baruteau 2008).

Without self-gravity the potential created by the disc does not affect its evolution. The only potential the disc sees is the one created by the central object and any embedded planets. The potential of a disc with a 2-D surface density field $\Sigma(\mathbf{r}')$ reads:

$$V(\mathbf{r}') = -G \int\int \frac{\Sigma(\mathbf{r}')\,\mathrm{d}\mathbf{r}'}{||(\mathbf{r}-\mathbf{r}')^2 + \epsilon^2||}^{\frac{1}{2}}, \tag{2.67}$$

where ϵ is a smoothing length, used to avoid singularities in the potential when $\mathbf{r} - \mathbf{r}' = 0$; to avoid confusion with smoothing length used in the planet potential calculation we will denote with ϵ_{sg} from now on. With a grid of $N \times N$ cells the potential calculation by direct summation requires $\mathcal{O}(N^2)$ operations, making it extremely time consuming for $N > 100$. The fact that the potential calculation reads as a convolution product allows the calculation of the potential in Fourier space. If M is the mass field and $K = ||\mathbf{r}^2 - \epsilon_{\mathrm{sg}}^2||^{-1/2}$ is defined as the Green's kernel, the potential can be written:

$$V = -G\mathcal{F}^{-1}\left[\mathcal{F}(M) \times \mathcal{F}(K)\right], \tag{2.68}$$

where $\mathcal{F}$ and $\mathcal{F}^{-1}$ are the direct and inverse Fourier transform operators respectively. This formulation reduces the number of operations required for the calculation of the potential on $N \times N$ grid to $\mathcal{O}(N \log N)$. The Fourier calculation can be performed numerically with Fast Fourier Transforms (FFTs) using the FFTW 2.1.5 MPI parallelised library. Implementing this in FARGO-ADSG is a complex and subtle task which we will not go into here, however a few things are worth noting. Aliasing issues mean that the FFTs are carried out on a grid with twice the number of radial cells as the hydro mesh; the periodicity of the azimuthal direction means that the same number of azimuthal cells can be used (hydro mesh: $(N_r \times N_\phi)$, FFT mesh: $(2N_r \times N_\phi)$). In 2-D polar co-ordinates the potential is a convolution product of the variables u, ϕ instead of r, ϕ, where $u = \log(r/r_{\mathrm{min}})$. This convolution can only be done if the radial grid has a logarithmic spacing (the radial spacing is not constant). Finally, the FFT calculation of the potential on a discretised mesh results in a radial self-acceleration which can violate Newton's

first law. To doctor this, the FFT algorithm is used to calculate the radial and azimuthal accelerations (g_r and g_ϕ) on the disc due to its self-gravity. See Baruteau (2008) for detailed analysis of all these points. These terms can be directly included as source terms in the Navier-Stokes equations . In FARGO-ADSG they are used to update the radial and azimuthal velocities in a step after `Substep 1`.

The radial and azimuthal accelerations take the following form on the discretised FFT grid as functions of u, ϕ:

$$g_r\left(u,\phi\right) = -Ge^{\frac{u}{2}}\frac{\Delta u\Delta\phi}{2N_rN_\phi}\mathcal{F}^{-1}\left[\mathcal{F}\left[S_r\right]\times\mathcal{F}\left[K_r\right]\right]\left(u,\phi\right) - G\Sigma\left(u,\phi\right)\Delta u\Delta\phi/B, \quad (2.69)$$

and:

$$g_\phi\left(u,\phi\right) = -Ge^{\frac{3u}{2}}\frac{\Delta u\Delta\phi}{2N_rN_\phi}\mathcal{F}^{-1}\left[\mathcal{F}\left[S_\phi\right]\times\mathcal{F}\left[K_\phi\right]\right]\left(u,\phi\right), \quad (2.70)$$

where S_r and S_ϕ are kernels related to the mass distribution in this disc, and K_r and K_ϕ are the Green's Kernels related to the mesh, the expressions for each of these terms can be found in Baruteau (2008). It is worth noting that because the mesh doesn't change shape or resolution throughout the simulation, K_r and K_ϕ only need to be calculated once at the beginning of the simulation. S_r and S_ϕ have to be calculated every time-step due to the underlying mass distribution evolving. B is equal to ϵ_{sg}/r; ϵ_{sg} must scale with r otherwise the convolution of V doesn't hold, B is therefore constant over the extent of the disc.

The last thing to mention in the implementation of self-gravity in FARGO-ADSG is the initialisation of the azimuthal velocity. In Sec. 2.3.1 we mentioned that the initial profile is reached through the balance of the gravitational influence of the central object, and pressure and centrifugal forces. The self-gravity results in an additional force to balance. The new azimuthal velocity profile therefore reads:

$$\upsilon_\phi\left(r\right) = r\left(\Omega_{\mathrm{K}}^2\left(r\right)\left[1-\left(1+a-2f\right)h^2\left(r\right)\right] - \frac{g_r\left(r\right)}{r}\right)^{\frac{1}{2}}. \quad (2.71)$$

Our Simulations

Chapter Contents

This chapter outlines the set-ups used for the simulations presented and discussed throughout this thesis. The general hydrodynamic disc set-up is outlined in Section 3.1 and we describe our implementation of a radiative Equation of State in Section 3.2. We discuss how the orbital evolution of the binary, and any embedded planets, is treated in Section 3.4, with the remainder of the Chapter used

to discuss disc boundary outflow conditions. Unless specified, the details in this chapter pertain to: an investigation into outflow condition choice at the inner disc boundary in circumbinary discs (Section 3.5), and examining the impact of shrinking the inner disc radius and embedding the central binary within the computational domain of the disc (Section 3.5.2); evaluating the impact of varying disc mass, through disc self-gravity, upon circumbinary disc structure and evolution (Chapter 4); using these results to then probe whether any changes imposed on the circumbinary disc affect the mass and orbital evolution of embedded, migrating protoplanetary cores (Chapter 5); and finally the influence of radiative effects, including binary irradiation and FLD radiative transport, on disc and planet evolution in circumbinary systems (Chapter 6).

3.1 Simulation Set-up

3.1.1 Disc Evolution

The equations of motion of the circumbinary disc system are detailed here in two-dimensional polar co-ordinates (r, ϕ) with the origin kept at the centre-of-mass of the binary. Throughout this thesis we take into account the action of the central binary on the disc, in addition to the influence of a protoplanetary core/planet, and/or the disc itself. Each of these influences are detailed below, whereas we discuss the orbital evolution of the binary and an interacting planet in Section 3.4.

Under the two-dimensional approximation we consider vertically integrated quantities, such as the disk surface density $\Sigma = \int_{-\infty}^{\infty} \rho \mathrm{d}z$. In this set-up the continuity equation reads:

$$\frac{\partial \Sigma}{\partial t} + \nabla \cdot (\Sigma \mathbf{v}) = 0. \tag{3.1}$$

The equations for the evolution of the radial and the angular momentum are given by:

$$\frac{\partial \Sigma \upsilon_r}{\partial t} + \nabla \cdot (\Sigma \upsilon_r \mathbf{v}) - \frac{\Sigma \upsilon_\phi^2}{r} = -\frac{\partial p}{\partial r} - \Sigma \frac{\partial \Phi}{\partial r} + f_r^{\mathrm{visc}}, \tag{3.2}$$

and

$$\frac{\partial \Sigma \upsilon_\phi}{\partial t} + \nabla \cdot (\Sigma \upsilon_\phi \mathbf{v}) + \frac{\Sigma \upsilon_r \upsilon_\phi^2}{r} = -\frac{1}{r}\frac{\partial p}{\partial \phi} - \frac{\Sigma}{r}\frac{\partial \Phi}{\partial \phi} + f_\phi^{\mathrm{visc}}. \tag{3.3}$$

Here, p is the vertically-averaged pressure, $(\upsilon_r,\, \upsilon_\phi)$ are the radial and azimuthal components of the gas velocity $\mathbf{v}$, $\left(f_r^{\rm visc},\, f_\phi^{\rm visc}\right)$ are the components of the vertically-averaged viscous force per unit volume (Eqs. (2.12) and (2.13)). Φ is the gravitational potential the disc sees. For a binary+self-gravitating disc+planet system, with its origin at the centre-of-mass of the binary, this takes the form:

$$\Phi = \sum_{k=1}^{2} \Phi_{{\rm s},k} + \Phi_{\rm SG} + \Phi_{\rm p} + \Phi_{\rm i}. \tag{3.4}$$

where $\Phi_{{\rm s},k}$ is the direct potential from the $k^{\rm th}$ star of the binary, with mass $M_{{\rm s},k}$:

$$\Phi_{{\rm s},k} = \begin{cases} -\frac{GM_{{\rm s},k}\left(3R_{{\rm Roche},k}^2 - d^2\right)}{2R_{{\rm Roche},k}^3}, & \text{for } d < R_{{\rm Roche},k} \\ -\frac{GM_{{\rm s},k}}{d}, & \text{if } \quad d \geqslant R_{{\rm Roche},k}. \end{cases} \tag{3.5}$$

Here $d = |\mathbf{r}' - \mathbf{r}_{{\rm s},k}|$ and $R_{{\rm Roche},k}$ is the radius of the $k^{\rm th}$ star's Roche lobe, as defined in Eggleton (1983),

$$R_{\rm Roche,1} = A\frac{0.4q_1^{\frac{2}{3}}}{0.6q_1^{\frac{2}{3}} + ln(1+q_1^{\frac{1}{3}})}, \tag{3.6}$$

where A is the orbital separation between the two binary stars, and $q_1 = M_1/M_2$. This prescription effectively treats the members of the binary as constant-density solid-body spheres with sizes equal to their respective Roche lobes. The second term in Eq. (3.4), $\Phi_{\rm SG}$, arises from the disc self-gravity and takes the form:

$$\Phi_{\rm SG} = \sum_{i}^{N_r}\sum_{j}^{N_\phi} \frac{Gm_{{\rm c},ij}}{|\mathbf{r_{ij}}|}, \tag{3.7}$$

where $\mathbf{r_{ij}} = \mathbf{r}_i - \mathbf{r}_j + \epsilon_{\rm SG}$. $\epsilon_{\rm SG}$ is a softening length used to avoid singularities in the calculation of the disc's potential; it takes a value equal to $0.4H$ in this work, where H is the disc thickness. The quantity $m_{{\rm c},ij}$ is the mass contained within cell ij, calculated with the surface density $\Sigma_{c,ij}$ and the surface area of the cell S_{ij}:

$$m_{{\rm c},ij} = \Sigma_{{\rm c},ij}\, S_{ij}.$$

The disc potential causes two additional acceleration terms – g_r and g_ϕ – to be included in the equations of motion of the disc elements. The description of how these terms are obtained is described in detail in (Baruteau 2008).

The last two terms in Eq. (3.4), $\Phi_{\rm p}$ and $\Phi_{\rm i}$, arise through the presence of an interacting planet or protoplanetary core. The first of these terms is included in

the evolution of the system if the mass of the body m_p is non-zero, and takes the form:

$$\Phi_\mathrm{p} = -\frac{Gm_\mathrm{p}}{\sqrt{r^2 + r_\mathrm{p}^2 - 2rr_\mathrm{p}\cos\left(\phi - \phi_\mathrm{p}\right) + \epsilon^2}}. \tag{3.8}$$

ϵ is a softening length used to avoid singularities in the calculation of the planet's potential, as well as take into account 3-D effects not captured in a 2-D simulation, such as a planet not opening a gap through the entire vertical extent of the disc. In this work the softening length takes a value equal to $0.4H$, where H is the disc thickness – note this is the same as the smoothing length used in the calculation of the disc self-gravity potential. Φ_i is an additional potential term caused by the acceleration of the binary centre-of-mass by the disc, and the planet. The inclusion of this term is discussed in Sections 3.4 and 4.5.

3.1.2 Hydrodynamic Model

Two codes were used to solve the continuity (Eq. (3.1)) and Navier-Stokes (Eq. (2.7)) equations of hydrodynamics of the gaseous disc, as well as integrating the orbits of the binary and planets.

The first code used was an upgraded version of the code FARGO (Masset 2000a), called FARGO-ADSG which includes the calculation of disc self-gravity as well as an adiabatic equation of state (Baruteau 2008; Baruteau and Masset 2008a). The author used this code exclusively, so this is the code focused upon in this, and previous chapters. The second code used is GENESIS (Masset 2000a; de Val-Borro et al. 2006), a code which uses an advection scheme based on the van Leer (1977) monotonic transport algorithm to solve the disc equations. The version of GENESIS used has the FARGO time stepping upgrade, as well as a module to calculate self-gravity. In both codes the binary and planetary orbits are evolved using a fifth-order Runge-Kutta integrator scheme (Press et al. 1992).

These codes were used to run 2-D hydrodynamic simulations in the plane of the binary's orbit. A grid resolution of $N_r \times N_\phi = 550 \times 550$ cells is used. Unless specified, this resolution is used for all the runs presented throughout this thesis. For the grid properties chosen for the self-gravitating simulations in the *Kepler* systems this equates to values of H/dr between 6 and 7. The radial grid-spacing is logarithmic, as required by the self-gravity calculations, with a resolution chosen to guarantee that the horseshoe region in the vicinity of the observed planet in

each system is properly resolved. This has the added benefit of having a finer grid in the inner region of the disc closest to the binary.

We follow a slightly different approach throughout our work in initialising the disc surface density, using a prescription used in several works (Pierens and Nelson 2013, e.g.) examining binary-disc-planet interactions:

$$\Sigma(r) = f_{\rm gap}\mathcal{X}\Sigma_0 r^{-3/2}, \tag{3.9}$$

where Σ_0 is defined such that 2% of the mass of the binary is contained within 30 au, $\mathcal{X}$ is a simple scaling factor defined and used in Chapters 4 and 5, and $f_{\rm gap}$ is a gap-function used to simulate the inner cavity, decreasing the time needed for the disc to reach equilibrium. This function is taken to be, from Günther et al. (2004):

$$f_{\rm gap} = \left(1 + \exp\left[-\frac{r - R_{\rm gap}}{0.1R_{\rm gap}}\right]\right)^{-1}, \tag{3.10}$$

where $R_{\rm gap} = 2.5a_{\rm b}$, the estimated gap size created by the tidal interaction of the binary on the disc (Artymowicz and Lubow 1994). Simulations have shown that binary-disc interactions modelled both with and without this function eventually obtain the same disc structure. We note that this choice of power-law slope ($\alpha = -3/2$) means there is a negligible vortensity gradient in the region of the disc where the gap function plays no role. In this area there will be very little contribution to the linear co-rotation torque acting on any embedded planet (Tanaka et al. 2002, e.g.), meaning any migration will be driven by the Lindblad torques.

Building on the results of Pierens and Nelson (2013) we choose disc parameters that match the disc models they ran which most closely recreated the *Kepler* systems. To simulate the anomalous viscosity in the disc, an alpha model prescription (Shakura and Sunyaev 1973) of effective kinematic viscosity is used, $\nu = \alpha c_s H$, where $\alpha = 10^{-3}$ is used throughout, c_s is the sound speed in the disc and H is the disc thickness. We consider a disc with a flaring index of 0, and hence a constant aspect ratio, $h = \frac{H}{r} = 0.05$. This corresponds to a locally isothermal equation of state, with a temperature profile given by $T = T_0 r^{-1}$. This locally isothermal set-up is used for the majority of the work presented in this thesis as we wanted to examine each physics addition separately – details pertaining to simulations using more realistic adiabatic, or radiative equations of state are included in the next section.

To simulate accretion onto planet cores, we follow the prescription of Kley (1999).

Accretion is modelled by removing a fraction of the gas within the planet's Hill sphere, $R_{\rm Hill} = a_{\rm p}(m_{\rm p}/3M_\star)^{1/3}$, from the disc and adding the equivalent mass to that of the planet. The rate at which gas is removed from the Hill sphere is determined by the accretion time-scale, $t_{acc} = f\, t_{dyn}$, where t_{dyn} is the orbital period of the planet, and f is an adjustable factor. For simulations where there is no accretion this corresponds to $f = 0$.

3.2 Radiative Model

As described in Chapter 1 an isothermal equation of state cannot accurately describe the processes which occur during disc evolution, planet formation or planet migration. The addition of a more realistic equation of state is required. In this section we describe how we build on the adiabatic equation of state implementation in FARGO-ADSG with the addition of radiative effects to create a version of FARGO we call FARGORAD.

We use the energy density evolution equation from FARGO-ADSG as a starting point, which reads:

$$\frac{\partial e}{\partial t} + \underbrace{\nabla\cdot(e\mathbf{v})}_{\substack{\text{advective}\\ \text{transport}}} = \underbrace{-p\nabla\cdot\mathbf{v}}_{\substack{\text{compression/}\\ \text{dilation}\\ \text{work}}} + \underbrace{Q_+}_{\substack{\text{viscous}\\ \text{heating}}} . \tag{3.11}$$

A description of the separate source terms which influence the evolution of the energy density is contained in Section 2.3.4, however we note here that all the terms act to increase the entropy of the disc. The thermal energy content and hence the temperature in the disc will only increase, unable to reach a steady state. It is also clear from this equation that the only sources of heat in a disc described by this evolution are those internal to the disc: heating due to pressure forces, and dissipation through the action of viscosity. A protoplanetary disc, whether around a single star, or a binary system, will be irradiated by the host star. This external source of radiative energy will heat the disc by a number of different mechanisms, dependent on the temperature of the star(s), and the conditions in the disc. Lastly, the only method the disc has of transporting heat throughout the disc is by conservative advective transport. To address these points and obtain a more physically realistic description of the thermal evolution of the disc, and obtain a more accurate picture of disc structure and planetary

evolution, we include a number of additional terms to Eq. (3.11):

$$\frac{\partial e}{\partial t} + \nabla\cdot(e\mathbf{v}) = -p\nabla\cdot\mathbf{v} + Q_+ + Q_{\rm irr} - Q_- - \nabla\cdot\mathbf{F}, \tag{3.12}$$

where $Q_{\rm irr}$ is a heating term caused by the radiation field of the central star(s), Q_- is a radiative cooling term, and $\nabla\cdot\mathbf{F}$ is a radiative flux. The inclusion of these terms allows the disc to cool, be heated by its host stars and transport energy through the disc by radiative diffusion. Writing the equation in this form we assume a single temperature approach like that in Kley et al. (2009). Other codes have implemented a two-temperature approach (Kley 1989; Bitsch et al. 2013, etc.). These solve equations similar to Eq. (3.12), but for the gas temperature – through the internal gas energy $e = c_v\Sigma T$, where $c_v = \mathcal{R}/\mu\,(\gamma-1)$ and the radiation temperature – through the radiation energy density $E = a_r T^4$, where $a_r = 4\sigma_r/c$ is the radiation constant. In our single temperature approach we assume that $E < e$. We still use an ideal equation of state to close the system of equations which FARGORAD solves:

$$p = \frac{\Sigma\mathcal{R}T}{\mu}. \tag{3.13}$$

With the expression for the thermal energy density we can write this as:

$$p = (\gamma-1)\,e, \tag{3.14}$$

which can also be expressed as:

$$p = \frac{c_s^2\Sigma}{\gamma}, \tag{3.15}$$

With the above expressions the adiabatic sound speed within the disc is given by:

$$c_{\rm s} = \sqrt{\frac{\gamma\,(\gamma-1)\,e}{\Sigma}}, \tag{3.16}$$

and is related to the isothermal sound speed: $c_s = \sqrt{\gamma}c_{s,\rm iso}$.

In a disc with a single, central star at $r = 0$ the disc height at a given radius, r, would still be given by the following expression:

$$H(r) = c_{\rm s}\sqrt{\frac{r^3}{GM_\star}}, \tag{3.17}$$

however in a circumbinary disc, we use the prescription used in Günther and Kley (2002) to describe the disc height at position $\mathbf{r}$, by taking into account the

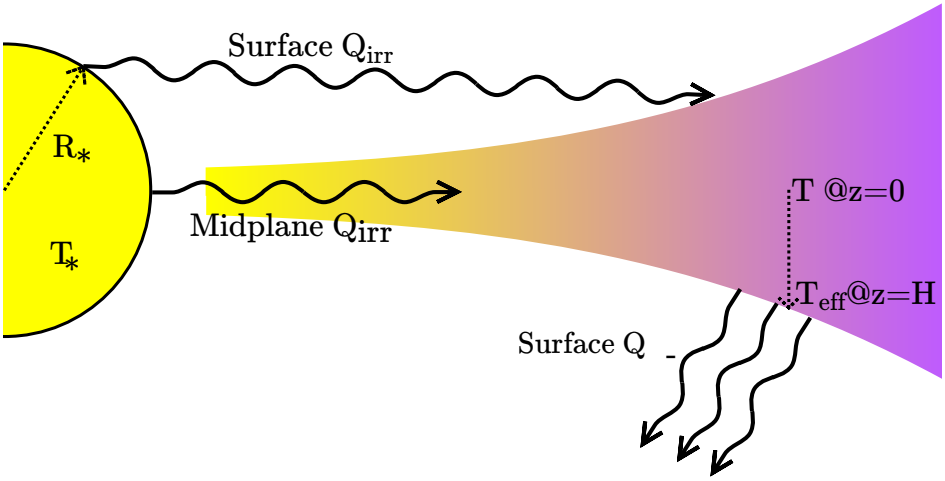

FIGURE 3.1: A sketch looking through the disc mid-plane showing the location in the disc cools radiatively, and the methods by which the stars can irradiate the disc Sec. 3.2.2.

contribution to the disc height from each star, k at position $\mathbf{r}_{\mathrm{s},k}$:

$$H(\mathbf{r}) = \left(\sum_{k=1}^{2} \frac{GM_{\mathrm{s},k}}{c_{\mathrm{s}}^2 \sqrt{|\mathbf{r} - \mathbf{r}_{\mathrm{s},k}|}} \right)^{-\frac{1}{2}} = \left(\sum_{k=1}^{2} H_k^{-2}(\mathbf{r}) \right)^{-\frac{1}{2}}. \tag{3.18}$$

$H_k(\mathbf{r})$ would be equal to Eq. (3.17) if $\mathbf{r}_{\mathrm{s},k} = 0$ and $M_{\mathrm{s},k} = M_\star$. The form of Eq. (3.18) indicates that the total height H is less than the individual heights H_k.

3.2.1 Surface Cooling

In our model the cooling term in Eq. (3.12) can be thought of as radiation transport in the vertical direction. In a 2-D disc however we assume the disc thickness is much smaller than the radial or azimuthal length-scales in the disc and we do not solve for the vertical structure (D'Angelo et al. 2003). We can write Q_-, neglecting the r and ϕ directions for the moment, as:

$$Q_- = \int_{-\infty}^{\infty} \nabla \cdot \mathbf{F_z} \mathrm{d}z \simeq \int_{-\infty}^{\infty} \frac{\partial F_z}{\partial z} \mathrm{d}z. \tag{3.19}$$

The lack of vertical structure in our disc allows us to equate the pressure scale height, H, with the photospheric scale height, and assume that the disc radiates

available energy at the locations $z = \pm H$:

$$Q_- = \int_{-H}^{H} \frac{\partial F_z}{\partial z} \mathrm{d}z = F_z(H) - F_z(-H) = 2F_z(H). \tag{3.20}$$

The disc will cool as a black-body with the flux associated with the temperature at the surface of the disc photosphere. Although we have not explicitly solved for the vertical disc structure, we have solved for the disc mid-plane temperature, T, which readers will remember is related to the surface density and energy density by $T = \frac{\mu(\gamma-1)e}{\mathcal{R}\Sigma}$. Following the approach of Hubeny (1990) which relates the mid-plane temperature to the effective temperature at the surface of the disc, using the LTE gray solution, we can write:

$$Q_- = 2\sigma_r T_{\mathrm{eff}}^4, \tag{3.21}$$

where σ_r is the Stefan-Boltzmann constant and T_{eff} is the effective temperature approximation at the surface of the disc. From Hubeny (1990):

$$T_{\mathrm{eff}}^4 = T^4 \left[\frac{3\tau}{8} + \frac{\sqrt{3}}{4} + \frac{1}{4\tau} \right]^{-1} = \frac{T^4}{\tau_{\mathrm{eff}}}, \tag{3.22}$$

where τ is the mean vertical optical depth of the disc, which takes into account any vertical structure in T or Σ which would be present in a more realistic 3-D calculation. In a 2-D code such as this we work with vertically integrated quantities, such as surface density describing the distribution of mass in the disc. It follows that $\tau = \int \rho \kappa_{\mathrm{R}} \mathrm{d}z$, which we approximate by $\tau = \rho \kappa_{\mathrm{R}} H$, where ρ is the mid-plane density. We equate the mid-plane density to the surface density with: $\rho = \Sigma / (2H)$, so we can rewrite τ as $\tau = \kappa_{\mathrm{R}} \Sigma / 2$. In the previous expressions κ_{R} is the Rosseland mean opacity for low-energy photons; we will describe in detail how this quantity is calculated in Section 3.2.4.

The form of Eq. (3.21) allows cooling across a range of different disc parameters; when the disc is optically thick ($\tau \geq 1$) the emitted flux is inversely proportional to τ, and proportional to τ in the opposite limit. We believe it will be important to capture both of these behaviours in our disc models, due to the very low and very high surface densities present in, and bounding, the circumbinary disc cavity.

3.2.2 Irradiation

A protoplanetary disc does not form and evolve in isolation. The star(s) at its centre can interact with it in a number of ways. The star emits radiation across a whole range of wavelengths: photons in the far-UV, extreme-UV and X-ray ranges can drive material off the disc through photo-evaporation (Dullemond et al. 2007; Clarke 2011; Alexander et al. 2014, etc.), whilst photons in less-energetic parts of the EM spectrum can interact with dust and gas in the disc heating the medium, as well as driving chemistry in the disc. It is this heating of the disc by the stars through irradiation which we want to implement here.

In particular with our simulations we want to investigate the effect of the highly variable irradiation field which the binary stars emit on the disc evolution, particularly in the inner regions of the disc which dictate the late stages of planet evolution in these systems. The stars' radiation field interacts with the disc in two ways: irradiation onto the upper layers on the surface of the disc, which in a mechanism similar to the inverse of the radiative cooling in the previous subsection, increases the mid-plane temperature of the disc. Figure 3.1 shows these two mechanisms in a disc around a single star. This picture is slightly modified when two stars are embedded in the centre of the disc.

In a circumbinary system the two component stars orbit their centre of mass, which in our disc simulations lies at the origin of the disc in a r, ϕ frame. Therefore neither of the stars sits at the centre of the disc. This adds a little more complexity into the calculation of the irradiative flux arriving at each cell, heating the disc. In the following subsection we will describe the derivation of the two irradiation mechanisms in the single star case, and the modifications needed with two stars in a circumbinary disc.

Disc Surface Irradiation

First we separate the single $Q_{\rm irr}$ in Eq. (3.12) into its two constituent parts: $Q_{\rm irr}^{\rm surf}$, the heating caused by irradiation of the disc surface; and $Q_{\rm irr}^{\rm mid}$, the mid-plane irradiative heating.

The heating rate or flux at the mid-plane of the disc caused by irradiation of the surfaces of the disc, by a star of effective surface temperature $T_\star$ and radius $R_\star$,

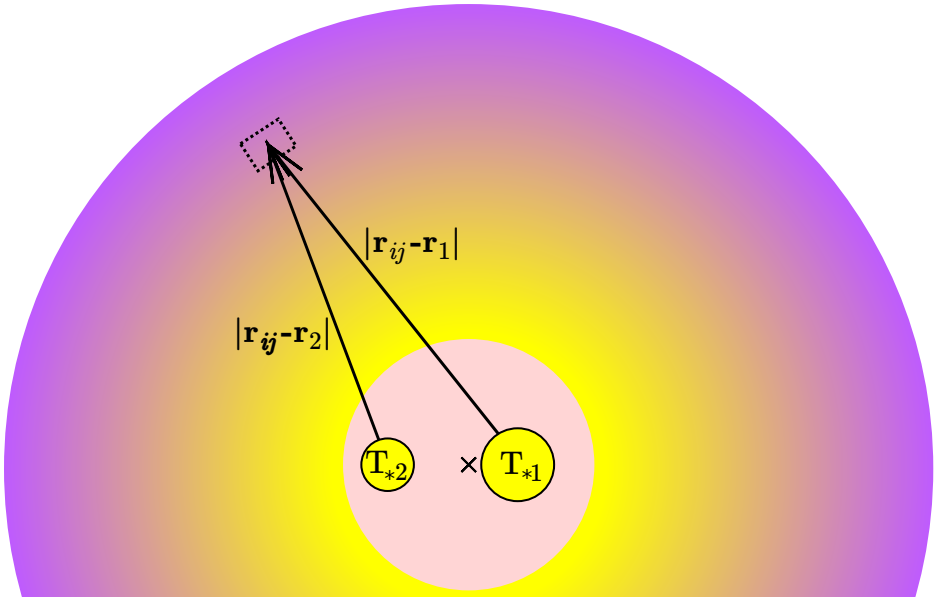

FIGURE 3.2: A face-on sketch of a circumbinary disc being irradiated by two stars, with temperatures $T_{\star,1}$ and $T_{\star,2}$, neither of which sit at the centre of the disc. Instead the centre of mass of the binary sits at the origin of the disc. The irradiative flux in cell ij will depend on the stellar parameters, as well as the disc and cell parameters.

is given by Menou and Goodman (2004):

$$Q_{\rm irr}^{\rm surf} = 2\sigma_r \frac{T_{\rm irr}^4}{\tau_{\rm eff}}. \tag{3.23}$$

The irradiation temperature, $T_{\rm irr}$ is given by:

$$T_{\rm irr}^4 = (1-\epsilon)\, T_\star^4 \left(\frac{R_\star}{r}\right)^2 W_{\rm g}, \tag{3.24}$$

where ϵ is the disc albedo, which we set to a value of 1/2. We note that in this formulation the additional stellar luminosity due to stellar accretion is not included (Pringle 1981; Hartmann et al. 2011). One of the reasons, which will become apparent in later sections, is that in hydrodynamic simulations of circumbinary discs the rate of accretion onto the stars is not well constrained and depends heavily on the inner disc outflow boundary condition used. It would also be problematic to isolate the accretion rate onto each star.

The term $W_{\rm g}$ is a geometric term, with two terms, to account for illumination of the disc, close to and far away from the star (first and second terms respectively).

From Chiang and Goldreich (1997):

$$W_{\rm g} = 0.4\left(\frac{R_\star}{r}\right) + \frac{H}{r}\left(\frac{d\ln H}{d\ln r} - 1\right). \tag{3.25}$$

The second term is meant to account for self-shadowing of the disc, and should be dropped if it is negative. However calculations have found that this can give rise to numerical instabilities, and should be calculated with a picture of the vertical thermal structure of the disc in mind. We therefore follow the practice of D'Angelo and Marzari (2012, and references within), and set the second term in parentheses to 2/7. In our simulations of radiative circumbinary discs we may find that the unique structure in the inner disc may produce a disc height profile which would shadow the outer disc, shielding it from irradiation, so finding a procedure which allows the disc to self-shadow may be a problem for future work.

Extending this prescription of disc surface irradiation by a single star to that of two stars is straightforward. The heating rate in the single-star case is axisymmetric, depending only on the radius in the disc. In the binary star case, the stellar positions must be taken into account, as well as the radial and azimuthal position of the cell. The heating rate at cell ij, where i corresponds to the radial index, and j corresponds to the azimuthal index, is:

$$Q_{\rm irr}^{\rm surf}\left(\mathbf{r}_{ij}\right) = 2\sigma_r\left(1-\epsilon\right)\sum_{k=1}^{2}\frac{T_{{\rm s},k}^4}{\tau_{\rm eff}}\left(\frac{R_{{\rm s},k}}{|\mathbf{r}|}\right)^2\mathbf{W}_{\rm g}, \tag{3.26}$$

where $|\mathbf{r}| = |\mathbf{r}_{ij} - \mathbf{r}_{{\rm s},k}|$, and $\mathbf{W}_{\rm g}$ is given by:

$$\mathbf{W}_{\rm g} = 0.4\left(\frac{R_{{\rm s},k}}{\mathbf{r}}\right) + \frac{2}{7}\frac{H\left(\mathbf{r}\right)}{\mathbf{r}}. \tag{3.27}$$

Disc Mid-plane Irradiation

For practical purposes the physical extent of the star can be assumed to be negligible compared to that of the scales present in the disc, so we treat the star as a point-source. For a single star located at the centre of the disc, the radiation can be propagated through the mid-plane of the disc in a purely radial direction. Thus the heating flux reads:

$$Q_{\rm irr}^{\rm mid} = \sigma_r 2HT_\star^4\left(\frac{R_\star}{r}\right)^2 e^{-\tau_i}\frac{1-e^{-\rho\kappa_\star\Delta r}}{\Delta r}. \tag{3.28}$$

The $e^{-\tau_i}$ term describes how much of the radiation emitted by the star has already been absorbed by the disc prior to arriving at cell i. The τ_i factor is integrated radially outwards from the inner edge of the disc to the radius r:

$$\tau_i\left(r_i\right) = \int_0^{r_i} \rho\kappa_\star \mathrm{d}r = \sum_0^i \rho\kappa_\star \Delta r. \tag{3.29}$$

The second term, $1-e^{-\rho\kappa_\star\Delta r}$ describes how much radiation is absorbed across the width of the cell, which goes into heating the gas. The quantity $\kappa_\star$ is the mean optical opacity, which should be calculated using the stellar spectrum (Dobbs-Dixon et al. 2010). As in Bitsch et al. (2013) in the optically thin limit, $\rho\kappa_\star\Delta r < 1$, we approximate the mid-plane irradiative heating flux to be:

$$Q_{\mathrm{irr}}^{\mathrm{mid}} = \sigma_r 2HT_\star^4 \left(\frac{R_\star}{r}\right)^2 e^{-\tau_i}\rho\kappa_\star. \tag{3.30}$$

If there is sufficient material in the intervening radii between the star and the target cell for the total ray optical depth, τ_i, to become > 10, then the heating flux in cells at larger radial distances is 0.

As in the disc surface irradiation case, a number of adaptations are required to fit this heating mechanism to two stars. The greatest complication arises because neither of the stars sit at the origin of the disc, therefore the purely radial propagation assumption fails. As can be seen in the disc sketch in Fig. 3.2, the rays propagate across multiple azimuthal zones. We are interested in investigating the effect of this non-axisymmetric heating field on the already non-axisymmetric disc structures present in circumbinary disc. We can follow a similar procedure to that used in adapting the disc surface irradiation to a circumbinary disc environment, by generalising any radial assumption of symmetry. Calculating the heating flux at a location within the disc, requires information about the intervening disc material. In the single star case when the irradiation source is centred in the disc, this is a simple procedure, as the disc parameters are defined at every grid cell, and the optical depth in each preceding radial zone is known. To calculate the irradiative flux arising from a non-centred source requires a ray-tracing like procedure. A ray is propagated from the source, through the disc, in the direction of the target cell. The optical depth is integrated along this ray, allowing the flux to be calculated at the cell in question. The general form of the heating flux at cell

ij, due to the irradiation of two stars, with temperatures $T_{\rm s}$ and radii $R_{\rm s}$ is:

$$Q_{\rm irr}^{\rm mid}\left(\mathbf{r}_{ij}\right) = \sigma_r 2H\left(\mathbf{r}\right)\sum_{k=1}^{2} T_{{\rm s},k}^4\left(\frac{R_{{\rm s},k}}{|\mathbf{r}|}\right)^2 e^{-\tau_{\rm ray}}\frac{1-e^{-\rho\kappa_\star \mathbf{\Delta r}}}{\mathbf{\Delta r}} \tag{3.31}$$

where as before $|\mathbf{r}| = |\mathbf{r}_{ij} - \mathbf{r}_{{\rm s},k}|$ is the distance between star, k, and the cell ij, $\tau_{\rm ray}$ is the optical depth along the ray - integrated along the vector $\mathbf{r}$ and $\mathbf{\Delta r}$ is the length of the ray segment along which the radiation is absorbed to heat the cell. We adopt a similar procedure as in the single star case, by setting an optically thin approximation, and a maximum ray optical depth – which sets the heating contribution in that cell from the star k to 0. Further details of the ray-tracing algorithm are given in Appendix A.

3.2.3 Flux-Limited Diffusion

We discussed earlier the lack of a term in the energy evolution equation which deals with the transport of heat through the disc by diffusion. With the radiative cooling term in Section 3.2.1 transport in the vertical direction is treated as the disc radiating energy away from its upper and lower surfaces. A cell of fluid can also radiatively cool in the horizontal direction, in the (r, ϕ)-plane of the disc. Unlike the radiative cooling from the surfaces of the disc which emits the energy into space, this radiative energy can be absorbed by neighbouring cells. This diffusive radiation mechanism can transport energy deposited in one region of the disc, through viscous heating, pressure work or irradiation, to another. To accurately capture the radiation flux across boundaries between optically thick and thin regions we use the Flux-Limited-Diffusion (FLD) approach of Levermore and Pomraning (1981), using the flux-limiter λ of Kley (1989), and omitting scattering processes:

$$\mathbf{F} = -\frac{4\sigma_r \lambda T^3}{\rho\kappa_{\rm R}}\nabla T = -D\nabla T. \tag{3.32}$$

The flux-limiter takes the form:

$$\lambda = \begin{cases} \frac{2}{3+\sqrt{9+10R^2}} & \text{for } R \leq 2.0 \\ \frac{10}{10R+9+\sqrt{81+180R}} & \text{for } R > 2.0, \end{cases} \tag{3.33}$$

where

$$R = \frac{1}{\rho\kappa_{\rm R}}\frac{|\nabla E_r|}{E_r} = \frac{1}{\rho\kappa_{\rm R}}\frac{|\nabla T^4|}{T^4}. \tag{3.34}$$

The flux-limiter depends on the local conditions in the disc. In the optically thick limit it approaches, $\lambda = 1/3$ and in the optically thin limit reduces the flux to $F = a_r T^4$. We include details of how we solve these equations on the finite-differenced grid of FARGO in Appendix B.

3.2.4 Opacities

In this section we have introduced two opacities: the Rosseland mean opacity, κ_{R} and the mean optical opacity, $\kappa_\star$. Some works may also consider the Planck mean opacity for photons in the same energy range as the Rosseland mean opacity, but the two are often set to be equivalent so we only use one in this work. The optical opacity is calculated in a similar fashion to that of the Planck mean opacity, but for higher energy photons. These quantities describe the optical properties of the material in the disc to the absorption and emissivity of radiation, as a function of temperature and density. One is able to calculate the opacities in the disc following the procedure in Dobbs-Dixon et al. (2010), taking into account wavelength-dependent opacities:

$$\kappa_{\mathrm{R}}\left(T,\rho\right)^{-1} = \frac{\int \kappa_{\nu,s}\left(T,\rho\right)^{-1} \frac{\partial B_\nu(T)}{\mathrm{d}T}\mathrm{d}\nu}{\int \frac{\partial B_\nu(T)}{\mathrm{d}T}\mathrm{d}\nu}, \tag{3.35}$$

where κ_ν is the frequency-dependent opacity and the s subscript denotes that scattering processes are included in the frequency-dependent opacities. The mean optical opacity is defined as:

$$\kappa_\star\left(T,\rho\right) = \frac{\int \kappa_{\nu,ns}\left(T,\rho\right) J_\nu\left(T_\star\right)\mathrm{d}\nu}{J_\nu\left(T_\star\right)\mathrm{d}\nu} \tag{3.36}$$

where ns denotes that scattering process are *not* included in calculating the frequency-dependent opacity. In reality the impinging radiation spectrum may not be a black-body, but we approximate that $J_\nu\left(T_\star\right) = B_\nu\left(T_\star\right)$. With these formulations Dobbs-Dixon et al. (2010) found an uncoupling between the cooling and stellar irradiation photospheres, with a decrease of a factor of 10 between κ_{R} and $\kappa_\star$. We use this result throughout this work. In our simulations we use the analytical power-law model from Bell and Lin (1994) as a function of temperature and mid-plane density, which fits the opacity to a number of regimes classified by a physical process in the disc:

$$\kappa_{\mathrm{R}} = \kappa_0 \rho^\alpha T^\beta. \tag{3.37}$$

TABLE 3.1: Coefficients for the various opacity regime present in the disc. Each regime, n acts over a temperature range between $T_{\max,n-1}$ and $T_{\max,n}$. All quantities are given in cgs units. See Bell and Lin (1994) for more details.

n	Regime	κ_0 $[cm^2/g]$	α	β	$T_{\max}$ $[K]$
1	Ice Grains	2×10^{-4}	0	2	$170\rho^0$
2	Sublimation of Ice Grains	2×10^{16}	0	-7	$200\rho^0$
3	Dust Grains	0.1	0	$1/2$	$2.3 \times 10^3\rho^{2/49}$
4	Sublimation of Ice Grains	2×10^{81}	1	-24	$2.0 \times 10^3\rho^{1/81}$
5	Molecules	1×10^{-8}	$2/3$	3	$1.0 \times 10^4\rho^{1/21}$
6	H-Scattering	1×10^{-36}	$1/3$	10	$3.1 \times 10^4\rho^{4/75}$
7	Bound-free & Free-free	1.5×10^{20}	1	$-5/2$	$1.8 \times 10^8\rho^{2/5}$
8	Electron Scattering	0.348	0	0	–

The coefficients α and β as well as the κ_0 constant, can be found in Tab. 3.1. One can see that the opacity depends more strongly on temperature than density. We reiterate that the mid-plane density is calculated using $\rho = \Sigma/2H$. The transition temperatures, $T_{\max}$ are calculated where $\kappa_n = \kappa_{n+1}$, or $\kappa_{0,n}\rho^{\alpha_n}T^{\beta_n} = \kappa_{0,n+1}\rho^{\alpha_{n+1}}T^{\beta_{n+1}}$. It follows that:

$$T_{\max,n} = \left(\frac{\kappa_{0,n+1}}{\kappa_{0,n}}\right)^{1/b_n} \rho^{a_n/b_n}, \tag{3.38}$$

where $a_n = \alpha_{n+1} - \alpha_n$ and $b_n = \beta_n - \beta_{n+1}$. We use the method of Lin and Papaloizou (1985) to smoothly transition between neighbouring regimes.

We have plotted the Rosseland mean opacity against temperature, for three density values typical of those found in circumbinary disc simulations, in Fig. 3.3. The strong dependence on temperature, and the relatively weak dependence on density can be easily seen, as well as the bumps caused by opacity transitions. For a given density and temperature, the optical opacity $\kappa_\star$ would be 10 times smaller than those found in Fig. 3.3.

3.2.5 Implementation into FARGO-ADSG

Throughout this section we have introduced a number of additional sources and sinks to the evolution of the energy density. Here, we outline how these terms affect the solution of the energy density evolution equation in FARGORAD, as well as changes or additional parameters required to initialise the code.

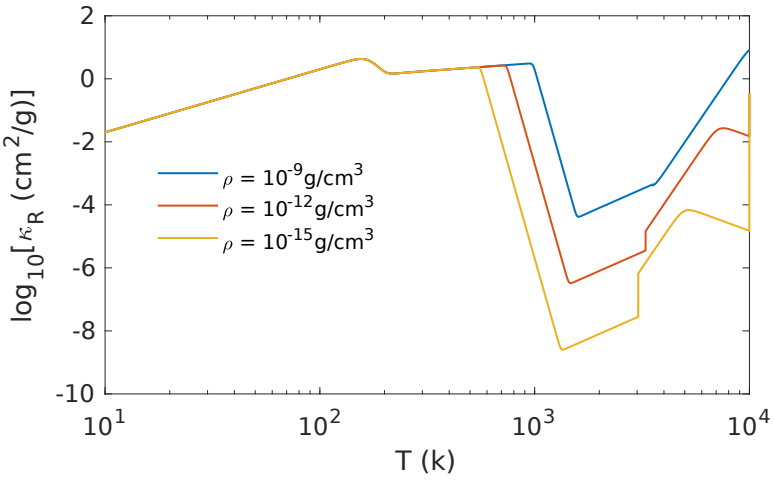

FIGURE 3.3: Log plot of Rosseland mean opacity against temperature, for high, medium and low density values typical of those found in circumbinary disc simulations. The transitions between neighbouring regimes are clearly visible. The details used to plot this function are found in Lin and Papaloizou (1985) and Bell and Lin (1994).

Initialisation

By default FARGO-ADSG initialises the surface density without the gap function defined in Section 3.1.2, and initialises the energy density with the following to ensure that the profiles of $\Sigma(r)$ and $T(r)$ are identical with or without the inclusion of an energy equation (Baruteau 2008):

$$e(r) = \frac{\mathcal{R}}{\mu(\gamma - 1)} \Sigma_0 h_0^2 r^{-\alpha - 1 + 2f}, \tag{3.39}$$

where Σ_0 and h_0 are the surface density and aspect ratio at $r = 1$, α is the power-law coefficient defining the surface density profile, and f is the flaring index which sets the temperature power-law profile $T(r) \propto r^{-1+2f}$. Initialising the surface density with a central cavity, and leaving Eq. (3.39) unaltered means that the above statement is no longer true, and the temperature profile is initialised with values $> 1.0 \times 10^5$ K in the central cavity, in discs with inner radii used throughout this work. Including the gap function (Eq. (3.10)) as a simple multiplicative factor in Eq. (3.39) solves these problems.

Solving the Energy Equation

As described earlier, FARGO-ADSG makes use of operator splitting to solve the energy equation evolution ($e^n \rightarrow e^{n+1}$):

- ($e^n \rightarrow e^{n+b}$) – an artificial viscosity (Stone and Norman 1992) is added as an additional source term in `Substep 2`,
- ($e^{n+b} \rightarrow e^{n+c}$) – the viscous heating and work due to pressure forces, update the energy equation with a predictor-corrector scheme in `Substep 3`,
- ($e^{n+c} \rightarrow e^{n+1}$) – finally, e is updated with the constrained transport technique through the flux of e/Σ in the `Transport` step.

With the inclusion of radiative cooling, irradiation and FLD we make a number of extensions and additions to this scheme. The form of the radiative cooling and disc surface irradiation terms lends themselves to being solved in `Substep 3` as additional source terms. These terms are calculated at time level $n + b$. We note here that in the inner regions of discs initialised with a cavity, we found that the optical depths calculated here lead to very efficient radiative cooling, leading to numerical instabilities. To solve this issue we implemented a separate radiative cooling substep after `Substep 3` which solves the sink term of the energy equation analytically.

$$\frac{\partial e}{\partial t} = -Q_- = -2\sigma_r \frac{T^4}{\tau_{eff}}. \tag{3.40}$$

Making use of $e = c_v \Sigma T$, we can then integrate this equation, and solve for T:

$$\begin{aligned}
c_v \Sigma \frac{\partial T}{\partial t} &= -2\sigma_r \frac{T^4}{\tau_{eff}} \\
\int_{T^{n+c}}^{T^{n+*}} \frac{\mathrm{d}T}{T^4} &= -\frac{2\sigma_r}{c_v \tau_{eff} \Sigma} \int_t^{t+\Delta t} \mathrm{d}t \\
\frac{1}{3}\left[\frac{1}{T^3}\right]_{T^{n+c}}^{T^{n+*}} &= \frac{2\sigma_r \Delta t}{c_v \tau_{eff} \Sigma} \\
T^{n+*} &= \left[\left(\frac{1}{T^{n+c}}\right)^3 + \frac{6\sigma_r \Delta t}{c_v \tau_{eff} \Sigma}\right]^{-1/3}.
\end{aligned} \tag{3.41}$$

With the updated mid-plane temperature, the new e value at time level $n+*$ can then be calculated.

TABLE 3.2: Code and cgs unit values of several quantities used in the code and post-processing, due to the choice of fundamental code units.

Quantity	Value [cgs]	Value [code]
T	1 K	251901
σ_r	$5.670 \times 10^{-5}\,\mathrm{erg \cdot cm^{-2} \cdot s^{-1} \cdot K^{-4}}$	14534.1
c	$2.998 \times 10^{10}\,\mathrm{cm \cdot s^{-1}}$	10063.9
a_r	$7.565 \times 10^{-15}\,\mathrm{erg \cdot cm^{-3} \cdot K^{-4}}$	5.7767
$\mathcal{R}/\mu$	$3.523 \times 10^{7}\,\mathrm{erg \cdot K^{-1} \cdot g^{-1}}$	1

This leaves the mid-plane, ray-traced irradiation and FLD parts of our energy equation left to solve. If both these mechanisms are included in simulations, the mid-plane heating and subsequent re-radiation through the mid-plane by FLD are treated as one substep in a new `Substep 4`, using an explicit-implicit operator splitting scheme, due to the time-step limitations imposed by the FLD algorithm (see Appendix B). If FLD is not included in the simulations, the ray-traced heating is still used to update e but through a purely explicit substep. After either the implicit or explicit `Substep 4` the energy density stands at time level $n + d$, and can finally be updated through the `Transport` step, which is unaltered by the addition of these terms.

It is our goal to use this updated version of FARGO to investigate the impact of heating of two non-centred sources both through disc surface and mid-plane irradiation on the inner disc structure of circumbinary discs, as well as the role that FLD plays by re-distributing this energy in the disc.

3.3 Computational Units

The following computational units are used: the total mass of the binary $M_\star = M_\mathrm{A} + M_\mathrm{B} = 1$, the gravitational constant $G = 1$, the radius $r = 1$ is equivalent to 1 au. Some results may be presented with the distance to the origin of the disc system scaled to the semi-major axis of the binary, a_b. To present the results of simulations we use the binary orbital period, $P_\mathrm{b} = 2\pi\sqrt{GM_\star/a_\mathrm{b}^3}$, as the unit of time. In those simulations with an adiabatic or radiative equation of state, the gas constant $\mathcal{R}$ is set to 1. The mean molecular weight of the gas $\mu = 2.35$ in atomic mass units, is also set to 1 in the code.

In simulations utilising the newly implemented radiative energy equation described above, the choice of these code units results in several derived quantities and constants used in the code and for post-processing to have values differing from their physical values. In Tab. 3.2 we give the values of several quantities in their cgs units and the values they take in code units.

3.4 Orbital Evolution

Table 3.3 contains the best-fit observed binary and planetary orbital and mass parameters of the *Kepler-16, -34,* and *-35* circumbinary planetary systems, as quoted in Doyle et al. (2011) and Welsh et al. (2012), which will be used as the central binaries for all the work presented here. These specific systems are chosen, not only because the planetary system's parameters are so well defined, but they span a wide range of binary orbital configurations: *Kepler-16* is a low eccentricity, non-unity mass ratio binary; *Kepler-34* is a high eccentricity, unity mass ratio binary; and *Kepler-35* is a low eccentricity, unity mass ratio binary.

As the eventual goal of this work is to recreate the observed state of the *Kepler* circumbinary systems, the binaries' orbital parameters remain fixed at their current observed values. In other words the binary members only interact with each other, not with the disc (or planet when included). It is worth noting that, as found in previous work (see Pierens and Nelson (2007), Kley and Haghighipour (2015), and Fleming and Quinn (2016)), if permitted there will be a back-reaction from the disc onto the binary. This can lead to orbital evolution of the binary, including shrinkage of $a_{\rm b}$ and growth of $e_{\rm b}$. We are aware that for the most massive discs presented here, these changes could be significant – an area which is definitely open for future investigation, but one we have been unable to invest time into at this stage. The binary configuration when the planets form and migrate in the disc, may also be significantly different to their current state. Interaction with the disc, and planet, will alter the initial parameters of the system. Acknowledging these issues, the binary orbital elements remain at their initialised, observed values however. The resulting equation of motion for the stars is as follows:

$$\frac{d^2\mathbf{r}_{{\rm s},k}}{dt^2} = -\frac{GM_{{\rm s},l}(\mathbf{r}_{{\rm s},k} - \mathbf{r}_{{\rm s},l})}{|\mathbf{r}_{{\rm s},k} - \mathbf{r}_{{\rm s},l}|^3} \tag{3.42}$$

for the two stars k and l.

TABLE 3.3: Binary and planet orbital parameters.

	Kepler-16	*Kepler-34*	*Kepler-35*
$M_{\rm A}$ $(\mathrm{M}_\odot)$	0.690	1.048	0.888
$M_{\rm B}$ $(\mathrm{M}_\odot)$	0.203	1.021	0.809
$m_{\rm p}$ $(\mathrm{M}_{\rm Jup})$	0.333	0.220	0.127
$q_{\rm b} = M_{\rm B}/M_{\rm A}$	0.294	0.974	0.912
$q = m_{\rm p}/M_\star$	3.54×10^{-4}	1.01×10^{-4}	7.13×10^{-5}
$a_{\rm b}$ (au)	0.224	0.228	0.176
$a_{\rm p}$ (au)	0.705	1.090	0.603
$e_{\rm b}$	0.159	0.521	0.142
$e_{\rm p}$	0.007	0.182	0.042
Reference	(Doyle et al. 2011)	(Welsh et al. 2012)	

The disc potential described in Section 3.1.1 above applies to a binary system that remains on a fixed orbit throughout its evolution and where the centre-of-mass of the binary system remains fixed in inertial space. For a binary that evolves in time due to the forces exerted on it by the disc, it is customary to work in a frame centred on the binary centre-of-mass and to include additional indirect terms in the disc potential to account for the acceleration of the binary centre-of-mass. We do not consider this situation here because our focus is on understanding the response of the disc to the potential generated by binary systems with well defined orbital elements, that match those of the *Kepler* circumbinary planets. For experimental purposes however, we can also consider a situation where the binary system maintains fixed orbital elements, but where the disc accelerates the centre-of-mass of the binary such that the centre-of-mass between the disc and the binary system is preserved. This can be achieved by including the indirect term in the disc potential due to the disc accelerating the binary centre-of-mass (while working in a frame that is centred on the binary centre-of-mass), but without evolving the orbital elements of the binary system. We undertake such a test calculation in Section 4.5 to demonstrate that our results are not influenced strongly by working with a binary system whose centre-of-mass is fixed in inertial space.

The equation of motion for a single planet of mass $m_{\rm p}$, interacting with the binary and disc system is as follows:

$$\frac{d^2\mathbf{r}_{\rm p}}{dt^2} = -\sum_{k=1}^{2} \frac{GM_{{\rm s},k}\left(\mathbf{r}_{\rm p} - \mathbf{r}_{{\rm s},k}\right)}{|\mathbf{r}_{\rm p} - \mathbf{r}_{{\rm s},k}|^3} + \mathbf{f}_{\rm dp} - \mathbf{f}_{\rm i}, \tag{3.43}$$

where $\mathbf{f}_{\rm dp}$ is the force acting on the planet from the disc, and is given by:

$$\mathbf{f}_{\rm dp} = \int_S \frac{\Sigma(\mathbf{r})\mathrm{d}\mathbf{r}}{\sqrt{r^2 + r_{\rm p}^2 - 2rr_{\rm p}\cos\left(\phi - \phi_{\rm p}\right) + \epsilon^2}}. \tag{3.44}$$

In the above equation ϵ is the same smoothing length used previously. The term $\mathbf{f}_{\rm i}$ represents the acceleration of the binary centre-of-mass by the gravity of the planet, however because the binary does not feel the gravitational influence of the planet (for the reasons given above), this term is set to 0.

3.5 Boundary Condition Study

In our journey to explore disc and planet evolution in circumbinary systems, the first issue that we address is the treatment of the inner disc region and boundary of the computational domain. This encompasses several aspects: the outflow condition used; the radius of the inner disc boundary; and the act of embedding the binary within the computational domain. This investigation is motivated by similar discussions in Marzari et al. (2009), Pierens and Nelson (2013), Kley and Haghighipour (2014), and Lines et al. (2015), which have found a range of different disc outcomes for a range of inner boundary conditions.

Below, a summary of outflow boundary conditions can be found. Each of these can be utilised at the inner or outer edge of the disc.

- Closed – or reflecting boundary condition. No flow of material is allowed across the disc edge. Material in the first (or last) active cell has its radial velocity set to 0.
- Open – material is allowed to freely leave the disc i.e. outflow. No inflow is allowed. A zero-gradient condition is set in both υ_r and Σ (please note that this is for the case of outflow only).
- Viscous – this is a limiting condition to stop the inner disc from emptying of gas too quickly. Material in the innermost cells is given a radial velocity, $\upsilon_r = \beta\upsilon_r(r_{\rm in})$, where $\upsilon_r(r_{\rm in}) = -3\nu/2r_{\rm in}$ is the viscous drift velocity and β is a free factor (Pierens and Nelson 2008a). We follow previous works which use this condition and set $\beta = 5$.

We also need to define how the azimuthal velocity is set at the inner and outer boundaries. Usually in hydrodynamical codes the viscous stress is maintained by setting v_ϕ to the sub-Keplerian orbital velocity at the locations $r_{\rm in}$ and $r_{\rm out}$. However at the inner edge the potential created by the binary is extremely non-Keplerian. We therefore set a zero-gradient condition for the azimuthal velocity at this location – v_ϕ in the first active cell takes the value of the second active cell. For all the simulations presented in this work an Open boundary condition is used at the outer edge of the disc, at $r_{\rm out} = 5.0\,{\rm au}$, to minimise wave reflections.

How best to model the inner boundary in hydrodynamic simulations of circumbinary discs has been examined a number of times (see above references). The condition imposed on the radial velocity has been shown to affect the structure of the inner disc, including the size of the tidally truncated cavity. It is unclear from these past results which boundary condition best models the transfer of mass and angular momentum in the inner disc, and therefore gives the most accurate rendering of the inner disc structure. For very eccentric binaries, and discs, material may be removed from the simulation at an Open boundary, when in fact it would have re-entered the disc (Marzari et al. 2009). Modelling this flow of material goes hand-in-hand with obtaining a physically accurate inner disc and cavity – it has previously been shown that gas can flow across the cavity and onto the binary (Artymowicz and Lubow 1996; Günther and Kley 2002). As it has been shown to affect the final stopping position of migrating protoplanets, modelling the inner disc region correctly is key in any discussion of the evolution of circumbinary planets. Although the binary stars involved in our simulations are not actively accreting material from the disc, or otherwise being acting upon by the disc, resolving the flow of material onto the central binary would be vital for addressing these issues.

3.5.1 Disc Response to Outflow Condition

To answer this question we have undertaken a systematic investigation into the impact of inner boundary condition choice on disc evolution in the three *Kepler* systems chosen. The simulations in this subsection adopt an inner radial boundary location equal to $1.5a_{\rm b}$, such that the binary system orbits interior to the computational domain as has been done in previous work. Isothermal, non-self-gravitating discs, with each of the Closed, Open and Viscous inner outflow

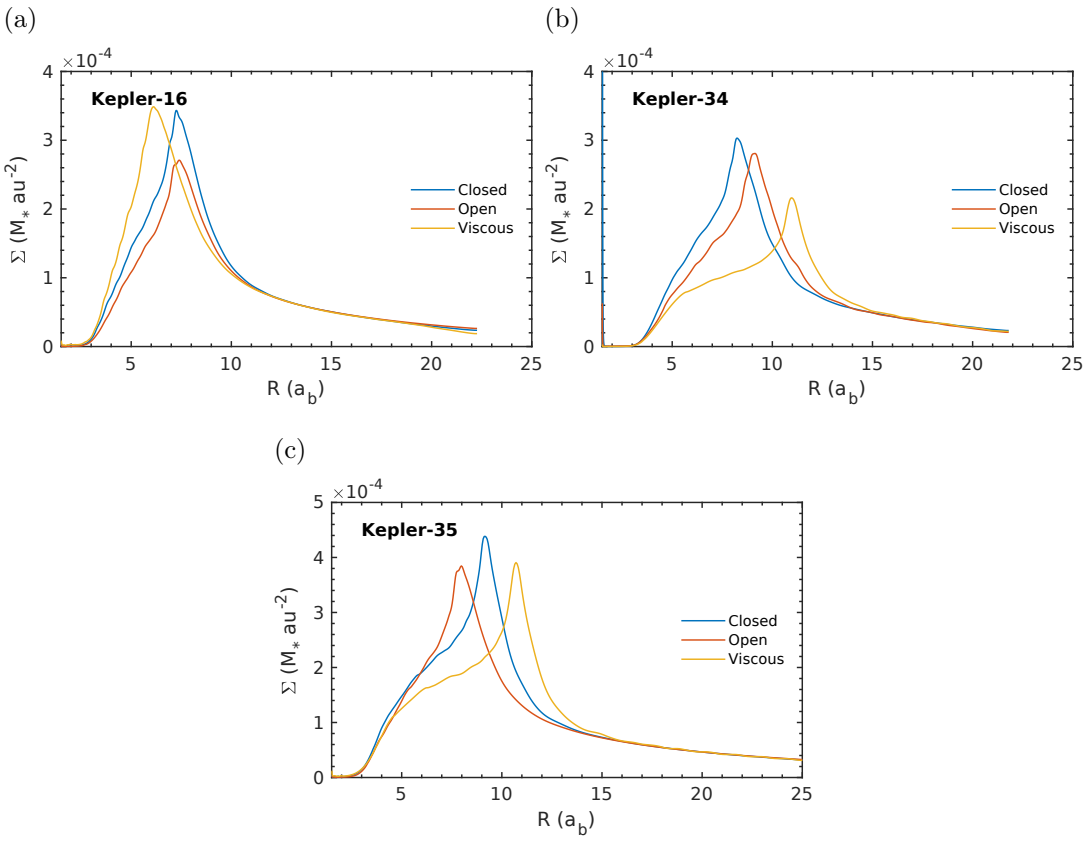

FIGURE 3.4: Azimuthally averaged surface density profiles for the Closed, Open and Viscous conditions in the three systems. The disc radii are scaled by the respective binary semi-major axes in each system – 0.224, 0.228 and 0.176 au for the *Kepler-16, -34,* and *-35* systems. The inner disc radius lies at $1.5a_{\rm b}$ in these simulations.

condition were run in the 3 binary systems. The simulations were run until the disc structures achieved quasi-steady state.

The disparity in results obtained when varying the boundary choice is clear in Fig. 3.4, with clear differences arising in peak surface density, and the radial extent of the eccentric inner cavity. We define the size of the cavity as the radial position of the peak surface density ($\Sigma_{\rm max}$) in the azimuthally-averaged surface density profile, or $r_{\rm max}$.

When comparing across the different systems, there are few common results for a given boundary condition – a rather confusing picture emerges. In the *Kepler-16* system the maximum surface density is obtained with a Viscous boundary condition, whilst the largest eccentric cavity occurs in the Open case. In both the *Kepler-34* and *-35* systems a large eccentric cavity can be seen in the Viscous

simulations, with the highest $\Sigma_{\rm max}$ achieved in Closed discs. In these two systems, each with a binary mass ratio close to unity, there is a large range in final disc configurations; both large and small inner cavities can been seen, with a difference of $\approx 50\%$ between the cavity sizes in the Closed and Viscous *Kepler-34* systems.

The cavity sizes obtained from these simulations are in poor agreement with those obtained in Pierens and Nelson (2013) and Kley and Haghighipour (2015). We attribute this to differences in how the gas velocities are treated at the inner and outer boundaries (Pierens and Nelson 2013), and the lack of an enforced mass-flow through the disc (Kley and Haghighipour 2015) – our discs are free to lose mass at their outer boundary.

Similar differences are also seen in the azimuthally-averaged eccentricity profiles, with a range of results seen throughout the different discs, as well as the temporal evolution; some boundary conditions approach equilibrium at a faster rate, possibly due to over- or under-estimating the flow of material from the inner disc onto the binary.

The origins of the discrepancies in simulation outcomes as a function of the inner boundary condition are uncertain, and it would probably require an exhaustive and painstaking study in order to provide a convincing explanation. Nonetheless, we expect that the steady-state disc structure (in some averaged sense) will arise because of a balance between the viscous evolution of the discs and the tidal torques due to the binary. The amplitudes of spiral density waves excited at Lindblad resonances, and their propagation into the disc and non-linear dissipation determine how the outward angular momentum flux from the binary is deposited into the orbiting disc material. The local viscous evolution also depends on local gradients in the disc, such that the steady profile achieved by the disc is expected to depend on the numerical set up to some extent. What is perhaps surprising is the observed strength of the dependency.

It is worth noting that the above issues relating to boundary conditions pertain to codes that employ fixed Eulerian meshes. Lagrangian, particle-based codes such as SPH (Artymowicz and Lubow 1994), do not suffer from this issue as they implicitly adopt free boundary conditions, although issues relating to controlling numerical viscosity near the cavity edge and low particle numbers within the cavity do start to arise.

3.5.2 Shrinking Inner Disc Radius

The lack of agreement between at least two boundary conditions in each system, motivated an investigation into a more realistic treatment of the inner disc. The choice of boundary condition tries to mimic the flow of material out of the disc and onto the central binary. Setting the inner boundary radius within the predicted extent of the cavity, but completely outside the orbit of the binary, requires a guess at how much material is really exchanged between the binary and the disc across the boundary. To completely capture this effect, the most realistic approach would be to completely embed the binary within the disc domain, an expensive procedure computationally as this would require small time steps for numerical stability.

By examining a suite of simulations (isothermal, non-SG) of the *Kepler-16* system, using ever smaller inner boundary radii – from 0.25 au down to a completely embedded case, 0.04 au – we aim to find a set-up which optimises accuracy and run-time, to use for our self-gravity and radiative equation of state simulations later. Whilst the number of radial grid cells is kept constant for all the different radial domain sizes shown here, we are confident that we are operating at a resolution high enough that issues caused by differences in radial cell size are negligible. In terms of the local scale height at the inner boundary, our radial cell size ranges from between 0.25 scale heights and 0.16 scale heights, for the smallest and largest inner radii respectively. The same Open outer boundary condition at 5.0 au was used again.

As $r_{\rm in}$ increases, the size of the inner cavity (Fig. 3.5a), and consequently $r_{\rm max}$ (Fig. 3.6a) also increases. It follows from increasing the cavity size, that the extent of excited cell eccentricity and overall disc eccentricity should increase – this can be seen in Figs. 3.5b and 3.6b. The cell eccentricity is calculated by treating each grid-cell as a particle, with the mass and velocity of the cell, orbiting the central binary. We then use the method in Pierens and Nelson (2013) to calculate the disc-integrated eccentricity:

$$e_d = \frac{\int_0^{2\pi}\int_{r_{\rm in}}^{r_{\rm out}} \Sigma e_{\rm c} r \, {\rm d}r \, {\rm d}\phi}{\int_0^{2\pi}\int_{r_{\rm in}}^{r_{\rm out}} \Sigma r \, {\rm d}r \, {\rm d}\phi}, \tag{3.45}$$

where $r_{\rm in}$ and $r_{\rm out}$ are the inner and outer radii of the disc, Σ is the grid element surface density and $e_{\rm c}$ is the eccentricity of the cell-as-a-particle. Note that when calculating the disc eccentricity we treat each cell as if it were a ballistic particle

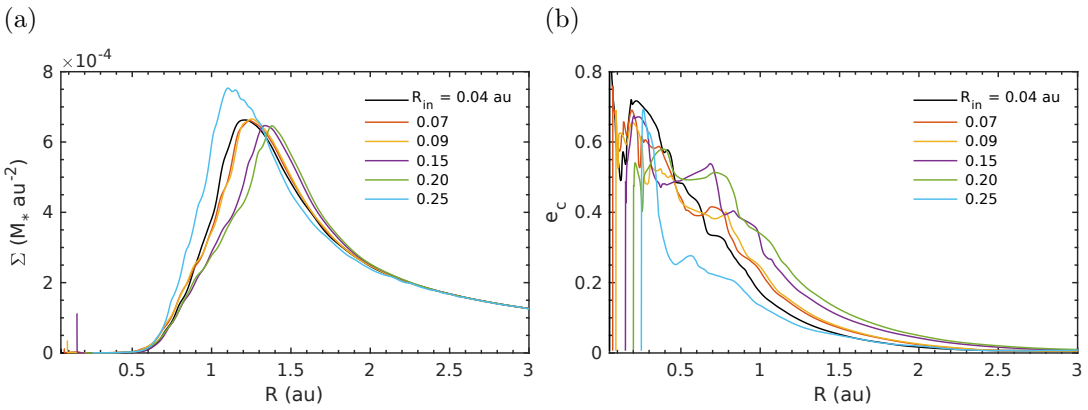

FIGURE 3.5: *(a)* Surface density distributions of increasing $r_{\rm in}$ boundary condition simulations in the *Kepler-16* system at steady-state. The general trend for the eccentric inner cavity to increase in size as the inner radius increases can be seen. *(b)* Azimuthally-averaged cell eccentricity profiles of increasing $r_{\rm in}$ boundary condition simulations in the *Kepler-16* system at steady-state. The increasing size of the eccentric cavity can also be seen.

orbiting around a single star containing the mass of the binary, and neglect the influence of the disc self-gravity on the calculation of the eccentricity. We note that the influence of self-gravity can be included (Marzari et al. 2009), but we have neglected this for simplicity as the magnitude change in the calculated disc eccentricity is small, although this may not be the case when we examine higher disc masses later.

The instantaneous longitude of pericentre can also be calculated for each cell, $\omega_{\rm c}$, and a disc weighted average calculated in a similar manner:

$$\omega_d = \frac{\int_0^{2\pi}\int_{r_{\rm in}}^{r_{\rm out}} \Sigma\omega_{\rm c} r \,{\rm d}r\,{\rm d}\phi}{\int_0^{2\pi}\int_{r_{\rm in}}^{r_{\rm out}} \Sigma r \,{\rm d}r\,{\rm d}\phi}. \tag{3.46}$$

When calculating $\omega_{\rm d}$ we only include the regions of the disc which show non-negligible $e_{\rm c}$ values, following the method of Kley and Haghighipour (2015), neglecting material on circular orbits in the outer disc. A global disc calculation of $\omega_{\rm d}$ shows libration around a small range of angles, whereas it is clear from observing 2-D surface density plots that the eccentric inner disc precession shows circulation. Kley and Haghighipour (2015) also showed that the local calculation agrees well with the position angle of the surface density peak, obtained from 2-D density plots. This peak often lies near the apocentre of the eccentric material forming the cavity wall. This angle is obviously 180° removed from the associated

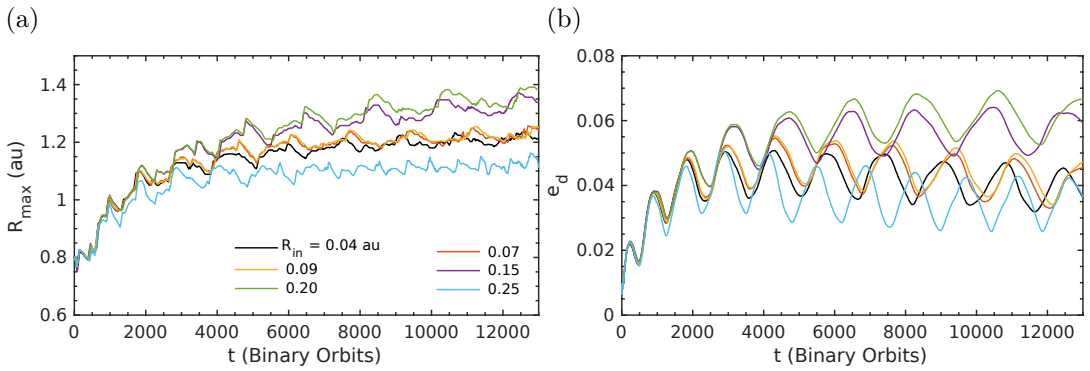

FIGURE 3.6: *(a)* Evolution of $r_{\max}$ with increasing $r_{\rm in}$ in the *Kepler-16* system, showing convergence to the embedded case as the inner radius shrinks. *(b)* Disc-averaged eccentricity evolution of increasing $r_{\rm in}$ boundary condition simulations in the *Kepler-16* system.

pericentre of the material. The radial distribution of cell eccentricity, average disc eccentricity, and the local average disc longitude of pericentre are all useful quantities for probing the instantaneous gas dynamics in the disc, as well as the evolution with time.

3.5.3 Discussion

Examining the results from these runs, we decided to choose $r_{\rm in} = 0.09\,$au as the inner boundary radius for the *Kepler-16* runs presented in the remainder of this article. It provides a speed-up over the completely embedded 0.04 au case, but as can be seen in Figs. 3.5 and 3.6, gives similar results. This corresponds to a disc where the Roche lobe of the lighter companion is always fully embedded in the active disc, and the primary star lies interior to the inner radius of the computational domain. Figure 3.7 shows the surface density distribution around and in the cavity surrounding the central binary once quasi-steady state has been reached. This snapshot was taken when the binary is at closest approach. The Roche lobe of the secondary star is shown in black – clearly embedded in the disc. The white circle represents the area lying interior to the inner boundary of the computational domain. The cross and star symbols represent the positions of the primary and secondary stars, respectively.

Due to the masses of each of the binary stars being equal in the *Kepler-34* and *-35* systems, the outer edge of the Roche lobes (i.e. the L1 Lagrange point) lie

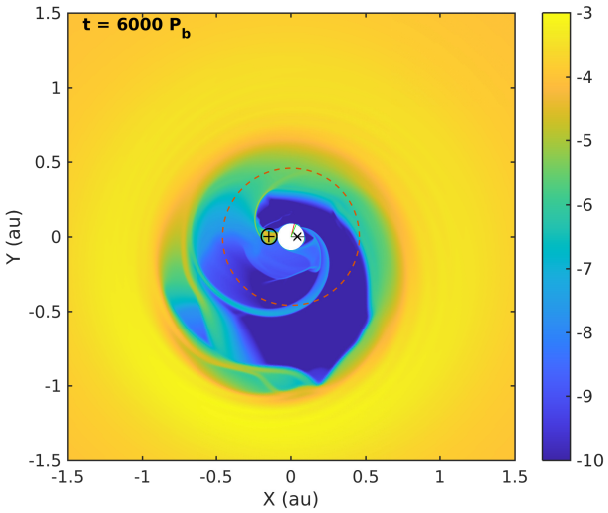

FIGURE 3.7: Log-scale plot of surface density of a *Kepler-16* binary embedded in the $r_{\rm in} = 0.09\,$au disc. Mass flow can be seen across the cavity through so-called streamer channels. This behaviour is not properly resolved by larger inner disc radii.

in close proximity to $r = 0$. It is clear that in this situation, where the binary mass ratio is close to unity, a simulation with its origin at the centre-of-mass cannot also have one star embedded in the disc and the the other sitting interior to the boundary of the computational domain, and the procedure adopted for the *Kepler-16* system cannot be used. Instead, an inner radius is chosen such that $> 70\%$ of the smallest Roche lobe is embedded in the disc at $r_{\rm min}$, corresponding to $r_{\rm in} = 0.04$ and $0.056\,$au for the *Kepler-34* and *-35* systems respectively. These choices for $r_{\rm in}$, and the grid resolution chosen for these simulations, results in cells which are moderately elongated in the azimuthal direction compared to the radial direction. While this is not atypical for simulations of the type presented here, it does introduce truncation errors that are formally not equal in the r and ϕ directions. Even with the binary system partially embedded in the disc an outflow boundary condition is still needed at the inner edge; for all simulations presented from now on the limiting Viscous outflow condition was used. The reasoning behind this decision relies on previous findings that the eccentric cavity inhibits accretion onto the central binary, which the Viscous outflow tries to do, by limiting the rate at which material can exit the disc. Whilst testing this disc set-up, we found that for this reduced inner boundary radius, the difference to disc structure caused by either an Open or Viscous outflow condition was negligible.

We have demonstrated, with a side-by-side comparison of the Closed, Open and Viscous outflow conditions in each system, that a wide range of behaviours can be seen. The lack of agreement for each boundary condition between systems, motivated development of a more realistic treatment of the inner disc. Surprisingly, the limiting Viscous condition, which lies between the Open and Closed behaviour, showed the most erratic results, with no clear relation to the Open or Closed model in any of the systems.

By systematically shrinking the inner boundary from the canonical value of $r_{\rm in} = 1.5a_{\rm b}$ that has been used in previous studies, until the central binary in the *Kepler-16* system is completely embedded in the computational domain and the circumbinary disc, we hoped to find a compromise between increased run-time due to a smaller time-step, and accurate modelling of mass-flow and angular momentum transfer around and onto the binary. The results from this investigation showed that models converged on the fully-embedded case as the inner boundary shrank, with $r_{\rm max}$, the location of the surface density maximum at the outer edge of the tidally cleared cavity, decreasing towards 1.2 au. The explanation as to why an embedded binary should give rise to a different disc structure than a binary–disc system with a larger inner radius is unclear. In Pierens and Nelson (2013) the role of non-linear mode coupling and the 3 : 1 outer Lindblad resonance was discussed with reference to the growth of disc eccentricity around circular and eccentric binaries. In the circular case, when the 3 : 1 outer Lindblad resonance was not contained in the computational domain, disc eccentricity growth was limited. Decreasing the inner disc radius means that a variety of additional resonances are present in the disc. Including these interior resonances may more realistically capture the exchange of angular momentum between the binary and disc, leading to convergence in the size and structure of the tidally truncated cavity which arises as a balance between outward angular flux from the spiral waves excited by the binary and viscous evolution. The smaller cavity size produced by these embedded binary–disc systems is promising for the next stage of our investigation in which we will introduce migrating protoplanets into the evolved self-gravitating discs. As has been previously shown, (Pierens and Nelson 2008a,b, 2013; Kley and Haghighipour 2014, 2015), the inwards migration of these cores is halted near the cavity edge. The larger cavities produced in these past works (using either an inner Closed, Open or Viscous boundary condition, at larger radii) ultimately meant that the final semi-major axes of the planets were larger than their observed *Kepler* counterparts.

The Role of Circumbinary Disc Self-Gravity on Disc Evolution

Chapter Contents

4.1 Introduction

The picture of planet formation and migration in circumbinary systems discussed earlier prompted by the issues discussed in Section 1.3.3 – where planetary cores form in the outer disc, interact with their surroundings to alter their masses and

orbits, and finally reach their observed positions – is an incomplete one. Many details of this process are not understood, just as in the single-star planet formation regime, with the added complication of the dramatic interaction of the disc with the binary. The consequences of this interaction are discussed in Section 1.2.4 in detail. The key-points are:

- the binary exerts a tidal torque on the circumbinary disc creating a central cavity
- the size of the cavity depends on the binary and disc parameters (Artymowicz and Lubow 1994)
- interaction of the binary with this feature lead to an asymmetric, eccentric, precessing disc (Pelupessy and Portegies Zwart 2013; Pierens and Nelson 2013; Kley and Haghighipour 2014).

The proximity of this truncation radius to the critical orbit stability limit of Holman and Wiegert (1999), as well as the observed semi-major axes of circumbinary planets, lead to the conclusion that understanding the processes and physics which shape the circumbinary disc (CBD) is key to explaining and predicting the orbits and properties of the circumbinary planets. Previous works examining the interaction of short-period binaries with their host discs have only investigated a small number of areas of disc physics which could lead to more a realistic picture of the circumbinary environment, and ultimately explain the ever-growing set of observations.

In this chapter we investigate the impact of self-gravity, and by extension disc mass, on the evolution and structure of circumbinary discs around several of the planet-hosting *Kepler* binary systems. Self-gravity has already been examined in low-mass circumbinary discs (Marzari et al. 2009), where it was discounted as an unimportant factor in the disc evolution. However, as pointed out in Lines et al. (2015), even at low-mass, disc self-gravity can modify the precession frequencies associated with low-frequency global eccentricity modes (Papaloizou 2002). The modest influence of self-gravity in circumbinary discs is in contrast to its apparent importance in determining the evolution of circumprimary discs (Marzari et al. 2009). While self-gravity has little impact at low disc mass, its influence becomes apparent at higher mass, modifying the physical size of the tidally truncated cavity and leading to the formation of large scale features in the circumbinary disc (Lines et al. 2015). In this chapter and the next, we investigate the effect of self-gravity

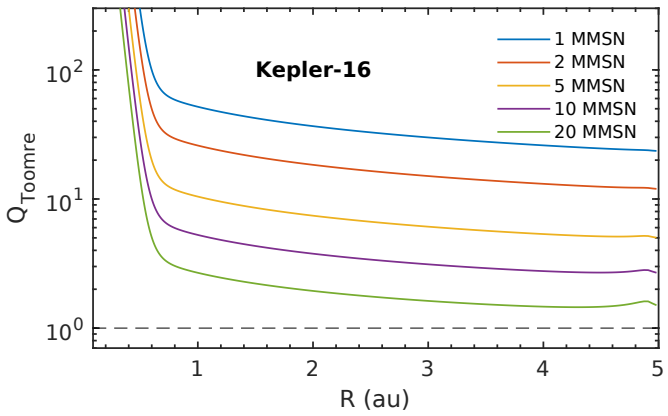

FIGURE 4.1: Radial profiles of the Toomre parameter corresponding to initial conditions in discs with masses corresponding to $1 - 20_{\mathrm{MMSN}}$. We can see that even the most massive discs satisfy the condition $Q > 1$ to remain stable, initially.

over a large range of disc masses and binary systems. The motivation is to probe the early dynamical history of circumbinary discs – as we increase the disc mass we examine earlier and earlier times in the system's history. We aim to address the questions: Does a high-mass disc leave a fingerprint on the planet population if circumbinary planets form early, or is this erased by the transition to a low-mass disc as the system evolves? Does the epoch when planets form, accrete gas, and migrate affect their final orbital configuration or mass? First of all, to answer these questions, we must investigate the behaviour of the discs themselves under the same conditions.

Using the disc set-up relating to an isothermal disc discussed in the previous chapter and the boundary conditions summarised in Tab. 4.1, and motivated by the preceding chapter, a set of runs examining the role of increasing the disc mass on the structure and dynamics of the circumbinary discs in the *Kepler-16, -34,* and *-35* systems was undertaken. As the initial disc mass of the system increases we effectively simulate the circumbinary environment at earlier moments in its lifetime. The disc masses used correspond approximately to scaled-up versions of the Minimum Mass Solar Nebula (MMSN) model; Σ_0 is chosen so that $0.02\,\mathrm{M}_\odot$ is contained interior to 30 au. This 1_{MMSN} model is then scaled by factors of 2, 5, 10, and 20 (refer to Fig. 4.1 for radial profiles of the Toomre parameter in these discs). The three binary systems examined in this work all have different total masses, so we use a Minimum Mass *Stellar* Nebula – where 1_{MMSN} contains 2% of the mass of the central binary, $\mathrm{M}_\star$.

TABLE 4.1: Inner and outer boundary conditions

	Kepler-16	*Kepler-34*	*Kepler-35*
$r_{\rm in}$ (au)	0.090	0.040	0.056
$r_{\rm in}$ BC		Viscous	
$r_{\rm out}$ (au)		5.0	
$r_{\rm out}$ BC		Open	

These initial conditions, with Σ_0 in Eq. (3.9) set to a value corresponding to a $1 \times$ MMSN disc, lead to a minimum Toomre parameter value of ≈ 25 at the outer edge of the disc (see Fig. 4.1). It is worth noting that the rotation profile in evolved circumbinary discs is non-Keplerian. Therefore whilst calculating the Toomre parameter, the assumption that the epicyclic frequency, κ, is equal to the orbital frequency in the disc, Ω, cannot be used. A more general formulation of the epicyclic frequency is used:

$$\kappa^2 \equiv \frac{2\Omega}{r}\frac{d}{dr}\left(r^2\Omega\right). \tag{4.1}$$

The Toomre parameter at the inner edge of the disc is very high due to the low surface densities enforced by the gap function in Eq. (3.9). This value of $Q > 1$ allows us to safely assume that this disc will be stable against gravitational fragmentation. For higher values of $\mathcal{X}$ this minimum value of Q decreases, as the disc mass increases. In the most massive model, corresponding to a 20 MMSN disc, $Q \approx 1.5$ at the outer radius.

We present each binary system in turn in our discussion of results below, whilst also splitting each set of runs into two disc families – Low-mass ($1_{\rm MMSN}$, $2_{\rm MMSN}$ and $5_{\rm MMSN}$) and High-mass ($10_{\rm MMSN}$ and $20_{\rm MMSN}$) discs. After presenting the outcomes of these numerous runs we explore the mechanisms which could explain our results, and discuss their implications for future work.

4.2 *Kepler-16* Results

4.2.1 Low-Mass Discs

In the *Kepler-16* system increasing the disc mass from a canonical $1_{\rm MMSN}$ model to an intermediate disc mass corresponding to $5_{\rm MMSN}$, makes little difference to

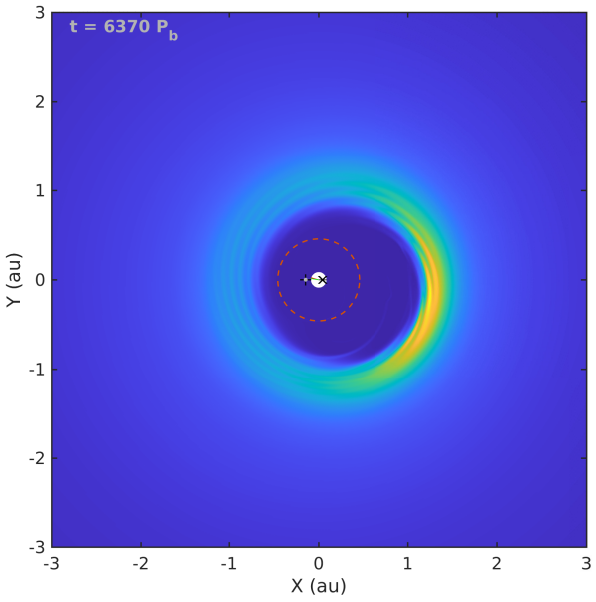

FIGURE 4.2: Surface density map of the *Kepler-16* 1_{MMSN} system at pseudo-steady-state. The characteristic eccentric inner cavity is clear, with an edge at ≈ 1.2 au, in good agreement with previous non-SG results.

the disc evolution or final disc structure. The low-mass discs show no departure from the non-SG $r_{\mathrm{in}} = 0.09$ au disc seen in the previous section. The pseudo-steady-state cavity size observed agrees well with the Pierens and Nelson (2013) results. A representative surface density map of the low-mass disc results, once they have reached steady-state, can be seen in Fig. 4.2.

The blue, red and yellow lines in Fig. 4.3 correspond to the 1, 2, and 5_{MMSN} models respectively. In Fig. 4.3a the surface density distributions have been scaled by their inverse disc mass so their overall shape can be compared. Beyond small changes in the relative peak value, the position and size of the disc cavity is nearly identical, reaching around 1.25 au at equilibrium. The evolution of the cavity size is similar between these three models – Fig. 4.3c. Increasing the disc mass has no effect on the rate at which the eccentric cavity grows in size as the simulations progress, with all models reaching a pseudo-steady state after $\approx 4000\, P_{\mathrm{b}}$.

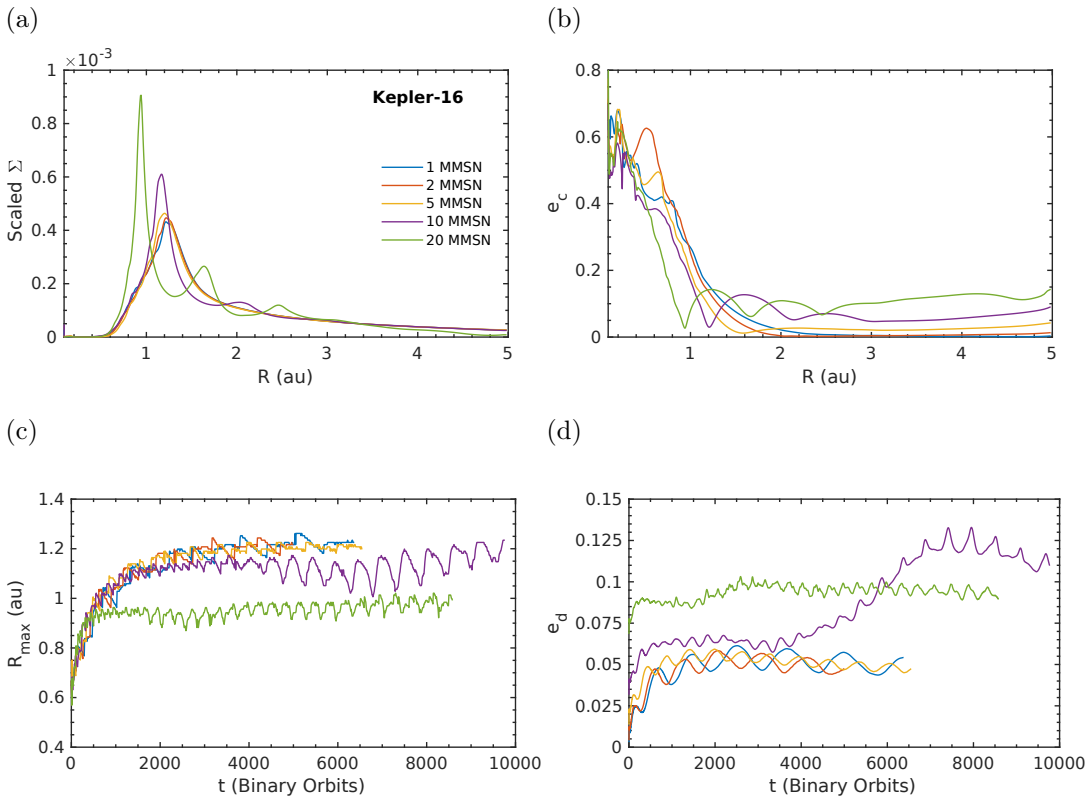

FIGURE 4.3: Disc structure and dynamics results at pseudo-steady-state, after 5000 P_b, in the *Kepler-16* system. *(a)* Scaled surface density distribution. *(b)* Azimuthally-averaged cell eccentricity. *(c)* Evolution of peak surface density position. *(d)* Evolution of disc-integrated eccentricity.

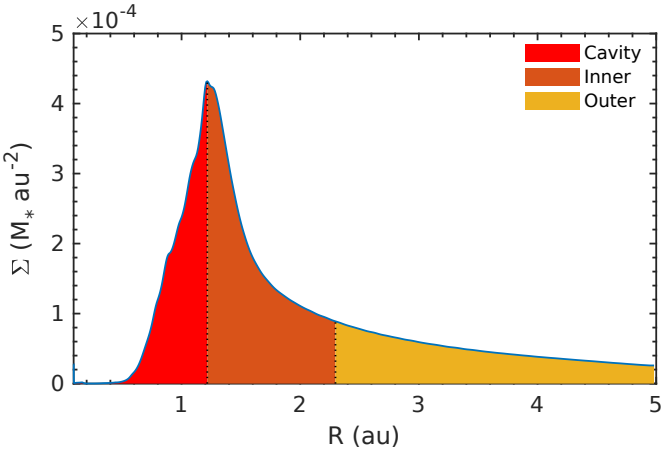

FIGURE 4.4: Surface density distribution with the cavity, inner and outer radial disc regions colour-coded. The cavity region, where the surface density gradient is positive is easiest to identify visually. The inner disc transitions to the outer disc when the average cell eccentricity drops below 0.01.

The discs in these models can be separated into three regions in radius (see Fig. 4.4):

- cavity – where material is evacuated or the density gradient is positive because of the dominant influence of the binary
- inner disc – where the density gradient is negative, but eccentricity is excited
- outer disc – where eccentricity is negligible, and the disc resembles that of a single-star case.

We note that the rise in eccentricity in this outer region as the disc mass increases is largely an artefact of not including the disc self-gravity in the calculation of the eccentricity. In the low-mass regime the cavity is dominated by the binary's influence, but the increasing strength of the disc's self-gravity leads to a slightly more tightly-bound cavity. The self-gravity acts to compact the system, shrinking the characteristic scale slightly compared to the non-SG case. It is noticeable in Fig. 4.3b that the inner region where the eccentricity is excited reduces as disc mass grows. The disc dynamics, traced by the eccentricity gradient, seem to be more sensitive to increasing disc self-gravity than the disc density structure.

Using the last panel in Fig. 4.3 we note several features. The global disc eccentricity growth rate is slightly faster as the disc mass increases, with all the low-mass discs reaching peak e_d ($\approx 0.05 \approx h$) at similar times. The oscillation of the disc eccentricity reaches lower amplitudes and shorter periods as the disc mass increases, caused by the circulation of the discs' longitude of pericentre relative to the binary's. The accelerations arising from self-gravity force faster circulation as the disc gravity increases the precession rate, but drive smaller amplitude oscillations in the eccentricity.

Figure 4.5 shows the ω_d evolution in the *Kepler-16* self-gravitating discs. We include a comparison of the local *vs.* global calculation (discussed in Section 3.5.2) – as well as with the maximum surface density position angle. Our results agree with those from both Pierens and Nelson (2013) and Kley and Haghighipour (2015), where the global calculation gives a near constant value of ω_d, but the local calculation and the maximum position angle show circulation. Comparing the evolution of ω_d in the low-mass discs, we observe the same trend as we saw in the oscillatory nature of e_d. As the disc mass increases, the periods for both the precession of ω_d, and the oscillations in e_d decrease by nearly a factor of 2, from 1200 to 700 P_b. As the forcing from the binary is not increasing, nor is there any additional component from the pressure forces in the disc, this increase in

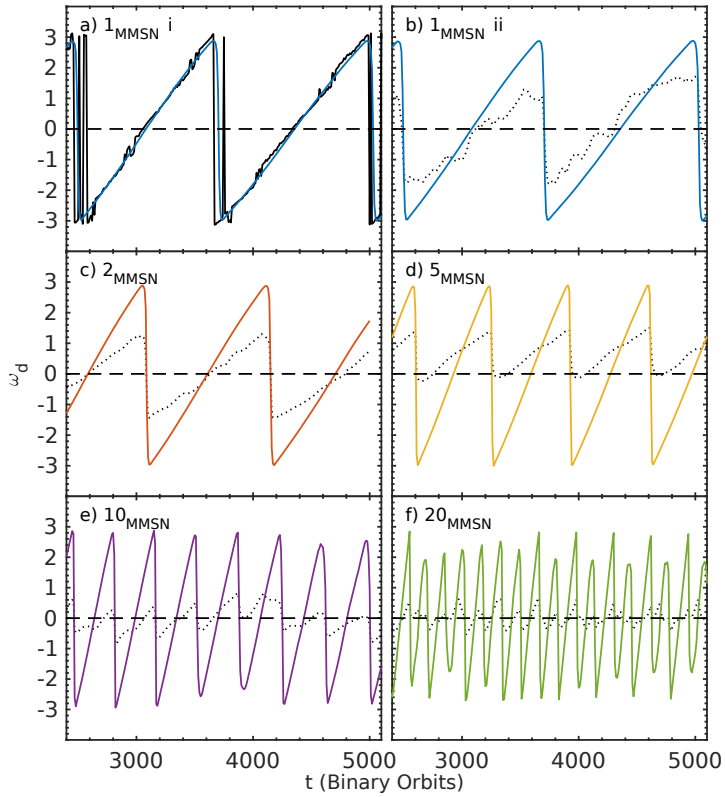

FIGURE 4.5: Snapshots of ω_d evolution in the *Kepler-16* low- and high-mass discs. Panel *(a)* shows the position angle of the surface density maxima ($+\pi$) in black, over-plotted with the local calculation of ω_d . Panels *(b)–(f)* show the local calculation of ω_d compared to the global calculation (black-dotted line), in the 1–20$_{\rm MMSN}$ discs.

frequency must be due to the increasing strength of the disc self-gravity. This difference in precession frequency is the clearest impact of self-gravity on disc evolution for low-mass discs in low binary eccentricity, *Kepler-16* type systems.

4.2.2 High-Mass Discs

Whilst low-mass discs show little variation as we move from 1 to 5$_{\rm MMSN}$, it is clear from Fig. 4.3 that increasing the disc mass to 10$_{\rm MMSN}$, and beyond, leads to dramatic modifications in disc structure, dynamics and evolution compared to the low-mass discs. Some of these changes are shared across high-mass disc models in all the *Kepler* systems, suggesting that they are caused predominantly by the disc self-gravity, with the binary properties having little impact.

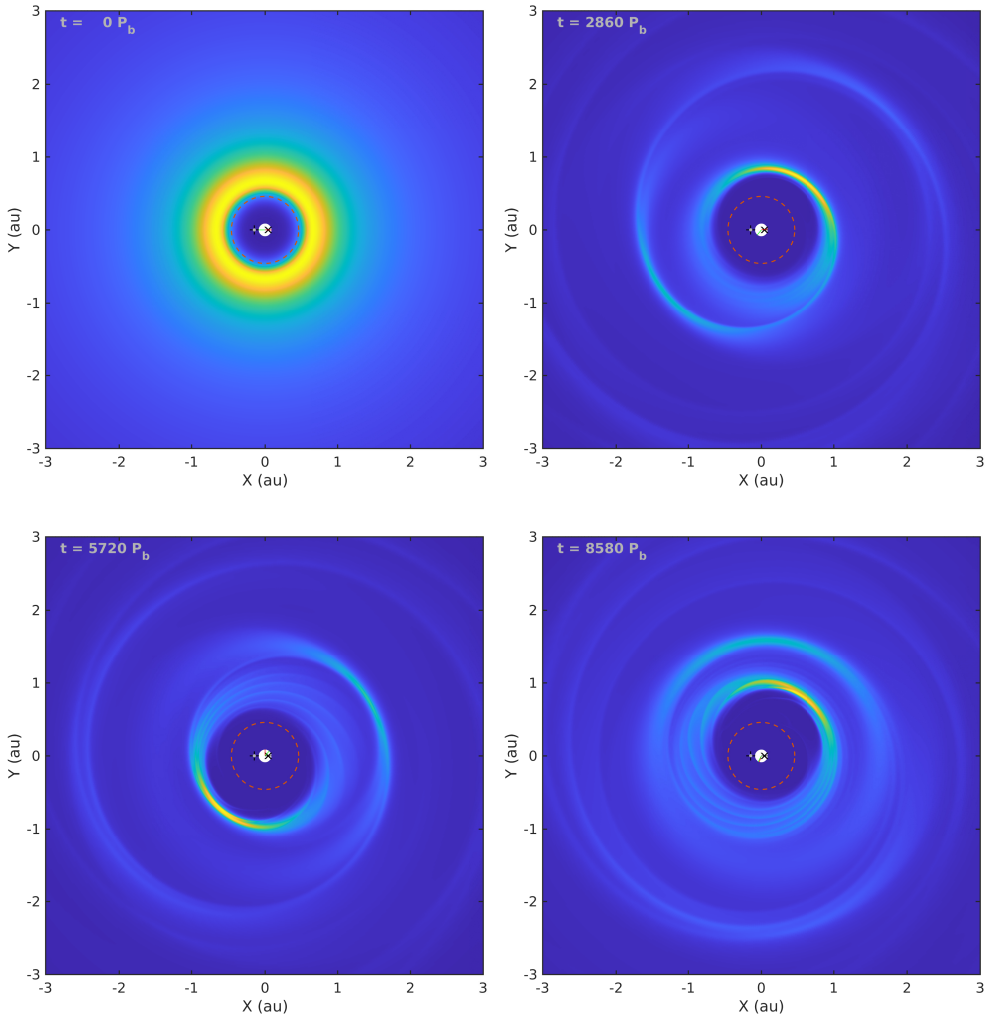

FIGURE 4.6: Surface density maps showing evolution of highly self-gravitating discs in the *Kepler-16* 20_{MMSN} system. The birth and evolution of a series of nested eccentric rings and spirals can be seen.

Doubling the disc mass from 5_{MMSN} to 10_{MMSN} in the *Kepler-16* system, brings us into a regime where the strength of the disc's self-gravity can start to significantly alter the disc structure seen in the low-mass discs. Referring to the purple line in Fig. 4.3a we see an enhancement in the relative peak surface density, as well as a decrease in r_{max}. The surface density falls away sharply exterior to this peak, reaching a minimum at ≈ 1.65 au, only to rise to a second peak at 2 au. Beyond this point the disc relaxes back to the background profile seen in the low-mass discs. The disc structure is modified even further in the 20_{MMSN} disc (green line in Fig. 4.3a), with the relative peak surface density obtaining a value twice that seen in the low-mass discs, and moving interior to 1 au. In the exterior of the

disc, a series of two further surface density maxima can be seen, at 1.6 and 2.5 au. These objects are maintained by disc self-gravity, overcoming the opposing influences of the gas's pressure and viscosity. The variation in surface density caused by these features is clear when examining the 2-D surface density maps of the disc. Figure 4.6 shows the evolution of the disc in the 20_{MMSN} model. The maxima observed are associated with a series of nested eccentric features which at times resemble eccentric rings, similar in form to the material bounding the inner cavity, and at other times resemble a large scale $m = 1$ spiral wave. It is also clear in these plots that the inner cavity, although eccentric, has not expanded significantly in size since the disc was initialised. In this model the strength of the self-gravity in the disc results in a significantly more compact disc cavity region.

These structures can also be seen in the discs' eccentricity profiles (Fig. 4.3b). The 10_{MMSN} and 20_{MMSN} models have similar eccentricity values in the binary-dominated cavity – only in a smaller region – with eccentricity minima and maxima in the outer disc. The eccentricity in the outer disc is excited above the non-negligible values common to the low-mass discs, with $e_{\mathrm{c}} \approx 0.1$. The peaks in surface density seen in Fig. 4.3a correspond to minima in the e_{c} profile, with maxima on either side. These surface density peaks are obviously associated with further eccentric structures in the disc, exterior to the eccentric inner cavity.

The extra sources of e_{c} are evident as raised values in the evolution and final value of global e_{d}. Figure 4.3d shows more complex behaviour for the evolution of e_{d} than in the low-mass cases. At early times the 10_{MMSN} model shows oscillatory behaviour around e_{d} similar to the low-mass discs. The slightly higher value is due to the raised e_{c} in the outer disc. At $t = 3000\,P_{\mathrm{b}}$, once the inner cavity has fully developed, e_{d} starts to increase, reaching a peak value around 0.13, and saturating at a final value close to 0.12. The growth of e_{d} is due to the creation of the additional eccentric features seen in Figs. 4.3a, 4.3b and 4.6. The 20_{MMSN} model starts with initial $e_{\mathrm{d}} \approx 0.08$, due to the contribution of self-gravity to the dynamics not accounted for in the calculation of disc eccentricity. The disc eccentricity is in a pseudo-steady state until $t = 1000\,P_{\mathrm{b}}$ when e_{d} increases for a further $2000\,P_{\mathrm{b}}$ until it saturates at 0.1. Strong self-gravity in the 20_{MMSN} disc explains the earlier onset of the second phase of e_{d} growth. The overall smaller value of e_{d} versus that in the 10_{MMSN} model can be explained by the fact that the inner cavity has a much smaller radial extent – the material beyond 1 au, with $e_{\mathrm{c}} \approx 0.1$ makes up a large proportion of the disc, containing much of the mass in

the disc, and so dominates $e_{\rm d}$.

The very short-term oscillations in $e_{\rm d}$ are caused by the circulation of the disc around the binary's fixed longitude of pericentre. The period of these oscillations is the same as the period taken for the inner cavity to circulate a full 2π radians. With this evidence we would predict that the high-mass discs follow the trend seen in the low-mass discs – with the period decreasing as disc mass increases. Examining panels *e* and *f* in Fig. 4.5, we see this is basically true. These more massive discs don't show perfect circulation, but instead show evidence of libration. Remember that the local calculation of $\omega_{\rm d}$ only includes material up to $\Sigma_{\rm max}$ in the azimuthally-averaged profile. Therefore the gas associated with the additional structures seen in these discs is not directly affecting $\omega_{\rm d}$. It is possible for these features to interact with the cavity-bounding material – through self-gravity – disrupting its circulation. This, as well as the non-constant extent of libration, suggests that the features in the outer disc have their own associated precession period, independent of the inner disc, which we discuss later in this chapter.

4.3 *Kepler-34* Results

4.3.1 Low-Mass Discs

The low-mass discs in the *Kepler-34* analogue systems show the most variation across all the low-mass models in the three systems investigated here. The $5_{\rm MMSN}$ disc around this highly eccentric binary departs from the behaviour observed in the $1_{\rm MMSN}$ and $2_{\rm MMSN}$ discs. As mentioned previously, the *Kepler-34* system produces a very eccentric and extended disc cavity, extending out to ≈ 2.3 au in the 1 and $2_{\rm MMSN}$ models – slightly larger than the *Kepler-34* results shown in Pierens and Nelson (2013), Kley and Haghighipour (2015) and Lines et al. (2015). In Fig. 4.7a the yellow line, corresponding to the $5_{\rm MMSN}$ model, shows a smaller cavity size ($r_{\rm max} = 2.0$) and higher relative $\Sigma_{\rm max}$, by a factor of 1.25. This is behaviour we are observing for the first time, i.e. this behaviour was not seen in the *Kepler-34* self-gravitating discs in Lines et al. (2015); however this could be due to the different treatment of the inner boundary. The eccentricity distribution in the $5_{\rm MMSN}$ case shows material on highly excited orbits in the cavity itself, with a dramatic drop-off in $e_{\rm c}$ as we move outwards in the disc. The disc self-gravity

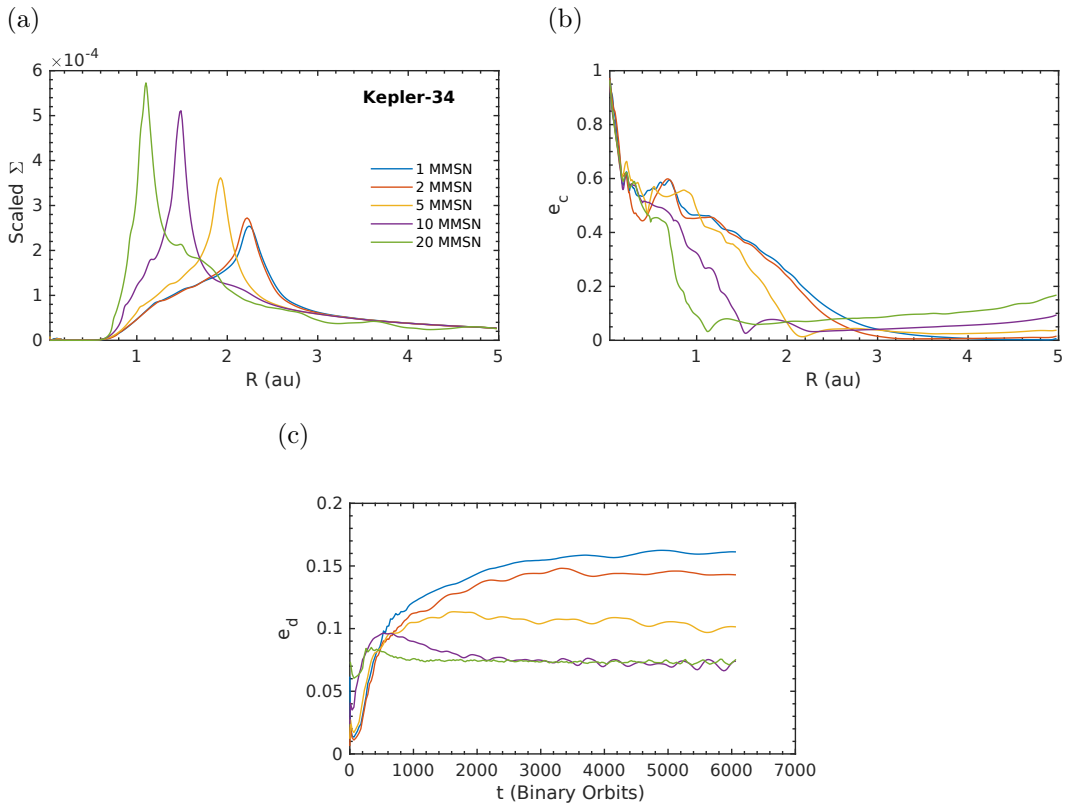

FIGURE 4.7: Disc structure and dynamics results at pseudo-steady-state, after 6000 $P_{\rm b}$, in the *Kepler-34* system. *(a)* Surface Density distribution. *(b)* Azimuthally-averaged cell eccentricity. *(c)* Evolution of disc-integrated eccentricity.

leads to a more radially confined eccentric cavity. The influence of the binary beyond ≈ 1.5 au appears to be small.

The $1_{\rm MMSN}$ and $2_{\rm MMSN}$ discs are very similar, with the doubling of mass having little effect on the structure or evolution. The final values of $e_{\rm d}$ in the $1_{\rm MMSN}$ and $2_{\rm MMSN}$ models reach values of ≈ 0.15, higher than the value found in Pierens and Nelson (2013) for similar disc parameters. These values are predictably higher than the *Kepler-16* models of the same mass, due to *Kepler-34*'s higher binary eccentricity. The $5_{\rm MMSN}$ disc reaches $e_{\rm d} = 0.1$ at equilibrium, due to the smaller values of $e_{\rm c}$ between 2 and 3 au, and the smaller radial extent of the cavity. Increasing the disc mass, and consequently the strength of self-gravity, acts to decrease the radial scale of the disc system, as observed for the *Kepler-16* analogue system discussed above. The general results from these low-mass discs further corroborate previous findings suggesting that the final, saturated value of $e_{\rm d}$ – as well as the cavity size – are strongly dependent on binary eccentricity, and not

mass ratio.

The discrepancy seen in $e_{\rm d}$ in Fig. 4.7c between the $1_{\rm MMSN}$ and $2_{\rm MMSN}$ models suggests that small changes in the calculated $e_{\rm c}$ distribution in the outer disc can make a significant difference to the global value of disc eccentricity, since this is where most of the mass is contained. Perhaps, to discount the region of the disc where little interaction with the binary occurs, a local calculation of $e_{\rm d}$ may highlight the evolution of the eccentric inner disc more accurately. There is little evidence of oscillations in the evolution of $e_{\rm d}$ for any of these low-mass discs, except for a very long period, low amplitude trend in the $5_{\rm MMSN}$ case. As we discussed in our *Kepler-16* results, the oscillations in the evolution of $e_{\rm d}$ are caused by interaction with the precessing eccentric cavity feature with that of the fixed longitude of pericentre of the binary. The highly eccentric, extended cavity in these discs means that the precession period is orders of magnitude greater than the period of the binary. Therefore pericentre alignment occurs so infrequently that the effect on the eccentricity of the disc is negligible. We start to see the impact of a shrinking eccentric cavity on the eccentricity oscillations in the $5_{\rm MMSN}$ results.

4.3.2 High-Mass Discs

The *Kepler-34* high-mass discs continue the trend seen in the low-mass discs. As we move to the $10_{\rm MMSN}$ model, the influence of the self-gravity causes $r_{\rm max}$ to reduce quite dramatically to 1.5 au – significantly smaller than the non-SG results from Pierens and Nelson (2013) and Lines et al. (2015) – and a value of 1.1 au in the $20_{\rm MMSN}$ disc. These results are promising for the introduction of an interacting planetary core in the next Chapter, as these locations are close to the observed orbital location of *Kepler-34 b* ($a_{\rm p}$= 1.1 au). The surface density distributions (Fig. 4.7a) are much smoother than those seen in the *Kepler-16* high-mass discs (Fig. 4.3a). Whilst there are no sharp peaks, there is evidence of less dramatic bumps in the profiles; the same features seen in *Kepler-16* are spread out over a wider radial area.

In Fig. 4.8 we present 2-D surface density maps for the evolution of the *Kepler-34* $20_{\rm MMSN}$ disc, in the same format as the previous grid for *Kepler-16*. Significant modification to the outer disc beyond the eccentric inner cavity can be seen. The washed-out bumps seen in Fig. 4.7a are also clear in this figure. The eccentric

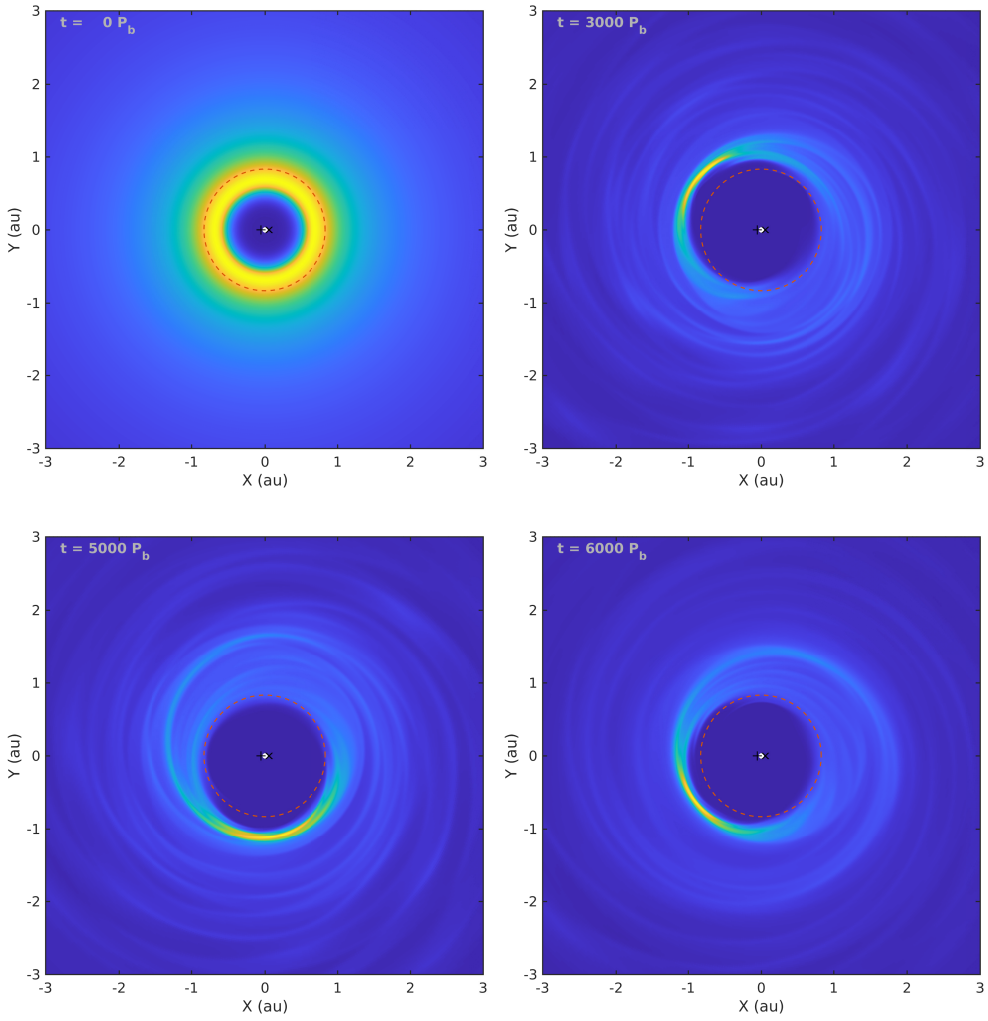

FIGURE 4.8: Surface density maps showing evolution of highly self-gravitating discs in the *Kepler-34* 20_{MMSN} system. Compared to the same model in the *Kepler-16* system, the additional features seen here are not as clearly defined.

rings described previously for the *Kepler-16* 10 and 20_{MMSN} models look more like a series of interacting spiral-arms in the *Kepler-34* system, but nonetheless the development of an eccentric ring feature with an $m = 1$ non-axisymmetric surface density enhancement can be observed.

An examination of the Toomre parameter profiles (Fig. 4.9) in these evolved massive discs reveals values very close to 1 in the high density features. Unsurprisingly the minima in Q correspond to regions of surface density maxima in the disc – the high densities seen at the apocentres of the eccentric rings in the disc give

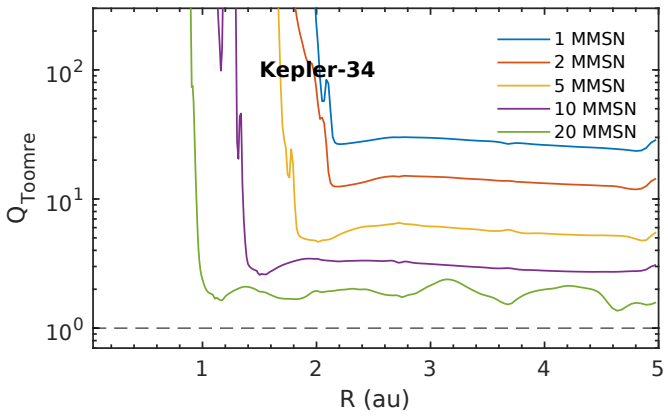

FIGURE 4.9: Radial profiles of the Toomre parameter corresponding to evolved disc conditions in the *Kepler-34* system, with masses corresponding to 1–20$_{\rm MMSN}$. Whilst the low-mass discs retain Q values > 1, the high-mass discs show regions where $Q \approx 1$.

rise to small values of the Toomre parameter. Although the Toomre Q value approaches unity, it is worth noting that we see no evidence of disc fragmentation in these massive discs. We suspect that further increases in disc mass may, however, lead to disc fragmentation, as we do see signs of low amplitude spiral wave structure developing early in the simulations associated with the disc response to self-gravity for the most massive discs.

The evolution of $e_{\rm d}$ is also different in this system (see Fig. 4.7c) compared to the same discs in the *Kepler-16* system. Both the 10$_{\rm MMSN}$ and 20$_{\rm MMSN}$ discs go through a short period of growth – although this is very short in the most massive disc ($200\,P_{\rm b}$) – followed by $1000\,P_{\rm b}$ of slow decline. Both discs then settle into a final value of $e_{\rm d} = 0.07$ – smaller than the low-mass discs. Examining the radial profiles of $e_{\rm c}$ in Fig. 4.7b, we see the shrinking of the eccentric cavity caused by the compaction associated with the more massive discs. There seems to be a delicate balance between the decrease of eccentric material in the cavity and inner disc of the 20$_{\rm MMSN}$ model, with an increase of more eccentric material in the outer, compared to the 10$_{\rm MMSN}$ which results in both discs obtaining the same value of $e_{\rm d}$.

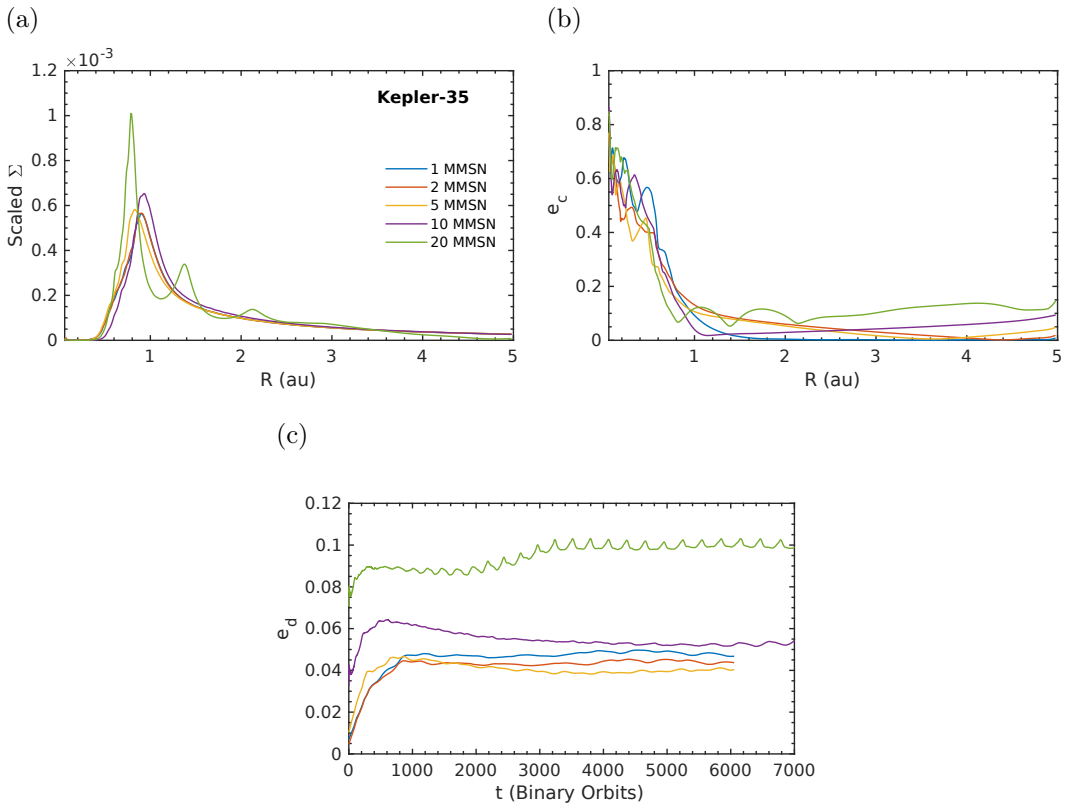

FIGURE 4.10: Disc Structure and Dynamics results at pseudo-steady-state, after 6000 P_b, in the *Kepler-35* system. *(a)* Surface Density distribution. *(b)* Azimuthally-averaged cell eccentricity. *(c)* Evolution of disc-integrated eccentricity.

4.4 *Kepler-35* Results

4.4.1 Low-Mass Discs

Kepler-35 AB has a similar eccentricity to *Kepler-16*, but a mass ratio comparable to *Kepler-34*, so we would expect disc structure and evolution to be close to those seen in the *Kepler-16* discs, as Artymowicz and Lubow (1994) found that the cavity size has a strong dependence on e_b, with only a weak dependence on the mass ratio. This seems to be the case when we examine the surface density and e_c profiles in Figs. 4.10a and 4.10b. The smaller e_b and a_b lead to a smaller cavity, with Σ_{max} lying interior to 1 au. The e_c profile mirrors this structure, with the eccentric inner region confined to within 1 au, and negligible differences in eccentricity gradient between the two binary systems. The surface density and e_c profiles are in good agreement with those seen for the results from Pierens and

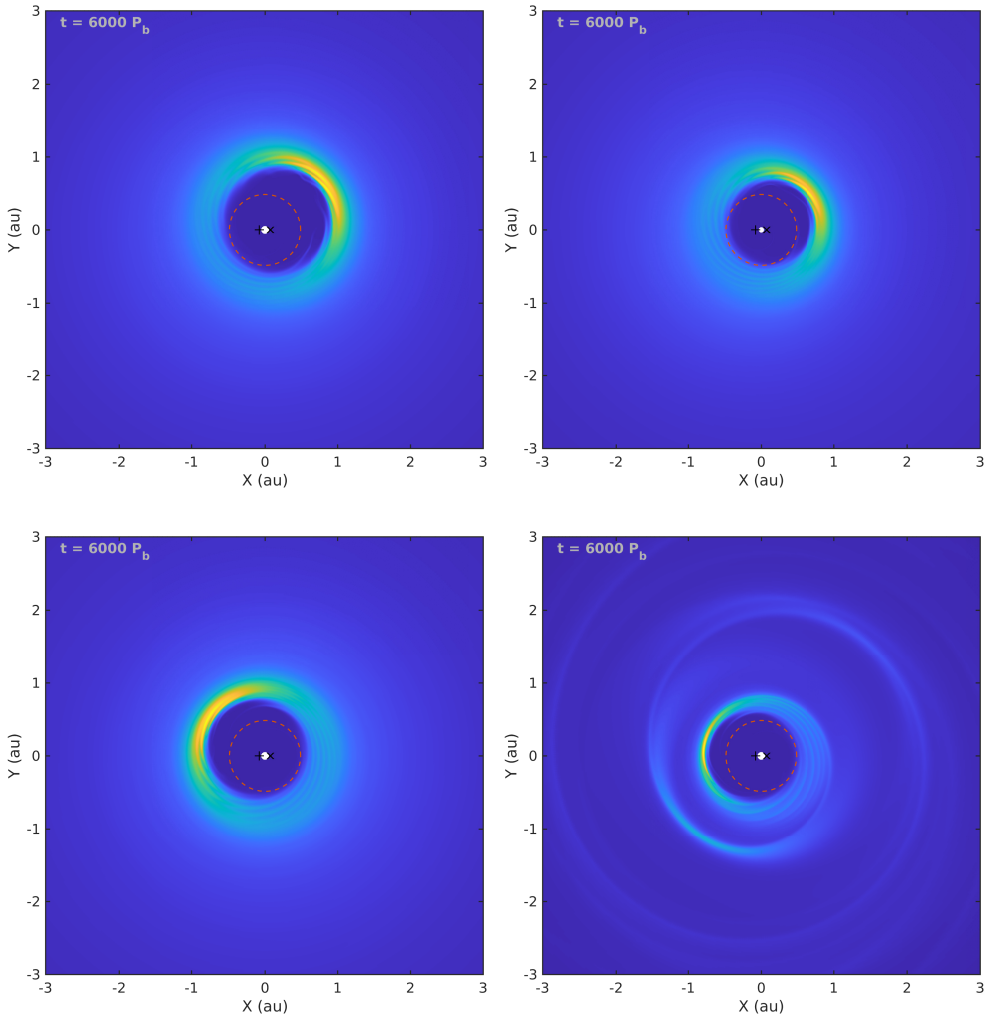

FIGURE 4.11: Surface density plots of self-gravitating discs in the *Kepler-35* system. A tight inner cavity can be seen in the low-mass 1_{MMSN} (top-left) and 5_{MMSN} (top-right) discs, as well as the high-mass 10_{MMSN} (bottom-left) model. The nested eccentric rings seen in the *Kepler-16* 10_{MMSN} and 20_{MMSN}, and *Kepler-34* 20_{MMSN} models can be seen in the highest mass, 20_{MMSN} model in this system.

Nelson (2013) with similar disc parameters. The first two panels in Fig. 4.11 show surface density plots in the 1_{MMSN} and 5_{MMSN} models at steady-state. These plots highlight the similarity in cavity size and disc structure found in the low-mass models in low-eccentricity binary systems.

The evolution of e_{d} shows no evidence of periodic oscillations, although the sampling frequency could hide finer oscillations. This lack of oscillatory behaviour seems to be the norm in the close-to-unity mass ratio binaries (i.e. *Kepler-34* and *-35*). This may be explained by the symmetry of the binary orbit – the central

stars are similar distances from the binary's centre of mass at both closest and furthest approach due to the low eccentricity, and equal masses of the component stars. The inner eccentric disc does not get periodically disturbed to a similar degree as in the lower mass-ratio *Kepler-16* binary, where circulation of the eccentric disc causes periodic apsidal alignment and misalignment between the binary and disc. Finally, examining Fig. 4.10c, we see that these low-mass discs reach similar $e_{\rm d}$ values as the *Kepler-16* models, as well as those seen in Pierens and Nelson (2013).

4.4.2 High-Mass Discs

The last set of simulations from our systematic investigation into the role of disc mass and self-gravity in the *Kepler* circumbinary systems are the high-mass discs in *Kepler-35*. Interestingly the peak surface density position in these discs is similar to those found in the low-mass regime – a finding not duplicated in the other systems – with all the peaks lying close to 1 au. Nonetheless, the trend of having a smaller more compact inner cavity for a more massive disc is reproduced in this system, albeit less dramatically than for *Kepler-16* and *-34*.

Further eccentric rings beyond 1 au are not excited in the $10_{\rm MMSN}$ model as Figs. 4.10a and 4.11c shows, although we cannot discount the possibility that they may arise on longer time scales than we have simulated for this system. There is also no evidence of further excited eccentric features in the $e_{\rm c}$ profile found in Fig. 4.10b, or in the evolution of $e_{\rm d}$ (Fig. 4.10c).

Examining the most massive $20_{\rm MMSN}$ disc, we see the appearance of the additional well-defined freely precessing eccentric ring features also found in *Kepler-16*. The self-gravity in this disc is strong enough for two further eccentric rings to be excited exterior to the inner cavity. This process occurs around $2000\,P_{\rm b}$ in the disc's evolution, as this is when we observe the $e_{\rm d}$ of the system start to increase. After a further $1000\,P_{\rm b}$ the disc has reached a pseudo-steady equilibrium $e_{\rm d} = 0.1$. This evolution and final value is similar to *Kepler-16*, despite this model having a much smaller eccentric inner cavity.

The respective lack, and presence, of eccentric features in the $10_{\rm MMSN}$, and $20_{\rm MMSN}$, models is shown in the last two panels of Fig. 4.11. The similarity of the $10_{\rm MMSN}$ case to the 1–$5_{\rm MMSN}$ models is clear, whereas the most massive disc shows the eccentric features found to be a common feature across these self-gravitating discs.

4.5 Origin of Eccentric Disc Features

In this section we investigate the origin of the additional eccentric rings in the most massive circumbinary discs presented above. We consider two contending ideas: (i) That secular gravitational interaction between the eccentric inner disc at the tidally cleared cavity edge and the outer disc leads to the excitation of an additional eccentric ring if the local precession frequencies in the disc are able to match (i.e. the additional eccentric feature results from a secular resonance in the self-gravitating disc); (ii) That the binary potential itself is responsible for the growth of the additional eccentric features, possibly through non-linear mode coupling similar to that occurring at the 3 : 1 resonance as examined by Papaloizou et al. (2001) and Pierens and Nelson (2013) in non-self-gravitating discs, but occurring over larger radial length scales in the self-gravitating discs; possibly due to changes in the epicyclic frequencies shifting the resonances outwards.

When considering scenario (i), we undertook an analysis of the rings' precession. By finding the surface density maxima in the azimuthally-averaged surface density profile, and isolating material in narrowly-defined annuli around these radial positions, we were able to obtain rough estimates of the individual precession periods of each eccentric ring. In the *Kepler-16* system, 10_{MMSN} disc, the inner eccentric cavity precesses with a period $= 420\,P_{\mathrm{b}}$. The first outer eccentric ring has a precession period almost 6 times greater, at $2440\,P_{\mathrm{b}}$. The second (and last) outer eccentric feature in this disc also has this same larger precession period, and for each system where two additional eccentric features arise we find that they precess at the same rate as each other. Undertaking this analysis for the more massive 20_{MMSN} discs in the *Kepler-16* and *-35* systems, which also show clearly defined outer eccentric rings, we see a similar pattern of behaviour. As we have already observed, the inner eccentric feature precesses rapidly in these discs – $170\,P_{\mathrm{b}}$ and $180\,P_{\mathrm{b}}$ in the *Kepler-16* and *-35* systems respectively. The first and second outer eccentric rings precess with a period almost exactly 2 times greater than the inner feature in the *Kepler-16* system, with both features having a precession period $\approx 340\,P_{\mathrm{b}}$. The outer rings' precession period in the *Kepler-35* system lies just outside this commensurability at $440\,P_{\mathrm{b}}$.

As these outer rings and the inner eccentric cavity precess with their own frequency, they interact with each other. This interaction can be seen in Fig. 4.12 – when the rings are aligned in the same quadrant of the disc they act to diminish

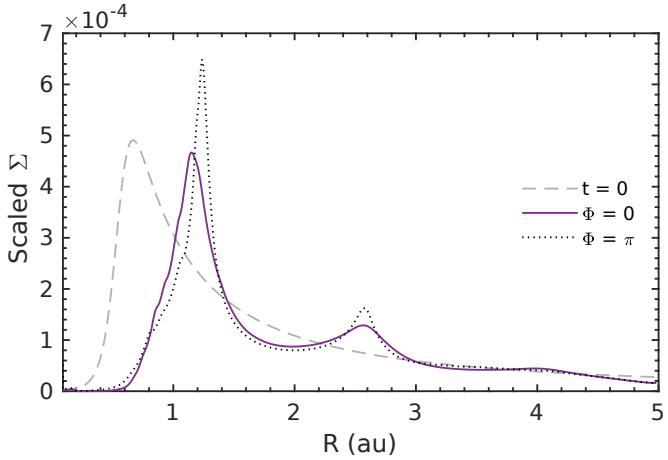

FIGURE 4.12: Interaction between two precessing eccentric rings through self-gravity. The purple profile is taken when the Longitudes of Pericentre of each ring are aligned and black when they are anti-aligned – or separated by π radians.

each other, resulting in reduced surface density maxima, and vice-versa when they are anti-aligned (or in opposite disc quadrants). The interaction between these freely precessing rings also seems to interfere with the circulation of the inner cavity, see panels e and f of Fig. 4.5. The disparity between the precession frequencies of the various eccentric modes in the discs clearly casts doubt on the idea that the additional eccentric features arise because of secular forcing by the inner eccentric disc, although there does seem to be a commensurate relation between the precession periods of the two outer additional eccentric features in discs where two of these arise.

The second approach to explain these intriguing features focused on the explicit interaction between the binary and disc. As discussed earlier in the paper, the eccentricity of the inner cavity is driven by non-linear mode coupling between an initial $m = 1$ eccentric mode present in the disc and the $m = 1$ component of the binary potential, leading to a forcing term in the disc that excites an $m = 2$ wave at the 3 : 1 Lindblad resonance whose outward propagation removes angular momentum from the disc material there. Pierens and Nelson (2013) also indicated that for an eccentric binary, additional higher-order binary potential components may also play a role. The question is whether or not the additional eccentric features also require direct coupling between the disc and the binary potential.

In the additional set of simulations we first use a disc set-up identical to those used in the *Kepler-16* 10_{MMSN} SG runs presented above, except with a larger

inner boundary radius to speed up the computations – as we are more interested with behaviour in the outer disc, and not an accurate description of the inner disc. The only other difference is that we modify the potential created by the central stars which the disc elements see at different radial locations throughout the disc. In the first case we transition from an inner region where the disc sees a potential created by the two binary stars, to an outer region where the disc sees a potential created by a central single star with the combined mass of the binary, with the cross-over occurring through a transition region of finite width. A second case, where we transition from a single- to binary-dominated potential moving out in the disc, was also computed.

We use a simple switch function from McNeil and Nelson (2009) of the form, $f(x) = 3x^2 - 2x^3$ which transitions smoothly and continuously from $f(x = 0) = 0$ to $f(x = 1) = 1$. We set the scaling factor $x = \frac{r-R_0}{R_1-R_0}$, where r is the radial location in the disc, and R_0 and R_1 are the inner and outer limits of the transition region respectively. To ensure we have an outer region sufficiently isolated from the influence of the binary potential we set $R_0 = 1$ and $R_1 = 2$ au.

We define two weighting coefficients which take the following values throughout the disc:

$$W_{\rm binary}(r) = \begin{cases} 1 & \text{for } r < R_0 \\ 0 & \text{for } r > R_1 \\ 1 - f(x) & \text{for } R_0 \leqslant r \leqslant R_1, \end{cases}$$
$$W_{\rm single}(r) = \begin{cases} 0 & \text{for } r < R_0 \\ 1 & \text{for } r > R_1 \\ f(x) & \text{for } R_0 \leqslant r \leqslant R_1. \end{cases} \tag{4.2}$$

In the second case, where the single-star potential dominates in the inner disc, $W_{\rm binary}$ takes the values of $W_{\rm single}$ from the first case and vice-versa. Using the above prescription the first term in Eq. (3.4) is replaced with the following transitioning potential:

$$\Phi_{\rm trans} = W_{\rm binary} \sum_{k=1}^{2} \Phi_{{\rm s},k} + W_{\rm single}\Phi_{\rm single}, \tag{4.3}$$

where $\Phi_{{\rm s},k}$ is the same as that shown previously in Eq. (3.5) and $\Phi_{\rm single} = -\frac{G(M_{\rm A}+M_{\rm B})}{r}$ is the potential created by a single central star of mass $M = M_{\rm A} + M_{\rm B}$. As can

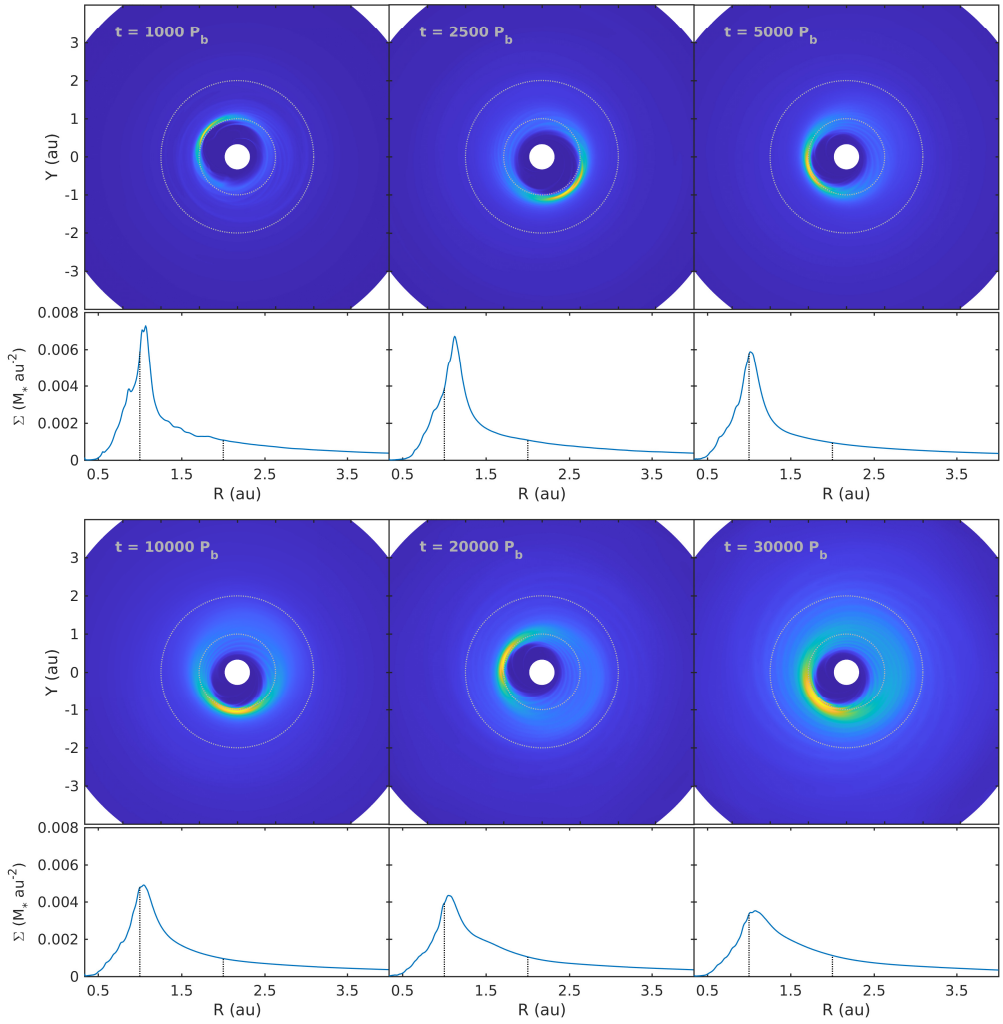

FIGURE 4.13: Snapshots of surface density maps and corresponding azimuthally-averaged surface density profiles for the *Kepler* 16 10_{MMSN}, binary-to-single potential transition (case 1). The grey and black dashed lines show the inner and outer limits of the potential transition at 1 and 2 au. No additional features are seen in the outer disc beyond the central cavity.

be seen from Eq. (4.2) W_{binary} and W_{single} are anti-symmetric so that at 1.5 au, halfway through the transition region, the potential is dominated by neither the binary or single-star potentials.

The results from these two simulations are presented as snapshots of the evolution of the disc surface density profile, in Figs. 4.13 and 4.14. Included are azimuthally-averaged surface density profiles of each snapshot, where perturbations from the background profile can sometimes be more easily seen. The limits of the transition region (1 to 2 au) are plotted in both plot-types. Times for the snapshots have

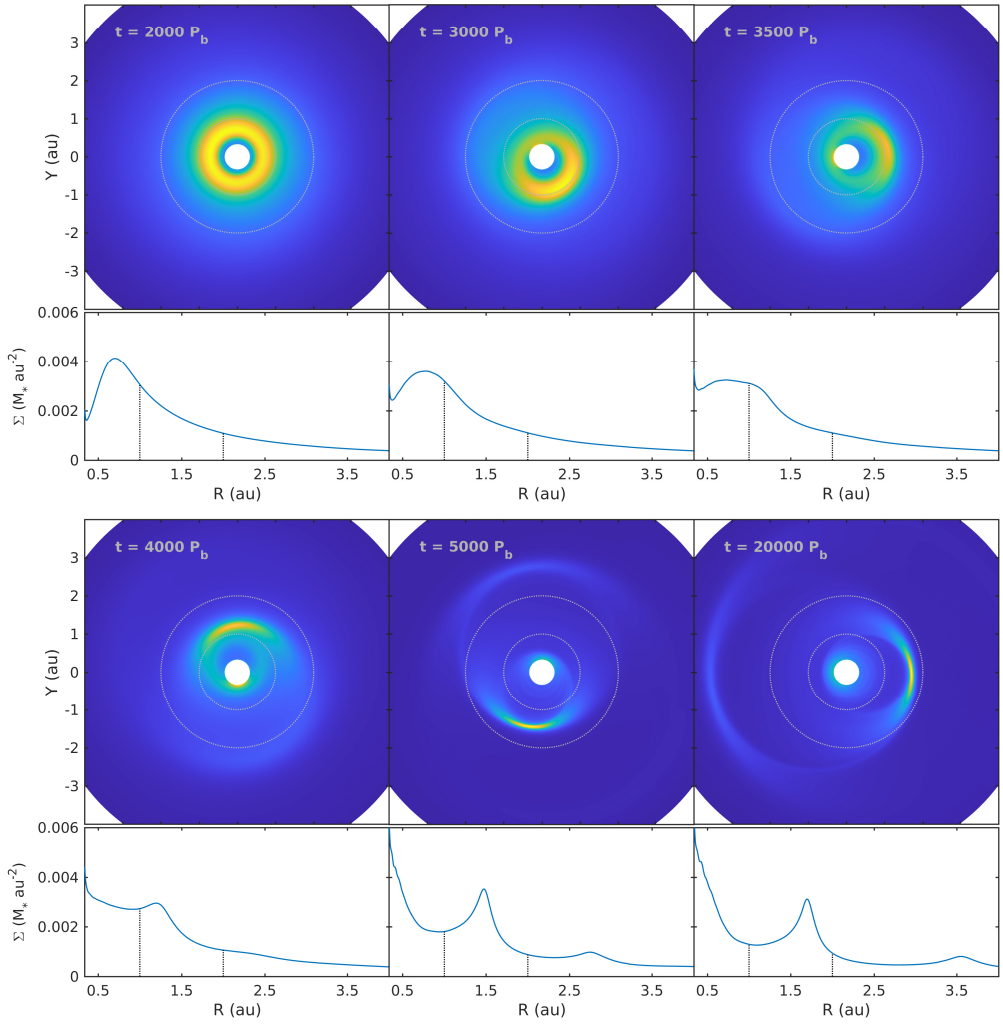

FIGURE 4.14: Snapshots of surface density maps and corresponding azimuthally-averaged surface density profiles for the *Kepler* 16 10_{MMSN}, single-to-binary potential transition (case 2). The grey and black dashed lines show the inner and outer limits of the potential transition at 1 and 2 au. The birth, and growth, of an eccentric feature in the outer binary-dominated region of the disc can be seen.

been chosen so that – where applicable – we see the birth of any new asymmetric features in the disc and the evolution of the discs to their pseudo-steady-state.

Examining the results from Fig. 4.13, where the binary dominates the potential in the inner disc, we see that the characteristic eccentric central cavity forms as expected. This disc looks almost identical to the *Kepler-16* low-mass discs throughout its whole lifetime. The disc reaches pseudo-steady-state quickly, with no additional eccentric features forming in the exterior disc. In contrast, the results from case 2 in Fig. 4.14, show a range of behaviour. For close to 2000 P_{b}

the inner disc is axisymmetric, with the gas following circular orbits. Little perturbation by the binary on the outer disc can be seen at this time. In the next snapshot at $t = 3000\,P_{\rm b}$ a large-scale trailing $m = 1$ spiral feature can be seen reaching from out beyond the transition region into the inner region. As this feature grows throughout the next few snapshots it perturbs the material in the inner disc. In the transition region, a surface density maximum develops associated with an eccentric ring that forms. The eccentric ring is very similar in structure and evolution to those seen in the high-mass *Kepler-16* discs. By combining the final snapshots of the inner region of case 1 with the outer region of case 2, we are essentially able to recreate the results seen for the $10_{\rm MMSN}$ *Kepler-16* disc, where the disc sees a potential created by a binary at all positions.

The lack of any additional eccentric rings or spirals in case 1 demonstrates that it is the effect of the binary potential on the self-gravitating disc which excites these features. As the central cavity has formed, along with the synonymous strong surface density maximum, if their creation was due to secular perturbations permitted by self-gravity then we would expect to see them in this case. The lack of the influence of the binary potential in the outer disc is the only ingredient missing from this simulation. The reverse of this can be said about case 2. Here we see an $m = 1$ spiral forming at early times in the outer disc, with no prior surface density maximum or asymmetry in the inner disc. This spiral arm has a pattern speed that is very similar to the precession frequencies of the additional eccentric features that eventually form. This spiral feature only begins to appear in the disc where the binary potential begins to dominate. With no eccentric ring present in the inner disc, there can be no strong secular perturbations on the outer disc exciting these eccentric features. Although this analysis disproves our previous suggestion that secular-like interactions with the inner eccentric disc could lead to the creation of the eccentric features seen in these discs, secular interactions still influence their interaction. In particular, secular forcing could still explain the close-to-commensurate precession frequency ratios seen for the two additional eccentric features seen in the *Kepler-16* $10_{\rm MMSN}$, $20_{\rm MMSN}$ and *Kepler-35* $20_{\rm MMSN}$ discs calculated earlier in this analysis.

Fixing the binary orbit as a way of minimising the parameter space, and because of our intent to reproduce the specific *Kepler* systems simulated here, could produce numerical artefacts in the disc. Whilst simulating a fully "live" binary in these discs is infeasible, because the resulting disc forces will cause the binary

orbital elements to diverge from those of the *Kepler* systems, we set up a test to ensure that the features we see arise due to true physical phenomena. In our self-gravitating runs above, the effect of the disc on the evolution of the binary was ignored. If this acceleration is included, the centre-of-mass of the binary is also accelerated, which also acts on the disc as an indirect term when working in a frame based on the binary centre-of-mass. To simulate a "pseudo-live" binary we calculated the acceleration on each binary component from the disc-binary interaction: $\ddot{\mathbf{r}}_{\rm A}$, $\ddot{\mathbf{r}}_{\rm B}$, and the acceleration on the binary centre-of-mass:

$$\ddot{\mathbf{r}}_{\rm cmbin} = \frac{M_{\rm A}\ddot{\mathbf{r}}_{\rm A} + M_{\rm B}\ddot{\mathbf{r}}_{\rm B}}{M_{\rm A} + M_{\rm B}}, \tag{4.4}$$

which can then be used to obtain an indirect potential throughout the disc, $\Phi_{\rm ind} = \ddot{\mathbf{r}}_{\rm cmbin} \cdot \mathbf{r}$. Whilst the disc-binary accelerations are not used to evolve the binary orbital elements, an indirect acceleration is included when evolving the disc:

$$\ddot{\mathbf{r}}_{\rm ind} = -\frac{\partial \Phi_{\rm ind}}{\partial r} = -\ddot{\mathbf{r}}_{\rm cmbin} \tag{4.5}$$

As outlined earlier in the paper, this approach allows the orbital elements of the binary system to remain fixed in time, while allowing the centre-of-mass of the binary system to move under the gravitational acceleration of the disc. It is equivalent to conserving the centre-of-mass of the combined disc-binary system while working in a frame based on the binary centre-of-mass, without allowing the binary orbital elements to change with time. The indirect force creates a uniform acceleration across the whole disc at each time step that involves the disc being accelerated in a direction that is opposite to that experienced by the binary centre-of-mass. Using this set-up we undertook a test of the *Kepler-16* $10_{\rm MMSN}$ model, as above, but with the full binary potential throughout the disc. As expected, we find that including this term has very little influence on the simulation results, as shown in Fig. 4.15. The reason why allowing the binary centre-of-mass to become live has little influence on the results is because the indirect term acts to accelerate the disc uniformly rather than differentially, such that any features that develop in the disc structure are unlikely to be influenced by this term.

4.6 Conclusions

Using a Viscous outflow condition at the inner disc boundary, as well as a value of $r_{\rm in}$ which partially embeds the binary in the disc, we have examined the impact

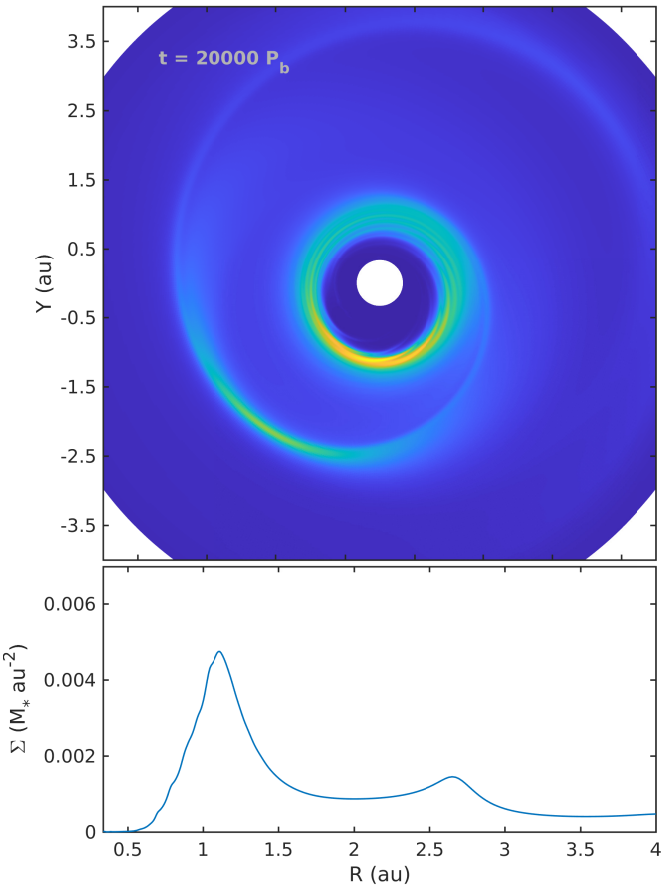

FIGURE 4.15: Snapshot of the surface density, and azimuthally averaged profile once steady-state has been reached. The indirect term has been included for the disc evolution. The appearance of the additional eccentric features, and the similarity to our stock self-gravitating disc models, reassures us that they are robust physical feature caused by self-gravity in massive circumbinary discs.

of disc self-gravity on the evolution and final structure of circumbinary discs in these systems. We focus on disc masses that are small enough that the disc is laminar and not in a gravito-turbulent state. We found that in those models with low binary eccentricity (namely the *Kepler-16* and *-35* systems), the inclusion of self-gravity in low-mass discs had little impact. The clearest difference between disc mass models in each system is the decreased period of disc precession. Examination of *Kepler-34*, which has a high binary eccentricity, showed that whilst the 1_{MMSN} and 2_{MMSN} models showed very similar results, at intermediate mass, the inclusion of self-gravity made a significant difference to the final disc structure. At quasi-steady state the 5_{MMSN} case had a location for the peak surface density position at the edge of the cavity of 1.9 au, nearly 0.5 au smaller than the lighter

discs. These results highlight again that it is binary eccentricity and not mass-ratio, which has the greatest impact on disc structure. For planets migrating in low-mass discs around binaries with small eccentricity, we would expect them to halt their migration at very similar locations given the similarity in disc structure. For more eccentric systems, such as *Kepler-34*, migration in a $5_{\rm MMSN}$ disc should lead to quite a different outcome compared to lower mass discs. The general effect of disc self-gravity in these low-mass systems is to increase the effective mass of the central binary such that radial length scales associated with disc features such as the central cavity become more compact, and high density features such as the surface density maximum associated with the edge of the cavity are more pronounced.

In the high-mass $10_{\rm MMSN}$ and $20_{\rm MMSN}$ models, the impact of self-gravity becomes very clear. Increasing the disc mass resulted in two very noteworthy changes: (i) significant shrinking of the size of the central eccentric cavity; (ii) formation of additional eccentric ring features in the disc lying outside of the central eccentric cavity. The shrinking cavity size arises because the self-gravity enhances the inward gravitational force that the disc experiences, providing additional opposition to the viscous and pressure forces in the disc acting to dissipate this feature. The additional eccentric features generate pronounced non-axisymmetric features in the disc surface density distributions, consisting of crescent, or ring-like features (material at apocentre moves more slowly and therefore the surface density is higher there), and a pronounced $m = 1$ global spiral wave. The appearance of these additional eccentric rings is most prominent in the high-mass discs around low-eccentricity binaries.

We examined two possible causes for these eccentric features that arise in high-mass discs. The first was resonant secular forcing by the high density eccentric ring that forms at the outer edge of the tidally truncated cavity. This idea, however, can be discounted for two reasons. The first is that material at the outer edge of the inner eccentric cavity precesses at a significantly faster rate than the additional eccentric ring features, and therefore the additional features are not in secular resonance with this material. The second is that simulations – where the gravitational potential due to the binary, transitioned from that of the binary system to that of a single central star at large disc radii – did not result in additional eccentric features being excited, even though the inner eccentric cavity still formed. The second possible cause for the formation of the additional

features was direct coupling to the binary potential at large disc radii. This was tested by using the inverse of the simulations which disproved our secular forcing hypothesis. Here the potential of the central star(s) transitioned from a single star in the inner disc to a binary system in the outer disc. Creation of the eccentric features in the outer disc was observed, without the creation of the inner central cavity. This result is the strongest evidence for the hypothesis that mode coupling between the eccentric binary potential and additional eccentric disc modes created by the disc self-gravity, is responsible for the creation of these additional features – similarly to the mechanism described in Papaloizou et al. (2001) and Pierens and Nelson (2013).

Although we have shown that the additional eccentric features are due to the binary potential acting on the disc at large radius, we have not yet managed to identify the mechanism responsible for creating these. As part of further investigation, we also ran simulations with transitions in the binary potential for the case of circular binaries, and in one case with the binary mass ratio being unity. We also find the growth of additional eccentric features in these simulations, indicating that the central binary does not need to be eccentric for these features to develop. Given that the epicyclic frequency differs in a self-gravitating disc compared to a Keplerian one, we examined whether or not the $3:1$ Lindblad resonance could shift outwards in the more massive discs to explain the origin of the first additional eccentric feature, but we find that the change in epicyclic frequency is small and the Lindblad resonance positions only shift by a few percent. The observation of a large scale $m = 1$ spiral feature also suggests that coupling at a shifted $3:1$ resonance is not responsible for the growth of the eccentric features (coupling at the $3:1$ resonance produces a $m = 2$ in the original analysis). At the present time the origin of these features remains unexplained.

We note that our adoption of a 2-D set-up prevents us from examining potentially important 3-D effects. These include the effects of disc warping when the disc and orbit plane of the central binary are misaligned (Larwood and Papaloizou 1997), which can in turn lead to the development of a parametric instability in the disc that may be a source of hydrodynamic turbulence (Ogilvie and Latter 2013). Similarly, the development of eccentric modes in the disc can also lead to parametric instability and hydrodynamic turbulence (Papaloizou 2005; Barker and Ogilvie 2014). A recent study has also shown that a Spiral Wave Instability can also exist in a disc that is tidally forced by a binary system, also leading to a parametric

instability and hydrodynamic turbulence (Bae et al. 2016). Clearly moving to 3-D will allow us to examine these and other effects, increasing the richness of the physical phenomena that can occur in planet forming circumbinary discs. In addition, it will be necessary to examine how changes in physical parameters such as the disc thickness, viscosity and surface density profiles influence the results, not to mention the influence of as-yet neglected physics such as magnetic fields, or radiative effects, before we can can make robust claims about the evolution of circumbinary discs.

The significantly different evolution observed for the massive circumbinary discs examined here raise a number of interesting issues concerning the formation and evolution of planets in these environments. In particular, it is clear that the different disc structure would be very important for early forming planets that arise when the disc is massive and self-gravity is important. The surface density maxima produced by the additional excited eccentric rings could act as planet-traps (Masset et al. 2006b), halting planet migration before they reach the edge of the inner cavity. The migrating cores could increase rapidly in mass at these locations due to an accumulation of material (Morbidelli et al. 2008). Although the eccentric features are not vortices (even if they have a similar appearance), they can nonetheless act as pressure bumps and trap small dust grains and pebbles that may grow and migrate through the disc via aerodynamic drag. Their non-axisymmetric structure will place limits on the particle sizes that can be locally trapped (radial migration must be slow enough that particles do not escape by crossing the radial width of these features in one synodic period), but one could certainly expect them to enhance the concentration of solid material locally and provide sites for efficient planet growth. Of course, these high-mass conditions will only occur at very early times in the most massive discs. We therefore need to examine the transition from these high-mass states to more common low-mass ones, and the impact of this transition on the planets which may have formed and migrated at early times. A high-mass past, where the disc is shaped by self-gravity, may leave a lasting imprint on the planets it produces. We will address the question of planetary evolution by investigating migration and accretion scenarios of embedded protoplanets, as well as disc mass transitions, in the next Chapter.

4.6.1 Summary

In this Chapter we have presented the results of hydrodynamic simulations from a thorough investigation into disc evolution applied to the *Kepler-16, -34,* and *-35* circumbinary systems. For low-mass discs (1–5_{MMSN}), the inclusion of disc self-gravity makes little difference on the disc structure and evolution, except in the 5_{MMSN} model around the very eccentric *Kepler-34*. We expect the results in our next Chapter, introducing interacting planets into these discs, to show very little variation from past works examining the same binary systems. The creation of additional eccentric features in the outer regions of massive discs (10 and 20_{MMSN}), although not completely understood at this point, will likely introduce novel behaviour into the planetary evolution scenarios simulated in these discs.

The Role of Circumbinary Disc Self-Gravity on Planet Evolution

Chapter Contents

5.1 Introduction

The evolution of planets in evolved self-gravitating circumbinary discs has not been studied in detail before, however their counterparts in non-self-gravitating discs have been. For an in-depth discussion of the current state of this field, we direct the reader to Sections 1.3 and 1.4; the key points pertaining to planetary migration and evolution in circumbinary disc are given below.

- Jovian-mass planets generally migrated into the central cavity, where they were captured into a 4 : 1 mean-motion-resonance with the binary. These giant planets often underwent close-encounters with the binary, with scattering events ejecting them from the system (Nelson 2003)
- Lighter, Saturnian-mass planets underwent stable migration to the disc cavity where they then remained in stable orbits (Pierens and Nelson 2008a)
- Less massive planets undergo Type-I migration until they are halted at the inner cavity edge by a strong positive co-rotation torque, counteracting the Lindblad torque – see Pierens and Nelson (2007, 2008a,b)

The techniques developed in these works were then applied to a number of the newly discovered *Kepler* circumbinary systems, in attempts to explain and recreate the orbits of their planets (Pierens and Nelson 2013; Kley and Haghighipour 2014, 2015). These studies had difficulty recreating both the semi-major axes and eccentricities for the observed planets, with a range of disc parameters and models. Understanding the physics and parameters which affect the environment in which the planets form and evolve – the circumbinary disc – is key to understanding the final, observed states of these intriguing systems. The inclusion of self-gravity is a step towards obtaining a physically realistic disc model which describes the evolution and structure of the circumbinary environment throughout its lifetime, with the goal of reproducing the observed circumbinary systems, and predicting the planetary architecture of future systems. To this end, the aim of the work presented this Chapter and the last, is to probe the early dynamical history of circumbinary discs – as we increase the disc mass we effectively examine earlier and earlier times in the system's history. We aim to address the questions: Does a high-mass disc leave a fingerprint on the planet population if circumbinary planets form early? Is this erased by the transition to a low-mass disc as the system

TABLE 5.1: Starting semi-major axes of protoplanetary cores in each of the *Kepler-16, -34,* and *-35* system models.

	$a_{\mathrm{p},0}$ (au)		
	Kepler-16	*Kepler-34*	*Kepler-35*
1_{MMSN}	2.0	2.5	2.5
2_{MMSN}	2.0	2.5	2.5
5_{MMSN}	2.0	2.5	2.5
10_{MMSN}	3.0	2.5	2.0
20_{MMSN}	3.0	2.5	2.5

evolves? Does the epoch when planets form, accrete gas, and migrate affect their final orbital configuration or mass?

Using the evolved self-gravitating discs in the *Kepler-16, -34,* and *-35* circumbinary systems from the previous chapter as a starting point, we examine the impact of self-gravity and disc mass on migration and accretion scenarios for protoplanetary cores. The scenarios are carried out in the evolved self-gravitating discs with masses equivalent to 1, 2, 5, 10 and 20×MMSN, in each of the binary systems. These different disc masses are proxies for different eras in the lifetime of the disc, so we can answer the questions raised above. To simulate the evolution of the system from a high- to low-mass disc state we also carry out simulations where the orbital evolution of the planet is tracked as the disc mass is exponentially dissipated.

The initial conditions used to set up the simulations of the disc models used as the starting point and basis of this work are detailed in Chapters 3 and 4. This section will instead focus on the procedure used to initialise the planet cores in the migration, gas accretion and disc dissipation scenarios presented throughout this Chapter. Figures 5.1 and 5.2 summarise the initial disc conditions the planets are inserted into – the pseudo-steady-state, azimuthally averaged surface density and eccentricity profiles for the 1, 2, 5, 10, and 20_{MMSN} models in the *Kepler-16, -34,* and *-35* systems. These snapshots are taken at $t = 6000\,P_{\mathrm{b}}$, once the disc has reached a pseudo-equilibrium. The structure and dynamics in the disc will modify, and be modified, by the introduction of an interacting protoplanetary core.

In our first set of simulations we launch protoplanetary cores, on initially circular orbits, in the outer regions of the evolved discs from Chapter 4 and allow them to

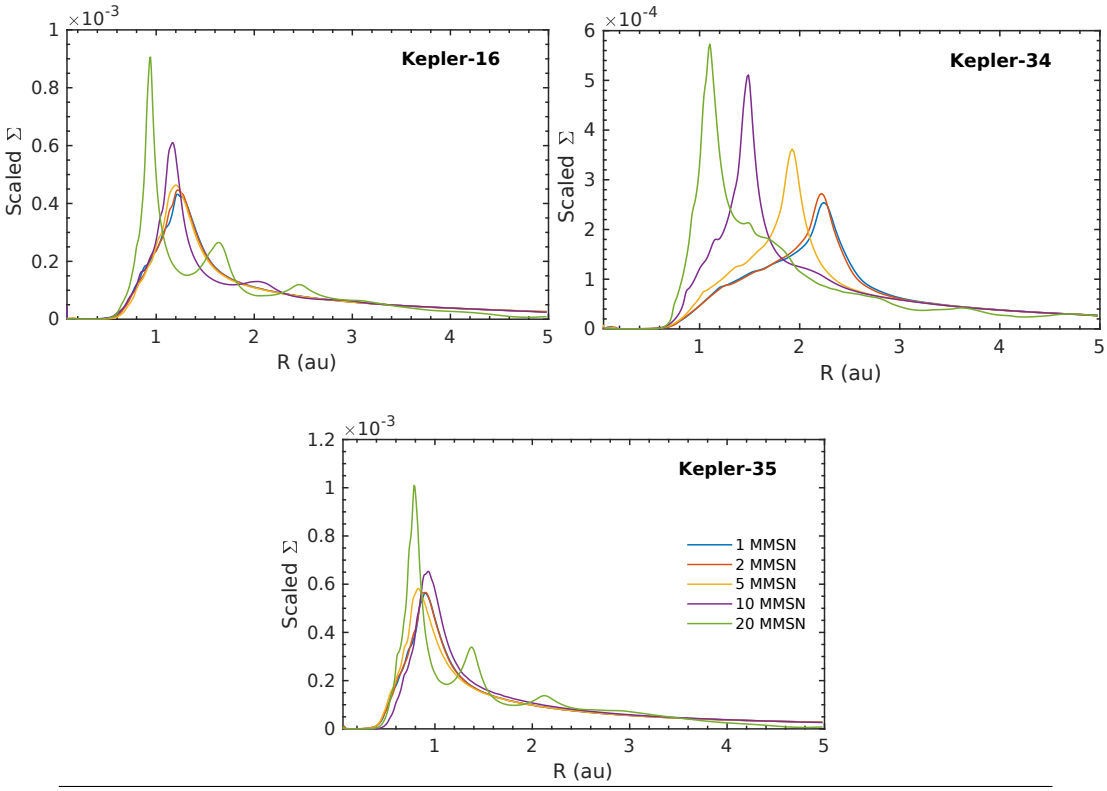

FIGURE 5.1: Azimuthally averaged surface density profile results of all self-gravitating disc models in the *Kepler-16, -34,* and *-35* systems from Chapter 4. One can see the central cavity in all disc models, and the density spikes associated with the additional eccentric features in the most massive 10 and 20_{MMSN} models. These profiles are calculated once the discs have reached pseudo-steady-state – $5000\,P_{\mathrm{b}}$ in the *Kepler-16* system, and $6000\,P_{\mathrm{b}}$ in the *Kepler-34* and *-35* systems.

interact with the discs. The initial mass of the core in each system is chosen so that $q_{\mathrm{p},0} = m_{\mathrm{p},0}/M_{\star} = 6 \times 10^{-5}$. If $M_{\star} = 1\,\mathrm{M}_{\odot}$ this is equivalent to a $20\,\mathrm{M}_{\oplus}$ core. We release the cores into the outer region of the disc, where the surface density profile is unperturbed by the binary, and the disc eccentricity is negligible. Referring to the profiles in Fig. 5.1 this lies at 2 au in the low-mass *Kepler-16* and *-35* models, and around 2.5 au in the low-mass *Kepler-34* systems. The situation in the high-mass systems is a little more complicated due to the additional eccentric features in the outer disc. Starting the planets at an initial starting position beyond 4 au – exterior to any strong eccentric features – means the time needed to migrate into the inner disc is too long. However, we speculate in Chapter 4 that the migrating planets could interact with these additional features to produce interesting behaviour, therefore we didn't want to place the planets too close to the binary. In the high-mass discs we used an approach which placed the planet

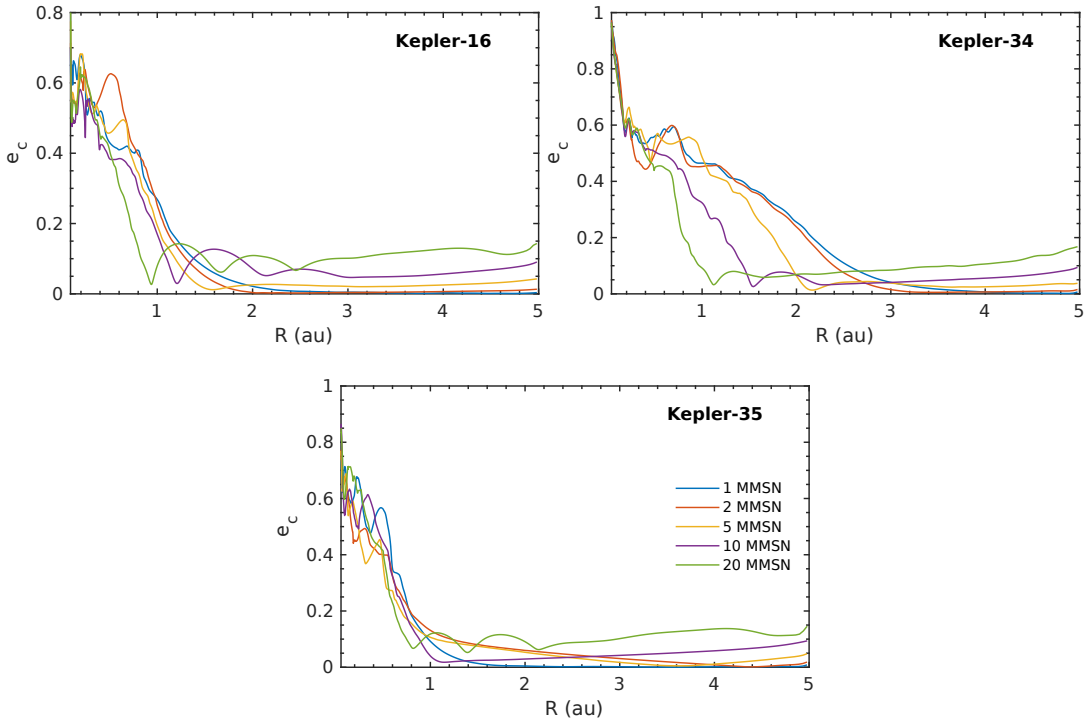

FIGURE 5.2: Azimuthally averaged cell eccentricity profile results of all self-gravitating disc models in the *Kepler-16, -34,* and *-35* systems from Chapter 4. The eccentric inner cavity can be seen in all models, with the additional eccentricity bumps associated with the eccentric features in the high-mass discs. Again, these profiles are taken once the models have reached pseudo-steady-state.

beyond the first additional feature, but not too far out in the outer disc. Table 5.1 summarises the starting semi-major axes of the cores in all our models. FARGO-ADSG modifies the initial planet semi-major axes with an initial self-gravity boost, which increases the starting position by $\approx 10\%$ in the most massive 20_{MMSN} models.

5.2 Migration of Protoplanetary Cores

In this section we present the results of simulations examining the migration of protoplanetary cores in evolved self-gravitating discs around the *Kepler-16, -34,* and *-35* binary systems. We insert a non-accreting core, with mass ratio $q_{\mathrm{p},0} = 6 \times 10^{-5}$, into each of the 1, 2, 5, 10, and 20_{MMSN} discs from Chapter 4, once the disc has reached a pseudo-steady state. In the *Kepler-16* system this is

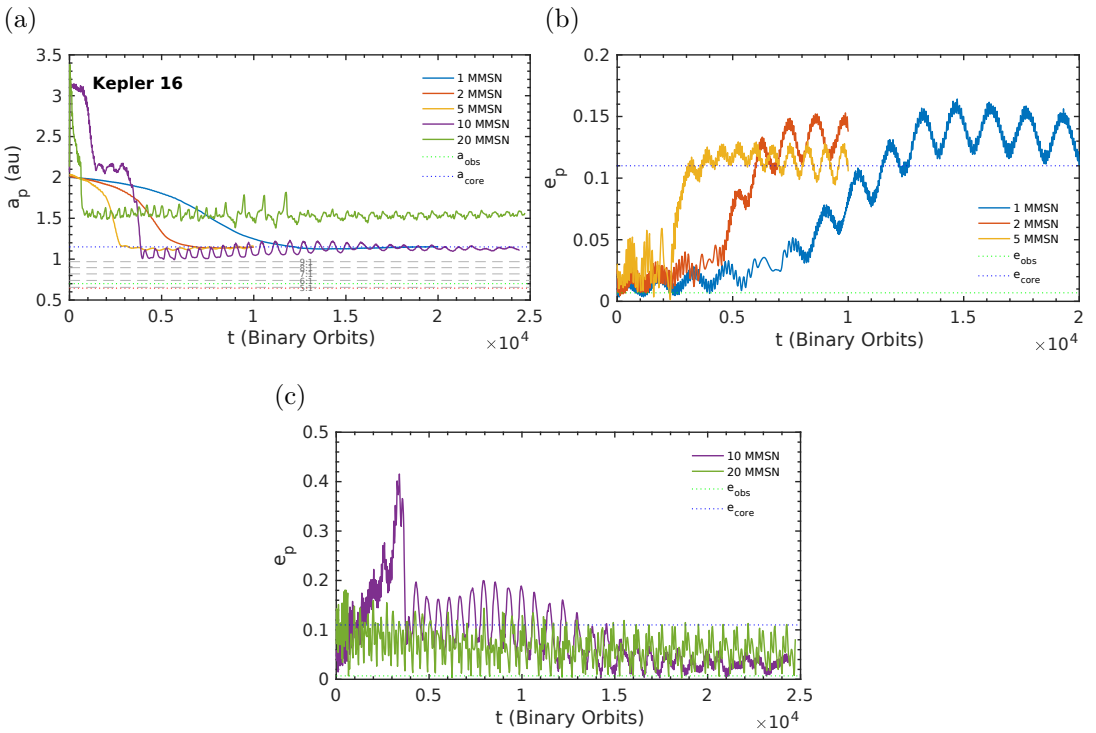

FIGURE 5.3: *(a)* The evolution of the $q_{\mathrm{p},0} = 6 \times 10^{-5}$ protoplanetary cores' semi-major axes in evolved self-gravitating discs around the *Kepler-16* system. The grey dashed lines in this plot show the positions of $n : 1$ mean-motion resonances with the binary, which have been shown to be unstable to planetary orbits (Dvorak 1986; Nelson 2003; Kostov et al. 2013; Kley and Haghighipour 2014, 2015). The red dotted line shows the location of a_{crit} from Holman and Wiegert (1999). *(b & c)* The cores' eccentricity evolution in the low- and high-mass disc models respectively. The green dotted lines in these plots show the values of a_{p} and e_{p} of the observed planet from Doyle et al. (2011), and the blue dotted lines show the final values of simulation with the same disc parameters and comparable core mass from Pierens and Nelson (2013).

at 5000 P_{b}, whilst the discs reach this state after 6000 P_{b} in the *Kepler-34* and *-35* systems. At this point in the simulation the inner eccentric cavity has a stable precession frequency, and in the high-mass discs, models which were shown to exhibit additional eccentric features at any point, have done so. The core mass used in these simulations lies in the regime where Type-I migration is rapid, but is not massive enough to open a gap in the disc i.e. the gap-opening criteria of Crida et al. (2006) is not met.

5.2.1 *Kepler-16* Results

Our results for the orbital evolution of protoplanetary cores in self-gravitating discs around *Kepler-16* are summarised in Fig. 5.3. The upper panel shows the evolution of the cores' semi-major axes, until a pseudo-steady orbit is reached. In addition to the 1–20_{MMSN} models being shown on this plot, several other quantities are plotted. The red dotted line is the semi-empirical critical semi-major axis for stable orbits around *Kepler-16* (Holman and Wiegert 1999); the green dashed line is the best-fit observed semi-major axis for *Kepler-16 b* from Doyle et al. (2011); the blue dotted line (with label a_{core}) shows the final values for the non-self-gravitating results with comparable disc and core properties from Pierens and Nelson (2013); and the grey dashed lines show the locations of the 5 : 1–9 : 1 mean motion resonances with the binary – locations which have been shown to lead to eccentricity growth, leading to ejections or scattering with the binary (Kostov et al. 2014; Kley and Haghighipour 2015; Kostov et al. 2016). The middle panel shows the evolution of the core eccentricity results for the low-mass (1–5_{MMSN}) disc models, with the high-mass results plotted in the bottom panel for clarity.

We can see that like the disc evolution models in Chapter 4, the evolution of the protoplanetary cores in the low and high-mass discs can be separated into two distinct regimes of behaviour. In the low-mass discs the cores migrate inwards, albeit with increased rates in the more massive models (the migration rate scales moderately super-linearly with the surface density at the planets' location (Baruteau and Masset 2008b)), from their initial starting position until they reach 1.2 au. This location corresponds well with the surface density peak in the material bounding the tidally truncated inner cavity (Fig. 5.1), a result fully expected from previous work. As can be seen in Fig. 5.3 the low-mass results agree extremely well with those from Pierens and Nelson (2013), but not with the observed state of *Kepler-16 b*. This result is slightly unexpected as the disc cavity size seen in our models is somewhat smaller than those in Pierens and Nelson (2013) due to our more realistic treatment of the inner disc boundary.

To explain this we must examine what dictates the halting position of these protoplanetary cores in circumbinary discs. From prior work (Pierens and Nelson 2007, 2013; Kley and Haghighipour 2014), we know the stopping behaviour of planets across a range of planetary masses. In the Type I regime, Earth-like planets are stopped by the growth of a strong positive co-rotation torque which counteracts

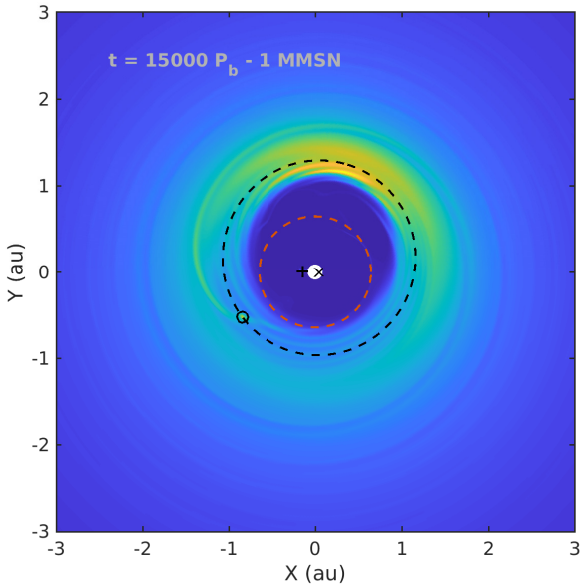

FIGURE 5.4: A snapshot of the 2-D surface density profile in the 1_{MMSN} model once the planet has reached a pseudo-steady-state orbit at the edge of the eccentric cavity. The instantaneous orbit of the planet is shown by the black-dashed ellipse, the red-dashed circle shows the location of the critical stability limit. The disc and planet system look nearly identical in the 2 and 5_{MMSN} models around the same system. The planet's inwards migration has been halted by a strong positive co-rotation torque balancing the negative Lindblad torque, once the eccentricity of the planet attains a value $\approx e_{\mathrm{d}}(a_{\mathrm{p}})$.

the influence of the negative Lindblad torque (Masset et al. 2006a; Pierens and Nelson 2007). These two torques balance each other when the surface density gradient is sufficiently positive. For more massive Saturn-like planets, a different stopping mechanism operates. If the planetary eccentricity is large enough, a torque reversal can be induced – at apoapse the planet orbits amongst material in the outer disc that is locally travelling faster than itself. When this material overtakes the planet it is focussed by the planet's gravity, leading to a positive torque. The reverse of this occurs at periapse, leading to a negative torque from the inner disc (Pierens and Nelson 2008a,b, 2013). When at a cavity edge, the inner torque is naturally smaller in magnitude than the outer torque, leading to a net positive torque arising from this effect. As can be seen in Figs. 5.1a, 5.2a and 5.3b, the migration of the protoplanets starts to slow when the planetary eccentricity reaches a significant level, $e_{\mathrm{p}} \approx 0.13$. This coincides when the local disc cell eccentricity and planetary eccentricity are comparable. These findings lead us to the same conclusion as Pierens and Nelson (2013), that for the protoplanetary core mass used here, it is the torque reversal induced by significant planetary

eccentricity which halts migration. Comparing our results with those in Pierens and Nelson (2013), the fact that the planet's stopping location is essentially the same in that study and this one, in spite of the different size of the cavity, arises because of differences in the planetary eccentricity and the structure of the cavity (eccentricity and surface density profile). Figure 5.4 shows the orbit of the core at the exterior edge of the cavity, where the protoplanet's eccentricity is high enough to induce a torque reversal.

In the high-mass disc regime we observe planetary evolution behaviour not seen in the low-mass discs, or previous work on this topic. Whilst the cores still migrate inwards, in the 10_{MMSN} model the core briefly halts at 2.2 au. During the period when it is trapped at this location its eccentricity grows significantly from 0.05 to a maximum of 0.4. When the core is then released its eccentricity is quickly damped and it migrates into the inner disc, halting at a location in good agreement with the low-mass results, $a_{\mathrm{p}} = 1.1$ au. Unlike the low-mass models the core's eccentricity is slowly damped by the large amount of gas in its vicinity, down to a value in good agreement with the observed value of *Kepler-16 b*. Whilst the core in the 20_{MMSN} model doesn't show signs of this trapping immediately, its inwards migration is halted at 1.5 au, a location significantly exterior to the prior results. Examining Figs. 5.5 and 5.6, we can start to explain this behaviour. The discovery of the additional eccentric features in high-mass self-gravitating circumbinary discs prompted us to theorise that they could act as planet traps. In the Type I regime, the positive surface density gradient creates a strong co-rotation torque which could counteract the Lindblad torque or, for more massive planets, the excited eccentricity in these regions could excite the eccentricity of the body sufficiently to induce a torque reversal. Whilst this process requires the planet to have a non-negligible eccentricity, it also requires there to be a surface density gradient across the extremes of the orbit. At apocentre it should find itself in an area of high surface density, and a low surface density at pericentre. In the discs which we obtain in these models, this can be achieved by the planet and disc eccentricities not being exactly equal, or a misalignment between the respective line of nodes. In this case the planet is on a less eccentric orbit than the surrounding disc material.

Despite this prediction, we see two different end results in the 10 and 20_{MMSN} models. In the least massive of these cases the core migrates inwards until it

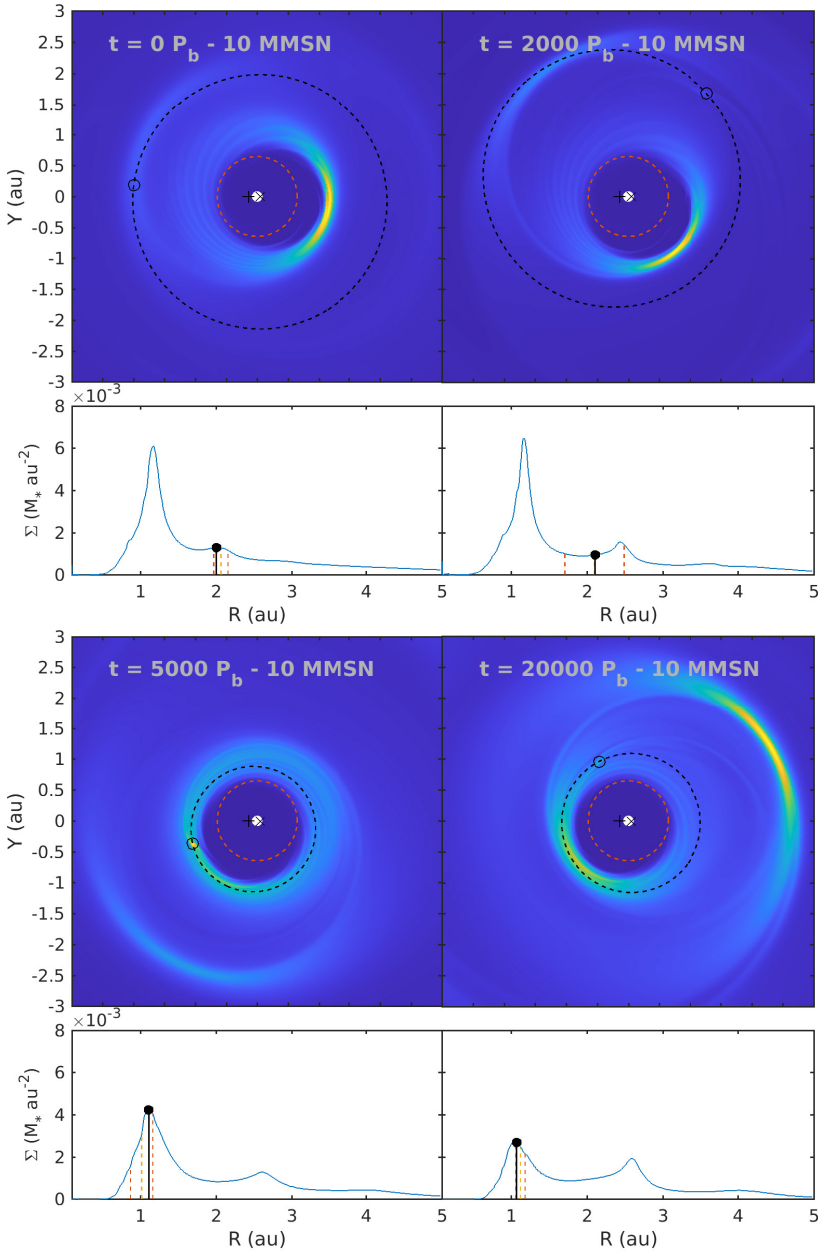

FIGURE 5.5: Evolution of the 2-D and azimuthally-averaged 1-D surface density profiles of the *Kepler-16* 10_{MMSN} model, over the course of the protoplanet's migration from its initial starting point, to its final location. The instantaneous orbit of the planet is shown by the black-dashed ellipse in the 2-D plots; the red-dashed circle shows the location of the critical stability limit. The black line in the 1-D profiles is the core's actual distance from the binary CoM, the orange dashed line is a_{p} and the inner and outer dashed red lines show the location of $r_{per} = a_{\mathrm{p}}(1 - e_{\mathrm{p}})$ and $r_{apo} = a_{\mathrm{p}}(1 + e_{\mathrm{p}})$ respectively.

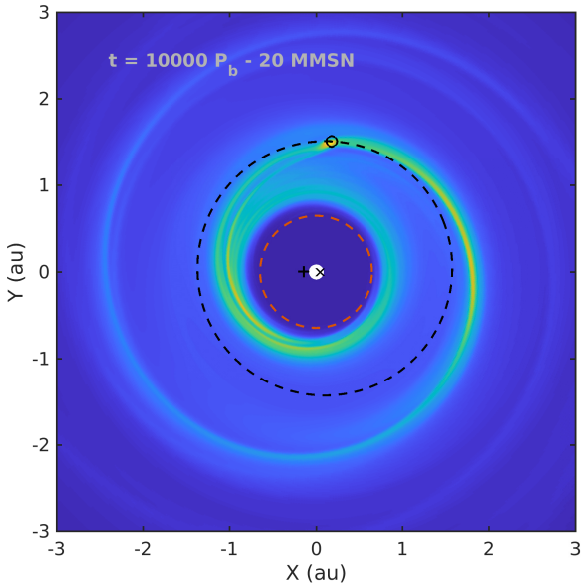

FIGURE 5.6: A 2-D surface density profile of the evolved 20_{MMSN} disc model around the *Kepler-16* binary. In this snapshot a protoplanetary core has been interacting with the disc for $1000\,P_{\mathrm{b}}$. The instantaneous orbit of the core is shown by the black-dashed ellipse. The core can be seen to be orbiting between the inner cavity, and the first eccentric feature. The planet's orbit crosses this feature, and because it has a period of precession ranging in the hundreds of binary orbits, the planet will cross and interact with this feature repeatedly. The eccentric feature is strong enough to trap the planet at this exterior position.

reaches the first eccentric feature. At this location it halts. Repeated interaction with this highly eccentric feature lead to the planet's own eccentricity being excited. This can be seen in the second panel of Fig. 5.5. However the planet's eccentricity becomes so high ($e_{\mathrm{p}} = 0.4$), the planet's pericentre position decreases until it interacts with the material bounding the inner eccentric cavity. A similar process to the initial trapping then occurs, the planet's orbit is circularised by the far less extended inner feature however. The core's semi-major axis shrinks until the orbit is moderately eccentric, which matches that of the observed *Kepler-16 b* relatively well, at the location of the inner cavity. The core in the 20_{MMSN} model can get trapped at the first outer eccentric cavity because the eccentric feature is more tightly localised due to the disc's stronger self-gravity. Therefore the planet's orbit doesn't take it into close proximity of the strong inner eccentric feature, and it remains trapped between the inner and first outer eccentric features.

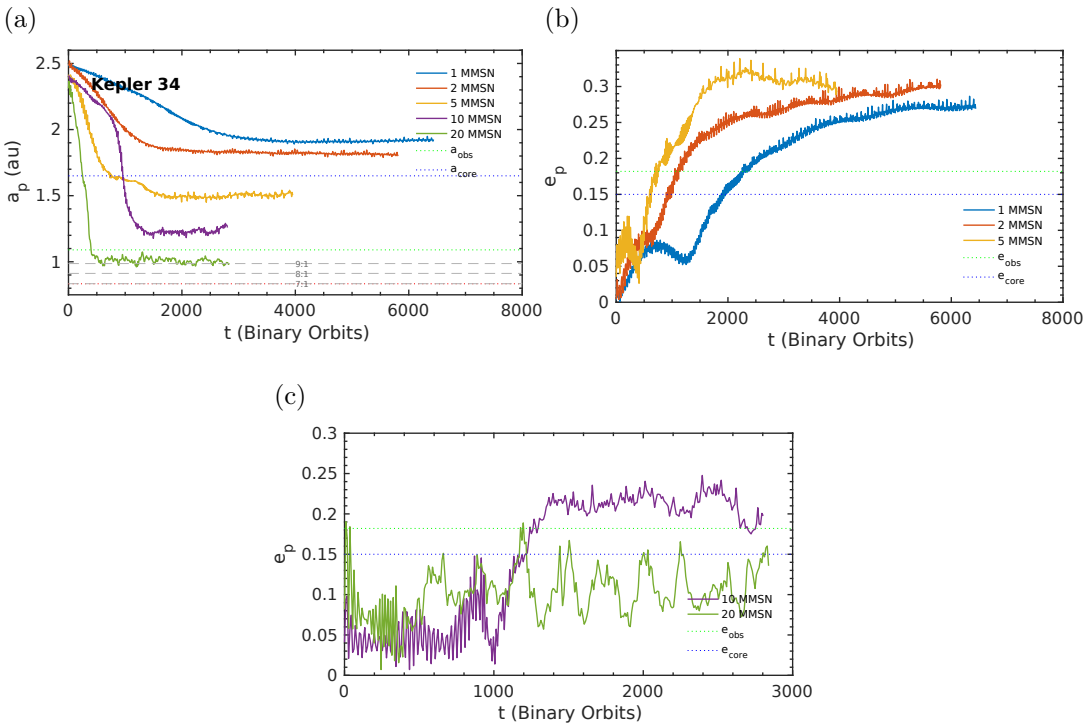

FIGURE 5.7: *(a)* Evolution of $q_{\mathrm{p},0} = 6 \times 10^{-5}$ protoplanetary cores' semi-major axes in evolved self-gravitating discs in the *Kepler-34* system. *(b & c)* Evolution of cores' eccentricity in the low- and high-mass disc models respectively.

5.2.2 *Kepler-34* Results

As a result of the variety in the evolved disc structures in the *Kepler-34* models, we see a large range of results for the migration of protoplanetary cores in these evolved discs. As we increase the disc mass from 1 to 20_{MMSN}, the size of the initially very eccentric, extended cavity in the least massive disc gradually decreases – self-gravity acts to compact the scale of the system. As can be seen from Fig. 5.7 a similar pattern can be seen in the final stopping positions of the migrating cores, where the halting of migration occurs because e_{p} increases and induces a torque reversal.

In the low-mass discs there is a clear trend for a_{p} to decrease from $a_{\mathrm{p}} \approx 1.95$ to 1.5 au, and for e_{p} to increase from $e_{\mathrm{p}} = 0.275$ to 0.3 as the disc mass rises from 1 to 5_{MMSN}. Looking at the disc eccentricity distributions in Fig. 5.2b, for a given radius one obtains a smaller value for the average disc cell eccentricity for larger disc masses – the core therefore has to migrate further through the disc so that $e_{\mathrm{p}} \approx e_{\mathrm{d}}$. The large e_{p} seen for the cores in these discs means the strength of

the co-rotation torque would be greatly diminished (Fendyke and Nelson 2014), therefore making torque reversal the dominant mechanism for halting migration. The low-mass discs, especially the 1_{MMSN} model, do not match the results obtained in Pierens and Nelson (2013), and show poor agreement with the observed *Kepler-34 b*. The discs in these models tend to have large, highly eccentric cavities compared to the equivalent models in Pierens and Nelson (2013). Our more realistic treatment of the inner disc boundary, allowing for a more accurate capturing of angular momentum flux through the disc due to the binary, is the likely explanation for this.

Whilst the low-mass disc results do not agree well with past results or the observed state of the *Kepler-34* planetary system, the 10_{MMSN} and 20_{MMSN} models agree relatively well with the planetary orbital elements quoted by Welsh et al. (2012). The final stopping positions in the 10_{MMSN} and 20_{MMSN} systems, 1.2 and 1.0 au respectively, bracket the observed value of $a_{\mathrm{p}} \approx 1.1$ au due to the compacting of the system as disc-mass and self-gravity increase. The trend for e_{p} to increase as the disc-mass increases is reversed in the high-mass regime, possibly due to the disc-mass in the vicinity of the planet providing significant damping. We see no evidence of the core being trapped in the outer disc in either model. Examining Figs. 5.8d and 5.8e, we can see that although additional eccentric features are present in the outer disc, in both the 10 and 20_{MMSN} models, they are far less well-defined than those in *Kepler-16*. The surface density gradients across these washed-out features are not strong enough to induce a torque reversal and halt the inwards migration of the cores in this system.

A common feature in all the disc models in this system can be observed in Fig. 5.8. One can clearly see that the orbits of the cores in each system are aligned with the precessing eccentric inner cavity. An examination of the planet's longitude of pericentre, alongside that of the mean disc longitude of pericentre shows this as well (Fig. 5.9). As the planet migrates into the inner disc, the phase and period of precession both evolve into lock-step with that of the inner disc cavity (which the local calculation of ω_{d} traces). The planet and eccentric feature precess with each other, in a pericentre-aligned fashion, a behaviour previously seen for full mass planets in non-self-gravitating discs in the *Kepler-34* system (Kley and Haghighipour 2015). This is not true in the most massive disc model presented here, 20_{MMSN}. In this case, the precession of the planet and disc are half a precession period out of phase such that their eccentric orbits are anti-aligned. In Chapter 4

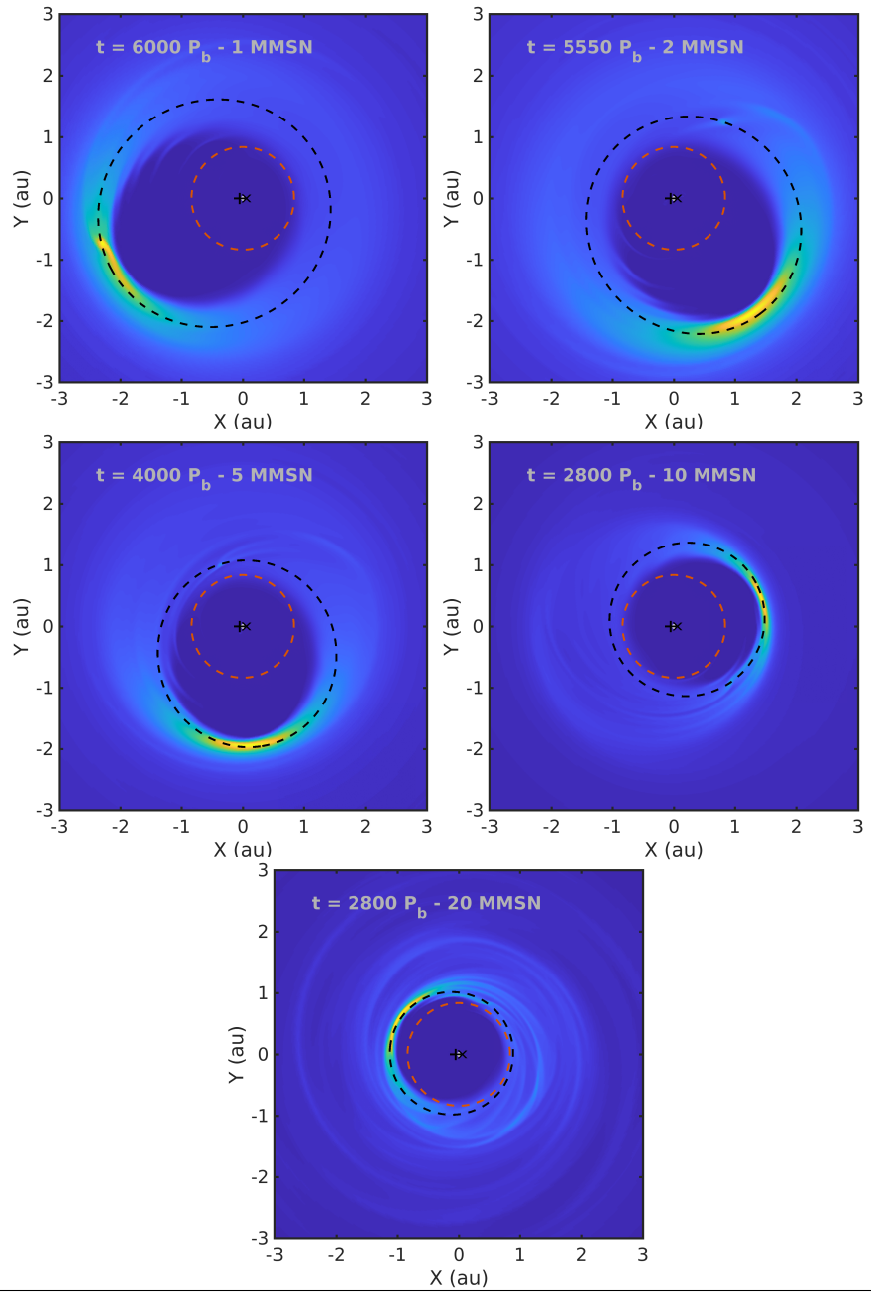

FIGURE 5.8: 2-D surface density profiles showing the structure of the binary-disc-core system once migration has halted for the 1–20$_{\mathrm{MMSN}}$ disc models around the *Kepler-34* binary. The planetary orbit is shown by the black-dashed line, with the red-dashed line showing the critical stability limit. For each of these models it can be seen that the planet migrates into the inner disc, where it then interacts with the strong eccentric feature. The stopping position can be seen to decrease as the disc mass increases. Clear evidence of pericentre-alignment between the core and the eccentric cavity can be seen.

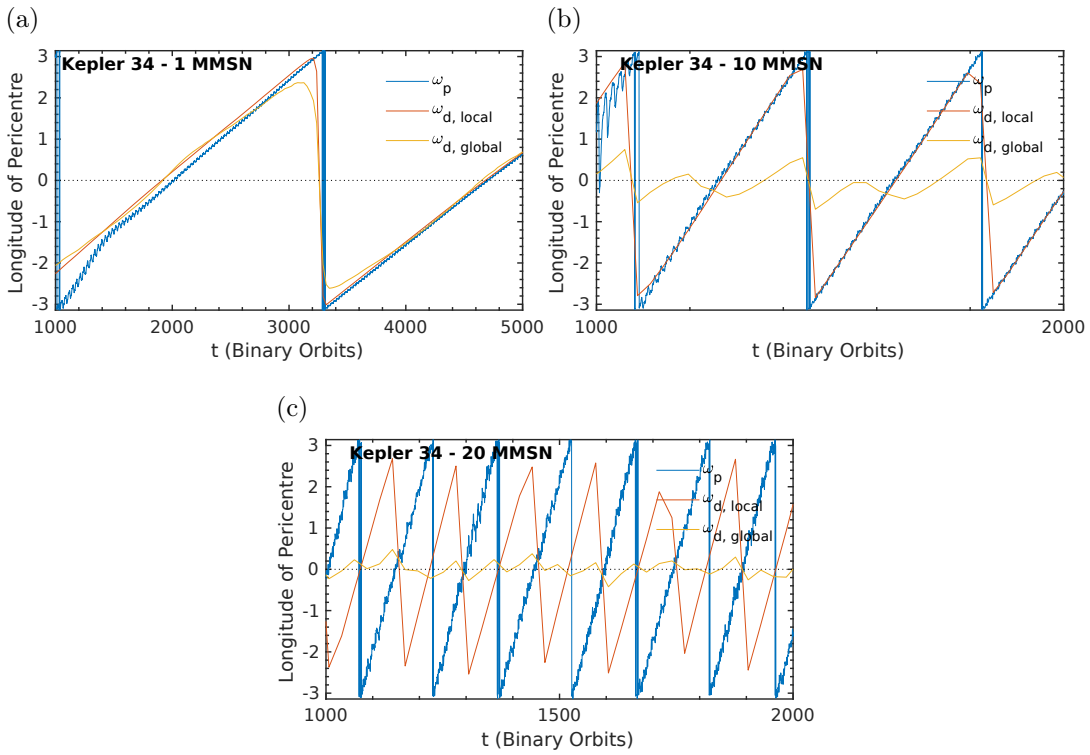

FIGURE 5.9: Evolution of longitude of pericentre of the disc-planet system in the 1, 10, and 20_{MMSN} disc mass models around *Kepler-34*. Both the global and local calculations of the disc longitude of pericentre are included (see the text for a description of the differences between these two calculations). In the 1–10_{MMSN} discs the planet evolves into a state where the phase and period of circulation of its precession match that of the inner eccentric cavity of the disc. The two match when the planet has halted its migration at the inner cavity.

we give an explanation for the global and local calculations of the disc eccentricity and longitude of pericentre. Whilst the global calculation takes into account all the material in the disc between r_{in} and r_{out}, the local calculation only takes into account material up to and just beyond the position of the surface density peak associated with the inner cavity. This procedure ignores the effect of exterior eccentric, precessing material in the outer disc.

We note that a second separate simulation of a protoplanetary core released at 3 au in the *Kepler-34* 20_{MMSN} disc model was undertaken to examine migration from a larger radius. This location corresponds to a radius between the second and third additional eccentric features in the disc. Whilst these features are relatively weak, they still alter the surface density profile of the disc. These regions of positive surface density gradient are sufficient to hamper any inwards migration

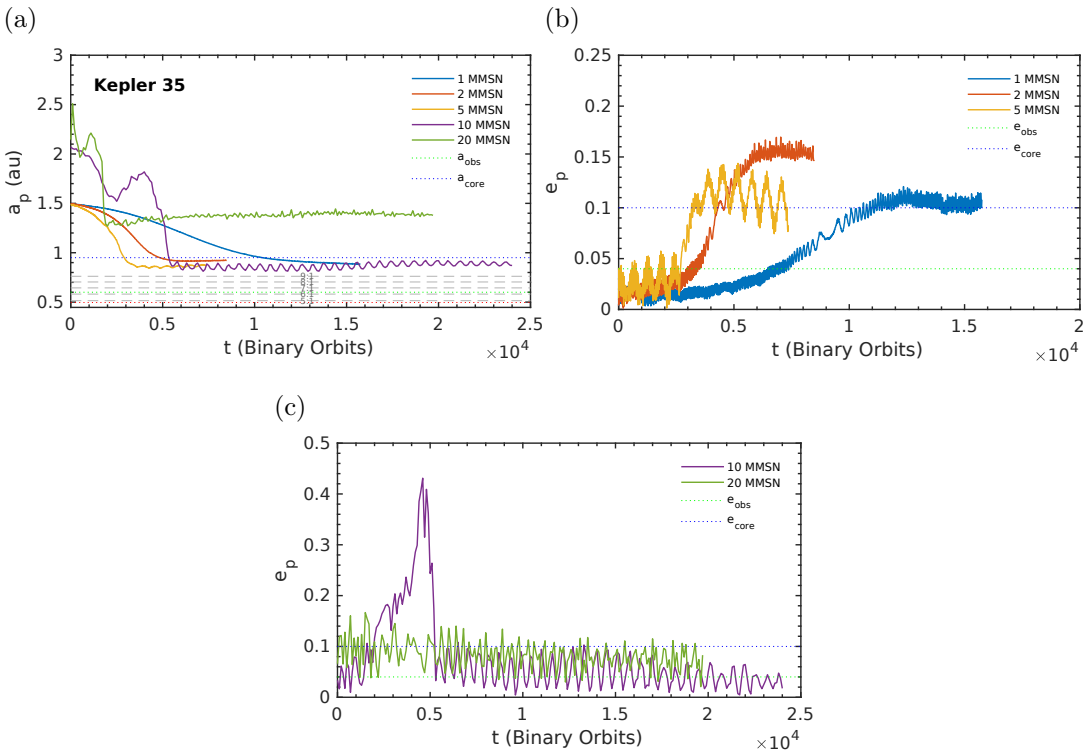

FIGURE 5.10: *(a)* Evolution of $q_{\mathrm{p},0} = 6 \times 10^{-5}$ protoplanetary cores' semi-major axes in evolved self-gravitating discs in the *Kepler-35* system. *(b & c)* Cores' eccentricity evolution in the low- and high-mass disc models respectively.

of the planet, but insufficient to excite sufficient eccentricity for it to escape. The forces acting on the planet at this outer position which normally result in inwards migrations are overcome by the small perturbations in surface density – whilst at the starting position of the first 20_{MMSN} core the rate of inwards migration is greater. These weak features could play an important role in the early stages of planet formation, trapping large numbers of planetesimals, boulders or pebbles – with low eccentricity – providing a reservoir for protoplanetary core creation. For clarity we have not included this simulation in the plots for this section, but we will discuss its further evolution in subsequent sections.

5.2.3 *Kepler-35* Results

The results from protoplanetary core migration in the evolved *Kepler-35* disc models look very similar to those from the *Kepler-16* models, with minor changes caused by the differences in evolved disc structure. This result was expected

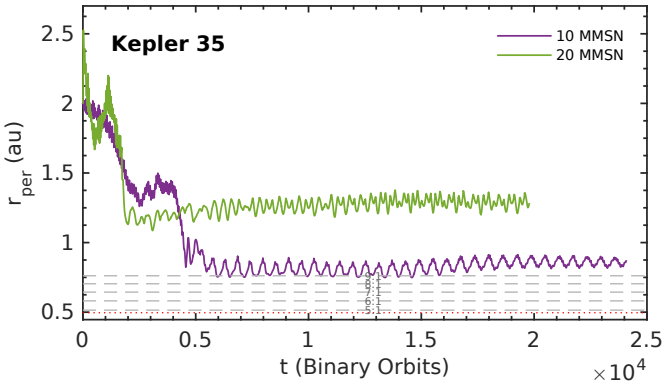

FIGURE 5.11: Evolution of pericentre distance of the protoplanetary cores in the 10_{MMSN} and 20_{MMSN} disc models. Of particular note is the decrease between 3000 and 5000 P_{b}. During this time the core has been trapped at the location of the first additional eccentric feature. Whilst its eccentricity is being excited, the pericentre distance is decreasing, to the point where it reaches the location of the inner eccentric cavity. Whilst the pericentre distance remains relatively constant, the eccentricity and semi-major axis are damped by this massive feature.

due to the similarity in evolution and final structure results from the previous Chapter for these low-eccentricity binaries. To recap, in the low-mass discs, the cores migrate inwards through the disc until they reach a location where their eccentricity is excited enough ($e_{\mathrm{p}} \approx e_{\mathrm{d}}(a_{\mathrm{p}})$) to induce a torque reversal. This location corresponds to the edge of the eccentric cavity. The location of this edge, which is easily identifiable as the peak in the surface density, lies at a smaller radius in the *Kepler-35* system than in *Kepler-16*, due to its lower binary eccentricity. The final semi-major axis for the cores in the 1–5_{MMSN} models is 0.9 au – slightly smaller than the previous Pierens and Nelson (2013) result – and e_{p} oscillates around 0.11 for all three models (Figs. 5.10a and 5.10b). The mean value of e_{p} results from a balance between the highly eccentric disc pumping up the eccentricity and the surrounding material damping the eccentricity. None of the final planetary orbital elements obtained in the low-mass regime are in good agreement with those quoted in Welsh et al. (2012) for *Kepler-35 b*.

The results from the high-mass models also show the same evolutionary history, with slightly different final values for a_{p} and e_{p}, as the *Kepler-16* high-mass models. The 10_{MMSN} model shows evidence of trapping by the $m = 1$ eccentric mode at 1.6–1.9 au, where its eccentricity gets rapidly excited to 0.5. This highly eccentric orbit then brings the pericentre close enough to the inner cavity to allow the planet to be captured by the large amount of material skirting the boundary.

This material damps the orbit of the planet, decreasing the semi-major axis ($a_{\rm p}$ = 0.9 au) and eccentricity($e_{\rm p}$ = 0.03), to a near-circular orbit (see Figs. 5.10a, 5.10c and 5.11).

The $20_{\rm MMSN}$ model, matching the evolution of the core in the *Kepler-16* $20_{\rm MMSN}$ disc, migrates inwards through the disc – keeping a low eccentricity, $e_{\rm p} \approx 0.08$ – until it is trapped at the first extra eccentric feature, with a final semi-major axis, $a_{\rm p}$= 1.4 au. The eccentricity damping provided by the disc is sufficient that it remains at this location. Both the 10 and $20_{\rm MMSN}$ discs produce cores whose final eccentricity is in good agreement with that of *Kepler-35 b*, but the simulated semi-major axes are too large.

5.3 Evolution of Accreting Protoplanetary Cores

The simulations presented so far in this chapter all adopted a fixed mass for the planetary cores, corresponding to a mass ratio between the planet and central binary of $q_{\rm p} = 6 \times 10^{-5}$. The actual mass ratios for the observed systems are all larger than this by various factors (see Tab. 3.3), and so we now consider what happens to the orbital elements if the planets accrete gas and achieve their observed masses while migrating. The results above indicate that the planets normally halt their migration at a location that is too far from the binary to provide good agreement with the observations, so we examine whether or not the stopping orbital radii decrease as we increase the planet masses to their observed values. Only the $10_{\rm MMSN}$ and $20_{\rm MMSN}$ cases for the *Kepler-34* system produce final stopping radii that agree well with the observations, and this occurs because of the dramatic shrinking of the cavity size in this case for discs where self-gravity is important.

For the simulations presented in this section we undertook accretion scenarios for the evolved binary-disc-planet *Kepler-16* and *Kepler-34* systems. The initial core mass ratio used throughout this work means that the protoplanetary core in the *Kepler-35* models is within $\approx 20\%$ of the observed planet mass, so we didn't simulate gas accretion in this case.

The accretion routine of Kley (1999) was used to grow the mass of the protoplanetary cores ($q_{\rm p,0} = 6 \times 10^{-5}$) to that of the observed planet mass in the specific

system ($q_{\rm p} = 3.54 \times 10^{-4}$ and 1.01×10^{-4} in the *Kepler-16* and *-34* systems respectively). This prescription removes a portion of the gas from the Hill-sphere and adds its mass to that of the planet. The accretion time-scale, i.e. the time in which the Hill-sphere is emptied of gas, is determined as a fraction of the dynamic time-scale of the planet, $t_{acc} = f\, t_{dyn}$. The variable constant f is tuned for the *Kepler-16* simulations so that the planet reaches its final mass over $5000\, P_{\rm b}$. We use this approach to inhibit the growth of the planet. A constant value is used ($f = 0.01^{-1}$) for all the disc-mass models in the *Kepler-34* system, as the final planet mass is relatively low.

The issue worth noting with this set-up, in relation to a realistic comparison with the masses of the observed circumbinary planets, is that when accretion is turned on in these simulations the planet finds itself at a location with a wealth of material. Even conservative estimates for the accretion time-scale lead to rapid mass-growth. If planets in circumbinary discs only reach a gas-accretion phase when they are already at the cavity edge, it would be logical to assume that the planet could quickly grow to Jovian mass unless gas accretion is very slow indeed, or occurs at the end of the disc lifetime. Our simulations apply to the former possibility, but it is worth noting that circumbinary systems are self-selecting because too much gas accretion leads to the formation of a Jovian-mass planet, and these tend to be much more unstable due to dynamical interaction with the central binary (Nelson 2003). Even if circumbinary planets grow to be of Jovian-mass close to the cavity edge, we are unlikely to see them as they have a significant probability of being ejected from the system. The accretion scenarios that we consider here are run from the point in the simulations from the last section when the planet has reached a pseudo-steady orbit.

5.3.1 *Kepler-16* Results

Kepler-16 b, with $m_{\rm p} \simeq 0.3\, M_{\rm Jup}$ is the most massive of the three circumbinary planets that we consider in this work (Doyle et al. 2011). Using the gap-opening criteria of Crida et al. (2006) which states that for a given set of disc parameters, a planet of mass ratio, q will open a gap if:

$$1.1 \left(\frac{q}{h^3}\right)^{-1/3} + \frac{50\alpha h^2}{q} \leq 1, \tag{5.1}$$

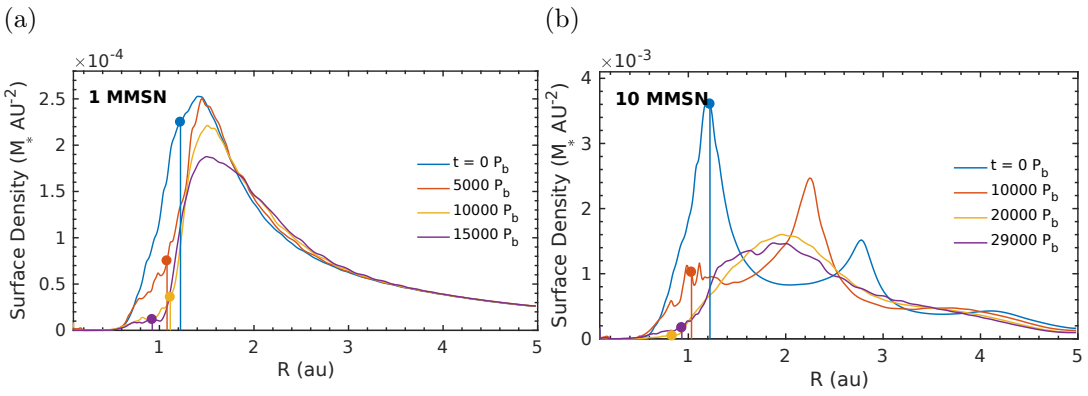

FIGURE 5.12: 1-D snapshots of the surface density profile in the 1_{MMSN} (a) and 10_{MMSN} (b) models in *Kepler-16*, once accretion onto the protoplanetary core is allowed. In the low-mass disc the core has grown from its initial mass to the final, observed mass of *Kepler-16 b* between the first and second profiles. It can be seen that whilst the planet has migrated further into the inner disc, it has also carved out a pseudo-gap in the inner edge of the cavity. In the massive disc, whilst the planet doesn't seem to open a gap, it does significantly alter the surface density profile over the whole radial extent.

one can see that for the viscous stress parameter and disc aspect ratio used in these simulations, the core will significantly alter the surface density profile of the disc when it approaches its final mass – as can be seen in Fig. 5.12. In the low-mass discs the core slowly migrates from its initial stopping position at $a_{\mathrm{p}} = 1.1\,\mathrm{au}$ further inwards to $a_{\mathrm{p}} = 0.75\,\mathrm{au}$, between the $6:1$ and $7:1$ MMRs with the binary (Fig. 5.13a). As the planets migrate into the cavity evacuated by the binary, they carve out this cavity further – opening one side of a gap. This process destroys the eccentric cavity, as the planet's mass dominates – resulting in a decrease in eccentricity $e_{\mathrm{p}} = 0.12 \rightarrow 0.03$. One anomaly in these results is the rapid outward migration of the core in the 5_{MMSN} model at $4000\,P_{\mathrm{b}}$ (Fig. 5.13). This is accompanied by a sharp decrease in e_{p}. Examining the evolution of the planet at this epoch, it can be seen that as the planet's mass grows it appears to interact with the $8:1$ MMR with the binary. These $n:1$ MMR locations have been shown to be unstable to planetary orbits because they excite the eccentricity (Nelson et al. 2000), and in this case the planet is scattered out. It is not ejected from the disc completely however, and is able to migrate back into the inner disc, avoiding further scattering events.

The planet in the 10_{MMSN} disc alters the surface density similarly to the planets in the low-mass discs. It can be seen in Fig. 5.12b that it doesn't open such a

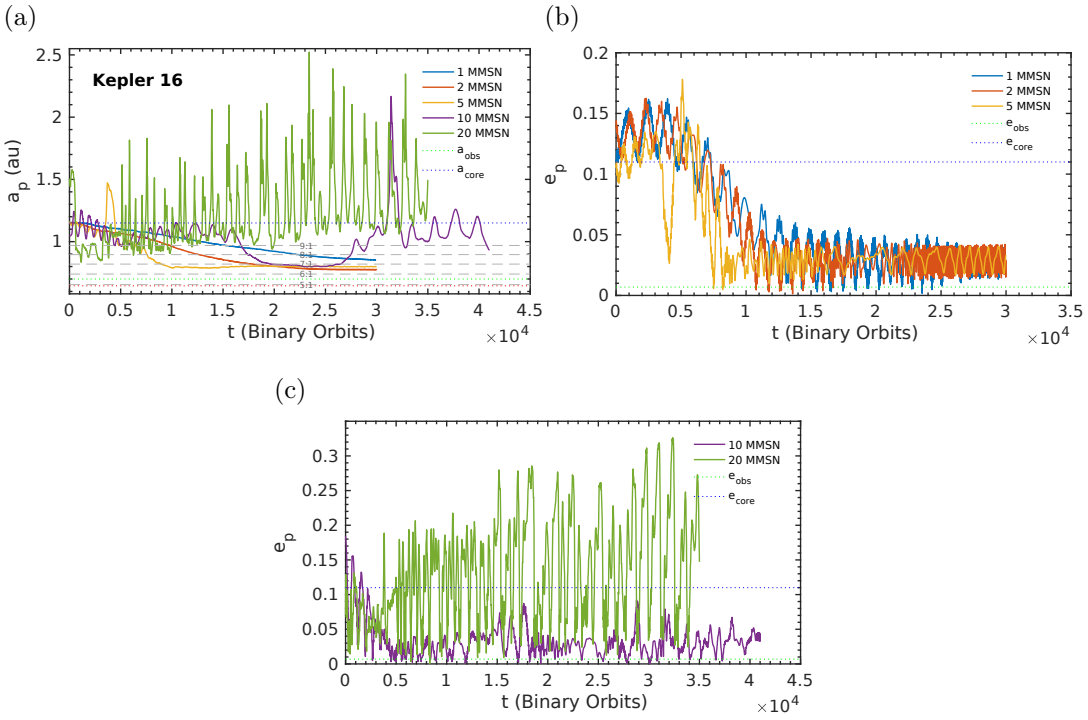

FIGURE 5.13: *(a)* Evolution of accreting protoplanetary cores' semi-major axes in evolved self-gravitating discs in the *Kepler-16* system. *(b & c)* Cores' eccentricity evolution in the low- and high-mass disc models respectively.

deep gap at the cavity edge. The presence of the planet leads to the destruction of the additional eccentric features in the outer disc. Any additional planet forming and evolving in the outer disc would have a very different migration pathway to the first planet, in a multi-planet formation and migration scenario – see (Kley and Haghighipour 2015). During the accretion phase of the simulation, slow inwards migration occurs to $a_{\rm p} = 1.0\,{\rm au}$, whilst the eccentricity of the core's orbit falls. The next $10000\,P_{\rm b}$ is spent at this distance, after which it migrates further into the inner disc, where it reaches $a_{\rm p} = 0.75\,{\rm au}$. For the remainder of the simulation lifetime it has an eccentricity $e_{\rm p} = 0.04$, an order of magnitude greater than that observed for *Kepler-16 b*. Over-estimating the eccentricity of cores in circumbinary discs seems to be a common outcome. It may be that post-disc evolution could alter the orbits of these objects. Between 2.5×10^4 and $3 \times 10^4\,P_{\rm b}$ the core seems to undergo a similar scattering event as that seen in the $5_{\rm MMSN}$ disc – oscillating around the $7:1$ MMR and consequently scattering out. This scattering and subsequent inwards migration seems to happen repeatedly over the course of the simulation. The mass of the disc is sufficient to maintain a significant

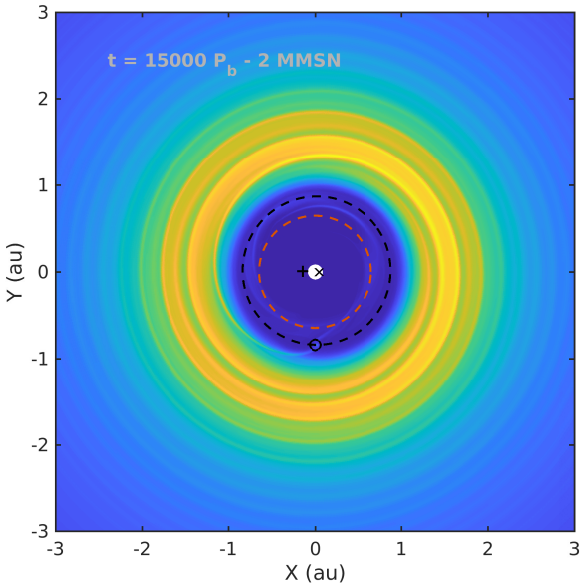

FIGURE 5.14: Surface density map of the *Kepler-16* 2_{MMSN} disc model once the core has grown to its observed mass and reached its final semi-major axis. The near-circularity of the planetary orbit is clear, whilst the complex interplay between the density waves launched from the Lindblad resonances with the planet, and those launched by the binary in the self-gravitating disc, has destroyed the eccentric inner cavity. A gap has been opened with a circular cavity interior to it.

eccentricity of its own, and excite that of the planet.

The evolution of the accreting core in the most massive 20_{MMSN} disc is even more disruptive. Initially, when its mass starts to grow, in the first few $1000\,P_{\mathrm{b}}$ of the simulation, it escapes the outer planet trap and migrates into the inner disc ($a_{\mathrm{p}} = 0.9\,\mathrm{au}$). During this phase it maintains a significant eccentricity ($e_{\mathrm{p}} \approx 0.1$) – because of this its orbit enters the region around the binary where the strongest $n : 1$ MMR exist ($n \lesssim 9$). It spends the remainder of the simulation lifetime undergoing repeated scattering and migration events, where its eccentricity dramatically rises to ≈ 0.3 and then circularises. If this continues, the core could in principal enter the critical stability limit during one of these events and be ejected from the system – although we have not yet seen this happen.

Figure 5.14 we can see that the structure of the circumbinary disc has been significantly altered by the growth of the planet to its observed mass. The opening of the gap, as well as strong spiral wakes launched at the Lindblad resonances with the planet act to destroy the eccentric cavity, making it more circular. This is clear in Fig. 5.15a; during the first $10000\,P_{\mathrm{b}}$ of the simulation, when the planet

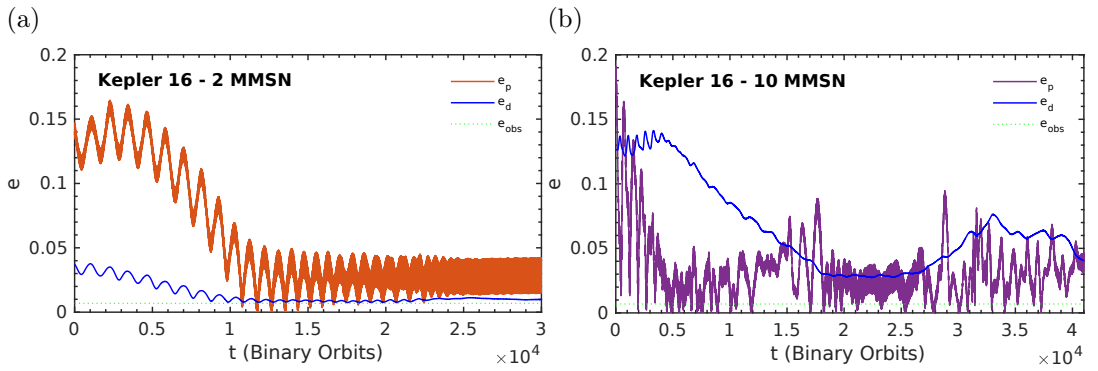

FIGURE 5.15: Comparison of planetary and disc (global) eccentricity evolution once gas accretion has started (at $t = 0\,P_{\rm b}$) in the 2 and $10_{\rm MMSN}$ models around the *Kepler-16* system(*(a)* and *(b)* respectively). The growth of the core to its observed mass in the first $5000\,P_{\rm b}$ of the scenario results in significant alteration of the disc eccentricity profile, as well as the average disc eccentricity. As the planet grows and it approaches the gap-opening regime, a decrease in disc eccentricity can be seen – in parallel to the decrease in planetary eccentricity. In the $10_{\rm MMSN}$ model the erratic changes in $a_{\rm p}$ beyond $2.5 \times 10^4\,P_{\rm b}$s are also accompanied by a significant growth in $e_{\rm d}$.

is accreting mass from the disc and migrating slowly inwards, the eccentricity of the disc decreases to 0.01. In the most massive discs, the growing and migrating planet disrupts the eccentric features in the exterior disc as well as the inner cavity – leading again to a decrease in $e_{\rm d}$ (Fig. 5.15b). The erratic changes in the orbit of the planets in the 10 and $20_{\rm MMSN}$ models also leads to corresponding fluctuations in the disc eccentricity. When the planet is on a wider, more eccentric orbit, the eccentricity of the disc can also grow.

In summary, we find that increasing the planet's mass in the low-mass discs leads to further inwards migration, and final orbital elements that are in rather good agreement with the observed values. Gas accretion in the high mass discs, however, leads to repeated interactions with the binary that cause the orbits of the planets to change erratically.

5.3.2 *Kepler-34* Results

Increasing the protoplanet's mass from $q_{\rm p,0} = 6 \times 10^{-5}$ to the observed mass of *Kepler-34 b* ($q_{\rm p} = 1 \times 10^{-4}$) – an increase of a little over 60% – results in little change of the orbital parameters. This is unsurprising as the core is still in the Type I planet migration regime in our disc models, and according to Eq. (5.1), is

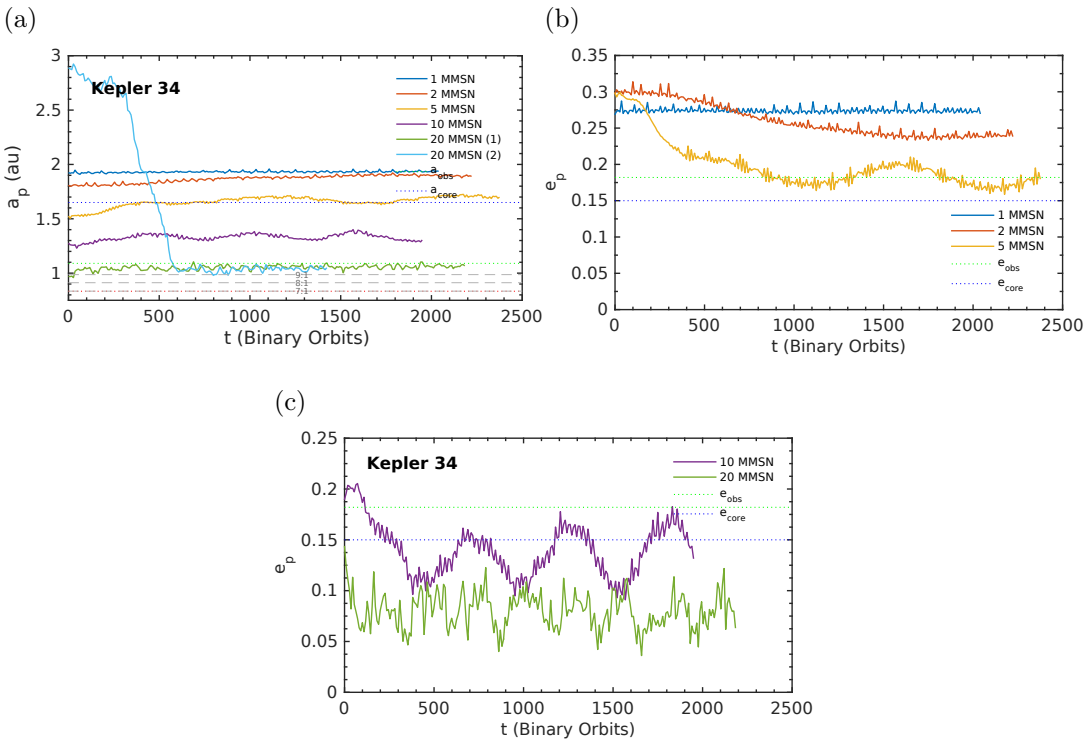

FIGURE 5.16: *(a)* Evolution of accreting protoplanetary cores' semi-major axes in evolved self-gravitating discs in the *Kepler-34* system. *(b & c)* Cores' eccentricity evolution in the low- and high-mass disc models respectively. The difference between the two cores in 20_{MMSN} models is the initial starting position. It can be seen that a small increase in planet mass is sufficient to alter the surface density in the outer disc, so that the previously trapped core can migrate inwards.

not capable of sufficiently disturbing the surface density distribution to open a gap. This lack of significant activity was apparent after a relatively short simulation time ($\approx 2000\,P_{\mathrm{b}}$), where after a period of relaxation the system reaches a pseudo-steady state. In Fig. 5.16 one can see a slight outward migration of the planets in the 2_{MMSN} and 5_{MMSN} models, associated with a circularisation of the orbit. A lack of change in the low-mass models mean that there is still poor agreement with the observed configuration of *Kepler-34 b*. The semi-major axes of the cores in this system are too large ($a_{\mathrm{p}} = 1.7$–$2\,\mathrm{au}$), with eccentricities which are too excited ($e_{\mathrm{p}} = 0.25$–0.275) – although good agreement with the observed eccentricity is obtained for the 5_{MMSN} core model where e_{p} is oscillating around 0.18. The 10 and 20_{MMSN} model cores also show little change when accretion is switched on, apart from a slight decrease in eccentricity in the 10_{MMSN} case due to more efficient damping by the disc.

The second 20_{MMSN} model run in the *Kepler-34* system which is initially released further out in the disc, but is trapped close to its starting position – mentioned at the end of Section 5.2.2 – shows the most dramatic response to accreting mass. The increased core mass is sufficient for it to escape the region of weak eccentric features, created by the self-gravitating disc response to the binary potential, in the outer disc. It quickly migrates through the disc, finally reaching $a_{\mathrm{p}} = 1.0\,\mathrm{au}$, the same as the first 20_{MMSN} model presented and in good agreement with the observed value of a_{p}, although both models have small values of e_{p}. In this system it is especially hard to produce a planet so close-in with a non-negligible eccentricity that matches the observations. Increasing e_{p}, hence lowering the pericentre distance, further increases the risk of destabilising encounters with the $n : 1$ MMR region and the chance of a catastrophic ejection event. This, along with post-disc dissipation evolution with the binary, may be the reason why we may yet to observe a very close-in circumbinary planet (like *Kepler-16* or *-35 b*) with a significant eccentricity like that of *Kepler-34 b*.

5.4 Evolution of Protoplanetary Cores in Dissipating Discs

From the beginning of this investigation we have been using the disc-mass as a proxy for the age of the circumbinary disc. It is logical to assume that when the disc first forms into a stable entity around the central binary it is at its most massive, and over the course of its lifetime loses mass due to a number of different processes – accretion onto the central binary, loss from photo-evaporative and/or magnetised winds from the surface of the disc, etc. Whilst we have simulated the disc structure and evolution at different eras throughout its lifetime, we have not investigated the effects of *transitioning* from a high-mass environment to that of a low-mass one. The dichotomy of results from Chapter 4 suggest that the additional eccentric features seen in the outer disc will disperse as the disc-mass and the strength of self-gravity decrease. Without a sustaining action, the viscous and pressure forces in the disc will dissipate these eccentric features. As self-gravity diminishes in the disc we would also expect the compactness of the system to relax back to that seen in the least-massive 1_{MMSN} disc – the eccentric cavity will increase in size, especially those seen in the *Kepler-34* system. The surface density profile will alter as the disc relaxes and we would expect the planet to

migrate outwards with the cavity. In those discs where the planets are halted by the counteracting of the Lindblad torque by the positive co-rotation torque, the planet may be able to stay at this stable stopping location whilst the disc relaxes. We are not investigating the mechanisms and physics which dictate disc mass-loss and dispersal – these are topics of ongoing research – and perhaps deserve their own work in the context of massive self-gravitating discs. Instead, and as a computation time saving exercise, we use a simple exponential decay to dissipate the mass of the disc:

$$\Sigma_{ij}^{n+1} = \Sigma_{ij}^{n} \exp\left(-\frac{\Delta t}{\tau}\right), \tag{5.2}$$

where Σ_{ij} is the cell surface density value, $\Delta t = t^{n+1} - t^{n}$, is the time between successive time levels n and $n+1$, and τ is the decay time constant. In each disc this value is chosen so that after 5000 $P_{\rm b}$ the total disc mass $m_{\rm d}$ will have decreased from its initial value down to the equivalent $1_{\rm MMSN}$ model in that system. For reference, to reach a $1_{\rm MMSN}$ disc from a $10_{\rm MMSN}$ or $20_{\rm MMSN}$ mass disc in the *Kepler-16* system, time constants of $\tau = 1520\,P_{\rm b}$ and $1175\,P_{\rm b}$ are used respectively. In the $20_{\rm MMSN}$ disc this is equivalent to a mass-loss rate, $\dot{M} = 6 \times 10^{-4} M_{\odot}{\rm yr}^{-1}$. This arbitrary mass-loss is not motivated by any particular process, and whilst this rate is unphysically efficient, the dynamical time-scales associated with the disc and planet such that they can respond to any changes in the disc. Once the disc has reached a total disc-mass equivalent to the initial $1_{\rm MMSN}$ disc mass, the dissipation mechanism is stopped, to allow the disc and planet to reach a pseudo-steady-state on time-scales of a few $\times$ 10,000 binary orbits. This procedure is started in the disc once – similarly to the previous subsection looking into accretion scenarios – the initial binary-disc-protoplanet systems from Section 5.2.1 have reached quasi-steady state. This allows us to track the response of planets, trapped at the cavity edge or by eccentric rings, to the diminishing disc mass and relaxation or dissipation of eccentric features. During this procedure, and in the post-dissipation evolution of the planets, we consider non-accreting cores.

5.4.1 *Kepler-16* Results

The similarity of the results from the 1–$5_{\rm MMSN}$ models seen in Section 5.2.1 for the *Kepler-16* system prompted us to only carry out disc dispersal simulations for the most massive $10_{\rm MMSN}$ and $20_{\rm MMSN}$ models. Figure 5.17 shows the response of the planets' semi-major axes (top panel) and eccentricities (bottom panel) to the

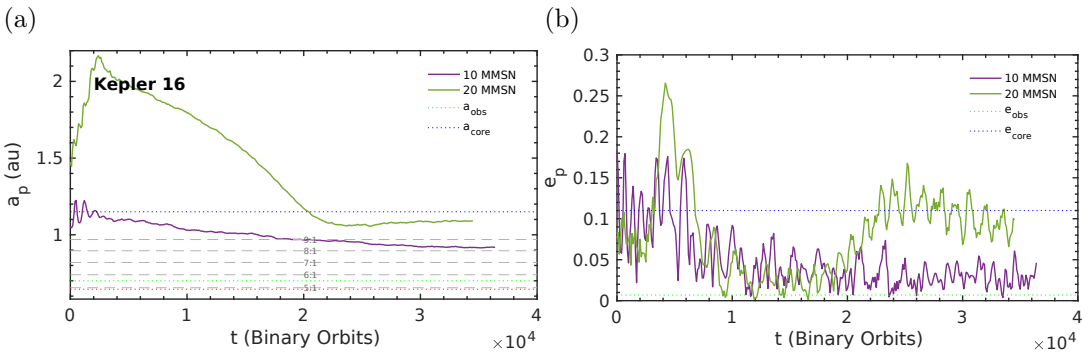

FIGURE 5.17: *(a)* Evolution of protoplanetary cores' semi-major axes in dissipating self-gravitating discs, in the *Kepler-16* system. *(b)* The cores' eccentricity evolution in the 10MMSN and 20MMSN disc models.

disc dispersal, which occurs during the first $5000\,P_{\rm b}$ of these plots. A significant amount of post-dissipation evolution of the cores can be seen, especially in the $20 \rightarrow 1_{\rm MMSN}$ model.

As previously detailed, the core in the $10_{\rm MMSN}$ disc is orbiting at the edge of the inner eccentric cavity when migration halts. When dissipation starts to occur, the semi-major axis of the core increases from 1 to 1.2 au – the position of $r_{\rm max}$, or the cavity edge in the least massive $1_{\rm MMSN}$ model. The eccentricity of the core also increases in this period, increasing from around 0.05 to 0.1. This increase in eccentricity, due to reduced damping by the disc, increases the positive torque contribution from the outer disc, even as it relaxes due to dissipation. The balance between reduced eccentricity damping and the diminishing influence of the positive torque from the outer disc, dictates whether the core migrates inwards or outwards as the disc dissipates. After this initial period of outwards migration, this balance inverts. The semi-major axis decreases – past the initial stopping distance – further into the inner disc as the eccentricity drops – reaching a final orbit with $a_{\rm p} = 0.9\,$au and $e_{\rm p} \approx 0.025$. This model gives better final agreement with the observed *Kepler-16* system than the low-mass models. When dissipation starts, the core's small $a_{\rm p}$ and non-negligible $e_{\rm p}$ mean its pericentre distance lies around 0.8 au. The core retains this small value during dissipation, and as the eccentricity is damped by the disc. The final semi-major axis corresponds to a location between the 8 : 1 and 9 : 1 MMR with the binary – the core's low eccentricity however keeps it clear of interaction with these destabilising regions. Examining the surface density profile and planetary orbit in Fig. 5.18, one can see the similarity to the

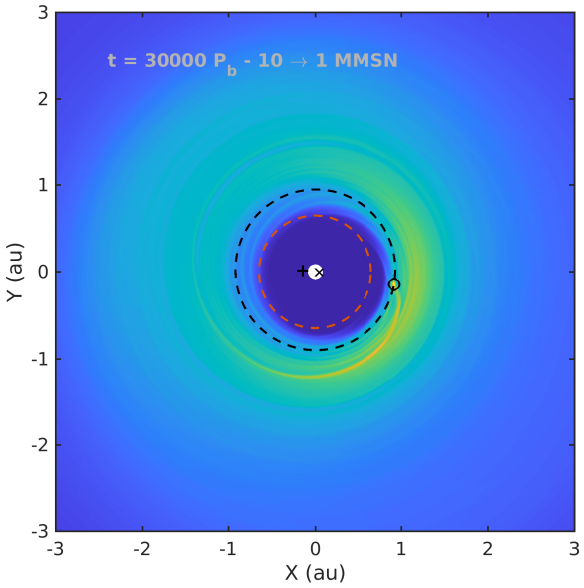

FIGURE 5.18: Surface density map of the *Kepler-16* 10_{MMSN} disc model once the disc has undergone mass dissipation, and the core has reached its final orbital position. Whilst the eccentric cavity has relaxed from the very compact initial 10_{MMSN} state to a cavity with a larger extent, the core has managed to retain a close-in, circular orbit.

low-mass *Kepler-16* discs (Fig. 5.4). The eccentric features in the outer disc have dissipated and the inner eccentric cavity has relaxed, to a size in good agreement with the 1–5_{MMSN} models. The difference in the shape of the planetary orbit is also clear, a more circular orbit inside, rather than tracing the outside edge of the cavity, is attained.

A very different evolution is seen in the 20_{MMSN} model. The core in this model is trapped at the location of the first eccentric feature in the outer disc when the process of dissipation begins. During dissipation the planet migrates outwards from $a_{\mathrm{p}} = 1.4$ to 2.2 au. After the first $2000\,P_{\mathrm{b}}$ of disc dissipation, migration reverses and the core migrates into the inner disc, reaching a final semi-major axis of 1.1 au. Examining the azimuthally averaged surface density profiles in Fig. 5.19 this evolutionary history can be explained. Comparing the three plots several important things can be extracted; the first being that between the first two panels the surface density profile has relaxed to one resembling a 10_{MMSN} profile. The tightly wound eccentric features in the 20_{MMSN} model dissipate outwards in the disc, but one relatively strong eccentric feature at 2.1 au can still be seen. If dissipation stopped here, we might see a migration scenario much like the 10_{MMSN}

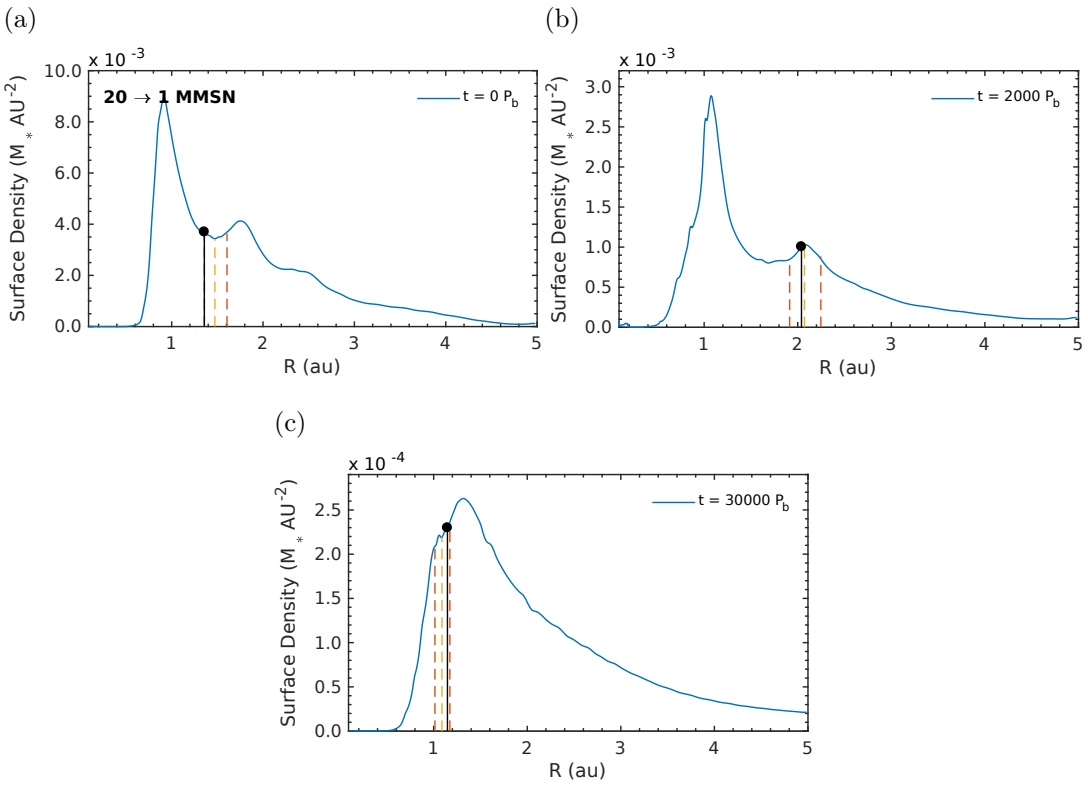

FIGURE 5.19: 1-D surface density profiles are shown here during the evolution of the 20_{MMSN} disc, and its embedded core. All line types and colours carry the same meaning as previous plots of this type. *(a)* shows the system at the beginning of disc dissipation, *(b)* is 2000 P_{b} orbits through this process, and *(c)* shows the system once the disc has relaxed and the planet has reached its final stopping position. The middle panel's surface density distribution looks very similar to those seen from 10_{MMSN}, whilst the last panel looks very similar to a 1_{MMSN} model. The planet initially migrates outwards as it follows the dissipating eccentric feature. Once this feature has completely dissipated, and the surface density gradient in the outer disc is negative once more, the planet then migrates into the inner disc. It finally stops at the edge of the inner cavity, $a_{\mathrm{p}} = 1.1\,\mathrm{au}$, in good agreement with the results from core migration in the 1–5_{MMSN} models presented earlier.

model from Section 5.2.1, where the planet gets trapped, but then subsequently escapes. Dissipation does continue however, and the core is free to immediately migrate into the inner disc, as the eccentric features are destroyed. The last panel shows the planet at its final location of $a_{\mathrm{p}} = 1.1\,\mathrm{au}$. This value and the surface density profile are very similar to the final state of the 1_{MMSN} model from Section 5.2.1, and its final $e_{\mathrm{p}} \approx 0.075$ is still an order of magnitude greater than the near circular orbit of *Kepler-16 b*. To summarise, the core – still trapped by the eccentric feature – migrates outwards as it follows the dissipating perturbation,

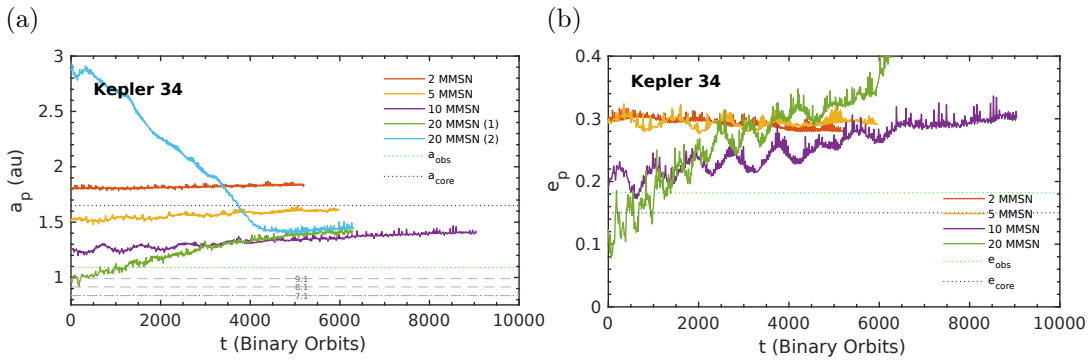

FIGURE 5.20: *(a)* Evolution of protoplanetary cores' semi-major axes in dissipating self-gravitating discs in the *Kepler-34* system. *(b)* The same cores' eccentricity evolution in these dissipating discs.

until the eccentricity of the core diminishes enough so that the positive torque contribution from the outer disc stops. The net negative torque migrates the core inwards towards the central cavity, where the eccentricity increases again, inducing another torque reversal, halting migration in the inner disc.

5.4.2 *Kepler-34* Results

In contrast to *Kepler-16*, in the *Kepler-34* system we undertook disc dissipation in the 2–20$_{\mathrm{MMSN}}$ models, as there was disc structure and planetary orbit differences across this whole range, reducing their disc mass to 1$_{\mathrm{MMSN}}$. With these models, we would expect the core semi-major axes and eccentricities to converge on the values reached by the core in the 1$_{\mathrm{MMSN}}$ model, as the disc mass dissipates. Examining Fig. 5.20a, the evolution of a_{p}, we see this is not the case. Whilst there is evidence of slight outwards migration as a result of the disc relaxing, they do not migrate significantly to $a_{\mathrm{p}} \approx 2\,\mathrm{au}$ – the location of the 1$_{\mathrm{MMSN}}$ model core. The 2$_{\mathrm{MMSN}}$ core shows little change, 5$_{\mathrm{MMSN}}$ migrates outwards to 1.6 au where it halts, and the high-mass discs all converge to 1.4 au. As the eccentric features in the outer disc dissipate, the core in the second 20$_{\mathrm{MMSN}}$ model is able to escape the outer disc and migrate into the inner disc, where it halts at 1.4 au, close to the stopping radius of the other 20$_{\mathrm{MMSN}}$ run with reducing disc mass, and the corresponding 10$_{\mathrm{MMSN}}$ case. Comparing the surface density maps in Fig. 5.21, the lack of agreement between the basic 1$_{\mathrm{MMSN}}$ migration scenario and the disc-dissipated 20→1$_{\mathrm{MMSN}}$ models is clear. Whilst there is some evidence of the disc relaxing

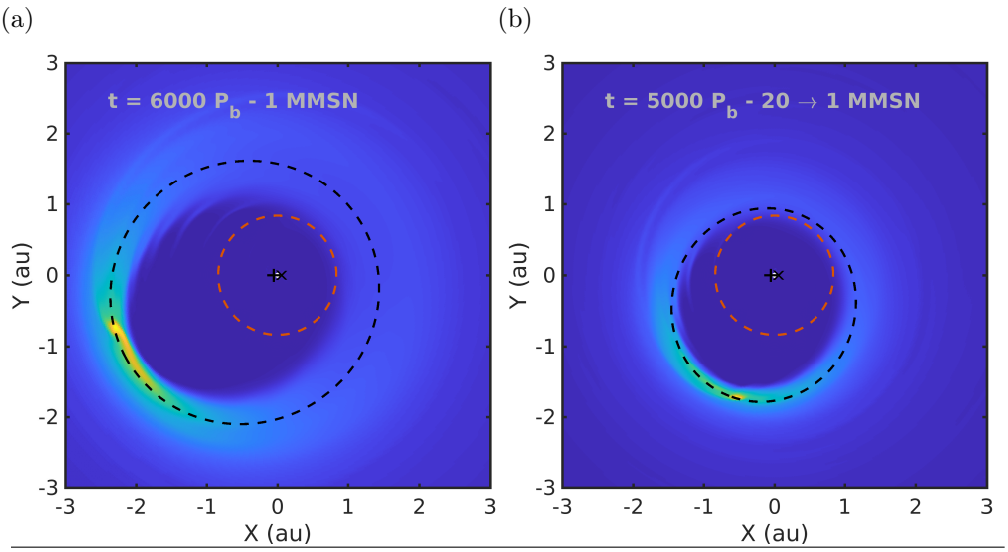

FIGURE 5.21: Surface density maps of the *Kepler-34* 1_{MMSN} system once the planet has reached its final orbit *(a)*, and the final state of the $20 \rightarrow 1_{\mathrm{MMSN}}$ dissipation model *(b)*, once the disc has relaxed and the planet has migrated outwards to the orbit seen here. Despite the mass being equal in these discs, the cavity in the dissipated case is still much smaller and less eccentric.

during its dissipation, the cavity in the latter model is still more tightly bound around the central binary. As a result the planet is in a much closer orbit than expected. It appears that the presence of the planet in the inner cavity interferes with the relaxation of the disc and prevents it from relaxing to the configuration expected from the 1_{MMSN} run. It is for this reason that we achieve a smaller stopping radius for the planets when the disc mass transitions from high to low-mass, and indicates that the history of the system influences the final stopping location of the planet.

5.4.3 *Kepler-35* Results

Similar results to *Kepler-16* in Section 5.2.1 prompted a similar approach for running disc dissipation scenarios in the *Kepler-35* systems; ignoring the low-mass models which show consistent results and focusing on the high-mass models which show the most variation, both with each other and the low-mass cases. The cores in the 10_{MMSN} and 20_{MMSN} models start in much the same positions as those in the *Kepler-16* models; the 10_{MMSN} core on a close-in orbit ($a_{\mathrm{p}} = 0.9\,\mathrm{au}$) with a low eccentricity, and the 20_{MMSN} core trapped in the outer disc by the first

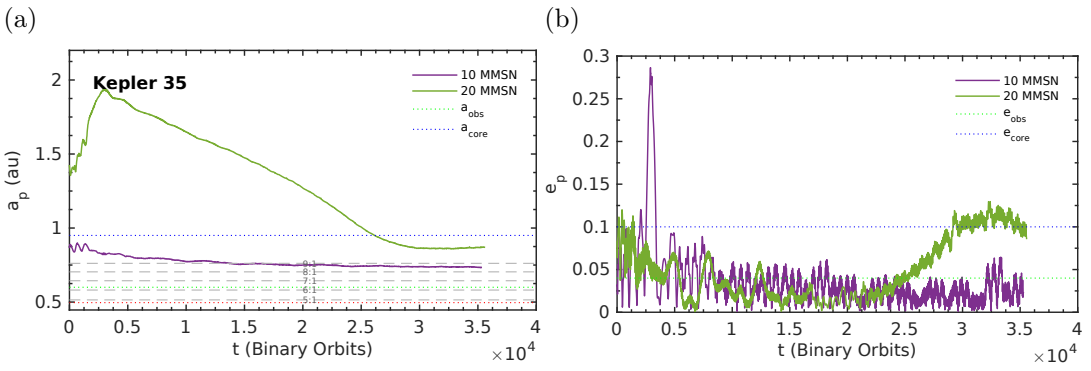

FIGURE 5.22: *(a)* Evolution of protoplanetary cores' semi-major axes in dissipating self-gravitating discs in the *Kepler-35* system. *(b)* The same cores' eccentricity evolution in these dissipating discs.

additional eccentric feature. Examining Fig. 5.22 the similarity continues – the cores follow the same migration pathway as their counterpart cores in the Sec. 5.4.1 simulations. The replication of the same evolutionary scenarios in different mass-ratio binary systems, suggest that the mechanisms observed in the above sections are relatively robust. For low-mass, isothermal discs, with the same structure, the zero torque location should be the same – hence planets in these discs halt migration at the same location. The core in the dissipating 20_{MMSN} model reaches the same semi-major axis as the core in the 1_{MMSN} model in our first set of simulations; when it reaches the inner disc the structure is the same because the disc has already relaxed. On the other hand, the core in 10_{MMSN} has already reached the inner disc, with a different disc structure. As the disc dissipates, the planet also has an impact on the final disc structure, which shifts the zero torque location – inwards in this case. The tendency for the cores in the 10_{MMSN} models to converge onto shorter period orbits between the 8 : 1 and 9 : 1 MMRs, resulting in better agreement with the observations than the other models when the planet mass is kept constant, is likely a fingerprint of the high-mass disc structure at 10_{MMSN}, which when it disperses allows the planets to achieve shorter period orbits with low eccentricities.

5.5 Discussion

This is the second half of an extended investigation which examines the influence of disc self-gravity on the evolution of gaseous circumbinary discs, and on the evolution of planets embedded in those discs. Whilst Chapter 4 dealt with examining this impact on the disc structure and evolution, in this present Chapter we use the end-points of these simulations as initial conditions for runs examining the orbital evolution of embedded planets. Most of the simulations that we present assume that the planet-binary mass ratio is fixed at $q = 6 \times 10^{-5}$. The aim of this work is to examine whether or not self-gravity can improve the level of agreement between the migration stopping locations of planets in the simulations and their currently observed orbital radii. In addition to examining the influence of disc mass, we also examined how the results changed when allowing planets to accrete gas so that they reached their observed masses while migrating, and the influence of allowing the disc mass to decrease with time such that high-mass discs transition to become low-mass discs after the planets have migrated to the their stopping radii. We summarise and discuss the results for the different binary systems below.

5.5.1 *Kepler-16*

We found that the cavity size in this case only changes significantly when the disc mass exceeds $10_{\rm MMSN}$. The migration of planetary cores of fixed mass in the lower mass discs resulted in them stopping close to the edge of the cavity, but with semi-major axes and eccentricities that were too large compared to the observations ($a_{\rm p} \sim 1.15$ au and $e_{\rm p} \sim 0.11$ versus observed values of 0.705 au and 0.007, respectively). The stopping location, however, was found to agree well with previous work presented in Pierens and Nelson (2013) that adopted different boundary conditions. Migration in the $20_{\rm MMSN}$ disc resulted in the planet being halted by one of the additional eccentric features further out in the disc that acted as a planet trap, so in spite of the disc cavity being significantly smaller in this case, the planet was unable to reach the cavity such that it could park closer to the central binary as required by the observations.

Allowing the planets to accrete gas so that they reach the mass inferred from observations (this requires the mass ratio to grow from 6×10^{-5} to 3.54×10^{-4})

resulted in much better agreement with observations for the low mass discs, although the planets still retain an eccentricity higher than that observed. Here, the planet grows in excess of the gap forming mass, and this allows it to push deeper into the tidally truncated cavity. Furthermore, the growth of the planet causes the eccentricity of the central cavity (and the other eccentric features) to diminish significantly, and this leads to the eccentricity of the planet orbits decreasing. For the lowest mass disc we obtain $a_{\rm p}$= 0.78 au which agrees rather well with the observed value for *Kepler-16 b*, and $e_{\rm p}$= 0.03 – significantly larger than the value infered from observations. We are confident we are exploring a formation and evolution likely to produce circumbinary planets in good agreement with the true population, however additional processes such as post-disc evolution need to be invoked to match both the semi-major axes and eccentricities of planets. The evolution of the accreting planets in the higher-mass $10_{\rm MMSN}$ and $20_{\rm MMSN}$ discs did not result in such good agreement with observations. Here, the planets have their eccentricities excited by the eccentric disc modes to values that cause them to interact more strongly with the central binary, leading to a sequence of scattering events that send them out into the disc and then back again over the full run times of the simulations.

Finally, allowing the disc mass to decrease for the heavy $10_{\rm MMSN}$ and $20_{\rm MMSN}$ discs, while keeping the planet-binary mass ratio $= 6 \times 10^{-5}$ caused the planets to end up orbiting closer to the star than when the disc masses were at their initial values. In particular, the reduction in disc mass causes the additional eccentric features in the disc to dissipate, and this allows the planet in the $20_{\rm MMSN}$ case to migrate inwards. The level of agreement with observations in these cases, however, is not as good as that obtained by allowing the planet masses to increase to their observed values. We conclude that for the *Kepler-16* system, self-gravity of the disc does not provide a positive contribution to obtaining agreement between observations and theoretical predictions.

5.5.2 *Kepler-34*

The binary system in *Kepler-34* has an eccentric orbit, and this leads to the formation of a wide and highly eccentric cavity when the disc mass is low. For large disc masses, however, self-gravity causes the disc cavity to shrink substantially, and this has a strong influence on the orbital evolution of embedded planets.

In the low mass discs the planets migrate inwards and stop at the edge of the cavity, which is too far from the binary for the stopping location to agree with the observations ($a_{\rm p} \sim 1.8$ au and $e_{\rm p} \sim 0.28$ versus the observed values 1.09 au and 0.182, respectively). In the high mass cases, however, we find that the additional eccentric features that form in the disc are somewhat weaker than in the *Kepler-16* run described above, and consequently the planets can normally migrate all the way to the central cavity in these cases. We find that the semi-major axes and eccentricities of the planets in the $10_{\rm MMSN}$ and $20_{\rm MMSN}$ discs straddle the observed values for *Kepler-34 b*, indicating that self-gravity in this case provides the possibility of obtaining much better agreement with the observations.

Switching on gas accretion makes very little difference to the results of these simulations because the final mass of *Kepler-34 b* is only 60% larger than the initial mass that we start with. Allowing the disc mass to decrease inevitably leads to the cavity sizes of the most massive discs increasing as the influence of self-gravity is diminished. Interestingly, however, we find that the presence of the planet prevents the cavity from relaxing to the size expected for a lower mass disc, and instead the amount of expansion observed is relatively modest. (The time to establish the approximately steady state cavity configuration, in the absence of planets, is typically ~ 3500 binary orbits. We have run our simulations for longer than this to ensure that we have achieved a quasi-steady state.) Although the planets in these more massive discs no longer show such good agreement with observations once the disc mass has diminished, they provide much better agreement than those planets that form and migrate in low mass discs. This leads us to conclude that self-gravity can have a positive impact on obtaining agreement between simulations and the observations of *Kepler-34 b* because of the rather dramatic influence that it has on the cavity size, and also because the system retains memory of its larger initial disc mass when the mass of the disc is slowly decreased. Formation of a planet in a heavy disc, followed by its migration and then rapid disc removal would seem to provide one way in which agreement with observations could be obtained for this system.

5.5.3 *Kepler-35*

As mentioned previously, the similar eccentricity of the *Kepler-16* and *-35* binaries leads to very similar outcomes both in terms of disc structure and orbital evolution.

Mass growth of *Kepler-35 b* from the initial planet-binary mass ratio of 6×10^{-5} was not considered because the final mass is only 20% larger than the initial mass. One consequence of this lower planet mass is that growth to a gap forming object that can push further into the inner cavity is difficult to invoke so that good agreement between the simulation outcomes and the observations of *Kepler-35 b* can be obtained, in contrast to the situation with *Kepler-16 b*. The final orbital radii of *Kepler-35 b* analogues were always too large by a factor of 1.5 compared to the observed values. Allowing the planet to be in the partial gap forming regime, such that it might push deeper into the cavity, can probably only be achieved by a significant reduction in the disc pressure scale height. Given that the two stars in *Kepler-35* are more massive and hotter than in the *Kepler-16*, it is not immediately obvious why the disc should be cooler in this case. Fitting this system using simulations therefore remains an unsolved problem, and will require a more sophisticated treatment of the disc thermodynamics to examine whether or not *Kepler-35 b* could have been in the gap forming regime when the protoplanetary disc was present.

In this work, gas accretion onto planets to their final masses and disc dissipation scenarios have been carried out separately. Combining the two, akin to the method in Pierens and Nelson (2013), in self-gravitating discs might help to fit the orbital properties of the planets but also shed light on the era in which the planets may have accreted their masses. Whilst disc-mass, and the influence of self-gravity can significantly alter disc structure, other physics will also play important roles. The inclusion of an adiabatic equation of state with radiative physics has been investigated in circumbinary systems, along with the effect on planet migration (Kley and Haghighipour 2014, 2015). The non-uniform, time dependent, radiation field produced by the two stars, however, has not yet been explored in combination with a more realistic thermal treatment of the disc. Finally, both theory and observations indicate that planets do not normally form in isolation, so the evolution of multi-planet systems (Kley and Haghighipour 2015) may provide better agreement with at least a subset of circumbinary planet observations.

5.5.4 Summary

With the results from the last Chapter as a starting point we have explored numerous planetary migration and accretion scenarios, as well as tracking the

planetary evolution as massive discs transition to a low mass 1_{MMSN} state. As hypothesised the eccentric features formed in the high-mass discs produced a variety of results across all the scenarios examined here. In some cases they acted as (temporary) planet traps, then releasing their captives into the inner discs, where the planets migrated into the more compact cavity structure to be found there. From this state, transitioning to a low mass state allowed the cavity structure to relax, as the strength of self-gravity decreased. In the most massive discs the planet relaxed back with the cavity, finally settling in an orbit in poor agreement with observations. However in several of the less massive discs, the state that the disc and planet system found before dissipation began, allowed it to stay in a relatively low eccentricity, short period orbit. Whilst carried out separately, allowing the cores to accrete mass from the disc resulted in planets on orbits relatively close to their observed counterparts, especially in the most massive discs. We conclude that a combination of migration, accretion and dissipation, with the right time scales for each, in a moderately high-mass self-gravitating disc could come close to recreating the *Kepler* circumbinary planets examined here. However it is clear that for the majority of the disc lifetime, self-gravity will play little role in structuring the circumbinary disc; if planets form at this time, we need additional mechanisms to shape the disc environment to allow them to reach the orbital configurations we observe them in.

Radiative Effects on Circumbinary Disc and Planet Evolution

Chapter Contents

6.1 Introduction

The thermal structure of protoplanetary discs is dictated by a balance between heating and cooling processes; including but not limited to, viscous dissipation, radiative cooling and stellar irradiation. In the outer regions of protoplanetary discs stellar irradiation of the disc's upper surfaces dominates, creating a flared structure where the disc aspect ratio increases with radius (Chiang and Goldreich 1997; Dullemond and Dominik 2004; Bitsch et al. 2013). In the inner disc the temperature is set by the balance between viscous heating and cooling, so the

viscosity of the disc determines the equilibrium structure (Bitsch and Kley 2011; Bitsch et al. 2013).

The migration of planets is also governed by the temperature structure in the disc (Ward 1997). For low-mass planets the entropy-gradient portion of the corotation torque can slow the rate of inward migration or even counteract the negative Lindblad torque, allowing outwards migration (see Section 1.4 and references therein for details). The radial temperature gradient in the disc directly impacts the entropy gradient, so modelling a realistic temperature profile is vital for accurately tracking the evolution of embedded low-mass planets. The inclusion of radiative effects (such as stellar irradiation, surface cooling and radiation transport) can significantly slow the rate of inwards migration of low-mass planets (Paardekooper and Mellema 2006).

The inclusion of a realistic equation of state, and radiative effects, has been examined in a limited context for discs and planets around binary systems. Müller and Kley (2012) examined the evolution of a circumstellar disc under the perturbing influence of a companion star on an exterior orbit. They included the effects of radiative cooling and viscous heating, finding that versus isothermal discs the disc eccentricity excited by the periastron passage of the companion was much lower. Discs with a lower disc aspect ratio had larger disc eccentricities. In a study examining the evolution of a circumbinary disc around the *Kepler-38* system Kley and Haghighipour (2014) found the inclusion of an adiabatic equation of state, viscous heating, radiative cooling and radiation transport resulted in discs with higher eccentricities for thicker discs. In both investigations the mass of the disc also had an impact on the evolution of disc structure, with lower-mass discs obtaining smaller central cavities in the circumbinary case.

Both the above cases did not include the inclusion of stellar irradiation in the energy evolution of the disc. The stars can not only irradiate the surface of the disc – the dominant heat source in the outer disc – but it can also irradiate the mid-plane of the disc directly through the disc's inner edge. In many cases this is not included in simulating protoplanetary discs as the inner disc is relatively opaque to the stellar irradiation, so all the heat is deposited at the disc inner edge, which then re-radiates as a black body. In a circumbinary disc the inner disc is evacuated of material due to the tidal torques exerted on the disc material by the central binary. Coupled with radiative heat transport through the mid-plane of the disc, this may allow stellar irradiation to penetrate further into the disc. With

TABLE 6.1: *Kepler-16* orbital and mass parameters, taken from Doyle et al. (2011).

$q = M_B/M_A$	a_b (au)	e_b
0.294	0.224	0.159

stellar irradiation of the disc surface, the influence of the stars' radiation could impact the temperature profile of the entire disc. The temperature profile this creates in the disc could then influence the migration of low-mass planets through the entropy-gradient corotation torque

In this section we present preliminary results of simulations examining the evolution of radiative circumbinary discs, as well as the migration of low-mass protoplanets embedded within them. In these simulations we include viscous, surface irradiation and mid-plane irradiation heating, surface radiative cooling, and FLD radiation transport. For details on how these are implemented see Chapters 2 and 3. We compare simulations containing various combinations of these processes with a purely isothermal disc, focusing on the impact of the ray-traced mid-plane irradiative heating, and radiation transport through the mid-plane. In Section 6.2 we summarise the set-up used to run these simulations; the results pertaining to the disc evolution and structure are presented in Section 6.3; the migration of low-mass protoplanetary cores is examined in Section 6.4.

6.2 Simulation Set-up

FARGORAD, our extension to FARGO-ADSG, was used to run several hydrodynamical simulations of 2-D circumbinary discs, and embedded protoplanetary cores. With the exception of the additional parameters used in the energy equation evolution, the binary-disc-planet parameters are similar to those used in Chapters 3–5. Our limited run of simulations were carried out with a binary with the observed orbital parameters and mass of *Kepler-16* (see Tab. 6.1). Like the previous two Chapters, the orbital parameters of the binary are kept fixed, ignoring the back reaction of the binary with the disc. We follow the procedure developed in Chapter 3 and partially embed the binary system within the computational domain of the disc, as well as using logarithmic spacing in the radial direction. Although we are not using the self-gravity module for this work, the additional resolution provided in the inner disc by this set-up is useful in capturing flows

TABLE 6.2: Summary of the radiative components included in each simulation. All the adiabatic (*AD*) runs include viscous heating, pressure work, radiative cooling and surface irradiation. RT stands for the ray-traced mid-plane irradiative heating. *RAD* corresponds to the fully radiative simulation.

Run Name	FLD	RT	Adiabatic EoS
ISO	✗	✗	✗
AD	✗	✗	✓
AD+FLD	✓	✗	✓
AD+RT	✗	✓	✓
RAD	✓	✓	✓

around the binary. A resolution of $N_r = 512$ cells is used between $r_{\rm in} = 0.09\,{\rm au}$ and $r_{\rm out} = 5.0\,{\rm au}$. The same number of cells is used in the azimuthal direction. At the boundaries, we use a Viscous outflow condition at the inner edge, with a β parameter of 5, and an Open outflow condition at the outer edge – the same parameters used in our self-gravity investigations.

6.2.1 Initial Conditions

To model the anomalous turbulence in the disc, the α-model prescription of Shakura and Sunyaev (1973) is used, with $\alpha = 1.0 \times 10^{-3}$. The surface density of the disc is initialised with the following distribution:

$$\Sigma\left(r\right) = \Sigma_0 f_{\rm gap} r^{-3/2}, \tag{6.1}$$

where $f_{\rm gap}$ is given by Eq. (3.10), and the gap extends to $2.5a_{\rm b}$. The mass contained within 30 au is set by the choice of Σ_0 to be equivalent to 1 Minimum Mass Solar Nebula (MMSN), which equates to $\Sigma_0 = 3000\,{\rm g cm^{-2}}$. A constant aspect ratio is set throughout the disc equal to $H/r = 0.05$, which assuming $M_\star = M_{\rm A} + M_{\rm B}$ equates to a temperature profile in the disc $T\left(r\right) \propto r^{-1}$. In the isothermal runs the kinematic viscosity and disc aspect ratio will not evolve from their initialised profiles.

6.2.2 Energy Evolution

Non-isothermal runs used an adiabatic equation of state, with an adiabatic exponent $\gamma = 1.4$, and mean molecular weight $\mu = 2.36$ in atomic mass units. In

TABLE 6.3: Observed stellar parameters of the *Kepler-16* binary system from Doyle et al. (2011), compared with the Pre-Main-Sequence parameters calculated from Siess et al. (2000) used for the stellar irradiation heating.

	Current values (Doyle et al. 2011)	PMS Values (Siess et al. 2000)
$M_{\rm A}\,(\mathrm{M}_\odot)$	0.690	0.690
$M_{\rm B}\,(\mathrm{M}_\odot)$	0.202	0.202
$R_{\rm A}\,(\mathrm{R}_\odot)$	0.649	1.11
$R_{\rm B}\,(\mathrm{R}_\odot)$	0.226	0.66
$T_{\star,\rm A}\,(\mathrm{K})$	4450	4000
$T_{\star,\rm B}\,(\mathrm{K})$	-	3200

addition to viscous heating and pressure work, all the adiabatic simulations also include radiative surface cooling (so that an equilibrium mid-plane temperature can be obtained), and disc surface irradiation from the two binary components. To test their influence on the evolution of the circumbinary environment, simulations were undertaken testing ray-traced mid-plane irradiative heating (RT) and flux-limited diffusion radiative transport (FLD) individually; Tab. 6.2 summarises the numerous set-ups. We call the simulation containing all the radiative heating, cooling, and transport processes fully radiative *RAD*.

Analytical formulas are used for the Rosseland mean opacity, with the opacity table of Bell and Lin (1994). The surface and mid-plane irradiation heating terms are calculated from the true position of each binary component. Each star has been given PMS values for their effective surface temperature and radii, constructed with values from the models of Siess et al. (2000) with an age one-tenth of the ZAMS time (see Tab. 6.3).

6.2.3 Planet Evolution

Once the circumbinary disc structure and temperature profile have reached a pseudo-steady-state a $20\,\mathrm{M}_\oplus$ protoplanetary core will be introduced on an initially circular orbit. As a time-saving exercise the initial semi-major axis of the planet will be chosen to be just exterior to the largest cavity of the runs presented. In the planetary potential calculation a smoothing length $\epsilon = 0.4H\,(\mathbf{r}_{\rm p})$ is used. For reference, the observed planet in *Kepler-16* is on an orbit with $a_{\rm p} = 0.705\,\mathrm{au}$ and $e_{\rm p} = 0.007$, and an inferred mass of $0.33\,\mathrm{M}_{\rm Jup}$ Doyle et al. (2011).

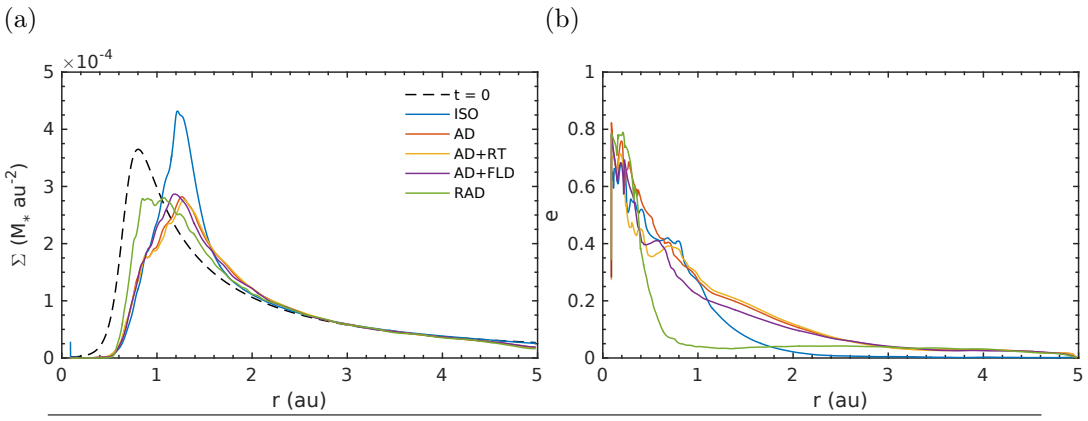

FIGURE 6.1: Azimuthally averaged surface density and disc eccentricity profiles in the isothermal, adiabatic and radiative discs. The fully radiative model (*RAD*) can be seen to have a very small eccentric cavity. Whilst the cavity size in the adiabatic models is similar to the isothermal model, the peak surface density value is about a third smaller.

6.3 Disc Evolution and Structure

Examining the surface density and disc eccentricity profiles of the discs once they have a reached a pseudo-equilibrium state (Fig. 6.1), several things can be noted. Perhaps the most obvious is that the eccentric cavity created in the fully radiative disc has not shifted significantly outward from the initialised gap function profile. Whilst the isothermal and adiabatic models (containing viscous heating, radiative cooling, surface irradiation), obtain a cavity with an edge at 1.2 au, the cavity edge in the *RAD* model lies at 0.8 au (Fig. 6.1a). It is likely that the zero-torque radius for a low-mass planet in this disc would be in very close proximity to the observed location of *Kepler-16 b*. Although the isothermal and adiabatic discs have similar cavity sizes, the adiabatic models' peak surface density value at the edge of the cavity is a third of the maximum value in the isothermal model. Examination of the outer disc shows that a significant amount of material may been lost through the outer boundary, possibly due to a pressure wave propagating outwards as the outer disc relaxes. Whilst we want to avoid wave-reflection at this edge, this should be monitored in radiative discs as the column density in the disc can affect the thermodynamics.

The reduced eccentric cavity size is clear in the cell eccentricity profile, Fig. 6.1b. The eccentricity drops dramatically in the *RAD* model, reduced to 0.01 within 0.8 au. At the same radial location the eccentricity in the isothermal and adiabatic models is between 0.28 and 0.4 – with the largest value in the isothermal

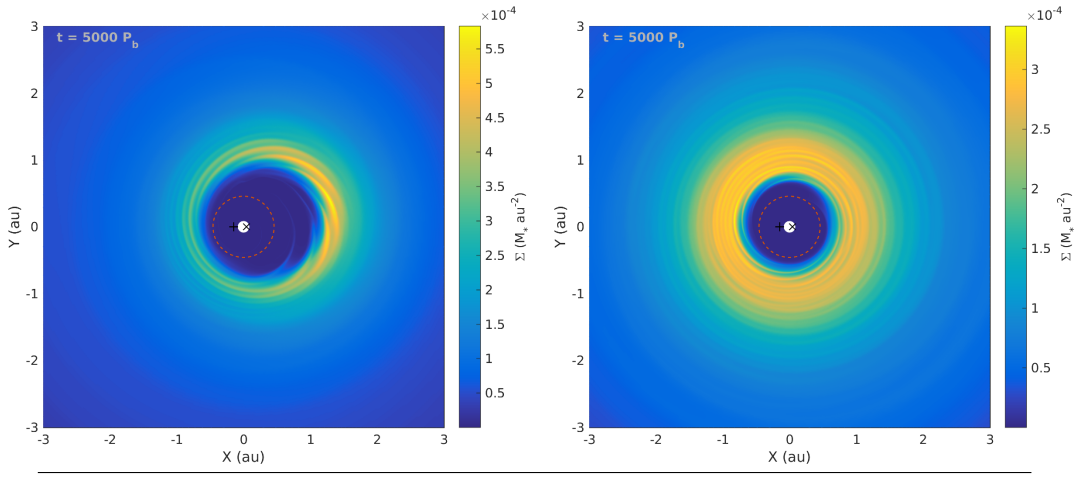

FIGURE 6.2: Side-by-side comparison of surface density maps in the adiabatic, with no RT or FLD (left panel) and fully radiative (right panel) disc models. A central cavity can be seen in the *RAD* case, but with little evidence of significant eccentricity. In the adiabatic disc, clearly defined density waves can be seen at the edge of the eccentric cavity.

model. The difference between the peak surface density values in the isothermal and numerous *AD* models can be explained by the eccentricity profile in the discs. The eccentricity in the isothermal disc is significant out to 2.0 au, whereas the *AD* discs maintain an eccentric structure out to 3.0 au. The greater extent of the eccentric material in these discs means the associated mass distribution is more diffuse, creating a lower peak surface density value. The difference in cavity structure is clear in 2-D surface density maps. Figure 6.2 shows the disc structure obtained in the *AD* and *RAD* models; the fully radiative model shows no significant eccentricity to the cavity, whilst the adiabatic disc exhibits a cavity with a significant eccentric extent, but also clearly defined density waves on the edge of the cavity. These same waves are also seen in isothermal discs, but are grouped much closer together.

Perhaps unsurprisingly, the disc-integrated eccentricity of the fully radiative model is lower than the isothermal and *AD* models (Fig. 6.3a). Whereas the eccentricity in the isothermal disc grows to $e_{\rm d} \approx h = 0.05$, the evolution of the nearly circular cavity in the *RAD* case reaches an equilibrium value ≈ 0.035. The inclusion of either mid-plane irradiation or FLD in the adiabatic models slightly increases the disc eccentricity value over the purely adiabatic model. The larger radial extent of the eccentric material in the *AD* models is evident in their disc eccentricity evolution. After $1500\,P_{\rm b}$ the disc eccentricity starts to increase from ≈ 0.05 to

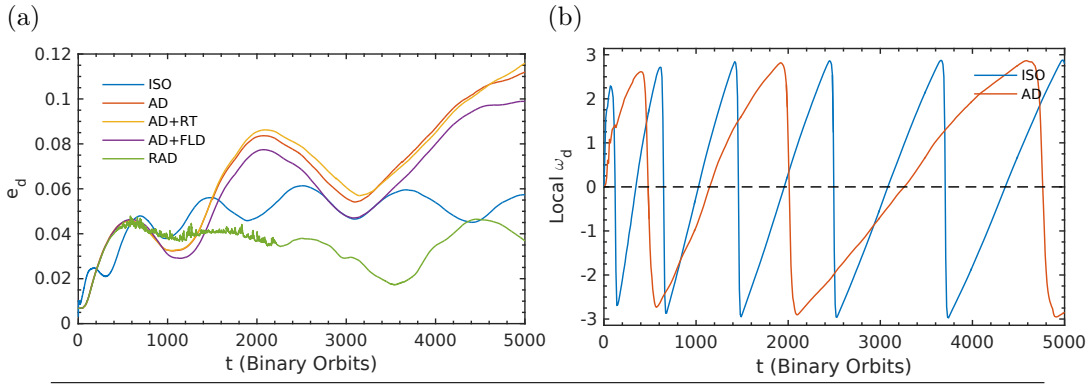

FIGURE 6.3: *(a)* Evolution of the global disc averaged eccentricity. The isothermal model shows the behaviour seen in Pierens and Nelson (2013) where the disc eccentricity saturates around the aspect ratio of the disc. The adiabatic runs show significant disc eccentricity growth, due to the large extent of eccentric material in the disc. Although the evolution is irregular at early times, the fully radiative disc seems to reach a disc eccentricity smaller than the isothermal case. *(b)* Comparison of longitude of pericentre (local calculation) evolution of the isothermal and *AD* model. The slow period of precession gives rise to the eccentricity oscillation in the adiabatic disc.

> 0.1. A very slow oscillation in the disc eccentricity is also evident. This oscillation is caused by precession of the central cavity; eccentricity maxima occur when the lines of nodes of the disc and binary are aligned. The very long period of the eccentricity oscillations, $\approx 3000\, P_{\rm b}$ in the adiabatic discs, compared to $\approx 1000\, P_{\rm b}$ in the isothermal disc, suggest that the eccentric cavity also precesses very slowly. By comparing the local calculation of the longitude of pericentre evolution, which tracks the evolution of material around the cavity and cavity edge, of the isothermal and adiabatic models in Fig. 6.3b we can see that this is true. The precession of the eccentric material skirting the boundary is not only influenced by its gravitational interaction with the binary, but also the pressure (gradients) in the disc.

The irregular evolution of the disc eccentricity seen in Fig. 6.3a for the *RAD* model is also apparent in the surface density evolution of the disc. Figure 6.4 shows snapshots of the disc during the initial $4000\, P_{\rm b}$ of the simulation. Whilst the first few $1000\, P_{\rm b}$ of a circumbinary simulation can be quite unordered as the binary tidally truncates the cavity, there is usually some semblance of structure as the $m = 2$ spiral wave gradually creates an eccentric cavity. This is seen in the surface density maps taken after $1000\, P_{\rm b}$ in the isothermal and adiabatic discs in Fig. 6.5. The spiral density waves which create the eccentric cavity can be clearly

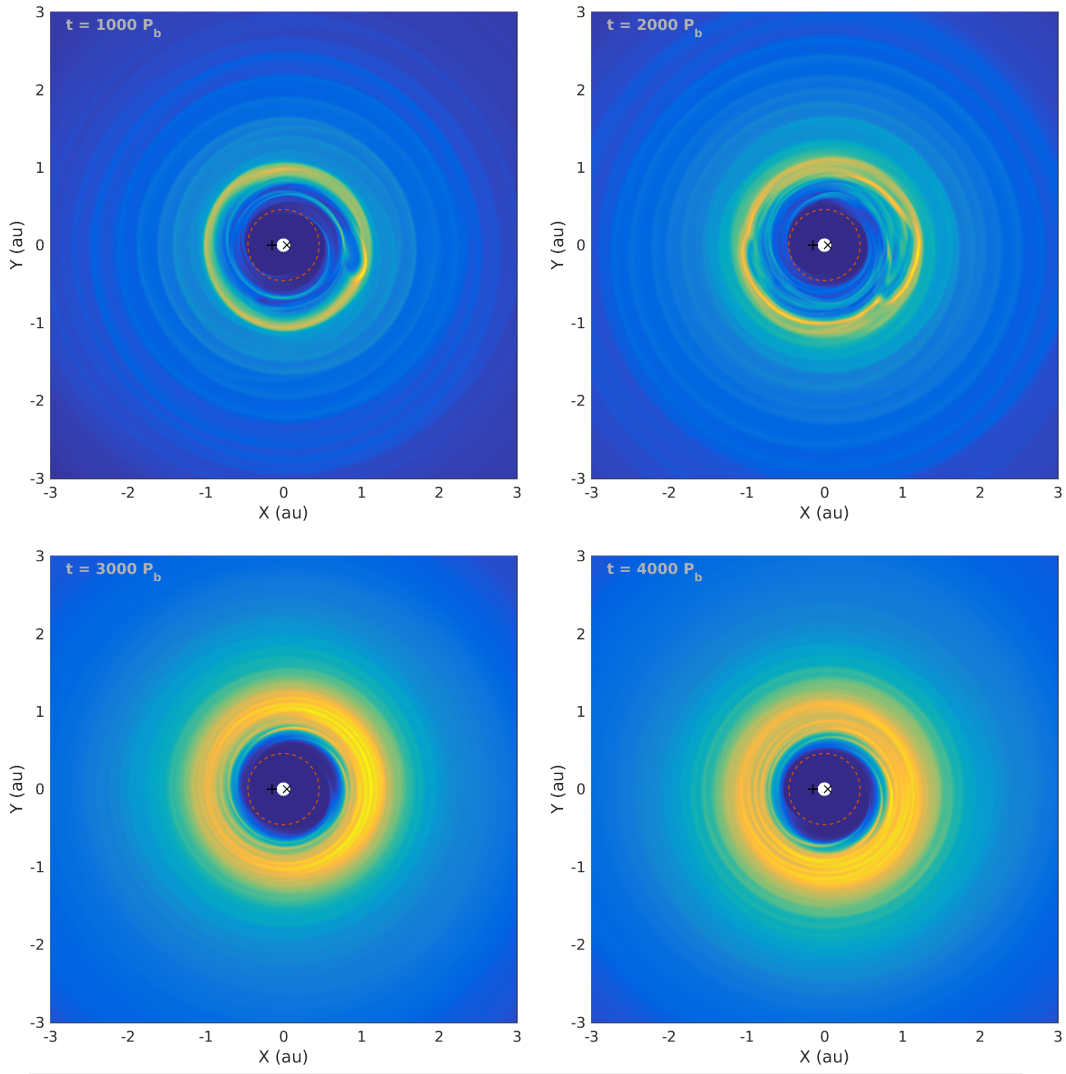

FIGURE 6.4: Evolution of the surface density distribution in the fully radiative disc. At early times there are signs of turbulence in the disc, with possible signs of radial convection, whilst at later times the disc reaches a pseudo-steady state, although it still doesn't form a clear eccentric cavity.

seen at the edge of the cavity, although less tightly wound in the adiabatic disc, as a consequence of increased pressure forces in the disc.

This is not the case in the first few snapshots of Fig. 6.4; there are signs that the usually coherent density waves are breaking up, creating a small vortex-like structure, which quickly dissipates under the forces of pressure and viscosity in the disc. The combination of mid-plane irradiation dramatically heating the inner disc material, and flux-limited diffusion transporting this heat into the high surface density area exterior to the cavity, could create very strong local gradients in

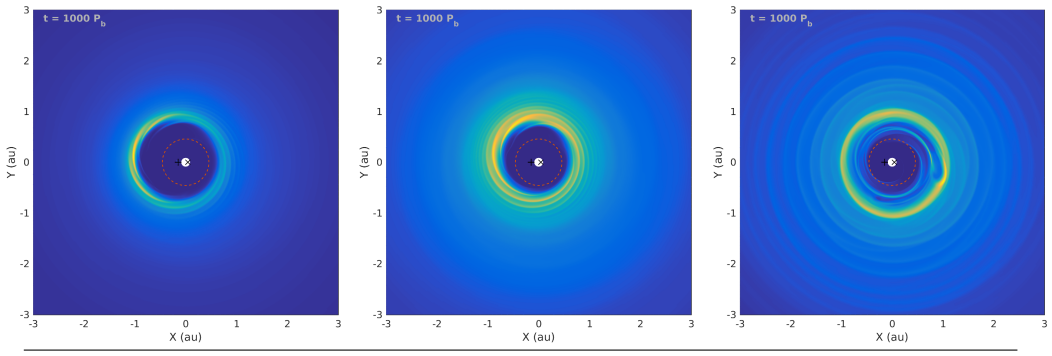

FIGURE 6.5: Comparison of surface density distributions after the first $1000\,P_{\rm b}$ in the *ISO*, *AD* and *RAD* models. Coherent structure is already forming in the isothermal and adiabatic runs, with the eccentric cavity clearly visible, as well as spiral density waves at the edge of the cavity. In the fully radiative disc, these density waves which carve out the cavity seem to be breaking up. This could be evidence of turbulent behaviour driven by a Rayleigh-like instability. Strong heating gradients could excite radial convection.

temperature and pressure. This could drive radial convection in the disc; combined with the non-Keplerian angular flow around the binary this creates a Rayleigh-like instability – exciting turbulence in the disc, which disrupts the spiral density waves and hence the creation of an eccentric cavity.

We will now examine the cause of the differences amongst the isothermal, adiabatic and radiative models; the temperature profiles within the discs. Whilst the radial profile can affect the evolution of embedded planets, it has also been shown (Kley and Haghighipour 2014, 2015, etc.) to impact the structure of circumbinary discs.

Figure 6.6 shows the radial mid-plane temperature profiles of the evolved adiabatic and radiative models once they have reached steady-state, compared with the static locally-isothermal profile. The inclusion of radiative cooling in all the non-isothermal runs presented here clearly acts to significantly reduce the temperature of the inner disc away from the r^{-1} profile. The *AD+RT* and fully radiative *RAD* runs, which both contain ray-traced mid-plane irradiation show the highest temperatures in the inner disc, with the inclusion of FLD in the fully radiative model allowing heat to be transported further into the disc. Despite the evacuated cavity, the mid-plane irradiation is still a heavily localised effect near the inner edge of the disc. Without FLD a large amount of heat is deposited in the inner disc raising the mid-plane temperature, but is then efficiently re-radiated through the surface cooling.

Beyond 0.8 au, where there are high surface densities skirting the edge of the

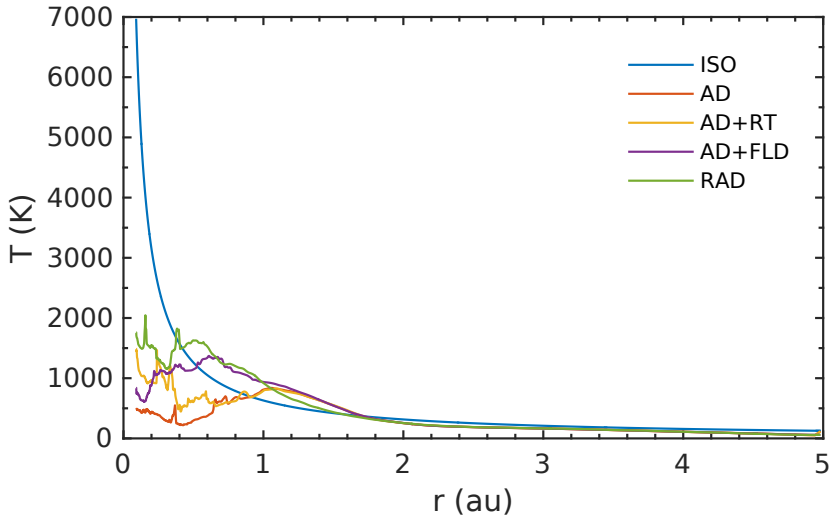

FIGURE 6.6: Azimuthally averaged mid-plane temperature profiles of the adiabatic and radiative disc models compared to the static isothermal profile. The inclusion of radiative cooling in all the non-isothermal models clearly lowers the temperature in the inner disc, below that of the isothermal model. Comparing the *AD* models with and without mid-plane irradiative heating, one can see that only the inner disc is significantly affected by this process.

cavity, viscous heating dominates over other processes, raising the mid-plane temperature above that of the isothermal profile. The irregular temperature profile in the inner disc is caused by strong heating and high temperatures in the streamer channels which connect the binary components with the cavity edge.

Changing the mid-plane temperature in the disc also alters the sound speed and hence the vertical structure of the disc. Hotter discs have a higher sound speed, and are therefore thicker than cooler discs. Readers will recall that to model the kinematic viscosity in the disc we used an α-prescription, which depends on the sound speed in the disc.

Comparing the kinematic viscosity profiles of the adiabatic and radiative models to that of the static isothermal profile (Fig. 6.7), several obvious features stand out. In the very inner disc, where the temperature in the non-isothermal disc is lower than the locally isothermal case, the kinematic viscosity is correspondingly lower due to a thinner disc, and a lower sound speed. As we move out in the disc in the models with ray-traced irradiative heating included (*AD+FLD* and *RAD*), the viscosity rises above that of the isothermal model; faster in the fully radiative model. In a significant fraction of the disc, between 0.4 and 2.0 au the kinematic

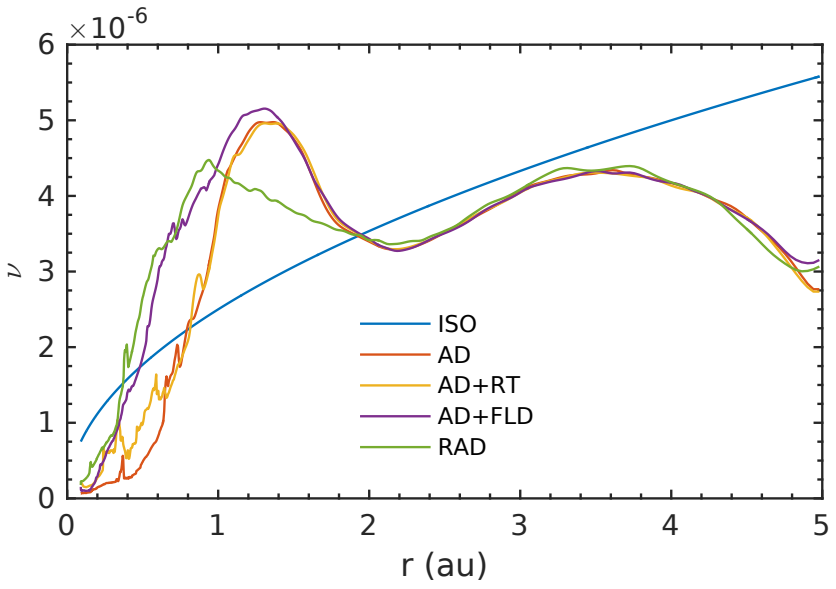

FIGURE 6.7: Kinematic viscosity profiles for all the disc models presented here, with the α-model prescription used to model the anomalous turbulence in the disc (Shakura and Sunyaev 1973). The changes in sound speed due to the decrease or increase in mid-plane temperature account for the changes in the viscosity of the disc. In the very inner disc the viscosity in the adiabatic and radiative models is lower than in the isothermal model. The viscosity rises above that of the isothermal disc in those regions where the temperature is higher. Higher viscosity will act to damp or inhibit any growing eccentricity.

viscosity is larger than that found in the isothermal model. Whilst the viscosity is also raised in the *AD* and *AD+RT* runs, it only rises above the isothermal profile outside 0.8 au. Raised viscosity will inhibit the growth of eccentricity in the disc material. If the viscosity is high enough in the inner disc, like the *RAD* model, it can result in a smaller less eccentric cavity. Further out in the disc, increased viscosity acts to smooth out sharp features in the surface density, accounting for the smoother surface density profiles in the *AD*, *AD+RT* and *AD+FLD* runs, and the wider extent of eccentric material between 2.0 and 3.0 au in these models.

The inclusion of ray-traced irradiative heating or flux-limited-diffusion can alter the mid-plane temperature, and hence the kinematic viscosity in the disc, affecting the final disc structure the disc obtains. In the case of ray-traced irradiative heating, the very inner disc temperature is elevated; FLD transports heat deposited in the inner disc either by viscous heating or irradiation outwards, raising the temperature in the cavity-edge region. When both these effects are included (the fully radiative *RAD* model), the large amount of heat deposited in the inner

disc is diffused by FLD, raising the temperature and the viscosity in the entire inner disc, cavity and cavity-edge region. The raised viscosity damps eccentricity growth, decreasing the cavity eccentricity and size. If an embedded planet can migrate to the location of the cavity edge in this model whilst maintaining a near-zero eccentricity orbit, it would be close to the observed orbit of the planet in *Kepler-16 b*.

6.4 Planet Migration

In this section we discuss the ongoing simulations examining the evolution of embedded planets in the disc models presented above. Once the discs have reached a pseudo-steady state we embed protoplanetary cores in the outer disc, on initially circular orbits and allow them to interact with the disc. We embed cores with a mass of $20\,M_{\oplus}$ at a position exterior to any disc material with significant eccentricity. Examining the surface density and cell eccentricity profiles in the previous section, we insert the cores at 1.5 au. In the *ISO*, *AD*, and *RAD* models we also run simulations with a planet inserted into the evolved discs with the observed mass and orbital location of *Kepler-16 b*; a $0.333\,M_{\rm Jup}$ planet at 0.7048 au. We start this planet on a circular orbit, although the eccentricity of *Kepler-16 b* is negligible anyway (0.0069) (Doyle et al. 2011).

The migration of low-mass planets in radiative discs can be slower than in their isothermal counterparts, even outwards migration is possible; although we see no sign of this in our adiabatic and fully radiative discs. This slowing of migration is caused by an asymmetry across the horseshoe region. The area in the horseshoe region ahead of the planet contains more material than in the isothermal case due to the inflow of cooler material exterior to the planet. Behind the planet the opposite is true, with a depletion of material. These effects lessen the strength of the negative Lindblad torque and can make the corotation torque positive, slowing inwards migration or reversing the direction altogether (Baruteau and Masset 2008a; Paardekooper and Papaloizou 2008; Kley and Crida 2008). For the corotation torque to remain unsaturated the radiative cooling time-scale must be comparable to the libration time-scale. The slower rate of inwards migration, coupled with the extra computational resources required for the inclusion of radiative effects means that we can only present preliminary results of the evolution of planets embedded in our models.

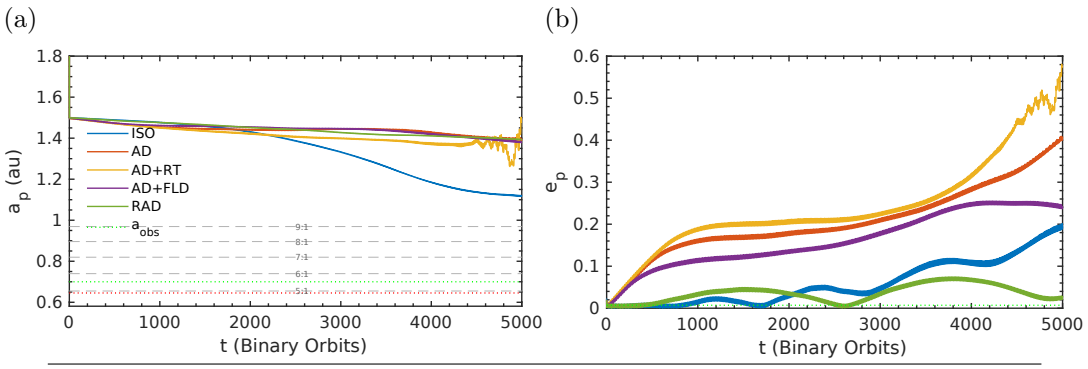

FIGURE 6.8: *(a)* Semi-major axis evolution of embedded protoplanetary cores in evolved isothermal, adiabatic and radiative discs. The orbital migration of planets in discs with an adiabatic equation of state and radiative cooling show decreased rates of inwards migration. Orbital migration will continue until the cores reach zero-torque radii. Those locations will depend on the surface density and temperature profile in each specific model. *(b)* Eccentricity evolution of the same cores. Significant eccentricity growth can be seen for the cores in the numerous *AD* models, due to the increased disc eccentricity. Little eccentricity growth is seen for the fully radiative model core.

6.4.1 Low-Mass Cores

All the cores in the models examined here show inwards migration as can be seen in Fig. 6.8a. It is possible that if the cores were initialised on orbits further out in the disc, where the disc surface density profile is unperturbed, the core in the fully radiative model could undergo outwards migration. If we examine the behaviour of similar mass cores in isothermal discs, and the disc structure obtained by our models in this work, we can make some predictions as to where these cores may halt their inwards migration. For cores of this mass, inwards migration is halted just inside the cavity edge, when the eccentricity of the core reaches a value similar to that of the disc eccentricity. At apocentre the planet finds itself moving faster than local material and a region of high density forms in front of the planet. At pericentre, the same happens but behind the planet. This results in a positive torque being applied to the planet, slowing then halting the inwards migration of the core (Pierens and Nelson 2013, Chapter 5). Kley and Haghighipour (2014, 2015), examining the evolution of more massive planets in radiative discs, but neglecting irradiative effects, found they halted at the cavity edge where the surface density gradient is positive.

Applying these ideas to the cores in our discs, we predict that the cores in the simulated *ISO*, *AD*, *AD+RT* and *AD+FLD* models will halt their migration around

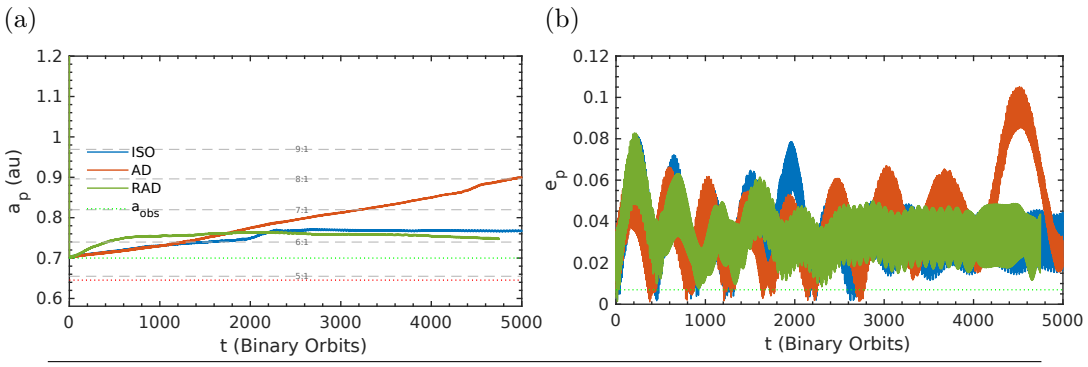

FIGURE 6.9: Orbital evolution of the planet embedded in the disc with the observed location, and mass, of *Kepler-16 b*. *(a)* Semi-major axis evolution in the *ISO*, *AD* and *RAD* disc models. Outwards migration can be seen as the giant planet carves out a gap, and finds a zero-torque radius. *(b)* Eccentricity evolution of the full-grown planets. The planets were initialised on a circular orbit, but in a region with high disc eccentricity.

1.0–1.1 au, although the high disc eccentricity in the adiabatic discs could affect this prediction. If the planets halt here, with an eccentricity comparable to that of the disc, poor agreement with the observed state of *Kepler-16 b* would be obtained. As mentioned earlier the smaller cavity, and lower disc eccentricity in the fully radiative model could produce a protoplanetary core on an orbit similar to *Kepler-16 b*. To reach the edge of the cavity in this disc at 0.8 au, the core must migrate through several unstable $n : 1$ mean motion resonances with the binary interior to 1.0 au. Our simulations in Chapter 5 found that although significant eccentricity can be excited by these features the presence of the disc can provide some stability, preventing significant scattering or ejection from the system as long as n is large.

6.4.2 Fully Formed Planets

As the fully formed 0.333 M_{Jup} planet opens a gap inside the eccentric cavity it starts to migrate outwards as its eccentricity grows (Fig. 6.9). At the initial semi-major axis corresponding to the observed location of *Kepler-16 b* the surface density gradient is positive in all the discs investigated. Therefore this outwards migration is not unexpected, especially as the planet is still opening a gap – a net positive torque is unlikely to be generated by the very low amount of disc material interior to the planet.

Past works comparing the migration of low-mass protoplanetary cores and observed-mass planets find that more massive planets in the Type II regime will migrate further into the cavity than those undergoing Type I migration. Pierens and Nelson (2013) found that a fully grown planet mimicking *Kepler-16 b* reached a final semi-major axis of 0.8 au, for a range of disc aspect ratios, and viscosities. Despite the differences in disc structure between our various models the planet in this case will probably obtain a similar final semi-major axis. A larger range in final planetary eccentricities was found in the previous models however, so the low eccentricity of the radiative disc could result in a massive planet on a near circular orbit, in good agreement with *Kepler-16 b*.

The small and near-circular cavity produced in the fully radiative disc, including the full assortment of heating and cooling effects and radiative transport, could produce both a low-mass core and fully grown planet on a close-in, low eccentricity orbit.

6.5 Summary

In this Chapter several simulations have been presented investigating radiative effects on the thermodynamics of circumbinary discs, and the evolution of protoplanetary cores and fully-grown planets within these discs with a more realistic equation of state.

Whilst the runs presented in this section are the subject of ongoing work, we are able to draw a few conclusions and predictions based on the results already obtained and the past work. Adiabatic or partially radiative discs see a similar size inner cavity to isothermal models, albeit with a lower peak surface density. In the most realistic disc, the fully radiative *RAD* model, the increased viscosity in the inner disc caused by efficient transport of heat deposited near the inner edge of the disc, a small inner cavity is seen.

Results from protoplanetary core migration in isothermal discs inform us that the objects in circumbinary discs will usually migrate to the edge of the eccentric cavity formed around the central binary. We expect that the cores in these radiative discs will be no different, although the thermodynamics may effect the rate of migration, through the action of the entropy-related portion of the corotation torque. This is promising for the fully radiative model as the edge of the cavity

lies in close proximity to the observed position of *Kepler-16 b*. Although the interacting core in our model has an initially low eccentricity, it is likely that it will increase as it migrates in. A mechanism has to be found to explain the low eccentricity seen for some of the observed circumbinary planets. Similar statements can be made for the migration of fully grown planets in these discs – whilst the Saturnian mass objects can migrate a little further into the inner disc than their protoplanetary core counterparts, they usually retain a significant eccentricity.

The small, low eccentricity cavity observed in the fully radiative disc is likely to be the model which best recreates the observed state of *Kepler-16 b*, when our planetary migration simualations have reached their conclusion. It is clear that the inclusion of radiative effects such irradiation, cooling and heat transport are important in recreating the dynamic environment around binary systems.

Chapter 7

Conclusions and Future Work

In Chapter 1 we examined the background of the exoplanet revolution which began in 1992 with the discovery of the first planet around a star outside of our Solar system. In particular we examined the detection and theories behind the formation and evolution of the small, but growing population of circumbinary planets. The detection of planets around close-binary systems by the *Kepler* space mission suggests that the processes governing planet formation are robust to a range of different environments. Planet formation seems to be a ubiquitous process; we find planets wherever we look.

Whilst the practice of exoplanet detection has evolved rapidly over the last three decades, theories of protoplanetary disc and planet formation and evolution struggle to explain the wide range of planetary properties and orbital architectures. Whilst the circumbinary environment can be a rigorous test bed for planet formation theories, due to the non-static nature of the disc, an accurate picture of the processes shaping this environment must be obtained to give this tool any descriptive or predictive power.

The *Kepler* population of circumbinary planets provide an ideal data set to test our models against, due to their extremely well defined stellar and planetary parameters. Theory developed prior to the detection of circumbinary planets was able to provide good first order agreement with the observed systems. It was found that planets embedded in the disc migrate inwards until they reach the central cavity tidally truncated by the binary. Depending on the mass of the planet this can occur for a number of processes. In most cases the planets' modelled orbits were were too wide or too eccentric. Generally the observed circumbinary planets are in orbits very close to the semi-analytical orbital stability limit found to exist around close-binary systems.

The models run to obtain these results generally employed simple disc physics, or contained limited planet evolution scenarios. It is likely that to obtain a better picture of the evolution of the circumbinary environment we need to include

additional areas of physics which affect the disc structure and evolution. With the *Kepler* planets as test cases, these models can then be used to explain and describe the underlying circumbinary planet population and perhaps highlight missing areas of parameter space for future exoplanetary detection missions such as *TESS, CHEOPS*, or *PLATO*.

In this thesis we have presented work aiming to build a better understanding of this interesting environment and the planets found within it. We have undertaken work focusing on three distinct areas: an investigation into the treatment of the outflow of material at the inner boundary (Chapter 3); examining the impact of disc-mass and self-gravity on the structure of the disc, and the evolution of embedded planets within it (Chapters 4 and 5); and the implementation of radiative effects within the FARGO code (Chapters 3 and 6).

How material is allowed to leave the computational domain of the disc in circumbinary discs models the rate of accretion onto the central stars. With a polar 2-D code we are left with the problem that material exiting the domain cannot re-enter it. Under or over-estimating the outflow of material out of the disc impacts the evolution of the inner disc quite dramatically – the area which we wish to model accurately. With three different outflow conditions – Open, Closed and Viscous – we found evidence of this effect, which prompted us to construct a model to lessen this effect. By shrinking the inner radius size, partially embedding the binary within the computational domain of the disc, and employing a Viscous outflow condition which allows outflow, but at a reduced rate compared to the Open condition, we hope to better capture the flow of material in and across the central cavity. We believe the additional computational time required with this set-up is worth the physical realism obtained.

With this disc set-up we ran a large set of simulations investigating the role of self-gravity, and the effect of disc-mass on the evolution of discs and embedded planets in three of the Kepler planet hosting binary systems, *Kepler-16, -34,* and *-35*. It is reasonable to assume that when the binary, and its host disc form, the disc is at its most massive. As it ages the disc loses mass through a number of different processes. To probe this evolution we have simulated 5 disc masses in each system, corresponding to total disc masses between 20–1_{MMSN}. As the disc mass decreases we are simulating later and later times in the disc. At each time, or disc-mass, the disc and binary system was allowed to reach a pseudo-steady-state; into this environment we embedded protoplanetary cores and allowed them

to interact.

In low eccentricity binaries the inclusion of self-gravity for low-disc masses had very little impact. In the high-eccentricity case (*Kepler-34*) even at low-disc masses, the action of self-gravity reduces the scale of the central cavity region, forming a smaller evacuated region and lower eccentricity cavity edge. The compacting of the scale of the inner disc continued for high-disc masses in all the binary systems modelled. The interaction between the binary and massive self-gravitating discs also creates complex eccentric features in the outer disc, not witnessed in the low-mass discs. These features are believed to be caused by non-linear mode coupling between the binary potential and additional eccentric modes in the disc potential arising from self-gravity, in a process similar to that which forms the central cavity.

We explored numerous planetary migration and accretion scenarios, as well as tracking the planetary evolution as the massive discs transition to a low mass 1_{MMSN} state, within the evolved discs above. In some cases the eccentric features formed in the high-mass discs acted as planet traps, then releasing their captives into the inner discs, where the planets migrated into the more compact cavity structure to be found there. From this state, transitioning to a low mass state allowed the cavity structure to relax, as the strength of self-gravity decreased. In the most massive discs the planet relaxed back with the cavity, finally settling in an orbit in poor agreement with observations. However in several of the less massive discs the state that the disc and planet system found before dissipation began, allowed it to stay in a relatively low eccentricity, short period orbit. Allowing the cores to accrete mass from the disc resulted in planets on orbits relatively close to their observed counterparts, especially in the most massive discs. We conclude that a combination of migration, accretion and dissipation, with the right time scales for each, in a moderately high-mass self-gravitating disc could come close to recreating the *Kepler* circumbinary planets examined here.

The simulations presented in the previous Chapters used a locally-isothermal approximation for the disc temperature. Isothermal discs have a constant aspect ratio and a static radial temperature profile. In the final investigation we test our implementation of radiative effects in discs with a more realistic adiabatic equation of state, around *Kepler-16*. FARGORAD includes viscous heating, radiative cooling, compression/dilation pressure work, mid-plane FLD heat transport and irradiative effects from both binary stars. As the simulations are still ongoing,

we can only make tentative conclusions. Whilst both FLD and mid-plane irradiation increase the temperature in the cavity and cavity-edge regions of the disc, individually they make little impact on the final disc structure compared to an isothermal or adiabatic disc, except for a reduced peak surface density due to increased viscosity. A disc with an adiabatic EoS, and both RT irradiation and FLD, has increased viscosity across the entire cavity region, damping eccentricity growth. The result is a very small cavity, with low disc eccentricity. An embedded planet in this disc could halt its migration very close to the observed location of *Kepler-16 b*, especially if it maintains a low eccentricity.

Our work has revealed behaviour in the evolution of circumbinary discs not seen before, and investigated their cause, and the impact they have on the evolution of embedded planets. Additional precessing rings in the outer regions of high-mass self-gravitating discs, shown to act as planet traps, could also trap smaller bodies such as planetesimals or dust. As the disc mass dissipates and the features weaken, this reservoir could then produce larger bodies. The small cavities produced in these discs could produce planets on orbits close to the observed population, if some way could be found to stabilise the planets there as the disc dissipates. It also seems that the increased viscosity arising in the inner region of fully radiative discs can create small, low eccentricity cavities. Ongoing simulations investigating the final orbital location of planets in these discs could yield promising results.

There are still aspects of circumbinary discs we have not been unable to investigate in this thesis. Obviously further investigation into the impact of radiative effects in realistic EoS is needed. 3-D effects are likely to be important; disc warping when the disc and orbit plane of the central binary are misaligned (Larwood and Papaloizou 1997), which can in turn lead to the development of a parametric instability in the disc that may be a source of hydrodynamic turbulence (Ogilvie and Latter 2013); the development of eccentric modes in the disc leading to parametric instability and hydrodynamic turbulence (Papaloizou 2005; Barker and Ogilvie 2014); and the formation of Spiral Wave Instabilities existing in a disc that is tidally forced by a binary system, can lead to a parametric instability and hydrodynamic turbulence (Bae et al. 2016). Equally importantly will be the inclusion of MHD, since the underlying angular momentum transport mechanism operating in circumbinary discs is likely to be of a magnetic origin (Balbus and Hawley 1991; Bai and Stone 2013, e.g.). Simulations carried out in 3-D will allow us to examine these and other effects. Finally, both theory and observations

indicate that planets do not normally form in isolation, so the evolution of multi-planet systems (Kley and Haghighipour 2015) may provide better agreement with at least a subset of circumbinary planet observations. Post-disc evolution of planetary systems with the debris of planet formation, planetesimals, could also have important consequences.

Mid-Plane Stellar Heating

To calculate the amount of stellar heating deposited into a grid cell i by irradiation propagating through the midplane of the disc, we need to calculate the difference between the amount arriving and that leaving:

$$F_\star e^{-\tau_i} - F_\star e^{-\tau_{i+1}} = F_\star e^{-\tau_i}\left(1 - \frac{e^{-\tau_{i+1}}}{e^{-\tau_i}}\right)$$
$$= F_\star e^{-\tau_i}\left(1 - e^{-(\tau_{i+1}-\tau_i)}\right) = F_\star e^{-\tau_i}\left(1 - e^{-\rho_i \kappa_{i,\star} \Delta r}\right), \tag{A.1}$$

where the $i+1$ index refers to the $i+1$th grid cell. The total flux emitted by a star is $L_\star = 4\pi\sigma_r R_\star^2 T_\star^4$. For a shell at a given radius r, the flux per unit area on a sphere is:

$$F_\star(r) = \frac{L_\star}{4\pi r^2} = \sigma_r T_\star^4 \left(\frac{R_\star}{r}\right)^2. \tag{A.2}$$

If we now work in a cylindrical system where the disc height is small compared to the other length-scales in the system, we can define the front surface area of a cell as:

$$\mathrm{d}A_{\text{face}} = r\Delta\phi\Delta z, \tag{A.3}$$

thus we can calculate the flux entering the cell face as:

$$F_\star \cdot \mathrm{d}A_{\text{face}} = \sigma_r T_\star^4 \left(\frac{R_\star}{r}\right) r\Delta\phi\Delta z. \tag{A.4}$$

Combining this result with the final result of Eq. (A.1) we can obtain the heating flux in a grid cell by stellar irradiation.

$$q_{\text{irr}}^{\text{mid}} = \sigma_r T_\star^4 \left(\frac{R_\star}{r}\right)^2 \cdot r\Delta\phi\Delta z \cdot e^{-\tau_i}\left(1 - e^{-\rho_i \kappa_{i,\star} \Delta r}\right) \tag{A.5}$$

This is not the final form of the heating flux, because the energy equation is formulated in terms of energy per unit surface area. The surface area of a grid cell in this context is not the face area, but the (r, ϕ)-plane surface area:

$$\mathrm{d}A_{\text{cell}} = r\Delta\phi\Delta r, \tag{A.6}$$

It is this surface area over which the flux is deposited, so to obtain the heating per unit area:

$$\begin{aligned} Q_{\mathrm{irr}}^{\mathrm{mid}} &= F_{\star} \cdot \frac{\mathrm{d}A_{\mathrm{face}}}{\mathrm{d}A_{\mathrm{cell}}} \cdot e^{-\tau_i} \left(1 - e^{-\rho_i \kappa_{i,\star} \Delta r}\right) \\ &= \sigma_r T_{\star}^4 \left(\frac{R_{\star}}{r}\right)^2 \cdot \frac{r \Delta\phi \Delta z}{r \Delta\phi \Delta r} \cdot e^{-\tau_i} \left(1 - e^{-\rho_i \kappa_{i,\star} \Delta r}\right), \end{aligned} \tag{A.7}$$

and finally, by taking $\Delta z = 2H\,(r)$:

$$Q_{\mathrm{irr}}^{\mathrm{mid}} = \sigma_r 2H\,(r)\, T_{\star}^4 \left(\frac{R_{\star}}{r}\right)^2 e^{-\tau_i} \frac{1 - e^{-\rho \kappa_{\star} \Delta r}}{\Delta r} \tag{A.8}$$

Although we have carried out this derivation for the single centered star case, the same argument can be extended to the binary irradiation case – obtaining Eq. (3.31). We will also include in this Appendix several details pertaining to the ray-tracing algorithm incorporated into FARGORAD.

Whilst the stars are treated as point sources of radiation, they are able to block radiation from the other star if it happens to lie on the line of sight between the source and the target cell. This results in a shadow behind each star as it blocks radiation from its companion. This cone will depend on the orbital configuration of the binary and the physical radius of the star. As the binary stars orbit their centre-of-mass these two shadow-cones will sweep round the disc, like the inverse of a light house.

When ray-tracing from the source to the target cell the ray segment length $\mathbf{\Delta r}$ depends on the grid spacing in the vicinity of the endpoint of the last ray segment:

$$\mathbf{\Delta r} = \epsilon \min\left(\Delta r_{ir}, r\Delta\phi_{jr}\right), \tag{A.9}$$

where ϵ is a constant ≥ 1 used to reduce the precision of the ray-tracing routine, and the labels ir and jr correspond to the indices of the closest cell to the last ray segment endpoint. We include the ϵ factor in our routine because gradients in the disc will be resolved across multiple grid cells, so it is not necessary to draw segments across individual cells – of course this also results in a boost to performance.

If the midplane irradiative heating term is included as well as the FLD algorithm described below, the two are combined into a single implicit substep. If not, it can be carried out in an explicit substep.

Flux-Limited-Diffusion Solver

The contents of this Appendix relate to the solution of the radiative transport FLD substep in FARGORAD:

$$\frac{\partial e}{\partial t} = -\nabla \cdot \mathbf{F} + Q_{\rm irr}^{\rm mid}. \tag{B.1}$$

If we include Eq. (3.32) and the expression which links the thermal energy density e to the temperature, we can write the above as a diffusion equation with relation to temperature:

$$\frac{\partial T}{\partial t} = \frac{1}{c_v \Sigma} \left[\nabla \cdot D \nabla T + Q_{\rm irr}^{\rm mid} \right], \tag{B.2}$$

where the diffusion coefficient D is given by:

$$D = \frac{4 a_r c \lambda T^3}{\rho \kappa_{\rm R}} \tag{B.3}$$

For simplicity we show here how this equation can be solved on a regular 2D finite-differenced mesh (Fig. B.1. In the orthogonal rectilinear co-ordinate system used in the FARGO code additional terms due to the geometry will arise, as well as those due to non-arithmetically spaced grids, but the general solution stencil is the same. Equation (B.2) can thus be rewritten:

$$\begin{aligned} \frac{T_{i,j}^{n+1} - T_{i,j}^{n}}{\Delta t} = & \frac{1}{c_v \Sigma_{i,j}} \Bigg[Q_{\rm irr}^{\rm mid} \Big|_{i,j}^{n} \\ & + \frac{1}{\Delta x} \left(\bar{D}_{i+1,j}^{x} \frac{T_{i+1,j} - T_{i,j}}{\Delta x} - \bar{D}_{i,j}^{x} \frac{T_{i,j} - T_{i-1,j}}{\Delta x} \right) \\ & + \frac{1}{\Delta y} \left(\bar{D}_{i,j+1}^{y} \frac{T_{i,j+1} - T_{i,j}}{\Delta y} - \bar{D}_{i,j}^{y} \frac{T_{i,j} - T_{i,j-1}}{\Delta y} \right) \Bigg]. \end{aligned} \tag{B.4}$$

The $\bar{D}_{i,j}^{x}$ and $\bar{D}_{i,j}^{y}$ terms denote averaged diffusion coefficients in the x and y directions respectively:

$$\bar{D}_{i,j}^{x} = \frac{1}{2} \left(D_{i,j} + D_{i-1,j} \right) \quad \text{and} \quad \bar{D}_{i,j}^{y} = \frac{1}{2} \left(D_{i,j} + D_{i,j-1} \right), \tag{B.5}$$

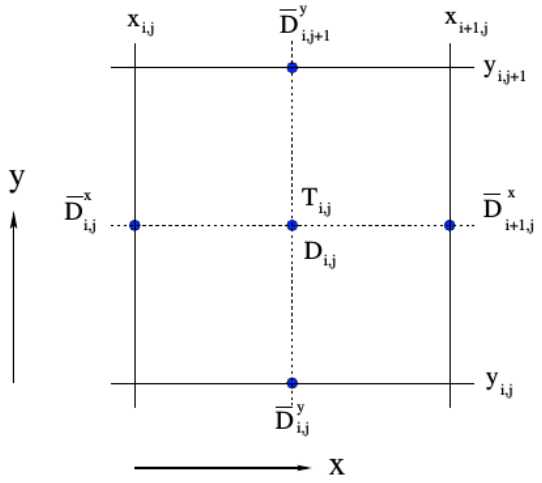

FIGURE B.1: A 2D staggered finite-difference grid. T and D are defined at cell-centres, whereas the averaged diffusion coefficients $\bar{D}$ are defined at cell interfaces. Image Credit: Kley et al. (2009).

the grid structure upon which these quantities are defined is shown in Fig. B.1.

Apart from the midplane heating term, no timelevels are defined for the quantities on the LHS of Eq. (B.4). For an explicit substep, like those carried out in the other substeps solving the energy equation, they would all be defined at $t = n$, such that T^{n+1} would simply be given by the old values of T^n. The simplicity of this method belies one key drawback; to remain stable it must meet the timestep criteria:

$$\Delta t \leq \min_{i,j} \left(\frac{\Delta x, \Delta y}{\tilde{D}_{i,j}} \right), \quad \text{where} \quad \tilde{D}_{i,j} = \frac{D_{i,j}}{c_v \Sigma_{i,j}}. \tag{B.6}$$

This can lead to extremely small timesteps which would require sub-cycling to match the size of the hydrodynamic timestep from the CFL condition, also making it very slow and inefficient. To overcome this problem Eq. (B.2) can be solved implicitly. All the T_{ij} terms on the RHS of the equation are evaluated at time $t = n + 1$. Although the D-coefficients depend on temperature, they are still evaluated at time level $t = n$, otherwise this would lead to a non-linear set of equations to solve. We can expand Eq. (B.2) and collect like terms of T to obtain a set of linear equations of the form:

$$U_1 T_{i-1,j} + U_2 T_{i+1,j} + U_3 T_{i,j-1} + U_4 T_{i,j+1} + B T_{i,j} = R_{i,j}, \tag{B.7}$$

where U_{1-4} are the coefficients containing the geometric terms and averaged diffusion coefficients from Eq. (B.2), $B = 1-(U_1+U_2+U_3+U_4)$ and the time level $t = n+1$ has been omitted from the T terms on the LHS. The single term on the RHS is the source term of the equation, and takes the form:

$$R_{i,j} = T^n_{i,j} + \frac{\Delta t}{c_v \Sigma^n_{i,j}} Q^{\rm mid}_{\rm irr}\Big|^n_{i,j} \tag{B.8}$$

The set of $N_r \times N_\phi$ equations of the form Eq. (B.7) can be written in matrix form:

$$M\mathbf{T}^{n+1} = \mathbf{R} \tag{B.9}$$

The matrix M is a sparse matrix with banded structure, and is usually diagonally dominant except when extended regions of optically thin regions exist (Kley et al. 2009). We solve this set of linear equations using an iterative SOR solver (the theory behind this process is contained in Section 2.2.6). As part of this, Chebyshev acceleration is used to converge on an optimised $\tilde{\omega}$ parameter (Press et al. 1992), and is solved implicitly using $odd-even$ sweeps. At the inner and outer disc boundaries the temperature can be set to constant values, the gradient in temperature can be defined, or the temperature can be interpolated from the existing gradient in the first (or last) two active cells. For the simulations presented in this thesis, we impose a zero-gradient condition on the temperature at both the inner and outer boundary conditions. The disc can then reach a temperature profile dictated by the balance between heating, cooling and transport mechanisms in the disc.

Bibliography

Alexander, R., 2012. "The dispersal of protoplanetary disks around binary stars". *ApJ*, 757, p. L29.

Alexander, R., Pascucci, I., Andrews, S., Armitage, P., Cieza, L., 2014. "The dispersal of protoplanetary disks". *Protostars and Planets VI*, pp. 475–496.

Alibert, Y., Carron, F., Fortier, A., Pfyffer, S., Benz, W., Mordasini, C., Swoboda, D., 2013. "Theoretical models of planetary system formation: mass vs. semi-major axis". *A&A*, 558, A109.

ALMA Partnership, Brogan, C. L., Pérez, L. M., Hunter, T. R., Dent, W. R. F., Hales, A. S., Hills, R. E., Corder, S., Fomalont, E. B., Vlahakis, C., Asaki, Y., Barkats, D., Hirota, A., Hodge, J. A., Impellizzeri, C. M. V., Kneissl, R., Liuzzo, E., Lucas, R., Marcelino, N., Matsushita, S., Nakanishi, K., Phillips, N., Richards, A. M. S., Toledo, I., Aladro, R., Broguiere, D., Cortes, J. R., Cortes, P. C., Espada, D., Galarza, F., Garcia-Appadoo, D., Guzman-Ramirez, L., Humphreys, E. M., Jung, T., Kameno, S., Laing, R. A., Leon, S., Marconi, G., Mignano, A., Nikolic, B., Nyman, L.-A., Radiszcz, M., Remijan, A., Rodón, J. A., Sawada, T., Takahashi, S., Tilanus, R. P. J., Vila Vilaro, B., Watson, L. C., Wiklind, T., Akiyama, E., Chapillon, E., de Gregorio-Monsalvo, I., Di Francesco, J., Gueth, F., Kawamura, A., Lee, C.-F., Nguyen Luong, Q., Mangum, J., Pietu, V., Sanhueza, P., Saigo, K., Takakuwa, S., Ubach, C., van Kempen, T., Wootten, A., Castro-Carrizo, A., Francke, H., Gallardo, J., Garcia, J., Gonzalez, S., Hill, T., Kaminski, T., Kurono, Y., Liu, H.-Y., Lopez, C., Morales, F., Plarre, K., Schieven, G., Testi, L., Videla, L., Villard, E., Andreani, P., Hibbard, J. E., Tatematsu, K., 2015. "The 2014 ALMA Long baseline campaign: First Results from high angular resolution observations toward the HL Tau region". *ApJ*, 808, p. L3.

Andre, P., Montmerle, T., 1994. "From T Tauri stars to protostars: Circumstellar material and young stellar objects in the rho Ophiuchi cloud". *ApJ*, 420, pp. 837–862.

Andre, P., Ward-Thompson, D., Barsony, M., 1993. "Submillimeter continuum observations of Rho Ophiuchi A - The candidate protostar VLA 1623 and prestellar clumps". *ApJ*, 406, pp. 122–141.

Andrews, S. M., Wilner, D. J., Zhu, Z., Birnstiel, T., Carpenter, J. M., Pérez, L. M., Bai, X.-N., Öberg, K. I., Hughes, A. M., Isella, A., Ricci, L., 2016. "Ringed Substructure and a gap at 1 au in the nearest protoplanetary disk". *ApJ*, 820, p. L40.

Angelo, I., Rowe, J. F., Howell, S. B., Quintana, E. V., Still, M., Mann, A. W., Burningham, B., Barclay, T., Ciardi, D. R., Huber, D., Kane, S. R., 2017. "Kepler-1649b: An exo-Venus in the Solar neighborhood". *AJ*, 153, p. 162.

Armitage, P. J., 2011. "Dynamics of Protoplanetary Disks". *ARA&A*, 49, pp. 195–236.

Armstrong, D. J., Osborn, H., Brown, D., Faedi, F., Gómez Maqueo Chew, Y., Martin, D., Pollacco, D., Udry, S., 2014. "On the abundance of circumbinary planets". *MNRAS*, 444, pp. 1873–1883.

Artymowicz, P., 1993. "On the wave excitation and a generalized torque formula for Lindblad resonances excited by external potential". *ApJ*, 419, p. 155.

Artymowicz, P., Clarke, C. J., Lubow, S. H., Pringle, J. E., 1991. "The effect of an external disk on the orbital elements of a central binary". *ApJ*, 370, pp. L35–L38.

Artymowicz, P., Lubow, S. H., 1994. "Dynamics of binary-disk interaction. I: Resonances and disk gap sizes". *ApJ*, 421, pp. 651–667.

Artymowicz, P., Lubow, S. H., 1996. "Mass flow through gaps in circumbinary disks". *ApJ*, 467, 2, pp. L77–L80.

Bae, J., Nelson, R. P., Hartmann, L., Richard, S., 2016. "Self-destructing spiral waves: Global simulations of a spiral-wave instability in accretion disks". *ApJ*, 829, p. 13.

Bai, X. N., Stone, J. M., 2013. "Wind-driven accretion in protoplanetary disks. I. Suppression of the magnetorotational instability and launching of the magnetocentrifugal wind". *ApJ*, 769, p. 76.

Balbus, S. A., Hawley, J. F., 1991. "A powerful local shear instability in weakly magnetized disks. I - Linear analysis. II - Nonlinear evolution". *ApJ*, 376, pp. 214–233.

Balbus, S. A., Papaloizou, J. C. B., 1999. "On the dynamical foundations of α disks". *ApJ*, 521, pp. 650–658.

Barker, A. J., Ogilvie, G. I., 2014. "Hydrodynamic instability in eccentric astrophysical discs". *MNRAS*, 445, pp. 2637–2654.

Baruteau, C., 2008. "Toward predictive scenarios of planetary migration". Doctoral dissertation.

Baruteau, C., Masset, F., 2008a. "On the corotation torque in a radiatively inefficient disk". *ApJ*, 672, 2, pp. 1054–1067.

Baruteau, C., Masset, F., 2008b. "Type I planetary migration in a self-gravitating disk". *ApJ*, 678, 1, pp. 483–497.

Batalha, N. M., Borucki, W. J., Bryson, S. T., Buchhave, L. A., Caldwell, D. A., Christensen-Dalsgaard, J., Ciardi, D., Dunham, E. W., Fressin, F., Gautier III, T. N., Gilliland, R. L., Haas, M. R., Howell, S. B., Jenkins, J. M., Kjeldsen, H., Koch, D. G., Latham, D. W., Lissauer, J. J., Marcy, G. W., Rowe, J. F., Sasselov, D. D., Seager, S., Steffen, J. H., Torres, G., Basri, G. S., Brown, T. M., Charbonneau, D., Christiansen, J., Clarke, B., Cochran, W. D., Dupree, A., Fabrycky, D. C., Fischer, D., Ford, E. B., Fortney, J., Girouard, F. R., Holman, M. J., Johnson, J., Isaacson, H., Klaus, T. C., Machalek, P., Moorehead, A. V., Morehead, R. C., Ragozzine, D., Tenenbaum, P., Twicken, J., Quinn, S., VanCleve, J., Walkowicz, L. M., Welsh, W. F., Devore, E., Gould, A., 2011. "Kepler's first rocky planet: Kepler-10b". *ApJ*, 729, p. 27.

Becker, J. C., Vanderburg, A., Adams, F. C., Rappaport, S. A., Schwengeler, H. M., 2015. "WASP-47: A Hot Jupiter System with Two Additional Planets Discovered by K2". *ApJ*, 812, p. L18.

Bell, K. R., Lin, D. N. C., 1994. "Using FU Orionis outbursts to constrain self-regulated protostellar disk models". *ApJ*, 427, pp. 987–1004.

Bitsch, B., Crida, A., Morbidelli, A., Kley, W., Dobbs-Dixon, I., 2013. "Stellar irradiated discs and implications on migration of embedded planets. I. Equilibrium discs". *A&A*, 549, A124.

Bitsch, B., Kley, W., 2011. "Range of outward migration and influence of the disc's mass on the migration of giant planet cores". *A&A*, 536.

Bitsch, B., Lambrechts, M., Johansen, A., 2015. "The growth of planets by pebble accretion in evolving protoplanetary discs". *A&A*, 582, A112.

Blum, J., Wurm, G., 2008. "The growth mechanisms of macroscopic bodies in protoplanetary disks". *ARA&A*, 46, pp. 21–56.

Bond, I. A., Bennett, D. P., Sumi, T., Udalski, A., Suzuki, D., Rattenbury, N. J., Bozza, V., Koshimoto, N., Abe, F., Asakura, Y., Barry, R. K., Bhattacharya, A., Donachie, M., Evans, P., Fukui, A., Hirao, Y., Itow, Y., Li, M. C. A.,

Ling, C. H., Masuda, K., Matsubara, Y., Muraki, Y., Nagakane, M., Ohnishi, K., Ranc, C., Saito, T., Sharan, A., Sullivan, D. J., Tristram, P. J., Yamada, T., Yamada, T., Yonehara, A., Skowron, J., Szymański, M. K., Poleski, R., Mróz, P., Soszyński, I., Pietrukowicz, P., Kozłowski, S., Ulaczyk, K., Pawlak, M., 2017. "The lowest mass ratio planetary microlens: OGLE 2016-BLG-1195Lb". *MNRAS*, 469, pp. 2434–2440.

Boss, A. P., 1997. "Giant planet formation by gravitational instability." *Science*, 276, pp. 1836–1839.

Butler, R. P., Vogt, S. S., Marcy, G. W., Fischer, D. A., Wright, J. T., Henry, G. W., Laughlin, G., Lissauer, J. J., 2004. "A Neptune-Mass planet orbiting the nearby M dwarf GJ 436". *ApJ*, 617, pp. 580–588.

Cabrera, J., Csizmadia, S., Lehmann, H., Dvorak, R., Gandolfi, D., Rauer, H., Erikson, A., Dreyer, C., Eigmüller, P., Hatzes, A., 2014. "The Planetary system to KIC 11442793: A Compact analogue to the solar system". *ApJ*, 781, p. 18.

Casertano, S., Lattanzi, M. G., Sozzetti, A., Spagna, A., Jancart, S., Morbidelli, R., Pannunzio, R., Pourbaix, D., Queloz, D., 2008. "Double-blind test program for astrometric planet detection with Gaia". *A&A*, 482, pp. 699–729.

Cassan, A., Kubas, D., Beaulieu, J.-P., Dominik, M., Horne, K., Greenhill, J., Wambsganss, J., Menzies, J., Williams, A., Jørgensen, U. G., Udalski, A., Bennett, D. P., Albrow, M. D., Batista, V., Brillant, S., Caldwell, J. A. R., Cole, A., Coutures, C., Cook, K. H., Dieters, S., Dominis Prester, D., Donatowicz, J., Fouqué, P., Hill, K., Kains, N., Kane, S., Marquette, J.-B., Martin, R., Pollard, K. R., Sahu, K. C., Vinter, C., Warren, D., Watson, B., Zub, M., Sumi, T., Szymański, M. K., Kubiak, M., Poleski, R., Soszynski, I., Ulaczyk, K., Pietrzyński, G., Wyrzykowski, Ł., 2012. "One or more bound planets per Milky Way star from microlensing observations". *Nature*, 481, pp. 167–169.

Chambers, J. E., 2014. "Giant planet formation with pebble accretion". *Icarus*, 233, pp. 83–100.

Chambers, J. E., Wetherill, G. W., 1998. "Making the terrestrial planets: N-body integrations of planetary embryos in three dimensions". *Icarus*, 136, pp. 304–327.

Charbonneau, D., Brown, T. M., D. W., L. D., Mayor, M., 2000. "Detection of planetary transits across a Sun-like star". *ApJ*, 529, 1, p. L45.

Charbonneau, D., Brown, T. M., Noyes, R. W., Gilliland, R. L., 2002. "Detection of an extrasolar planet atmosphere". *ApJ*, 568, pp. 377–384.

Chatterjee, S., Ford, E. B., Matsumura, S., Rasio, F. A., 2008. "Dynamical outcomes of planet-planet scattering". *ApJ*, 686, pp. 580–602.

Chatterjee, S., Tan, J. C., 2014. "Inside-out planet formation". *ApJ*, 780, p. 53.

Chatterjee, S., Tan, J. C., 2015. "Vulcan planets: Inside-out formation of the innermost super-Earths". *ApJ*, 798, p. L32.

Chernov, S. V., Ivanov, P. B., Papaloizou, J. C. B., 2017. "Dynamical tides in exoplanetary systems containing hot Jupiters: confronting theory and observations". *MNRAS*, 470, pp. 2054–2068.

Chiang, E. I., Goldreich, P., 1997. "Spectral energy distributions of T Tauri stars with passive circumstellar disks". *ApJ*, 490, pp. 368–376.

Chiang, E., Laughlin, G., 2013. "The minimum-mass extrasolar nebula: in situ formation of close-in super-Earths". *MNRAS*, 431, pp. 3444–3455.

Clarke, C., 2011. "The dispersal of disks around young stars". *Physical processes in circumstellar disks around young stars*. Ed. by P. J. V. Garcia, pp. 355–418.

Clarke, C. J., Gendrin, A., Sotomayor, M., 2001. "The dispersal of circumstellar discs: the role of the ultraviolet switch". *MNRAS*, 328, pp. 485–491.

Colella, P., Woodward, P. R., 1984. "The piecewise parabolic method (PPM) for gas-dynamical simulations". *Journal of Computational Physics*, 54, pp. 174–201.

Coleman, G. A. L., Nelson, R. P., 2014. "On the formation of planetary systems via oligarchic growth in thermally evolving viscous discs". *MNRAS*, 445, pp. 479–499.

Coleman, G. A. L., Nelson, R. P., 2016a. "Giant planet formation in radially structured protoplanetary discs". *MNRAS*, 460, pp. 2779–2795.

Coleman, G. A. L., Nelson, R. P., 2016b. "On the formation of compact planetary systems via concurrent core accretion and migration". *MNRAS*, 457, pp. 2480–2500.

Cossou, C., Raymond, S. N., Pierens, A., 2013. "Convergence zones for Type I migration: an inward shift for multiple planet systems". *A&A*, 553, p. L2.

Courant, R., Friedrichs, K., Lewy, H., 1928. "Über die partiellen differenzengleichungen der mathematischen physik". *Mathematische Annalen*, 100, pp. 32–74.

Cresswell, P., Dirksen, G., Kley, W., Nelson, R. P., 2007. "On the evolution of eccentric and inclined protoplanets embedded in protoplanetary disks". *A&A*, 473, pp. 329–342.

Cresswell, P., Nelson, R. P., 2006. "On the evolution of multiple protoplanets embedded in a protostellar disc". *A&A*, 450, pp. 833–853.

Crida, A., Morbidelli, A., Masset, F., 2006. "On the width and shape of gaps in protoplanetary disks". *Icarus*, 181, pp. 587–604.

Csizmadia, S., Pasternacki, T., Dreyer, C., Cabrera, J., Erikson, A., Rauer, H., 2013. "The effect of stellar limb darkening values on the accuracy of the planet radii derived from photometric transit observations". *A&A*, 549, A9.

D'Angelo, G., Bate, M. R., Lubow, S. H., 2005. "The dependence of protoplanet migration rates on co-orbital torques". *MNRAS*, 358, pp. 316–332.

D'Angelo, G., Henning, T., Kley, W., 2002. "Nested-grid calculations of disk-planet interaction". *A&A*, 385, pp. 647–670.

D'Angelo, G., Henning, T., Kley, W., 2003. "Thermo-hydrodynamics of circumstellar disks with high-mass planets". *ApJ*, 599, pp. 548–576.

D'Angelo, G., Lubow, S. H., 2008. "Evolution of migrating planets undergoing gas accretion". *ApJ*, 685, pp. 560–583.

D'Angelo, G., Marzari, F., 2012. "Outward migration of jupiter and saturn in evolved gaseous disks". *ApJ*, 757, p. 50.

Davies, M. B., Adams, F. C., Armitage, P., Chambers, J., Ford, E., Morbidelli, A., Raymond, S. N., Veras, D., 2014. "The long-term dynamical evolution of planetary systems". *Protostars and Planets VI*, pp. 787–808.

Dawson, R. I., Johnson, J. A., Fabrycky, D. C., Foreman-Mackey, D., Murray-Clay, R. A., Buchhave, L. A., Cargile, P. A., Clubb, K. I., Fulton, B. J., Hebb, L., Howard, A. W., Huber, D., Shporer, A., Valenti, J. A., 2014. "Large eccentricity, low mutual inclination: The three-dimensional architecture of a hierarchical system of giant Planets". *ApJ*, 791, p. 89.

de Val-Borro, M., Edgar, R. G., Artymowicz, P., Ciecielag, P., Cresswell, P., D'Angelo, G., Delgado-Donate, E. J., Dirksen, G., Fromang, S., Gawryszczak, A., Klahr, H., Kley, W., Lyra, W., Masset, F., Mellema, G., Nelson, R. P., Paardekooper, S.-J., Peplinski, A., Pierens, A., Plewa, T., Rice, K., Schäfer, C., Speith, R., 2006. "A comparative study of disc–planet interaction". *MNRAS*, 370, 2, pp. 529–558.

Dipierro, G., Price, D., Laibe, G., Hirsh, K., Cerioli, A., Lodato, G., 2015. "On planet formation in HL Tau". *MNRAS*, 453, pp. L73–L77.

Dobbs-Dixon, I., Cumming, A., Lin, D. N. C., 2010. "Radiative hydrodynamic simulations of HD209458b: Temporal variability". *ApJ*, 710, pp. 1395–1407.

Doyle, L. R., Carter, J. A., Fabrycky, D. C., Slawson, R. W., Howell, S. B., Winn, J. N., Orosz, J. A., Prša, A., Welsh, W. F., Quinn, S. N., Latham, D., Torres, G., Buchhave, L. A., Marcy, G. W., Fortney, J. J., Shporer, A., Ford, E. B., Lissauer,

J. J., Ragozzine, D., Rucker, M., Batalha, N. M., Jenkins, J. M., Borucki, W. J., Koch, D., Middour, C. K., Hall, J. R., McCauliff, S., Fanelli, M. N., Quintana, E. V., Holman, M. J., Caldwell, D. A., Still, M., Stefanik, R. P., Brown, W. R., Esquerdo, G. A., Tang, S., Furesz, G., Geary, J. C., Berlind, P., Calkins, M. L., Short, D. R., Steffen, J. H., Sasselov, D., Dunham, E. W., Cochran, W. D., Boss, A., Haas, M. R., Buzasi, D., Fischer, D. A., 2011. "Kepler-16: a transiting circumbinary planet." *Science*, 333, 6049, pp. 1602–1606.

Duchêne, G., Kraus, A., 2013. "Stellar Multiplicity". *ARA&A*, 51, pp. 269–310.

Dullemond, C. P., Dominik, C., 2004. "Flaring vs. self-shadowed disks: The SEDs of Herbig Ae/Be stars", 417, pp. 159–168.

Dullemond, C. P., Hollenbach, D., Kamp, I., D'Alessio, P., 2007. "Models of the structure and evolution of protoplanetary disks". *Protostars and Planets V*, pp. 555–572.

Dullemond, C. P., Monnier, J. D., 2010. "The Inner regions of protoplanetary disks". *ARA&A*, 48, pp. 205–239.

Dunhill, A. C., Alexander, R. D., 2013. "The curiously circular orbit of Kepler-16b". *MNRAS*, 435, 3, pp. 2328–2334.

Dutrey, A., Guilloteau, S., Simon, M., 1994. "Images of the GG Tauri rotating ring". *A&A*, 286, pp. 149–159.

Dvorak, R., 1986. "Critical orbits in the elliptic restricted three-body problem". *A&A*, 167, pp. 379–386.

Eggleton, P. P., 1983. "Approximations to the radii of Roche lobes". *ApJ*, 268, pp. 368–369.

Enoch, M. L., Corder, S., Dunham, M. M., Duchêne, G., 2009. "Disk and envelope structure in Class 0 protostars. I. The resolved massive disk in Serpens Firs 1". *ApJ*, 707, pp. 103–113.

Evans II, N. J., Dunham, M. M., Jørgensen, J. K., Enoch, M. L., Merín, B., van Dishoeck, E. F., Alcalá, J. M., Myers, P. C., Stapelfeldt, K. R., Huard, T. L., Allen, L. E., Harvey, P. M., van Kempen, T., Blake, G. A., Koerner, D. W., Mundy, L. G., Padgett, D. L., Sargent, A. I., 2009. "The Spitzer c2d Legacy results: Star-Formation rates and efficiencies; evolution and lifetimes". *ApJS*, 181, pp. 321–350.

Fabrycky, D. C., Ford, E. B., Steffen, J. H., Rowe, J. F., Carter, J. A., Moorhead, A. V., Batalha, N. M., Borucki, W. J., Bryson, S., Buchhave, L. A., Christiansen, J. L., Ciardi, D. R., Cochran, W. D., Endl, M., Fanelli, M. N., Fischer, D., Fressin, F., Geary, J., Haas, M. R., Hall, J. R., Holman, M. J., Jenkins,

J. M., Koch, D. G., Latham, D. W., Li, J., Lissauer, J. J., Lucas, P., Marcy, G. W., Mazeh, T., McCauliff, S., Quinn, S., Ragozzine, D., Sasselov, D., Shporer, A., 2012. "Transit Timing observations from Kepler. IV. Confirmation of Four multiple-planet systems by simple physical models". *ApJ*, 750, p. 114.

Fabrycky, D. C., Winn, J. N., 2009. "Exoplanetary Spin-orbit alignment: Results from the ensemble of Rossiter-McLaughlin observations". *ApJ*, 696, pp. 1230–1240.

Fendyke, S. M., Nelson, R. P., 2014. "On the corotation torque for low-mass eccentric planets". *MNRAS*, 437, pp. 96–107.

Fleming, D. P., Quinn, T. R., 2016. "Coevolution of binaries and gaseous discs". *ArXiv e-prints*.

Flock, M., Ruge, J. P., Dzyurkevich, N., Henning, T., Klahr, H., Wolf, S., 2015. "Gaps, rings, and non-axisymmetric structures in protoplanetary disks. From simulations to ALMA observations". *A&A*, 574, A68.

Ford, E. B., Rowe, J. F., Fabrycky, D. C., Carter, J. A., Holman, M. J., Lissauer, J. J., Ragozzine, D., Steffen, J. H., Batalha, N. M., Borucki, W. J., Bryson, S., Caldwell, D. A., Dunham, E. W., Gautier III, T. N., Jenkins, J. M., Koch, D. G., Li, J., Lucas, P., Marcy, G. W., McCauliff, S., Mullally, F. R., Quintana, E., Still, M., Tenenbaum, P., Thompson, S. E., Twicken, J. D., 2011. "Transit Timing observations from Kepler. I. Statistical Analysis of the first four months". *ApJS*, 197, p. 2.

Gammie, C. F., 1996. "Layered accretion in T Tauri disks". *ApJ*, 457, p. 355.

Gammie, C. F., 2001. "Nonlinear outcome of gravitational instability in cooling, gaseous disks". *ApJ*, 553, pp. 174–183.

Gillon, M., Jehin, E., Lederer, S. M., Delrez, L., de Wit, J., Burdanov, A., Van Grootel, V., Burgasser, A. J., Triaud, A. H. M. J., Opitom, C., Demory, B.-O., Sahu, D. K., Bardalez Gagliuffi, D., Magain, P., Queloz, D., 2016. "Temperate Earth-sized planets transiting a nearby ultracool dwarf star". *Nature*, 533, pp. 221–224.

Gillon, M., Triaud, A. H. M. J., Demory, B.-O., Jehin, E., Agol, E., Deck, K. M., Lederer, S. M., de Wit, J., Burdanov, A., Ingalls, J. G., Bolmont, E., Leconte, J., Raymond, S. N., Selsis, F., Turbet, M., Barkaoui, K., Burgasser, A., Burleigh, M. R., Carey, S. J., Chaushev, A., Copperwheat, C. M., Delrez, L., Fernandes, C. S., Holdsworth, D. L., Kotze, E. J., Van Grootel, V., Almleaky, Y., Benkhaldoun, Z., Magain, P., Queloz, D., 2017. "Seven temperate terrestrial planets

around the nearby ultracool dwarf star TRAPPIST-1". *Nature*, 542, pp. 456–460.

Goldreich, P., Schlichting, H. E., 2014. "Overstable librations can account for the paucity of Mean Motion Resonances among exoplanet pairs". *AJ*, 147, p. 32.

Goldreich, P., Tremaine, S., 1979. "The excitation of density waves at the Lindblad and corotation resonances by an external potential". *ApJ*, 233, pp. 857–871.

Gomes, R., Levison, H. F., Tsiganis, K., Morbidelli, A., 2005. "Origin of the cataclysmic Late Heavy Bombardment period of the terrestrial planets". *Nature*, 435, pp. 466–469.

Günther, R., Kley, W., 2002. "Circumbinary disk evolution". *A&A*, 387, pp. 550–559.

Günther, R., Schafer, C., Kley, W., 2004. "Evolution of irradiated circumbinary disks". *A&A*, 423, 0223, pp. 559–566.

Hands, T. O., Alexander, R. D., Dehnen, W., 2014. "Understanding the assembly of Kepler's compact planetary systems". *MNRAS*, 445, pp. 749–760.

Hartmann, L., Zhu, Z., Calvet, N., 2011. "On rapid disk accretion and initial conditions in protostellar evolution". *arXiv:1106.3343*.

Hayashi, C., 1981. "Structure of the solar nebula, growth and decay of magnetic fields and effects of magnetic and turbulent viscosities on the nebula". *Prog. Theor. Phys. Suppl.* 70, pp. 35–53.

Hébrard, G., Lecavelier Des Étangs, A., Vidal-Madjar, A., Désert, J.-M., Ferlet, R., 2004. "Evaporation rate of hot Jupiters and formation of Chthonian planets". *Extrasolar Planets: Today and Tomorrow*. Ed. by J. Beaulieu, A. Lecavelier Des Etangs, C. Terquem. Vol. 321. Astronomical Society of the Pacific Conference Series, p. 203.

Hellary, P., Nelson, R. P., 2012. "Global models of planetary system formation in radiatively-inefficient protoplanetary discs". *MNRAS*, 419, 4, pp. 2737–2757.

Helled, R., Bodenheimer, P., Podolak, M., Boley, A., Meru, F., Nayakshin, S., Fortney, J. J., Mayer, L., Alibert, Y., Boss, A. P., 2014. "Giant planet formation, evolution, and internal structure". *Protostars and Planets VI*, pp. 643–665.

Hellier, C., Anderson, D. R., Collier Cameron, A., Doyle, A. P., Fumel, A., Gillon, M., Jehin, E., Lendl, M., Maxted, P. F. L., Pepe, F., Pollacco, D., Queloz, D., Ségransan, D., Smalley, B., Smith, A. M. S., Southworth, J., Triaud, A. H. M. J., Udry, S., West, R. G., 2012. "Seven transiting hot Jupiters from WASP-South, Euler and TRAPPIST: WASP-47b, WASP-55b, WASP-61b, WASP-62b, WASP-63b, WASP-66b and WASP-67b". *MNRAS*, 426, pp. 739–750.

Holman, M. J., Wiegert, P. A., 1999. "Long-term stability of planets in binary systems". *AJ*, 117, pp. 621–628.

Howell, S. B., Sobeck, C., Haas, M., Still, M., Barclay, T., Mullally, F., Troeltzsch, J., Aigrain, S., Bryson, S. T., Caldwell, D., Chaplin, W. J., Cochran, W. D., Huber, D., Marcy, G. W., Miglio, A., Najita, J. R., Smith, M., Twicken, J. D., Fortney, J. J., 2014. "The K2 mission: Characterization and early results". *PASP*, 126, p. 398.

Hubeny, I., 1990. "Vertical structure of accretion disks - A simplified analytical model". *ApJ*, 351, pp. 632–641.

Huré, J.-M., Pierens, A., 2005. "Accurate numerical potential and field in razor-thin, axisymmetric disks". *ApJ*, 624, pp. 289–294.

Ida, S., Lin, D. N. C., 2010. "Toward a deterministic model of planetary formation. VI. Dynamical interaction and coagulation of multiple rocky embryos and super-earth systems around solar-type stars". *ApJ*, 719, pp. 810–830.

Jackson, B., Barnes, R., Greenberg, R., 2008. "Tidal heating of terrestrial extrasolar planets and implications for their habitability". *MNRAS*, 391, pp. 237–245.

Jacob, W. S., 1855. "On certain Anomalies presented by the Binary Star 70 Ophiuchi". *MNRAS*, 15, p. 228.

Jensen, E. L. N., Akeson, R., 2014. "Misaligned protoplanetary disks in a young binary star system". *Nature*, 511, pp. 567–569.

Johansen, A., Oishi, J. S., Mac Low, M.-M., Klahr, H., Henning, T., Youdin, A., 2007. "Rapid planetesimal formation in turbulent circumstellar disks". *Nature*, 448, pp. 1022–1025.

Kelling, T., Wurm, G., Köster, M., 2014. "Experimental study on bouncing barriers in protoplanetary disks". *ApJ*, 783, p. 111.

Kipping, D. M., Torres, G., Buchhave, L. A., Kenyon, S. J., Henze, C., Isaacson, H., Kolbl, R., Marcy, G. W., Bryson, S. T., Stassun, K., Bastien, F., 2014. "Discovery of a transiting planet near the snow-line". *ApJ*, 795, p. 25.

Kley, W., 1989. "Radiation hydrodynamics of the boundary layer in accretion disks. I - Numerical methods". *A&A*, 208, pp. 98–110.

Kley, W., 1999. "Mass flow and accretion through gaps in accretion discs". *MNRAS*, 303, pp. 696–710.

Kley, W., Bitsch, B., Klahr, H., 2009. "Planet migration in three-dimensional radiative discs". *A&A*, 506, pp. 971–987.

Kley, W., Burkert, A., 2000. "Disks and planets in binary systems (invited review)". *Disks, Planetesimals, and Planets*. Ed. by G. Garzón, C. Eiroa, D. de Winter, T. J. Mahoney. Vol. 219. Astronomical Society of the Pacific Conference Series, p. 189.

Kley, W., Crida, A., 2008. "Migration of protoplanets in radiative disks". *A&A*, 487, pp. L9–L12.

Kley, W., Haghighipour, N., 2014. "Modelling circumbinary planets: The case of Kepler-38". *A&A*, 564, A72.

Kley, W., Haghighipour, N., 2015. "Evolution of circumbinary planets around eccentric binaries: The case of Kepler-34". *A&A*, 581, A20.

Kley, W., Nelson, R. P., 2010. "Planets in Binary Star Systems". Springer Netherlands. Chap. Early evolution of planets in binaries: Planet–disk interaction, pp. 135–164. ISBN: 978-90-481-8687-7.

Kokubo, E., Ida, S., 1998. "Oligarchic growth of protoplanets". *Icarus*, 131, pp. 171–178.

Korycansky, D. G., Papaloizou, J. C. B., 1996. "The response of a gaseous disc to a binary encounter". *Disks and Outflows Around Young Stars*. Ed. by S. Beckwith, J. Staude, A. Quetz, A. Natta. Vol. 465. Lecture Notes in Physics, Berlin Springer Verlag.

Kostov, V., 2015. "KIC-5473556: the largest and longest-period Kepler transiting circumbinary planet". *AAS/Div. Extrem. Sol. Syst. Abs.*

Kostov, V. B., McCullough, P. R., Carter, J. A., Deleuil, M., Díaz, R. F., Fabrycky, D. C., Hébrard, G., Hinse, T. C., Mazeh, T., Orosz, J. A., Tsvetanov, Z. I., Welsh, W. F., 2014. "Kepler-413b: A slightly misaligned, Neptune-size transiting circumbinary planet". *ApJ*, 787, 1, A14.

Kostov, V. B., McCullough, P. R., Hinse, T. C., Tsvetanov, Z. I., Hébrard, G., Díaz, R. F., Deleuil, M., Valenti, J. A., 2013. "A gas giant circumbinary planet transiting the F star primary of the eclipsing binary star KIC 4862625 and the independent discovery and characterization of the two transiting planets in the Kepler-47 system". *ApJ*, 770, 1, p. 52.

Kostov, V. B., Orosz, J. A., Welsh, W. F., Doyle, L. R., Fabrycky, D. C., Haghighipour, N., Quarles, B., Short, D. R., Cochran, W. D., Endl, M., Ford, E. B., Gregorio, J., Hinse, T. C., Isaacson, H., Jenkins, J. M., Jensen, E. L. N., Kane, S., Kull, I., Latham, D. W., Lissauer, J. J., Marcy, G. W., Mazeh, T., Müller, T. W. A., Pepper, J., Quinn, S. N., Ragozzine, D., Shporer, A., Steffen, J. H.,

Torres, G., Windmiller, G., Borucki, W. J., 2016. "Kepler-1647b: The largest and longest-period Kepler transiting circumbinary planet". *ApJ*, 827, p. 86.

Kozai, Y., 1962. "Secular perturbations of asteroids with high inclination and eccentricity". *AJ*, 67, p. 591.

Lada, C. J., 1987. "Star formation - From OB associations to protostars". *Star Forming Regions*. Ed. by M. Peimbert, J. Jugaku. Vol. 115. IAU Symposium, pp. 1–17.

Lada, C. J., 2006. "Stellar Multiplicity and the Initial Mass Function: Most stars are single". *ApJ*, 640, pp. L63–L66.

Lambrechts, M., Johansen, A., Morbidelli, A., 2014. "Separating gas-giant and ice-giant planets by halting pebble accretion". *A&A*, 572, A35.

Landau, L., Lifshitz, E., 1987. "Fluid Mechanics". Vol. 6. Elsevier Science. ISBN: 9780080570730.

Larson, R. B., 1989. "The evolution of protostellar disks". *The Formation and Evolution of Planetary Systems*. Ed. by H. A. Weaver, L. Danly, pp. 31–48.

Larwood, J. D., Papaloizou, J. C. B., 1997. "The hydrodynamical response of a tilted circumbinary disc: linear theory and non-linear numerical simulations". *MNRAS*, 285, pp. 288–302.

Levermore, C. D., Pomraning, G. C., 1981. "A flux-limited diffusion theory". *ApJ*, 248, pp. 321–334.

Levison, H. F., Kretke, K. A., Duncan, M. J., 2015a. "Growing the gas-giant planets by the gradual accumulation of pebbles". *Nature*, 524, pp. 322–324.

Levison, H. F., Kretke, K. A., Walsh, K. J., Bottke, W. F., 2015b. "Growing the terrestrial planets from the gradual accumulation of sub-meter sized objects". *PNAS*, 112, pp. 14180–14185.

Levison, H. F., Morbidelli, A., 2003. "The formation of the Kuiper belt by the outward transport of bodies during Neptune's migration". *Nature*, 426, pp. 419–421.

Li, G., Holman, M. J., Tao, M., 2016. "Uncovering Circumbinary Planetary Architectural Properties from Selection Biases". *The Astrophysical Journal*, 831, 1, p. 96.

Lidov, M. L., 1962. "The evolution of orbits of artificial satellites of planets under the action of gravitational perturbations of external bodies". *P&SS*, 9, pp. 719–759.

Lin, D. N. C., Papaloizou, J., 1979. "Tidal torques on accretion discs in binary systems with extreme mass ratios". *MNRAS*, 186, pp. 799–812.

Lin, D. N. C., Papaloizou, J., 1985. "On the dynamical origin of the solar system". *Protostars and Planets II*. Ed. by D. C. Black, M. S. Matthews, pp. 981–1072.

Lin, D. N. C., Papaloizou, J. C. B., 1986. "On the tidal interaction between protoplanets and the protoplanetary disk. III - Orbital migration of protoplanets". *ApJ*, 309, pp. 846–857.

Lines, S., Leinhardt, Z. M., Baruteau, C., Paardekooper, S.-J., Carter, P. J., 2015. "Modelling circumbinary protoplanetary disks: I. Fluid simulations of the Kepler-16 and 34 systems". *A&A*, 582, A5.

Lines, S., Leinhardt, Z. M., Baruteau, C., Paardekooper, S.-J., Carter, P. J., 2016. "Modelling circumbinary protoplanetary disks. II. Gas disk feedback on planetesimal dynamical and collisional evolution in the circumbinary systems Kepler-16 and 34". *A&A*, 590, A62.

Lines, S., Leinhardt, Z. M., Paardekooper, S.-J., Baruteau, C., Thebault, P., 2014. "Forming circumbinary planets: n -body simulations of kepler-34". *ApJ*, 782, 1, p. L11.

Lissauer, J. J., 1995. "Urey prize lecture: On the diversity of plausible planetary systems". *Icarus*, 114, pp. 217–236.

Lissauer, J. J., 1999. "Three planets for Upsilon Andromedae". *Nature*, 398, p. 659.

Lissauer, J. J., Fabrycky, D. C., Ford, E. B., Borucki, W. J., Fressin, F., Marcy, G. W., Orosz, J. A., Rowe, J. F., Torres, G., Welsh, W. F., Batalha, N. M., Bryson, S. T., Buchhave, L. A., Caldwell, D. A., Carter, J. A., Charbonneau, D., Christiansen, J. L., Cochran, W. D., Desert, J.-M., Dunham, E. W., Fanelli, M. N., Fortney, J. J., Gautier III, T. N., Geary, J. C., Gilliland, R. L., Haas, M. R., Hall, J. R., Holman, M. J., Koch, D. G., Latham, D. W., Lopez, E., McCauliff, S., Miller, N., Morehead, R. C., Quintana, E. V., Ragozzine, D., Sasselov, D., Short, D. R., Steffen, J. H., 2011. "A closely packed system of low-mass, low-density planets transiting Kepler-11". *Nature*, 470, pp. 53–58.

Livio, M., Spruit, H. C., 1991. "On the mechanism of angular momentum transport in accretion disks". *A&A*, 252, pp. 189–192.

Lynden-Bell, D., Pringle, J. E., 1974. "The evolution of viscous discs and the origin of the nebular variables." *MNRAS*, 168, pp. 603–637.

Malhotra, R., 1995. "The origin of Pluto's orbit: Implications for the Solar System beyond Neptune". *AJ*, 110, p. 420.

Marois, C., Macintosh, B., Barman, T., Zuckerman, B., Song, I., Patience, J., Lafrenière, D., Doyon, R., 2008. "Direct imaging of multiple planets orbiting the star HR 8799". *Science*, 322, p. 1348.

Marois, C., Zuckerman, B., Konopacky, Q. M., Macintosh, B., Barman, T., 2010. "Images of a fourth planet orbiting HR 8799". *Nature*, 468, pp. 1080–1083.

Marzari, F., Scholl, H., Thébault, P., Baruteau, C., 2009. "On the eccentricity of self-gravitating circumstellar disks in eccentric binary systems". *A&A*, 508, 3, pp. 1493–1502.

Marzari, F., Thébault, P., Scholl, H., 2008. "Planetesimal evolution in circumbinary gaseous disks: A hybrid model". *ApJ*, 681, pp. 1599–1608.

Masset, F. S., 2000a. "FARGO: A Fast Eulerian Transport Algorithm for Differentially Rotating Disks". *Disks, Planetesimals, and Planets*. Ed. by G. Garzón, C. Eiroa, D. de Winter, T. J. Mahoney. Vol. 219. Astronomical Society of the Pacific Conference Series, p. 75.

Masset, F. S., 2000b. "FARGO: A fast eulerian transport algorithm for differentially rotating disks". *A&AS*, 141, pp. 165–173.

Masset, F. S., 2002. "The co-orbital corotation torque in a viscous disk: Numerical simulations". *A&A*, 387, pp. 605–623.

Masset, F. S., 2011. "On type-I migration near opacity transitions. A generalized Lindblad torque formula for planetary population synthesis". *Celestial Mechanics and Dynamical Astronomy*, 111, pp. 131–160.

Masset, F. S., Casoli, J., 2009. "On the horseshoe drag of a low-mass planet. II. Migration in adiabatic disks". *ApJ*, 703, pp. 857–876.

Masset, F. S., D'Angelo, G., Kley, W., 2006a. "On the migration of protogiant solid cores". *ApJ*, 652, 1, p. 730.

Masset, F. S., Morbidelli, A., Crida, A., Ferreira, J., 2006b. "Disk surface density transitions as protoplanet traps". *ApJ*, 642, 1, p. 478.

Masset, F. S., Papaloizou, J. C. B., 2003. "Runaway migration and the formation of hot Jupiters". *ApJ*, 588, pp. 494–508.

Mathieu, R. D., Ghez, A. M., Jensen, E. L. N., Simon, M., 2000. "Young binary stars and associated disks". *Protostars and Planets IV*, p. 703.

Mayor, M., Queloz, D., 1995. "A Jupiter-mass companion to a solar-type star". *Nature*, 378, pp. 355–359.

McLaughlin, D. B., 1924. "Some results of a spectrographic study of the Algol system." *ApJ*, 60.

McNeil, D. S., Nelson, R. P., 2009. "New methods for large dynamic range problems in planetary formation". *MNRAS*, 392, pp. 537–552.

Menou, K., Goodman, J., 2004. "Low-mass protoplanet migration in T Tauri α-disks". *ApJ*, 606, pp. 520–531.

Meschiari, S., 2012a. "Circumbinary planet formation in the Kepler-16 system. I. N-Body simulations". *ApJ*, 752, 1, A72.

Meschiari, S., 2012b. "Planet formation in circumbinary configurations: Turbulence inhibits planetesimal accretion". *ApJ*, 761, 1, p. L7.

Morbidelli, A., Crida, A., Masset, F., Nelson, R. P., 2008. "Building giant-planet cores at a planet trap". *A&A*, 478, pp. 929–937.

Mordasini, C., Alibert, Y., Benz, W., 2009. "Extrasolar planet population synthesis. I. Method, formation tracks, and mass-distance distribution". *A&A*, 501, pp. 1139–1160.

Mordasini, C., Alibert, Y., Klahr, H., Henning, T., 2012. "Characterization of exoplanets from their formation. I. Models of combined planet formation and evolution". *A&A*, 547, A111.

Movshovitz, N., Bodenheimer, P., Podolak, M., Lissauer, J. J., 2010. "Formation of Jupiter using opacities based on detailed grain physics". *Icarus*, 209, pp. 616–624.

Müller, T. W. A., Kley, W., 2012. "Circumstellar disks in binary star systems Models for γ Cephei and α Centauri". *A&A*, 539, A18.

Müller, T. W. A., Kley, W., Meru, F., 2012. "Treating gravity in thin-disk simulations". *A&A*, 541, A123.

Muto, T., Suzuki, T. K., Inutsuka, S.-i., 2010. "Two-dimensional study of the propagation of planetary wake and the indication of gap opening in an inviscid protoplanetary disk". *ApJ*, 724, pp. 448–463.

Mutter, M. M., Pierens, A., Nelson, R. P., 2017a. "The role of disc self-gravity in circumbinary planet systems – I. Disc structure and evolution". *MNRAS*, 465, 4, p. 4735.

Mutter, M. M., Pierens, A., Nelson, R. P., 2017b. "The role of disc self-gravity in circumbinary planet systems – II. Planet evolution". *MNRAS*, 469, 4, p. 4504.

Nayakshin, S., 2015. "Tidal downsizing model - I. Numerical methods: saving giant planets from tidal disruptions". *MNRAS*, 454, pp. 64–82.

Nayakshin, S., Fletcher, M., 2015. "Tidal Downsizing model - III. Planets from sub-Earths to brown dwarfs: structure and metallicity preferences". *MNRAS*, 452, pp. 1654–1676.

Nelson, R. P., 2003. "On the evolution of giant protoplanets forming in circumbinary discs". *MNRAS*, 345, pp. 233–242.

Nelson, R. P., Gressel, O., 2010. "On the dynamics of planetesimals embedded in turbulent protoplanetary discs". *MNRAS*, 409, pp. 639–661.

Nelson, R. P., Papaloizou, J. C. B., Masset, F., Kley, W., 2000. "The migration and growth of protoplanets in protostellar discs". *MNRAS*, 318, 1, pp. 18–36.

Neveu-VanMalle, M., Queloz, D., Anderson, D. R., Brown, D. J. A., Collier Cameron, A., Delrez, L., Díaz, R. F., Gillon, M., Hellier, C., Jehin, E., Lister, T., Pepe, F., Rojo, P., Ségransan, D., Triaud, A. H. M. J., Turner, O. D., Udry, S., 2016. "Hot Jupiters with relatives: discovery of additional planets in orbit around WASP-41 and WASP-47". *A&A*, 586, A93.

Ogilvie, G. I., Latter, H. N., 2013. "Hydrodynamic instability in warped astrophysical discs". *MNRAS*, 433, pp. 2420–2435.

Ogilvie, G. I., Lubow, S. H., 2002. "On the wake generated by a planet in a disc". *MNRAS*, 330, pp. 950–954.

Okuzumi, S., Momose, M., Sirono, S.-i., Kobayashi, H., Tanaka, H., 2016. "Sintering-induced dust ring formation in protoplanetary disks: application to the HL Tau disk". *ApJ*, 821, p. 82.

Orosz, J. A., Welsh, W. F., Carter, J. A., Brugamyer, E., Buchhave, L. A., Cochran, W. D., Endl, M., Ford, E. B., MacQueen, P., Short, D. R., Torres, G., Windmiller, G., Agol, E., Barclay, T., Caldwell, D. A., Clarke, B. D., Doyle, L. R., Fabrycky, D. C., Geary, J. C., Haghighipour, N., Holman, M. J., Ibrahim, K. A., Jenkins, J. M., Kinemuchi, K., Li, J., Lissauer, J. J., Prša, A., Ragozzine, D., Shporer, A., Still, M., Wade, R. A., 2012a. "The neptune-sized circumbinary planet Kepler-38b". *ApJ*, 758, 1, A87.

Orosz, J. A., Welsh, W. F., Carter, J. A., Fabrycky, D. C., Cochran, W. D., Endl, M., Ford, E. B., Haghighipour, N., MacQueen, P. J., Mazeh, T., Sanchis-Ojeda, R., Short, D. R., Torres, G., Agol, E., Buchhave, L. A., Doyle, L. R., Isaacson, H., Lissauer, J. J., Marcy, G. W., Shporer, A., Windmiller, G., Barclay, T., Boss, A. P., Clarke, B. D., Fortney, J., Geary, J. C., Holman, M. J., Huber, D., Jenkins, J. M., Kinemuchi, K., Kruse, E., Ragozzine, D., Sasselov, D., Still, M., Tenenbaum, P., Uddin, K., Winn, J. N., Koch, D. G., Borucki, W. J., 2012b. "Kepler-47: a transiting circumbinary multiplanet system". *Science*, 337, pp. 1511–.

Paardekooper, S.-J., Baruteau, C., Crida, A., Kley, W., 2010. "A torque formula for non-isothermal Type I planetary migration–I. Unsaturated horseshoe drag". *MNRAS*, 401, June, pp. 1950–1964.

Paardekooper, S.-J., Baruteau, C., Kley, W., 2011. "A torque formula for non-isothermal Type I planetary migration – II. Effects of diffusion". *MNRAS*, 410, July, pp. 293–303.

Paardekooper, S.-J., Leinhardt, Z. M., Thébault, P., Baruteau, C., 2012. "How not to build Tatooine: The difficulty of in situ formation of circumbinary planets Kepler 16b, Kepler 34b, and Kepler 35b". *ApJL*, 754, 2, p. L16.

Paardekooper, S.-J., Mellema, G., 2006. "Halting type I planet migration in non-isothermal disks". *A&A*, 459, pp. L17–L20.

Paardekooper, S.-J., Papaloizou, J. C. B., 2008. "On disc protoplanet interactions in a non-barotropic disc with thermal diffusion". *A&A*, 485, pp. 877–895.

Paardekooper, S.-J., Papaloizou, J. C. B., 2009a. "On corotation torques, horseshoe drag and the possibility of sustained stalled or outward protoplanetary migration". *MNRAS*, 394, pp. 2283–2296.

Paardekooper, S.-J., Papaloizou, J. C. B., 2009b. "On the width and shape of the corotation region for low-mass planets". *MNRAS*, 394, pp. 2297–2309.

Papaloizou, J. C. B., 2002. "Global m = 1 modes and migration of protoplanetary cores in eccentric protoplanetary discs". *A&A*, 388, 2, pp. 615–631.

Papaloizou, J. C. B., 2005. "The local instability of steady astrophysical flows with non circular streamlines with application to differentially rotating disks with free eccentricity". *A&A*, 432, pp. 743–755.

Papaloizou, J. C. B., Larwood, J. D., 2000. "On the orbital evolution and growth of protoplanets embedded in a gaseous disc". *MNRAS*, 315, pp. 823–833.

Papaloizou, J. C. B., Lin, D. N. C., 1995. "Theory of accretion disks I: Angular momentum transport processes". *ARA&A*, 33, pp. 505–540.

Papaloizou, J. C. B., Nelson, R. P., Masset, F., 2001. "Orbital eccentricity growth through disc-companion tidal interaction". *A&A*, 366, 1, pp. 263–275.

Papaloizou, J., Lin, D. N. C., 1984. "On the tidal interaction between protoplanets and the primordial solar nebula. I - Linear calculation of the role of angular momentum exchange". *ApJ*, 285, pp. 818–834.

Peiró, J., Sherwin, S., 2005. "Finite difference, finite element and finite volume methods for partial differential equations". *Handbook of Materials Modeling, ISBN 978-1-4020-3287-5. Springer Science+Business Media B.V., 2005, p. 2415.* Ed. by S. Yip, p. 2415.

Pelupessy, F. I., Portegies Zwart, S., 2013. "The formation of planets in circumbinary discs". *MNRAS*, 429, pp. 895–902.

Pepliński, A., Artymowicz, P., Mellema, G., 2008a. "Numerical simulations of type III planetary migration - I. Disc model and convergence tests". *MNRAS*, 386, pp. 164–178.

Pepliński, A., Artymowicz, P., Mellema, G., 2008b. "Numerical simulations of type III planetary migration - II. Inward migration of massive planets". *MNRAS*, 386, pp. 179–198.

Pepliński, A., Artymowicz, P., Mellema, G., 2008c. "Numerical simulations of type III planetary migration - III. Outward migration of massive planets". *MNRAS*, 387, pp. 1063–1079.

Perryman, M., Hartman, J., Bakos, G. Á., Lindegren, L., 2014. "Astrometric Exoplanet Detection with Gaia". *ApJ*, 797, p. 14.

Picogna, G., Kley, W., 2015. "How do giant planetary cores shape the dust disk? HL Tauri system". *A&A*, 584, A110.

Pierens, A., Nelson, R. P., 2007. "On the migration of protoplanets embedded in circumbinary disks". *A&A*, 472, pp. 993–1001.

Pierens, A., Nelson, R. P., 2008a. "On the evolution of multiple low mass planets embedded in a circumbinary disc". *A&A*, 478, 3, pp. 939–949.

Pierens, A., Nelson, R. P., 2008b. "On the formation and migration of giant planets in circumbinary discs". *A&A*, 483, 2, pp. 633–642.

Pierens, A., Nelson, R. P., 2013. "Migration and gas accretion scenarios for the Kepler 16, 34 and 35 circumbinary planets". *A&A*, 556, A134.

Pollack, J. B., Hubickyj, O., Bodenheimer, P., Lissauer, J. J., Podolak, M., Greenzweig, Y., 1996. "Formation of the giant planets by concurrent accretion of solids and gas". *Icarus*, 124, 1, pp. 62–85.

Press, W. H., Teukolsky, S. A., Vetterling, W. T., Flannery, B. P., 1992. "Numerical recipes in C. The art of scientific computing".

Pringle, J. E., 1981. "Accretion discs in astrophysics". *ARA&A*, 19, pp. 137–162.

Rasio, F. A., Tout, C. A., Lubow, S. H., Livio, M., 1996. "Tidal decay of close planetary orbits". *ApJ*, 470, p. 1187.

Rein, H., 2012. "A proposal for community driven and decentralized astronomical databases and the Open Exoplanet Catalogue". *arXiv:1211.7121*.

Rossiter, R. A., 1924. "On the detection of an effect of rotation during eclipse in the velocity of the brigher component of beta Lyrae, and on the constancy of velocity of this system." *ApJ*, 60.

Safronov, V. S., 1972. "Evolution of the protoplanetary cloud and formation of the earth and planets."

Scholl, H., Marzari, F., Thébault, P., 2007. "Relative velocities among accreting planetesimals in binary systems: The circumbinary case". *MNRAS*, 380, 3, pp. 1119–1126.

Schwamb, M. E., Orosz, J. A., Carter, J. A., Welsh, W. F., Fischer, D. A., Torres, G., Howard, A. W., Crepp, J. R., Keel, W. C., Lintott, C. J., Kaib, N. A., Terrell, D., Gagliano, R., Jek, K. J., Parrish, M., Smith, A. M., Lynn, S., Simpson, R. J., Giguere, M. J., Schawinski, K., 2013. "Planet Hunters: A transiting circumbinary planet in a quadruple star system". *ApJ*, 768, 2, A127.

Seager, S., Mallén-Ornelas, G., 2003. "on the unique solution of planet and star parameters from an extrasolar planet transit light curve". *Scientific Frontiers in Research on Extrasolar Planets*. Ed. by D. Deming, S. Seager. Vol. 294. Astronomical Society of the Pacific Conference Series, pp. 419–422.

Shakura, N. I., Sunyaev, R. A., 1973. "Black holes in binary systems. Observational appearance." *A&A*, 24, pp. 337–355.

Siess, L., Dufour, E., Forestini, M., 2000. "An internet server for pre-main sequence tracks of low- and intermediate-mass stars". *A&A*, 358, pp. 593–599.

Snellgrove, M. D., Papaloizou, J. C. B., Nelson, R. P., 2001. "On disc driven inward migration of resonantly coupled planets with application to the system around GJ876". *A&A*, 374, pp. 1092–1099.

Stamatellos, D., Whitworth, A. P., 2008. "Can giant planets form by gravitational fragmentation of discs?." *A&A*, 480, pp. 879–887.

Stolker, T., Dominik, C., Avenhaus, H., Min, M., de Boer, J., Ginski, C., Schmid, H. M., Juhasz, A., Bazzon, A., Waters, L. B. F. M., Garufi, A., Augereau, J.-C., Benisty, M., Boccaletti, A., Henning, T., Langlois, M., Maire, A.-L., Ménard, F., Meyer, M. R., Pinte, C., Quanz, S. P., Thalmann, C., Beuzit, J.-L., Carbillet, M., Costille, A., Dohlen, K., Feldt, M., Gisler, D., Mouillet, D., Pavlov, A., Perret, D., Petit, C., Pragt, J., Rochat, S., Roelfsema, R., Salasnich, B., Soenke, C., Wildi, F., 2016. "Shadows cast on the transition disk of HD 135344B. Multi-wavelength VLT/SPHERE polarimetric differential imaging". *A&A*, 595, A113.

Stone, J. M., Norman, M. L., 1992. "ZEUS-2D: A radiation magnetohydrodynamics code for astrophysical flows in two space dimensions. I - The hydrodynamic algorithms and tests." *ApJS*, 80, pp. 753–790.

Tanaka, H., Taku, T., Ward, W. R., 2002. "Three-dimensional interaction between a planet and an isothermal gaseous disk. I. corotation and lindblad torques and planet migration". *ApJ*, 565, pp. 1257–1274.

Terquem, C., 1998. "The response of accretion disks to bending waves: Angular momentum transport and resonances". *ApJ*, 509, pp. 819–835.

Terquem, C., 2008. "New composite models of partially ionized protoplanetary disks". *ApJ*, 689, pp. 532–538.

Terquem, C., Papaloizou, J. C. B., 2007. "Migration and the formation of systems of hot super-Earths and Neptunes". *ApJ*, 654, pp. 1110–1120.

Thommes, E. W., Duncan, M. J., Levison, H. F., 2003. "Oligarchic growth of giant planets". *Icarus*, 161, pp. 431–455.

Thorsett, S. E., Arzoumanian, Z., Taylor, J. H., 1993. "PSR B1620-26 - A binary radio pulsar with a planetary companion?" *ApJ*, 412, pp. L33–L36.

Tsiganis, K., Gomes, R., Morbidelli, A., Levison, H. F., 2005. "Origin of the orbital architecture of the giant planets of the Solar System". *Nature*, 435, pp. 459–461.

van Leer, B., 1977. "Towards the ultimate conservative difference scheme. IV. A new approach to numerical convection". *J. Comput. Phys.* 23, 3, pp. 276–299.

Varga, R. S., 1962. "Matrix iterative analysis".

Ward, W., 1997. "Protoplanet migration by nebula tides". *Icarus*, 126, 2, pp. 261–281.

Ward, W. R., 1991. "Horsehoe orbit drag". *Lunar and Planetary Science Conference*. Vol. 22. Lunar and Planetary Science Conference.

Weidenschilling, S. J., 1977. "The distribution of mass in the planetary system and solar nebula". *Ap&SS*, 51, pp. 153–158.

Weidenschilling, S. J., 2000. "Formation of planetesimals and accretion of the terrestrial planets". *Space Sci. Rev.* 92, pp. 295–310.

Welsh, W. F., Orosz, J. A., Carter, J. A., Fabrycky, D. C., 2014. "Recent Kepler Results on circumbinary planets". *Formation, Detection, and characterization of extrasolar habitable planets*. Ed. by N. Haghighipour. Vol. 293. IAU Symposium, pp. 125–132.

Welsh, W. F., Orosz, J. A., Carter, J. A., Fabrycky, D. C., Ford, E. B., Lissauer, J. J., Prša, A., Quinn, S. N., Ragozzine, D., Short, D. R., Torres, G., Winn, J. N., Doyle, L. R., Barclay, T., Batalha, N., Bloemen, S., Brugamyer, E., Buchhave, L. A., Caldwell, C., Caldwell, D. A., Christiansen, J. L., Ciardi, D. R., Cochran, W. D., Endl, M., Fortney, J. J., Gautier III, T. N., Gilliland, R. L., Haas, M. R., Hall, J. R., Holman, M. J., Howard, A. W., Howell, S. B., Isaacson, H., Jenkins, J. M., Klaus, T. C., Latham, D. W., Li, J., Marcy, G. W., Mazeh, T., Quintana, E. V., Robertson, P., Shporer, A., Steffen, J. H., Windmiller, G., Koch, D. G., Borucki, W. J., 2012. "Transiting circumbinary planets Kepler-34 b and Kepler-35 b". *Nature*, 481, 7382, pp. 475–479.

Welsh, W. F., Orosz, J. A., Short, D. R., Cochran, W. D., Endl, M., Brugamyer, E., Haghighipour, N., Buchhave, L. A., Doyle, L. R., Fabrycky, D. C., Hinse, T. C., Kane, S. R., Kostov, V., Mazeh, T., Mills, S. M., Müller, T. W. A.,

Quarles, B., Quinn, S. N., Ragozzine, D., Shporer, A., Steffen, J. H., Tal-Or, L., Torres, G., Windmiller, G., Borucki, W. J., 2015a. "Kepler 453 b—The 10th Kepler transiting circumbinary planet". *ApJ*, 809, 1, p. 26.

Welsh, W. F., Orosz, J., Quarles, B., Haghighipour, N., 2015b. "Kepler-47: A three-planet circumbinary system". *AAS/Div. Extrem. Sol. Syst. Abs.*

Williams, J. P., Cieza, L. A., 2011. "Protoplanetary Disks and Their Evolution". *ARA&A*, 49, pp. 67–117.

Wolszczan, A., Frail, D. A., 1992. "A planetary system around the millisecond pulsar PSR1257 + 12". *Nature*, 355, pp. 145–147.

Wright, J. T., Marcy, G. W., Fischer, D. A., Butler, R. P., Vogt, S. S., Tinney, C. G., Jones, H. R. A., Carter, B. D., Johnson, J. A., McCarthy, C., Apps, K., 2007. "Four New exoplanets and hints of additional substellar companions to exoplanet host stars". *ApJ*, 657, pp. 533–545.

Wu, Y., Murray, N., 2003. "Planet migration and binary companions: The case of HD 80606b". *ApJ*, 589, pp. 605–614.

Wyatt, M. C., 2008. "Evolution of debris disks". *ARA&A*, 46, pp. 339–383.

Yang, Y., Hashimoto, J., Hayashi, S. S., Tamura, M., Mayama, S., Rafikov, R., Akiyama, E., Carson, J. C., Janson, M., Kwon, J., de Leon, J., Oh, D., Takami, M., Tang, Y.-w., Kudo, T., Kusakabe, N., Abe, L., Brandner, W., Brandt, T. D., Egner, S., Feldt, M., Goto, M., Grady, C. A., Guyon, O., Hayano, Y., Hayashi, M., Henning, T., Hodapp, K. W., Ishii, M., Iye, M., Kandori, R., Knapp, G. R., Kuzuhara, M., Matsuo, T., Mcelwain, M. W., Miyama, S., Morino, J.-I., Moro-martin, A., Nishimura, T., Pyo, T.-S., Serabyn, E., Suenaga, T., Suto, H., Suzuki, R., Takahashi, Y. H., Takato, N., Terada, H., Thalmann, C., Turner, E. L., Watanabe, M., Wisniewski, J., Yamada, T., Takami, H., Usuda, T., 2017. "Near-infrared imaging polarimetry of inner region of GG Tau A disk". *AJ*, 153, p. 7.

Young, D. M., 1950. "Iterative methods for solving partial differential equations of elliptic type". Doctoral dissertation.

Zhang, H., Yuan, C., Lin, D. N. C., Yen, D. C. C., 2008. "On the orbital evolution of a Jovian planet embedded in a self-gravitating disk". *ApJ*, 676, pp. 639–650.

Zhang, K., Blake, G. A., Bergin, E. A., 2015. "Evidence of Fast Pebble Growth Near Condensation Fronts in the HL Tau Protoplanetary Disk". *ApJ*, 806, p. L7.

Zsom, A., Ormel, C. W., Güttler, C., Blum, J., Dullemond, C. P., 2010. "The outcome of protoplanetary dust growth: pebbles, boulders, or planetesimals? II. Introducing the bouncing barrier". *A&A*, 513, A57.